Nika Valenčič

Fusing the Vector Bosons

Higgs production through VBF and WW scattering at the current and future LHC

Nika Valenčič Fusing the Vector Bosons

2015

Nika Valenčič

Fusing the Vector Bosons

Higgs production through VBF and WW scattering at the current and future LHC

Fusing the Vector Bosons

Higgs production through VBF and WW scattering at the current and future LHC

ACADEMISCH PROEFSCHRIFT

ter verkrijging van de graad van doctor
aan de Universiteit van Amsterdam
op gezag van de Rector Magnificus
prof. dr. D.C. van den Boom
ten overstaan van een door het College voor Promoties ingestelde
commissie, in het openbaar te verdedigen in de Agnietenkapel
op dinsdag 10 november 2015, te 14:00 uur

door

Nika Valenčič

geboren te Postojna, Slovenië

Promotiecommissie:

Promotor:	prof. dr. S. C. M. Bentvelsen (Universiteit van Amsterdam)
Copromotor:	dr. P. Ferrari (Nikhef)
Copromotor:	dr. N. P. Hessey (Nikhef)
Overige leden:	prof. dr. R. J. M. Snellings (Universiteit Utrecht)
	dr. T. Lenz (Universität Bonn)
	prof. dr. J. J. Engelen (Universiteit van Amsterdam)
	prof. dr. W. J. P. Beenakker (Universiteit van Amsterdam)
	prof. dr. ir. P. J. de Jong (Universiteit van Amsterdam)
	prof. dr. ir. E. N. Koffeman (Universiteit van Amsterdam)
	prof. dr. O. B. Igonkina (Radboud Universiteit Nijmegen)

Faculteit der Natuurwetenschappen, Wiskunde en Informatica

Fusing the vector bosons: Higgs production through VBF and WW scattering at the current and future LHC
Typeset by LaTeX
Cover design by Joost de Haas - www.joostdehaas.nl
Cover art by Deepa Rao, *Tree of Knowledge*, 2012
Printed by Gildeprint Drukkerijen - The Netherlands

This work is part of the research program of the *Stichting voor Fundamenteel onderzoek der Materie (FOM)*, which is part of the *Nederlandse organisatie voor Wetenschappelijk Onderzoek (NWO)*. It was carried out at the *Nationaal Instituut voor Subatomaire Fysica (Nikhef)* in Amsterdam, the Netherlands.

DEKLICI, KI SE JE ZALJUBILA V FIZIKO OSNOVNIH DELCEV

I beg you to have patience
with everything unresolved in your heart
and to try to love the questions themselves
as if they were locked rooms
or books written in a very foreign language.

Don't search for the answers,
which could not be given to you now,
because you would not be able to live them.

AND THE POINT IS TO LIVE EVERYTHING.

LIVE THE QUESTIONS NOW.

Perhaps then, someday far in the future
you will gradually, without even noticing it,
live your way into the answer.

Rainer Maria Rilke

CONTENTS

INTRODUCTION

Since the summer of 2012 the world finally makes sense. At least the world of particle physics where the *discovery* of a *Higgs boson* successfully concluded the 40-year long search for this last missing piece of the *Standard Model* puzzle.

The Standard Model (SM) is a quantum field theory describing the dynamics and interactions between the sub-atomic particles. It was first formulated in the 1970s and up until this day every theoretical prediction made by the SM has been verified by the experiments. All but one.

Equations governing the interactions and motion of SM particles assume these particles are *massless* which is not what we observe. From our prestigious experimental setups to our common sense observations we perceive mass as one of the characteristics of matter. The Brout-Englert-Higgs mechanism [1–6], or shortly the Higgs mechanism, circumvents this setback of the SM. It predicts the existence of an omnipresent scalar field, the excitation of which is the Higgs boson particle. By interacting with this field, the before massless SM particles obtain their masses.

The Higgs mechanism is a very elegant addition to the SM but whether it is the correct one still needed to be experimentally verified by searching for the Higgs boson particle itself. Since the Higgs mechanism does not predict the mass of the Higgs boson, a very broad and general hunt had to be carried out.

At the beginning of the Higgs boson searches, possible values of the Higgs mass were somewhere between 10 GeV and 1 TeV. The exclusion limits grew ever more stringent with time and the measurements at the Large-Electron-Positron (LEP) collider and Tevatron cornered the mass of the Higgs boson somewhere between $114.4\,\text{GeV} < m_H < 147\,\text{GeV}$ or $m_H > 179\,\text{GeV}$ [7, 8]. In 2010 the Large Hadron Collider (LHC) started its operation and one of its main goals was to find the Higgs boson. On July 4^{th} 2012, the two general purpose experiments around the LHC ring, ATLAS and CMS, finally confirmed the existence of *a* Higgs boson with the mass of $m_H = 125\,\text{GeV}$ [9, 10]. Whether or not this is indeed the Higgs boson predicted by the SM still needs to be confirmed through measurements of its properties and its production and decay rates.

The SM predicts various decay channels for the Higgs boson and the decay chain studied in this manuscript focuses on the Higgs events decaying first into two W bosons and then subsequently into two lepton-neutrino pairs; $H \to WW^{(*)} \to \ell^+\nu_\ell\ell^-\bar{\nu}_\ell$. The SM also predicts various mechanisms to create the Higgs boson at the LHC. The one that provides the largest amount of events goes via gluon fusion through a top-quark loop.

This thesis probes for a different one, the one that has never been experimentally observed before in the $H \to WW^{(*)}$ channel - the Vector Boson Fusion (VBF). The quest to find the VBF production mode in the $H \to WW^{(*)}$ channel is the main focus of this thesis.

The VBF offers a very specific and clean experimental signature with two highly energetic and well separated jets produced mostly in the forward direction and is crucial for the measurement of the Higgs boson couplings to the vector bosons. Any discrepancies in the (VBF) production rates or coupling measurements from the SM predictions may lead to an indirect detection of New Physics, which might provide hints to a few questions the SM does not

have an answer to. In order to exploit these measurements fully, they should be obtained with the highest precision possible.

The VBF $H \rightarrow WW^{(*)}$ channel suffers from many backgrounds, with one of the most dominant ones coming from the leptonic decays of top-quarks. In order to measure the properties of the Higgs boson as precisely as possible, the backgrounds have to be properly and accurately modelled. Evaluating the systematic uncertainties on the background modelling and reducing them is therefore an essential task to ensure high sensitivity measurements.

However, the statistical limitations also contribute to the total uncertainty on the measurements and they can only be reduced by providing more data. Hence many efforts are put into upgrading the LHC and its experiments towards the so called High Luminosity phase (HL-LHC) which will deliver a factor hundred times more data compared to the current amounts in the next 20 years. With more data and higher collision energies at the HL-LHC many rare processes become available to study and allow for further insights into which theory really *pulls the strings* behind the scenes.

The scattering of the vector bosons is one of these processes that can be fully explored only with an increased dataset. It provides an opportunity to study further aspects of the electroweak symmetry breaking and this thesis explores its sensitivity at the upgraded LHC.

With the increased datasets we can observe more exotic and rare phenomena. On the other hand, reduced statistical uncertainties make the understanding of systematic uncertainties so much more important. The much sought contributions from New Physics may be staring us directly in the eyes, yet we cannot see them being blinded by the error bars. It seems that after all, both God and the Devil are in the details.

Original contributions and the organisation of the manuscript

This manuscript is divided into two parts: Part 1 is focused on the Run-1 using the data collected at the LHC between years 2010 and 2012 and is described in Chapters 1 - 6. Part 2 is dedicated to the HL-LHC and includes Chapters 7 through 10. My original contributions can be found in Chapters 6 through 10.

Part 1: The first run of the LHC

- **Chapter 1:** describes the theoretical background of the Standard Model and the Higgs mechanism.

- **Chapter 2:** provides a general overview of the properties of the SM Higgs boson and describes its production and decay modes at the LHC.

- **Chapter 3:** describes the LHC and the ATLAS detector and summarises their performance during the Run-1 operation.

- **Chapter 4:** reviews the object and event reconstruction algorithms used in the ATLAS experiment during the 2012 data-taking and outlines the particularities of these algorithms and requirements for the $H \rightarrow WW^{(*)}$ analysis.

The following three chapters are dedicated to the search for the VBF production mode in the $H \rightarrow WW^{(*)}$ channel. The analysis concentrates on $20.3\ \text{fb}^{-1}$ of the recorded data by the ATLAS detector during the 2012 data-taking at $\sqrt{s} = 8\,\text{TeV}$. I actively participated in the analysis between 2013 and 2014.

◦ **CHAPTER 5:** gives an overview of the (VBF) $H \to WW^{(*)}$ analysis. It outlines the background processes to the Higgs signal and describes the VBF event selection.

◦ **CHAPTER 6:** describes the evaluation of background contributions in the VBF $H \to WW^{(*)}$ signal-enriched region and is particularly dedicated to one of the largest backgrounds arising from top-quark decays. I was responsible for evaluating the systematic uncertainties on the top-quark background estimation where I studied various sources of systematic uncertainties and through my work eliminated some of them. This is not only important for obtaining a more accurate experimental measurement but also for a deeper understanding of the top-quark background modelling. I also worked on optimising the event selection in the top-quark background control region (a region predominantly containing top-quark events used for estimating the modelling between the top-quark MC and the data) and contributed to the final decision to change the nominal top-quark MC generator. I was also responsible for other smaller tasks, like evaluating the systematic uncertainties on the VBF signal.

◦ **CHAPTER 7:** describes the statistical procedure applied in the $H \to WW^{(*)}$ data analysis and presents the results on the VBF signal strength measurement, emphasising the impact of the systematic uncertainties on the final results. The measurement of the Higgs boson couplings and combination with the ggF analysis is also summarised.

PART 2: FUTURE RUNS AT THE LHC

◦ **CHAPTER 8:** summarises the main upgrade procedures for the LHC and the ATLAS detector in the next decades, with a greater focus on the Phase-II upgrade during 2024-2026.

In order to give accurate and reliable predictions of the detector performance and its impact on physics searches, the upgraded ATLAS detector must be accurately simulated. As a part of my ATLAS qualification task I worked on building an accurate geometric description of the upgraded ATLAS detector, more specifically on the simulation of the strip end-cap sensors in the new Inner Tracker (ITk) which will replace the current Inner Detector.

◦ **CHAPTER 9:** is dedicated to the feasibility study analysing the prospects of the $H \to WW^{(*)}$ analysis at the HL-LHC and is done within the scope of the European Committee for Future Accelerators (ECFA). I was part of a small group (5 people) and my contributions are focused on the VBF production mode where I optimised the event selection and ran the analysis framework for the HL-LHC conditions.

◦ **CHAPTER 10:** is dedicated to the feasibility study analysing the possible increase in sensitivity of vector boson scattering and New Physics at the HL-LHC, in particular to the benefits of extending the forward tracking capabilities of the ITk. I was part of a small group (3 people) and therefore participated in all aspects of the analysis: Monte Carlo sample generation, event selection, performance studies and statistical analysis.

The manuscript finishes with conclusions and summary.

Part I.

THE FIRST RUN OF THE LHC

1 THE STANDARD MODEL OF PARTICLE PHYSICS

1.1 The Universe as we know it

Once upon a time, we *knew* that 4 basic elements built our Universe; air, water, fire and earth. We *know* better now. We *know* that our Universe, ourselves and all matter surrounding us is actually built out of a few different particles; electrons orbiting a nucleus which is composed of protons and neutrons, together forming atoms. The difference between what all the great thinkers of our ancient times knew and what we know now is only in how energetic are the probes with which we study ourselves and the world around us. By now we have discovered the complete particle zoo at our energy scale (few hundred GeV) but we are also quite confident that there is something more beyond our current understanding of the Universe. There are far too many open questions and mysteries about our surroundings to imply that what we know now is the ultimate answer. Apart from theory and imagination we have no detailed knowledge of what awaits us at the TeV scale and in order to explore the Universe further, we need probes with higher energy. With the help of future high(er) energy particle colliders we hope to get more insights into the structure of matter and the Universe.

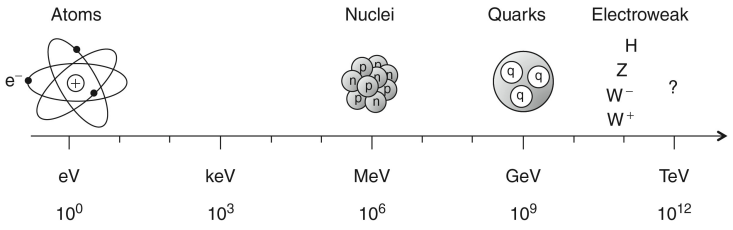

Figure 1.: Our perception of the Universe at different energy scales from atomic physics to modern particle physics at the TeV scale [11].

1.1.1 Fundamental particles and interactions

In the vast scope of theoretical physics, experimental data favours one theory in particular. Even though there are a couple of phenomena for which the *Standard Model* does not provide a clear answer, it still represents a consistent and complete description of reality at our current energy scale.

The Standard Model of particle physics is a *renormalizable Quantum Field Theory* (QFT) describing the matter content of the Universe. It divides particles into those which constitute matter and those which carry the interactions between them.

FORCES: At the level of particle physics, three fundamental interactions guide all natural phenomena; electromagnetic, weak and strong force and are described in Table 1. Each interaction is described by a QFT where a *gauge boson*, a spin-1 force carrying particle, steers the interactions between matter particles. Gravity, responsible for all large-scale structures in the Universe, is not included in the Standard Model since it is much weaker than the other three forces[1].

Force	gauge boson		spin	Q	mass [GeV]
Electromagnetic	photon	γ	1	0	0
Weak	W boson	$W^{\pm}$	1	± 1	80.385 ± 0.015
	Z boson	Z	1	0	91.1876 ± 0.0021
Strong	gluon	g	1	0	0
Gravity	graviton ?	G	2	0	0

Table 1.: All four fundamental interactions and their properties [12]. Q represents the electric charge in the units of the electron charge.

MATTER: Table 2 shows all twelve elementary fermions, spin-1/2 particles, which make up all visible matter in our Universe. Fermions are split into three generations where the second and the third generation are the exact copies of the first one, differing only in the larger masses of constituent particles.

Depending whether they interact via strong force or not, fermions are being divided into two groups: quarks and leptons. *Quarks* carry the so called *color charge* and can undergo strong interactions alongside the weak and electromagnetic interactions, while *leptons* cannot. Due to the nature of the strong force, quarks are never observed as free particles and are confined into *hadrons*, bound states with neutral colour charge. Hadrons composed of three quark states are called *baryons* (e.g. a proton composed of uud quarks) with a half-integer spin, while those composed of quark and anti-quark pairs are called *mesons* (e.g. pion π^+ composed of a $u\bar{d}$ pair) and have an integer spin.

Leptons only interact through electromagnetic and weak force, apart from neutrinos which can only interact via weak force since they do not carry electric charge nor colour charge.

	Leptons				Quarks			
	particle		mass [MeV]	Q	particle		mass [MeV]	Q
I. generation	electron	e^-	$0.511 \pm 0.11 \times 10^{-7}$	-1	up	u	$2.3^{+0.7}_{-0.5}$	$+2/3$
	electron neutrino	ν_e	$< 2 \times 10^{-6}$	0	down	d	$4.8^{+0.7}_{-0.3}$	$-1/3$
II. generation	muon	μ^-	$105.66 \pm 35 \times 10^{-7}$	-1	charm	c	$(1.275 \pm 0.025) \times 10^3$	$+2/3$
	muon neutrino	ν_μ	$< 0.19 \times 10^{-6}$	0	strange	s	95 ± 5	$-1/3$
III. generation	tau	τ^-	1776.82 ± 0.16	-1	top	t	$(173.21 \pm 0.51 \pm 0.71) \times 10^3$	$+2/3$
	tau neutrino	ν_τ	$< 18.2 \times 10^{-6}$	0	bottom	b	$(4.18 \pm 0.03) \times 10^3$	$-1/3$

Table 2.: All twelve spin-1/2 elementary fermions and their properties [12].

For every fermion and boson there exists an *anti*-particle, with exactly the same mass and spin but opposite electric charge (some neutral particles are their own anti-particles, like the photon).

1 Relative strength of the gravitational force between two particles at the distance of 1 fm is 10^{-37} times smaller than the strong force, 10^{-34} times smaller than the electromagnetic force and 10^{-29} times smaller than the weak force

This chapter focuses on the theoretical description of the Standard Model (SM) through the concepts of QFT. Each of the three fundamental interactions is described by a local gauge invariant symmetry group. Quantum electrodynamics (QED) is described by the $U(1)_{EM}$ symmetry group and explains the dynamics and interactions of electrically charged fermions. Quantum chromodynamics (QCD) is understood under the $SU(3)$ symmetry group and describes the interactions between particles carrying the color charge. The Glashow-Weinberg-Salam (GWS) model combines the electromagnetic and weak force under the $SU(2)_L \otimes U(1)_Y$ electroweak symmetry group and combined with the Higgs mechanism and QCD forms the complete description of the Standard Model. All these SM building blocks are described in a greater detail in the following sections. But before the properties of each QFT are scrutinised, a very important concept in physics deserves its "few lines of fame" - symmetries.

1.1.2 Theoretical description of interactions in the Standard Model

Symmetries

In a Quantum Field Theory (QFT) particles are seen as excitations (quanta) of their fields[2] $\psi(x)$, e.g. the photon is perceived as a quantum of the electrodynamic field A_μ. The Lagrangian density[3] $\mathcal{L}$ is defined as a function of fields and their derivatives

$$\mathcal{L}(x) = \mathcal{L}(\psi, \partial_\mu \psi) \tag{1}$$

and describes the dynamics of particles.

Symmetries represent one of the key points in *gauge* theories and they arise whenever a $\mathcal{L}$ is invariant under a *continuous* transformation of its variables (fields). There are several different types of symmetries[4] and for a construction of a gauge invariant QFT, like the SM, *internal* symmetries play a very important role.

Internal symmetries act on internal quantum numbers. They are divided into *global* symmetries (the transformations are the same for all points of space-time) and *local* or *gauge* symmetries (transformations differ at different points in space-time). The invariance of the Lagrangian, $\delta\mathcal{L} = 0$, on the *continuous global* symmetries leads to conserved currents j_μ,

$$\partial_\mu j^\mu = 0, \tag{2}$$

and is better known as the *Noether's theorem*, while *continuous local* symmetries implicate the existence of gauge bosons, i.e. the interactions between fields in the $\mathcal{L}$.

A QFT describes symmetries through *groups* and all continuous local symmetries form a Lie group[5]. The properties of all three fundamental interactions are understood through the *gauge invariance principle* which ensures that all interactions are renormalisable and invariant under local phase transformations.

2 From this point on the field $\psi(x)$ will be written only as ψ, but a dependence on space-time coordinates is implied.

3 Lagrangian L is an integral over the spatial coordinates of the Lagrangian density $L = \int \mathrm{d}^3\mathcal{L}$. However, from here onwards, the Lagrangian density $\mathcal{L}$ will be simply called the "Lagrangian".

4 Symmetries are primarily divided into *discrete* (e.g. time and charge reversal) and *continuous* symmetries. The latter are additionally separated into *geometric or space-time* symmetries (e.g. space translation and rotation) and *internal* symmetries.

5 A Lie group is a continuous group where an element in a group can be expressed by an analytic function[13].

Quantum electrodynamics - QED

The dynamics of massive spin-1/2 particles - fermions, is described by the Dirac equation[6]. The associated Dirac Lagrangian is defined as

$$\mathcal{L} = i\bar{\psi}\gamma^{\mu}\partial_{\mu}\psi - m\psi\bar{\psi}, \tag{3}$$

where ψ ($\bar{\psi} = \psi^{\dagger}\gamma^{0}$) is the Dirac spinor (field) and γ^{μ} are the Dirac gamma matrices.

The Dirac Lagrangian is invariant under the *global* phase transformation of $U(1)_{EM}$ - the unitary and abelian[7] gauge symmetry group that transforms the fields and their derivatives as

$$\begin{aligned} \psi &\xrightarrow{U(1)_{EM}} \psi' = e^{ig_{EM}\alpha}\psi, \\ \partial_{\mu}\psi &\xrightarrow{U(1)_{EM}} \partial_{\mu}\psi' = e^{ig_{EM}\alpha}\partial_{\mu}\psi \end{aligned} \tag{4}$$

and $e^{ig_{EM}\alpha}$ is its one-dimensional representation. According to the Noether's theorem, the invariance under the $U(1)_{EM}$ global gauge symmetry results in a conserved current defined by

$$j^{\mu}_{EM} = g_{EM}\bar{\psi}\gamma^{\mu}\psi. \tag{5}$$

Invoking a local gauge symmetry from a global one (by making the parameter α dependent on space-time coordinates) breaks the invariance of the theory since the fields and their derivatives do not transform in the same way any more;

$$\begin{aligned} \psi &\xrightarrow{U(1)_{EM}} \psi' = e^{ig_{EM}\alpha(x)}\psi, \\ \partial_{\mu}\psi &\xrightarrow{U(1)_{EM}} \partial_{\mu}\psi' = e^{ig_{EM}\alpha(x)}\partial_{\mu}\psi + ig_{EM}e^{ig_{EM}\alpha(x)}(\partial_{\mu}\alpha(x))\psi. \end{aligned} \tag{6}$$

However, introducing an additional gauge vector field $A_{\mu} = A_{\mu}(x)$ and replacing the derivative ∂_{μ} with the *gauge-covariant derivative* D_{μ}, restores the local gauge invariance. The gauge-covariant derivative is defined as

$$D_{\mu} \equiv \partial_{\mu} + ig_{EM}A_{\mu}(x) \tag{7}$$

and ensures that field derivatives $D_{\mu}\psi$, transform in the same way as fields do under the local phase transformation;

$$D_{\mu}\psi \xrightarrow{U(1)_{EM}} D_{\mu}\psi' = e^{ig_{EM}\alpha(x)}D_{\mu}\psi, \tag{8}$$

provided that the vector field A_{μ} transforms as

$$A_{\mu} \xrightarrow{U(1)_{EM}} A'_{\mu} = A_{\mu} - \partial_{\mu}\alpha(x). \tag{9}$$

The concept of introducing new vector boson fields to the local gauge theory in order to restore its broken invariance is the key point of all gauge theories. The vector field A_{μ} is associated with the *photon*, the quantum of the field A_{μ} and represents the gauge boson of QED responsible for establishing the interactions between fermions.

6 The Dirac equation is defined as $(i\gamma^{\mu}\partial_{\mu} - m)\psi = 0$.

7 Different transformations of the group commute with each other.

The QED Lagrangian can be rewritten as

$$\begin{aligned}\mathcal{L} &= i\bar{\psi}\gamma^\mu D_\mu\psi - m\psi\bar{\psi} \\ &= \bar{\psi}(i\gamma^\mu\partial_\mu - m)\psi - g_{EM}A_\mu\bar{\psi}\gamma^\mu\psi \\ &= \mathcal{L}_{free} - j^\mu A_\mu,\end{aligned} \tag{10}$$

where j^μ represents the conserved current with the same form as in Equation 5. The constant g_{EM} in $U(1)_{EM}$ definition represents the coupling strength between a fermion and a photon and it coincides with the electric charge of a particle. However, $\mathcal{L}$ is not yet complete since it lacks additional (gauge invariant) terms related to the kinetic energy (photon propagation) and the mass of the gauge boson. The kinetic term of the photon is described by the field strength tensor $F_{\mu\nu}$, defined as

$$F_{\mu\nu} = \partial_\mu A_\nu - \partial_\nu A_\mu \tag{11}$$

and the photon's mass term is proportional to $\propto m_\gamma^2 A_\mu A^\mu$. The mass term remains invariant under the local gauge transformation *only* if m_γ equals zero;

$$m_\gamma^2 A^\mu A_\mu \xrightarrow{U(1)_{EM}} m_\gamma^2(A^\mu - \partial^\mu\alpha(x))(A_\mu - (\partial_\mu\alpha(x))) \neq m_\gamma^2 A^\mu A_\mu. \tag{12}$$

The local gauge invariance of QED is restored by introducing a *massless* gauge boson - the photon. The complete Lagrangian for QED is therefore defined as

$$\mathcal{L}_{QED} = \mathcal{L}_{free} - j^\mu A_\mu - \frac{1}{4}F_{\mu\nu}F^{\mu\nu} \tag{13}$$

and directly leads to Maxwell's equations with a source j^μ.

Quantum chromodynamics - QCD

Quantum chromodynamics describes the dynamics and interactions between fermions carrying the *color* charge, i.e. quarks. In the SM all flavours of quarks (u, d, s, c, t, b) appear in three *color* states - red, green and blue and Ψ signifies a color triplet of Dirac fields defined as

$$\Psi \equiv \begin{pmatrix} \psi_{red} \\ \psi_{green} \\ \psi_{blue} \end{pmatrix}, \qquad \overline{\Psi} \equiv \left(\overline{\psi_{red}}, \overline{\psi_{green}}, \overline{\psi_{blue}}\right). \tag{14}$$

Analogous to QED, the Lagrangian for QCD looks like

$$\mathcal{L} = i\,\overline{\Psi}\gamma^\mu\partial_\mu\Psi - m\overline{\Psi}\Psi, \tag{15}$$

where m is a 3×3 diagonal mass matrix for a specific quark flavour and is the same for all three color states.

Quantum chromodynamics is invariant under the $SU(3)$ symmetry group[8]. The local phase transformation representing the $SU(3)$ group is described by

$$\Psi \xrightarrow{SU(3)} \Psi' = e^{ig_s\,\alpha^a(x)T^a}\Psi \tag{16}$$

where $T^a = \frac{1}{2}\lambda^a$ are the 3×3 matrices representing the eight generators of the $SU(3)$ group related to the Gell-Mann matrices λ^a, and $\alpha^a(x_\mu)$ are eight space-time dependent functions[9].

8 $SU(N)$ stands for an N-dimensional *special unitary group* with N^2-1 generators with determinant 1.

9 The product $\alpha^a(x)T^a$ is short for a dot product $\alpha^1 T^1 + \cdots + \alpha^8 T^8$.

Comparable to QED, the Lagrangian stays invariant under the *local* gauge transformation only if the gauge covariant derivative D_μ, defined as

$$D_\mu \equiv \partial_\mu + ig_S\, T^a \cdot G^a_\mu = \partial_\mu + ig_S\, G_\mu, \tag{17}$$

replaces ∂_μ. In addition, the new massless gauge boson fields G^a_μ have to transform as

$$G^k_\mu \xrightarrow{SU(3)} G'^k_\mu = G^k_\mu - \partial_\mu \alpha_k(x) - g_S f_{ijk} \alpha_i(x) G^j_\mu, \tag{18}$$

where f_{ijk} are the so called *structure constants* of the $SU(3)$ group defined by the commutation relation $[\lambda_i, \lambda_j] = 2if_{ijk}\lambda_k$. Additional gauge boson fields appear in eight color states, $a = 1, \ldots, 8$ for each generator of the $SU(3)$ group and are associated with eight *gluons* of the strong force. Transformations of gauge bosons under the $SU(3)$ symmetry group differ from transformations of the gauge boson under the $U(1)_{EM}$ by the last term in Equation 18 - $f_{ijk}\alpha_i(x)G^j_\mu$. This term appears since the generators of the $SU(3)$ group *do not* commute between each other, indicating the *non-abelian* nature of QCD.

Following the analogy from QED, the complete QCD Lagrangian requires a kinetic term for the gauge bosons in a form of a field strength tensor $F^{\mu\nu}$. In the case of QCD, the $F^{\mu\nu}$ is defined as

$$F^{\mu\nu}_i = \partial^\mu G^\nu_i - \partial^\nu G^\mu_i - g_S f_{ijk} G^\mu_j G^\nu_k, \tag{19}$$

and where $F^{\mu\nu}$ lead to the Maxwell's equations in QED, its non-abelian nature in QCD leads to self-interactions between gluons;

$$\begin{aligned} &\text{triple gauge boson interactions} : ig_S Tr(\partial_\nu G_\mu - \partial_\mu G_\nu)[G_\mu, G_\nu], \\ &\text{quartic gauge boson interactions} : \frac{1}{2} g_S^2 Tr[G_\mu, G_\nu]^2. \end{aligned} \tag{20}$$

The complete QCD Lagrangian is therefore defined as

$$\mathcal{L}_{QCD} = \overline{\Psi}(i\gamma^\mu \partial_\mu - m)\Psi - (g_S \overline{\Psi}\gamma^\mu T\, \Psi) G_\mu - \frac{1}{4} F^{\mu\nu}_i F_{i\,\mu\nu}, \tag{21}$$

where g_S represents the strong coupling constant between quarks and gluons.

Interactions between Dirac fields (quarks) and gauge bosons (gluons) of the $SU(3)$ symmetry group give rise to eight quark-color currents

$$j^{\mu,a}_S = \overline{\Psi}\gamma^\mu T^a \Psi. \tag{22}$$

However, quark currents are not real QCD Noether's currents since $\partial_\mu j^\mu \neq 0$. In QCD, both Dirac fields and gauge bosons carry the color charge (in contrast to QED, where the photon is electrically neutral), hence the actual conserved Noether's currents ($\partial^\mu I^a_\mu = 0$) have contributions from both quark and gluon fields

$$I^a_\mu = j_S{}^a_\mu + f_{abc} F^b_{\mu\nu} G^\nu_c. \tag{23}$$

Weak Interactions

The weak interaction is quite different from electromagnetic and strong interactions. First of all, it has two types of currents: a neutral current mediated by the Z boson and a charged current mediated by $W^\pm$ bosons. Contrary to electromagnetic and strong currents, the charged weak current arises only between fermions with electric charges differing for one unit. Addi-

tionally, the weak interaction is also the only interaction which *violates parity* and has massive force carriers.

Any Dirac field ψ can be decomposed into its *left-handed* (LH) and *right-handed* (RH) component, $\psi = \psi_R + \psi_L$, through *chiral projection operators* P_R and P_L, defined as

$$P_R = \frac{1+\gamma^5}{2} \longrightarrow P_R\psi = \psi_R, \qquad P_L = \frac{1-\gamma^5}{2} \longrightarrow P_L\psi = \psi_L, \tag{24}$$

where γ^5 denotes a Dirac matrix defined as $\gamma^5 \equiv i\gamma^0\gamma^1\gamma^2\gamma^3$. Experiments show that the charged weak current couples only to LH *particles* or RH *anti-particles* and *not* to RH particles nor LH anti-particles. This is macroscopically expressed as violation of parity. To be more exact, the charged current is mediated only between LH particle states differing for one unit of electric charge.

The gauge symmetry group describing the weak interaction is, similar to QCD, the non-Abelian $SU(N)$ gauge symmetry group, where a suitable choice is the special unitary group of dimension two $SU(2)_L$ that transforms the fields φ as

$$\varphi \xrightarrow{SU(2)_L} \varphi' = e^{ig_W\alpha(x)\cdot\tau}\varphi, \tag{25}$$

where τ represents the three generators of the $SU_L(2)$ group, 2×2 matrices related to the Pauli spin matrices $\tau = \frac{1}{2}\sigma$. Since the weak interaction couples only to LH particles and RH anti-particles, the fields φ are described as a two-component vector of LH chiral Dirac fields, the so called *weak isospin* doublets, defined as

$$\varphi(x): \quad \begin{pmatrix} \nu_\ell(x) \\ \ell(x) \end{pmatrix}_L \text{ or } \begin{pmatrix} \boldsymbol{u}(x) \\ \boldsymbol{d}(x) \end{pmatrix}_L, \tag{26}$$

where ℓ represents all three lepton families ($\ell = e^-, \mu^-, \tau^-$) and $\boldsymbol{u}, \boldsymbol{d}$ up- and down-type quarks ($\boldsymbol{u} = u, c, t$, $\boldsymbol{d} = d, s, b$).

Both particles in the isospin doublet have a total weak isospin, I_W, equal to one half. The third component of the weak isospin I_W^3, is positive for the upper component of the weak isospin doublet $I_W^3(\nu_\ell, u) = +1/2$ and negative for the lower component $I_W^3(\ell, d) = -1/2$. Right-handed particles and left-handed antiparticles do not participate in the weak interaction and are therefore defined as *isospin singlets* with $I_W = I_W^3 = 0$

$$(\ell)_R, \quad (\boldsymbol{u})_R, \quad (\boldsymbol{d})_R. \tag{27}$$

The isospin singlets do not couple to the gauge bosons of the symmetry and are therefore not affected by the $SU(2)_L$ local symmetry gauge transformation. Right-handed neutrino states are left out from the weak isospin singlets since there has been no direct evidence so far of their existence (although recent observations of neutrino oscillations might suggest otherwise).

The local gauge invariance under the $SU(2)_L$ symmetry can be restored following the same procedure as in QCD. Three new gauge bosons W^k, transforming as denoted in Equation 18[10], and a gauge invariant derivative, as defined in Equation 17, are needed to restore the $SU(2)$ gauge invariance. The interactions described by the $SU(2)_L$ symmetry group give rise to three Noether's currents j_W^μ,

$$j_W^{\mu,k} = g_W\overline{\varphi_L}\gamma^\mu\tau^k\varphi_L. \tag{28}$$

10 The structure constant now represents the commutator relation $[\tau^i, \tau^j] = 2\epsilon_{ijk}\tau^k$.

The actual physical charged weak currents correspond to the exchange of the $W^{\pm}$ bosons. They are equivalent to raising or lowering the isospin of the weak isospin doublet $j^{\mu}_{W,+}$ and $j^{\mu}_{W,-}$, and can be written as a linear combination of two of the Noether's currents j^{μ}_1 and j^{μ}_2 as

$$j^{\mu}_{W,\pm} = \frac{1}{\sqrt{2}}(j^{\mu}_1 \pm i j^{\mu}_2). \tag{29}$$

An additional manipulation reveals the *vector-axialvector* (V-A) nature of weak currents

$$j^{\mu}_{W,+} = \frac{g_W}{\sqrt{2}}\overline{\nu_{\ell L}}\gamma^{\mu}\frac{1}{2}(1-\gamma^5)\ell_L, \qquad j^{\mu}_{W,-} = \frac{g_W}{\sqrt{2}}\overline{\ell_L}\gamma^{\mu}\frac{1}{2}(1-\gamma^5)\nu_{\ell L}. \tag{30}$$

The remaining current $j^{\mu}_{W,3}$, can be associated with the *weak neutral current* which is mediated by the Z boson, and couples to *all* left-handed fermions f_L,

$$j^{\mu}_{W,3} = g_W\overline{f_L}\gamma^{\mu}\frac{1}{2}(1-\gamma^5)f_L. \tag{31}$$

Even if the arguments look peachy and convincing, there are two things intrinsically wrong with the above description of the weak interaction. One was already mentioned earlier and deals with the fact that all experiments observe the three gauge bosons as having masses greater than zero and quite considerably greater than zero ($\sim 80,90\,\mathrm{GeV}$) for that matter. However, the idea of local gauge invariance holds only because the newly introduced gauge bosons (W_k) are massless (see Equation 12). This particular feature of gauge invariance did not cause any problems in QED nor QCD since both photons and gluons are massless. In the case of the weak interaction, however, it highly contradicts all experimental findings.

The second clash between the theory of weak interactions and experimental measurements is due to the neutral current. All experiments show that the neutral weak current couples to *both*, the left- and right-handed chiral states (not equally) and not only to the left-handed states as indicated in Equation 31. The "cure" for both issues of weak interactions hides in the electroweak unification and the Higgs mechanism, which are the focus points of the next section.

1.2 The Higgs mechanism

Many theoretical physicists dream of grand unification of all four forces (including gravity) into one fundamental interaction. So far a few of them only partially succeeded in this grand gesture. Maxwell was first to unify the electrostatic and magnetic force into electromagnetism and Glashow, Weinberg and Salam (GWS) [14–16] showed that electromagnetic and weak force are actually different manifestations of one fundamental electroweak interaction[13]. The GWS model together with the *Higgs mechanism* [1–6] represents one of the greatest successes of theoretical particle physics in the past century. The GWS model combines the electromagnetic and weak forces under the $SU(2)_L \otimes U(1)_Y$ symmetry group and the Higgs mechanism provides masses for gauge bosons and fermions through spontaneous symmetry breaking.

1.2.1 The Electroweak Unification

The theoretical description of quantum electrodynamics via the $U(1)_{EM}$ gauge symmetry group is well understood and agrees perfectly with experimental findings. The description of the weak interaction through the $SU(2)_L$ symmetry is unfortunately not completely

experiment-proof, but it still holds a convincing representation of the parity violating nature of the weak interaction.

In the GWS electroweak model, the description of the weak interaction through the $SU(2)_L$ symmetry group with left-handed isospin doublets ψ, is combined with the $U(1)_Y$ symmetry group representing electromagnetism, where the electric charge Q is replaced by the *weak hypercharge* Y[11]. The weak hypercharge is defined as a linear combination of the electric charge and the third component of the weak isospin, I_W^3. By construction, the Y and I_W generators commute,

$$Y = 2(Q - I_W^3). \tag{32}$$

Such a definition of the weak hypercharge ensures the invariance under both $SU(2)_L$ and $U(1)_Y$ local gauge transformations since Y is the same for both Dirac fields in the isospin doublet[12]. Table 3 shows the quantum numbers for all fermions under the $SU(2)_L \otimes U(1)_Y$ symmetry group.

Particle	$SU(2)_L : I_W^3$		$U(1)_Y : Y$		$U(1)_{EM} : Q$
	LH	RH	LH	RH	
ℓ	$-1/2$	0	-1	-2	-1
ν_ℓ	$+1/2$	0	-1	0	0
$\boldsymbol{u}$	$+1/2$	0	$+1/3$	$+4/3$	$+2/3$
$\boldsymbol{d}$	$-1/2$	0	$+1/3$	$-2/3$	$-1/3$

Table 3.: Quantum numbers of $SU(2)_L \times U(1)_Y$ symmetry group: electric charge Q, third component of the weak isospin I_W^3 and hypercharge Y for all SM fermions. ℓ indicates all three leptons families e^-, μ^-, τ^- and $\boldsymbol{u}$ and $\boldsymbol{d}$ all three families of up- and down-type quarks. LH represents the left-handed doublet and RH the right-handed singlet in $SU(2)_L$ symmetry group.

In the electroweak theory, the product of transformations generated by I_W^3 and Y describes the transformations of isospin doublets;

$$\psi \xrightarrow{SU(2)_L \otimes U(1)_Y} \psi' = e^{ig_Y \frac{Y}{2}\alpha(x)} e^{ig_W \alpha(x)\cdot\tau}\psi, \tag{33}$$

where g_W and g_Y are the coupling strength constants of the electroweak interaction. In order to preserve the local gauge invariance of the electroweak theory, four massless gauge bosons need to be introduced - $W_\mu^1, W_\mu^2, W_\mu^3$ for $SU(2)_L$ and B_μ for $U(1)_Y$. A gauge invariant derivative of the electroweak theory is defined as

$$D_\mu \equiv \partial_\mu + ig_W \tau_a W_\mu^a + ig_Y \frac{Y}{2} B_\mu \tag{34}$$

and leads to the Lagrangian of electroweak theory, which can be split into two contributions;

$$\mathcal{L} = \mathcal{L}_{gauge} + \mathcal{L}_{fermions}. \tag{35}$$

The dynamics of all four gauge bosons are described by

$$\mathcal{L}_{gauge} = -\frac{1}{4} W_{\mu\nu}^i W_i^{\mu\nu} - \frac{1}{4} B_{\mu\nu} B^{\mu\nu}, \tag{36}$$

11 Left-handed neutrinos interact only through weak interaction and therefore transform as $SU(2)_L$ doublets. But since they are electrically neutral they do not transform under $U(1)_{EM}$. In order for neutrinos to transform under the unified electroweak symmetry group, Y must be used instead of Q as a generator of the $U(1)$ group.

12 If Y would differ between the fields in the weak isospin doublet, then the $SU(2)_L \otimes U(1)_Y$ symmetry would be broken since the upper and lower component of the weak isospin doublet would transform differently under $U(1)_Y$ symmetry group.

where $W^i_{\mu\nu}$ and $B_{\mu\nu}$ represent the field strength tensors for the W^k_μ and B_μ fields, respectively and have the same form as defined in Equation 19 and Equation 11. The fermionic part of the Lagrangian is divided into two terms since ψ_R does not couple to weak isospin while ψ_L does;

$$\begin{aligned}\mathcal{L}_{fermions} = & \\ &= \overline{\psi_R} i\gamma^\mu \left(\partial_\mu + \frac{ig_Y}{2} B_\mu Y\right) \psi_R + \overline{\psi_L} i\gamma^\mu \left(\partial_\mu + \frac{ig_Y}{2} B_\mu Y + \frac{ig_W}{2} \tau^a W^a_\mu\right) \psi_L.\end{aligned} \tag{37}$$

Thus far, all four gauge bosons are still left massless. Furthermore, the mass term for fermions, $\propto m_\ell \overline{\psi}\psi$, is also missing and adding such a mass term "by hand" to the electroweak Lagrangian would violate the $SU(2)_L$ invariance;

$$m_\ell \overline{\ell}\ell = m_\ell \overline{\ell} \left(\frac{1}{2}(1-\gamma^5) + \frac{1}{2}(1+\gamma^5)\right) \ell = m_\ell \left(\overline{\ell_R}\ell_L + \overline{\ell_L}\ell_R\right). \tag{38}$$

Therefore, the local gauge invariance of the electroweak unification, besides the massless gauge bosons, also condemns fermions to the eternal masslessness, which highly contradicts all experimental facts about particle physics. However, the GWS model would not be such an ingenious theory if this nuisance would not be taken care of.

Indeed, a mechanism exists that generates masses for the $W^\pm$ and Z gauge bosons and all fermions while keeping the photon massless and the whole theory invariant and renormalisable. The price of such a mechanism is *spontaneous breaking* of the (local gauge) symmetry of the electroweak theory to the electromagnetic $U(1)_{EM}$ symmetry,

$$SU(2)_L \otimes U(1)_Y \longrightarrow U(1)_{EM}. \tag{39}$$

The mechanism also postulates the existence of a scalar (spin-0) field - the Higgs boson and is discussed next.

1.2.2 The Electroweak Symmetry Breaking (EWSB)

The 60s and the 70s of the previous century were very fruitful years for theoretical particle physics. Many important insights were placed as foundations for the *Higgs mechanism* which completes the description of the Standard Model. One of them was the *Goldstone theorem* stating that a *spontaneous* breaking of a continuous global symmetry is always accompanied by massless scalar particles - *Goldstone bosons*. The Goldstone bosons occur for every broken generator of symmetry group carrying their quantum numbers. If additionally, the theory also possesses the local gauge invariance then a very beneficial cooperation between the massless gauge fields and the additional massless Goldstone bosons occurs. The additional degrees of freedom corresponding to the Goldstone boson are absorbed by the gauge bosons of the broken generators and they obtain mass.

A simplified example of a spontaneous symmetry breaking (SSB) is shown through the global phase transformation $U(1) = e^{i\alpha}$. A potential $V(\phi)$ of a complex scalar field $\phi = \frac{1}{\sqrt{2}}(\phi_1 + i\phi_2)$, is added to the Lagrangian invariant under the $U(1)$ symmetry group, where fields transform as $\phi \longrightarrow \phi' = e^{+i\alpha}\phi$;

$$\begin{aligned} V(\phi) &= \mu^2(\phi^*\phi) + \lambda(\phi^*\phi)^2, \\ \mathcal{L} &= (\partial_\mu\phi)^*(\partial^\mu\phi) - V(\phi). \end{aligned} \tag{40}$$

For a potential $V(\phi)$ to have the lowest energy state (vacuum), λ must be positive. Additionally, depending on whether μ^2 is positive or negative, two possible minima of the potential $V(\phi)$ exist, as is shown in Figure 2. In case $\mu^2 > 0$ the potential reaches the global

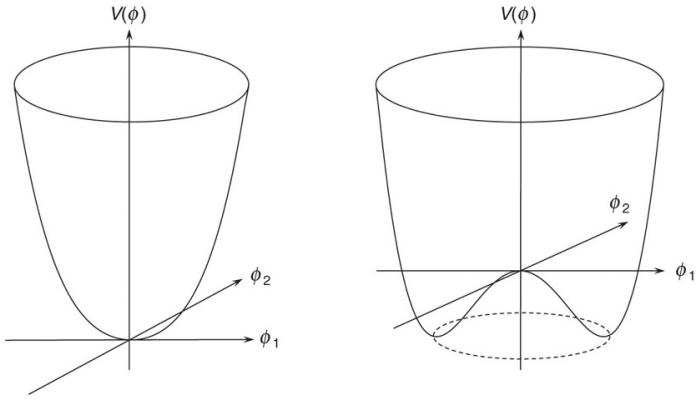

Figure 2.: The potential for a complex scalar field $V(\phi) = \mu^2(\phi^*\phi) + \lambda(\phi^*\phi)^2$ for $\mu^2 > 0$ (left) and $\mu^2 < 0$ (right) [11].

minimum at $\phi = 0$ and the Lagrangian from Equation 40 represents a scalar particle ϕ with mass μ and a four-point self interaction term proportional to λ. For negative values of μ^2 however, $\mu^2(\phi^*\phi)$ can no longer be interpreted as a mass term and the potential obtains an infinite set of minima lying on a circle (indicated in Figure 2) with radius

$$\phi_0^2 = \phi_1^2 + \phi_2^2 = \frac{-\mu^2}{\lambda} \equiv v^2. \tag{41}$$

In this case, the vacuum is not unique and has a *non-zero* vacuum expectation value (vev) v. Furthermore, it loses the $U(1)$ symmetry since

$$\phi_0 = ve^{i\beta} \xrightarrow{U(1)} \phi_0' = ve^{i\beta}e^{i\alpha} \neq \phi_0, \tag{42}$$

where β is real and arbitrary. Whenever a symmetry of the Lagrangian is not respected by the vacuum state, the symmetry becomes *spontaneously broken*.

Without any loss of generality, a vacuum state can be chosen as $\phi_0 = (\phi_1, \phi_2) = (v, 0)$. The field ϕ can be perturbatively expanded around the vacuum state ϕ_0 with two real fields, h and ξ, as

$$\phi(x) = \frac{1}{\sqrt{2}}(v + h + i\xi). \tag{43}$$

Rewriting the Lagrangian of Equation 40 in terms of fields h and ξ, reveals a Lagrangian $\mathcal{L}'$ described by a massless field ξ and a massive field h with spontaneously generated mass $m_h = \sqrt{2\lambda v^2}$;

$$\mathcal{L}' = \underbrace{\frac{1}{2}(\partial_\mu h)(\partial^\mu h) + \frac{1}{2}(\partial_\mu \xi)(\partial^\mu \xi)}_{\text{kinetic terms}} - \underbrace{\lambda v^2 h^2}_{\text{mass term}} - \tag{44}$$
$$\underbrace{- \lambda v h^3 - \frac{1}{4}\lambda(h^4 + \xi^4) - \lambda v h \xi^2 - \frac{1}{2}\lambda h^2 \xi^2}_{\text{interaction terms}} + \frac{1}{4}\lambda v^4.$$

In a spontaneous breaking of a *global symmetry*, the initial Lagrangian $\mathcal{L}$ with a massless field transforms into a Lagrangian $\mathcal{L}'$ with one massive and one massless field - the Goldstone boson. Both Lagrangians still describe the same physics and the $U(1)$ symmetry is still present. It is just "hidden" due to the specific choice of vacuum state.

The process of SSB does not completely solve the problem of acquiring masses for particles. It actually makes it worse since whenever a SSB occurs, massless Goldstone bosons appear for every broken generator of the symmetry. However, one of the most imaginative tricks of nature takes place when a global gauge symmetry is replaced by a local gauge symmetry, just like the symmetries in the Standard Model. In this case, the massless Goldstone bosons are "gauged" away into the mass terms of gauge bosons.

In order to implement the Higgs mechanism in the Standard Model, a term

$$\mathcal{L} = (\partial_\mu \phi)^\dagger (\partial^\mu \phi) - \mu^2 (\phi^\dagger \phi) - \lambda (\phi^\dagger \phi)^2 \tag{45}$$

is added to the electroweak Lagrangian from Equation 35 that is invariant under $SU(2)_L \otimes U(1)_Y$ local gauge symmetry group. In this case, ϕ represents a complex $SU(2)_L$ doublet of scalar fields;

$$\phi(x) = \begin{pmatrix} \phi^+ \\ \phi^0 \end{pmatrix} = \frac{1}{\sqrt{2}} \begin{pmatrix} \phi_1 + i\phi_2 \\ \phi_3 + i\phi_4 \end{pmatrix} \tag{46}$$

The simplest arrangement of the four fields ϕ_1, ϕ_2, ϕ_3 and ϕ_4 is that they form an isospin doublet with $Y = +1$, a positive upper component ϕ^+ and a neutral lower component ϕ^0. After the spontaneous symmetry breaking ($\mu^2 < 0$), the vacuum becomes degenerated and one of the most suitable choices for the lowest energy state is

$$\phi_0(x) = \frac{1}{\sqrt{2}} \begin{pmatrix} 0 \\ v \end{pmatrix}. \tag{47}$$

Any choice of ϕ_0 that breaks the symmetry of the Lagrangian is an acceptable choice, however this specific choice additionally ensures the conservation of electric charge. In case the vacuum is left invariant under any subgroup of the original $SU(2)_L \otimes U(1)_Y$ gauge symmetry, the gauge bosons associated with this subgroup remain massless. By choosing $\phi_0^T = \frac{1}{\sqrt{2}}(0, v)$ as the vacuum, both $SU(2)_L$ and $U(1)_Y$ symmetries are spontaneously broken into $U(1)_{EM}$ which still remains a symmetry of the vacuum.

The complex $SU(2)_L$ field doublet ϕ can be expanded and parametrised around the vacuum state as

$$\phi_0(x) = \frac{1}{\sqrt{2}} e^{i\xi_i \tau_i / v} \begin{pmatrix} 0 \\ v + H(x) \end{pmatrix} = \frac{1}{\sqrt{2}} \begin{pmatrix} \xi_2 + i\xi_1 \\ v + H(x) - i\xi_3 \end{pmatrix}. \tag{48}$$

Due to the local gauge invariance of the Lagrangian, the Goldstone bosons of the electroweak symmetry breaking (ξ_1, ξ_2, ξ_3) can be "gauged" away by an appropriate choice of the *unitary gauge*[13]

$$\phi \longrightarrow \phi' = e^{-i\boldsymbol{\xi}\boldsymbol{\tau}/2v}\phi = \frac{1}{\sqrt{2}}\begin{pmatrix} 0 \\ v + H(x) \end{pmatrix}. \tag{49}$$

In Equation 49, the vacuum is expressed only in terms of a real scalar field - the massive Higgs boson. Before the SSB there were twelve particle degrees of freedom: four real scalar fields $\phi_1, \phi_2, \phi_3, \phi_4$ and two transversal polarisation states for each massless gauge boson W_1, W_2, W_3 and B. The SSB introduces a massive scalar field (Higgs boson) and three massless Goldstone bosons. The Goldstone bosons are absorbed into the longitudinal polarisation states of the three vector bosons, belonging to the three broken generators, and so they obtain mass ($W^{\pm}$, Z bosons). The remaining massless vector boson remains massless (photon) since the symmetry group it belongs to remains unbroken. After the SSB, the total number of degrees of freedom also equals twelve: one massive scalar, a longitudinal and two transversal polarisation states for each massive gauge boson and two polarisation states of a massless gauge boson.

Gauge boson masses

In order to provide masses for the gauge bosons $W^{\pm}$ and Z, the $SU(2)_L \otimes U(1)_Y$ invariant Higgs Lagrangian from Equation 40 should be added to the electroweak Lagrangian $\mathcal{L}_{gauge}$ from Equation 35, including the covariant derivative defined in Equation 34;

$$\mathcal{L}_{Higgs} = (D_\mu\phi)^\dagger(D^\mu\phi) - V(\phi). \tag{50}$$

The term responsible for generating masses of the gauge bosons is the kinetic term of the Higgs Lagrangian;

$$\begin{aligned}(D_\mu\phi)^\dagger(D^\mu\phi) = &\frac{1}{8}(v+H)^2 g_W^2 (W_\mu^1 W^{1\mu} + W_\mu^2 W^{2\mu}) + \\ &+ \frac{1}{8}(v+H)^2 (g_W W_\mu^3 - g_Y B_\mu)(g_W W^{3\mu} - g_Y B^\mu).\end{aligned} \tag{51}$$

The physical states of the $W^{\pm}$ are a linear combination of fields W_μ^1 and W_μ^2,

$$W_\mu^{\pm} = \frac{1}{\sqrt{2}}(W_\mu^1 \mp i W_\mu^2). \tag{52}$$

Equation 51 directly provides masses for $W^{\pm}$ bosons. It depends on the vacuum expectation value of the Higgs field and the coupling strength of the weak interaction,

$$m_W = \frac{1}{2} g_W v. \tag{53}$$

Experimental measurements of m_W and g_W are used to evaluate the vacuum expectation value;

$$v \approx 246\,\text{GeV}. \tag{54}$$

13 The unitary gauge is a special gauge in which only the physical states appear in the Lagrangian, without the Goldstone bosons.

A linear combination of the two remaining gauge fields, W^3_μ and B_μ, represents the physical states of a massive Z boson and a massless photon γ (A);

$$\begin{aligned} A_\mu &= \cos\theta_W B_\mu + \sin\theta_W W^3_\mu \quad \longrightarrow \quad m_A = 0, \\ Z_\mu &= -\sin\theta_W B_\mu + \cos\theta_W W^3_\mu \quad \longrightarrow \quad m_Z = \frac{g_W v}{2\cos\theta_W}. \end{aligned} \tag{55}$$

The *weak mixing angle* θ_W, is defined as the ratio of the electroweak coupling strengths $\tan\theta_W = g_Y/g_W$. Through the above relations, the GWS model predicts the ratio of $W^\pm$ and Z boson masses as

$$\frac{m_W}{m_Z} = \cos\theta_W \tag{56}$$

and experimental measurements of this relation provide a convincing argument for the validity of the Higgs mechanism. The measured value of the electroweak mixing angle is [12]

$$\sin^2\theta_W = 0.23146(12) \pm 5.2 \cdot 10^{-5} \tag{57}$$

and additionally relates the unit of electric charge $|e|$ with electroweak coupling constants g_W and g_Y,

$$|e| = g_W \sin\theta_W = g_Y \cos\theta_W. \tag{58}$$

Fermion masses

The scalar field $\phi(x) = \begin{pmatrix} \phi^+ \\ \phi^0 \end{pmatrix}$, that creates masses for vector bosons through the Higgs mechanism, also provides mass terms for fermions, but this time through the *Yukawa* interaction. The Yukawa Lagrangian is defined as

$$\mathcal{L}_{Yukawa} = -g_\ell \overline{L}_L \phi \ell_R - g_d \overline{Q}_L \phi d_R - g_u \overline{Q}_L \phi_c u_R + h.c., \tag{59}$$

and is invariant under the $SU(2) \otimes U(1)_Y$ transformation. Fields $Q^T = (u, d)$ and $L^T_L = (\nu_\ell, \ell)$ represent quark and lepton doublets respectively, for all three families and $\phi_c = i\tau_2\phi^*$ represents the complex conjugate of the Higgs field and is needed to generate a gauge invariant mass term for the upper component of the Q field (up quarks).

After the SSB, the Higgs doublet acquires a vacuum expectation value as defined in Equation 49 and the Yukawa Lagrangian becomes

$$\mathcal{L}_{Yukawa} = \frac{-g_\ell v}{\sqrt{2}} \left(\overline{\ell_L} \ell_R + \overline{\ell_R} \ell_L \right) - \frac{g_\ell}{\sqrt{2}} H \left(\overline{\ell_L} \ell_R + \overline{\ell_R} \ell_L \right), \tag{60}$$

where for simplification, only one lepton family is considered but the same results are obtained also for quark doublets. The first term in Equation 60 can be interpreted as the mass term for fermions and is related to the Yukawa coupling g_f as

$$m_f = \frac{g_f v}{\sqrt{2}}. \tag{61}$$

The second term describes the interaction between the Higgs field and the fermions and is proportional to m_f/v.

Experimental measurements of neutrino oscillations indicate that neutrinos have non-zero masses, which implies that there has to be a corresponding mass term in the Lagrangian.

However, at this point we still do not know what is the true nature of neutrinos and consequently what is the mechanism for generating their masses[14].

1.2.3 The Standard Model

The spontaneous symmetry breaking of the electroweak symmetry and the Higgs mechanism conclude the theoretical description of the Standard Model. The complete Standard Model Lagrangian can be expressed as

$$\begin{aligned}
\mathcal{L}_{SM} = & -\frac{1}{4}B_{\mu\nu}B^{\mu\nu} - \frac{1}{4}W_{i\,\mu\nu}W_i^{\mu\nu} - \frac{1}{4}G^a_{\mu\nu}G^{a\,\mu\nu} + && \text{gauge bosons} \\
& + \overline{\psi_L}\gamma^\mu D_\mu \psi_L + \overline{\psi_R}\gamma^\mu \left(i\partial_\mu + g_Y \frac{Y}{2} B_\mu\right)\psi_R + && \text{EW int. - quarks and leptons} \\
& + \overline{q}\gamma^\mu \left(i\partial_\mu - g_S T G_\mu\right) q + && \text{QCD int. - quarks and gluons} \\
& + |D_\mu \phi|^2 - \mu^2(\phi^\dagger\phi) - \lambda(\phi^\dagger\phi)^2 + && \text{the Higgs potential} \\
& - g_\ell \overline{L}\phi R - g_d \overline{Q}\phi d_R - g_u \overline{Q}\phi_c u_R, && \text{the Yukawa term}
\end{aligned} \tag{62}$$

where D_μ is defined as in Equation 34 and the term addressing the neutrino masses is left out. The $\mathcal{L}_{SM}$ is invariant under the combined $SU(3) \otimes SU(2)_L \otimes U(1)_Y$ symmetry group which is spontaneously broken to $SU(3) \otimes U(1)_{EM}$.

The Standard Model with its 25 free parameters[15] is one of the biggest triumphs of modern particle physics. Experimental measurements agree with the SM theoretical predictions at the level of quantum corrections and with an accuracy of a few per-mille, imply a great agreement between the SM theory and experimental findings. Most of these measurements, like the Z and W boson properties, were carried out at particle colliders before the LHC [17]. The more and more advanced theoretical calculations and the measurements obtained at the LHC (and future colliders) will provide even more stringent tests for the SM [18].

Nevertheless, even with a great success of the SM, some questions are still left unanswered...

- Why are there exactly 3 families of fermions and why are masses of each family of leptons and quarks (excluding neutrinos) so similar?
- Are quarks and leptons really elementary particles?
- What is the true nature of neutrinos? Are they Majorana or Dirac particles and how do they obtain mass?
- Why are the strengths of strong, weak and electromagnetic forces so different from gravity?
- What is the mechanism behind the inflation of the early Universe?
- What does dark energy and dark matter consist of?
- Why is there more matter than antimatter in the Universe?

14 If neutrinos are considered as Dirac particles, then a Yukawa term for neutrinos suggests the existence of the ν_R, which has not been observed so far. An alternative mechanism for generating neutrino masses might be the *seesaw* mechanism, where neutrinos are considered as Majorana particles (their own anti-particles).

15 If neutrinos are considered as Dirac particles, the 25 of the SM parameters are: 12 fermion masses (Yukawa couplings to the Higgs field), 3 coupling constants of gauge interactions (g_Y, g_W, g_S), 2 parameters of the Higgs potential (v and m_H) and 8 mixing angles of quark and neutrino mixing matrices (CKM and PMNS matrices). Additionally, a complex phase leading to the CP violation in QCD can also be included as a free parameter of the SM.

- What is the true reason for total lepton and baryon number conservation?
- What triggers the spontaneous symmetry breaking?... and many others.

All these questions point to the fact that the Standard model is *not* the final answer, it is more of a "low energy" description of the Complete and Ultimate Theory of Everything there is, there was and there will be[16]. This grand theory might consist of a simple equation with a free parameter or two, from which all the laws we know and also those that are still hidden to us will emerge.

The discovery of a Higgs boson in the summer of 2012 was a historic event which brought us one of the last missing pieces of the Standard Model puzzle. But, *there is no rest for...*particle physicists. The discovery of a Higgs boson not only motivates us more to find the answers on these questions, the "bump" at $m_H = 125\,\text{GeV}$ actually triggers additional questions, like;

- Is the newly discovered particle really *the* SM Higgs boson?
- Is there only one Higgs boson?
- Is it solely responsible for the EWSB?, etc.

Some of these questions are more within our reach than others. The Run-1 of the LHC already provided first measurements of the Higgs boson properties which are described in the next chapter. As for the remaining questions, answers will hopefully be found in the future runs of the LHC. Maybe, by the end of the LHC data-taking in $\sim$ 2035, we will crossover from the current, thoroughly investigated, electroweak scale and settle at the TeV scale with more ideas of what could be hiding under the question mark in Figure 1.

16 Interestingly enough, this theory of everything can be abbreviated as CUTE.

2 THE HIGGS BOSON

To determine whether the Higgs mechanism is indeed the mechanism responsible for delivering masses to SM particles, the Higgs boson, a scalar and neutral particle must be identified. However, the Universe has a sense of humour and to keep us in suspense for 40 years, it left out a minor detail regarding the value of the Higgs boson mass, which is conceived as one of the free parameters of the SM and, so far as we know today, can be only determined experimentally.

This chapter is dedicated to the properties of the Higgs boson. Starting with theoretical assumptions on the Higgs boson mass and its experimental findings in Section 2.1, the focus shifts to the LHC and Section 2.2 describes the structure of proton-proton collisions at the LHC, followed by the Higgs production and decay modes. This chapter concludes with an overview of the $H \to WW^{(*)} \to \ell^+\nu_\ell\ell^-\bar{\nu}_\ell$ decay channel, which is the focus of the data analysis described in this manuscript.

2.1 Properties of the SM Higgs boson

The mass and self couplings of the SM Higgs boson are determined by the Higgs Lagrangian from Equation 50. By inserting the vacuum $\phi_0^T = (0, v + H(x))$ and the vacuum expectation value $v^2 = -\mu^2/\lambda (v = 246\,\text{GeV})$, the Higgs Lagrangian transforms into

$$\mathcal{L}_H = \frac{1}{2}(\partial_\mu H)(\partial^\mu H) - V(\phi) = \frac{1}{2}(\partial_\mu H)^2 - \lambda v^2 H^2 - \lambda v H^3 - \frac{1}{4}\lambda H^4. \tag{63}$$

The mass of the Higgs boson, the term proportional to H^2, depends on the parameters of the Higgs potential

$$m_H = 2\lambda v^2 = -2\mu^2, \tag{64}$$

as do triple and quartic Higgs boson self interaction terms which are proportional to H^3 and H^4 respectively;

$$g_{HHH} \propto \frac{m_H^2}{v}, \quad g_{HHHH} \propto \frac{m_H^2}{v^2}. \tag{65}$$

The parameters of the Higgs potential, λ and μ, are not specified in the Standard Model and the mass of the Higgs boson also represents a free parameter of the theory. There are however, several theoretical restrictions constraining the value of the Higgs mass and are described below.

2.1.1 The Higgs mass

In order to keep the perturbativity of the Standard Model and the stability of the electroweak vacuum, the possible values for m_H ought to lie in a certain range, specified by various

theoretical limits. The overview of theoretical constraints on m_H presented below is based on [19].

- **Unitarity and Perturbativity:**

Scattering of the longitudinally polarised vector bosons can lead to unitarity violation with its scattering amplitude growing with the center of mass energy. Assuming $m_H \ll \sqrt{s}$, the unitarity condition for the amplitude provides an upper bound on the Higgs mass

$$m_H \lesssim 710\,\text{GeV}. \tag{66}$$

Assuming the opposite limit $m_H \gg \sqrt{s}$, some *New Physics* (NP) must appear at the $\sqrt{s} \lesssim 1.2\,\text{TeV}$ to restore unitarity. Additionally, in order to preserve the perturbative nature of the Standard Model, the mass of the Higgs boson must be less than 1 TeV, since at those energy scales the first and/or second order loop corrections become comparable to the leading order.

- **Triviality:**

The four-point Higgs boson self interaction term, λ, has a logarithmic dependence on the energy scale squared when including the higher order loop corrections

$$\lambda(q^2) \propto \left[1 - \frac{3}{4\pi^2}\lambda(v^2)\log\left(\frac{q^2}{v^2}\right)\right]^{-1}. \tag{67}$$

For low energies $q^2 \ll v^2$, the quartic coupling vanishes $\lambda(q^2) \to 0$ and the theory becomes *trivial* - i.e. not self interacting. In the opposite limit when $q^2 \gg v^2$, the quartic self coupling starts growing and eventually becomes infinite, $\lambda(q^2) \to \infty$. This regime describes an improper Standard Model theory with extremely strong interactions and infinitesimally narrow Higgs potential with zero vacuum expectation value $v^2 = \frac{-\mu^2}{\lambda} \to 0$. The energy scale Λ at which the quartic self coupling becomes infinite is

$$\Lambda = v\exp\left(\frac{4\pi^2}{3\lambda}\right) = v\exp\left(\frac{4\pi^2 v^2}{m_H^2}\right), \tag{68}$$

and defines a scale at which some New Physics should appear in order to "fix" the divergences in $\lambda(q^2)$. Equation 68 reflects an "inversely proportional" relation between the Higgs mass and the energy scale. If the Standard Model theory is supposed to be valid (finite λ) up to the Planck scale $\Lambda = 10^{16}\,\text{GeV}$, then the Higgs mass ought to be small, and if the SM theory is valid only up to $\Lambda = 1\,\text{TeV}$ then the Higgs mass should be large.

$$\begin{gathered}\Lambda = 10^{16}\,\text{GeV} \longrightarrow m_H = \mathcal{O}(200\,\text{GeV}),\\ \text{or}\\ \Lambda = 1\ \text{TeV} \longrightarrow m_H = \mathcal{O}(1\,\text{TeV}).\end{gathered} \tag{69}$$

- **Stability:**

Including contributions from gauge bosons and fermions (top and bottom quarks) into the running of the Higgs quartic self coupling $\lambda(q^2)$, impacts the $\lambda \to 0$ regime. If λ is too small, the top quark contribution dominates and drives λ to negative values $\lambda(q^2) < 0$, leading to a non-stable vacuum with no minimum. This regime defines the lower bound for the

Higgs mass. In order to preserve the vacuum stability of the Standard Model the Higgs mass should be

$$m_H \gtrsim 130\,\text{GeV}, \quad \text{if SM is valid up to } \Lambda = 10^{16}\,\text{GeV}, \tag{70}$$
$$\text{or}$$
$$m_H \gtrsim 70\,\text{GeV}, \quad \text{if SM is valid only up to } \Lambda = 1\,\text{TeV}.$$

Figure 3 visualises the theoretical restrictions on the m_H as a function of the energy scale Λ, showing which regions avoid the non-perturbative regime of the SM and instabilities of the EW vacuum.

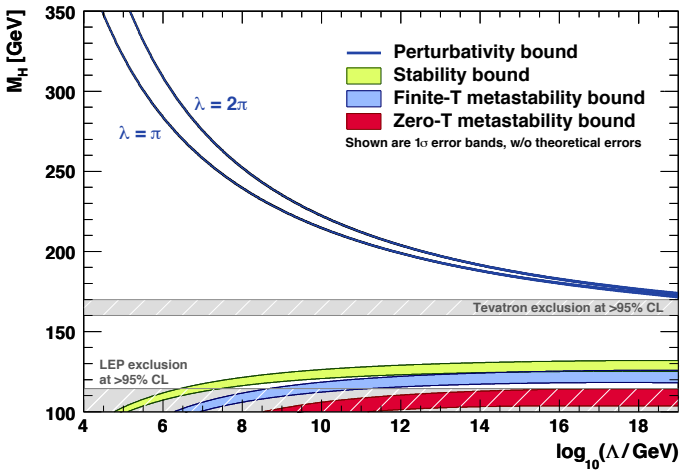

Figure 3.: Theoretical restrictions on the Higgs boson mass. The blue lines indicate the preturbativity bounds and their difference indicates the size of theoretical uncertainties. The stability bound is shown in light green band and the meta-stability bounds in blue and red bands. No theoretical uncertainties are shown for the stability bands. The grey areas indicate the exclusion limits by LEP and Tevatron. For a more detailed information see [20].

- **Experimental results:**

Before the start of the LHC, both the Large Electron-Positron (LEP) collider at CERN [21] and Tevatron [22] at Fermilab, provided experimental limits on the Higgs boson mass, favouring light Higgs scenarios. LEP [7] provided a lower bound on the Higgs boson mass with $m_H \geq 114.4\,\text{GeV}$ and a decade later Tevatron [8] measured more stringent exclusion limits where the values of m_H between 100 GeV and 106 GeV and between 147 GeV and 179 GeV were excluded. In the summer of 2012 both general experiments at the LHC, ATLAS [9] and CMS [10], confirmed an *excess of data* equivalent to approximately five standard deviations in a mass range that agreed with previously set limits. Their combination[1] [12] yields the Higgs boson mass of

$$m_H = 125.6 \pm 0.3\,\text{GeV}. \tag{71}$$

1 During the course of writing this manuscript, the ATLAS and CMS Higgs mass combination has been updated and the latest results equal to $m_H = 125.09 \pm 0.21(\text{stat.}) \pm 0.11(\text{syst.})\,\text{GeV}$ [23].

The measured value of the Higgs mass (Equation 71) determines the value of the quartic coupling λ and guarantees its perturbativity up to the Planck scale. The high energy evolution of $\lambda(q^2)$ shows that it becomes negative already a couple of orders of magnitude below the Planck scale $\lambda = \mathcal{O}(10^{10} - 10^{12})\,\text{GeV}$, where some New Physics is expected. Moreover, $m_H = 125.6 \pm 0.3\,\text{GeV}$ generates an electroweak vacuum which is at the edge between stability and metastability[2], favouring the metastable state once the experimental and theoretical uncertainties of all relevant SM observables are taken into account. Fortunately, a slow running of $\lambda(q^2)$ at high energies ensures that the EW metastable vacuum is long-lived compared to the age of the Universe [24, 25] and avoids its premature collapse.

Figure 4 shows the SM phase diagram in terms of the Higgs and the top-quark pole masses. The experimental values (within uncertainties) of m_H and m_t force the SM vacuum to a metastable phase.

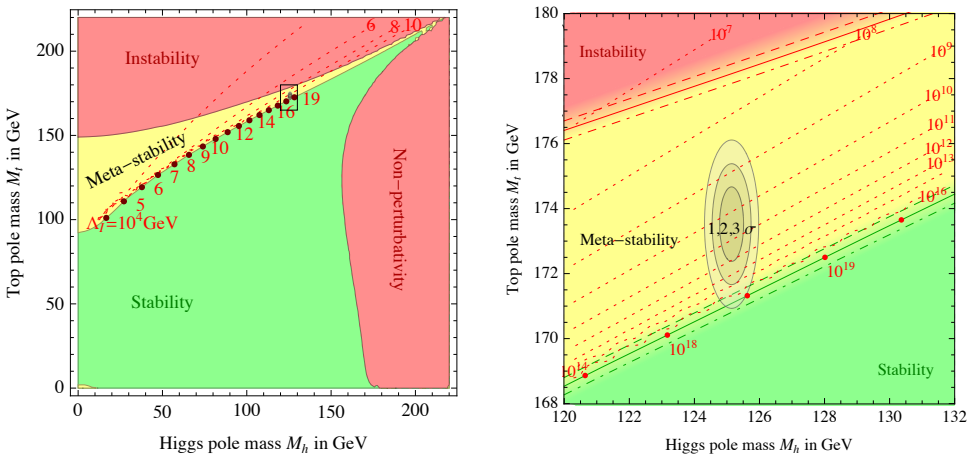

Figure 4.: The SM phase diagram in terms of Higgs and top pole masses. The left figure portrays the regions of absolute stability, meta-stability and instability of the SM vacuum, and non-perturbative region of the Higgs quartic coupling. The right figure represents the zoom in the region of the favoured experimental range of m_H and m_t. The grey ellipses denote allowed regions at 1σ, 2σ and 3σ [25].

2.1.2 The Higgs spin and parity

The SM predicts a neutral Higgs boson with even parity (P) and charge conjugation (C), $J^{CP} = 0^{++}$. Whether the newly discovered particle at the LHC is indeed the SM Higgs boson needs yet to be experimentally confirmed. The spin states which are being scrutinised at the LHC are spin-1 and spin-2. Since the Higgs boson is observed to decay into two photons, a spin-1 hypothesis is rejected according to the Landau-Yang theorem[3], which also ensures that the Higgs boson has even charge conjugation. Another important aspect which must be studied is whether the Higgs boson is a pure or a mixed CP state[4]. If the discovered Higgs

2 Metastable vacuum represents only a local energy minimum and can transition (tunnel) to a true stable vacuum, a global minimum.

3 A spin-1 particle cannot decay into two photons since the wave function of the two photon system becomes asymmetric, which is forbidden by the Bose-Einstein statistics.

4 Even though a pure CP-odd component is rejected by the Landau-Yang theorem, the Higgs boson can still be a mixed CP state with a large CP-odd component

boson is not a pure CP state but rather a mixed one, it would imply a CP violation in the Higgs sector (incorporated in some Beyond Standard Model models) which might be large enough to explain the matter-antimatter asymmetry in the Universe.

Both, ATLAS and CMS experiments, examined the collected data for different spin and parity combinations. The non-SM spin hypotheses are excluded at 99% confidence level [12, 26, 27] and the observations are consistent with the SM Higgs boson with $J^{PC} = 0^{++}$.

2.2 HIGGS AT THE LHC

Colliding protons at the center of mass energy of $\sqrt{s} = 8\,\text{TeV}$ during the Run-1 of the LHC operation was successful - after all, the Higgs boson has been found. Before diving into Higgs production and decay modes which made it possible to observe the excess of data events around 125 GeV, a few general features about the structure of the proton-proton collisions are described first.

2.2.1 Structure of proton-proton collisions at the LHC

Protons are not elementary particles and are composed of *partons* - three *valence* quarks (uud) and a *sea* of virtual gluons producing quark anti-quark pairs. At such high beam energies as are present at the LHC, the proton-proton (p-p) collisions are described as interactions between their partons. The total hadronic cross-section for a p-p collision producing a massive particle, like a Higgs boson H ($pp \to H + X$)[5], depends on the cross-section of the *hard subprocess*. The hard subprocess is nothing else but a collision of two partons, i and j, weighted by their *parton distribution functions* (PDFs) $f_{i/p}(x_i, \mu_F)$, directly producing a Higgs boson ($ij \to H$). The PDFs represent the probability that a parton with a momentum fraction x_i, at the *factorisation scale* μ_F, inside the proton undergoes the hard scattering (HS). The factorisation scale corresponds to the energy scale at which the HS process (having a high momentum transfer Q^2 and is described by the perturbative QCD), is separated from the soft scattering process (described by the non-perturbative QCD, i.e. an *underlying event* - UE). The μ_F defines the scale at which the PDFs are evaluated.

The total cross-section for the p-p collision producing a Higgs boson is therefore defined as

$$\sigma_{pp} = \sum_{i,j} \int dx_i dx_j f_{i/p}(x_i, \mu_F) f_{j/p}(x_j, \mu_F) \hat{\sigma}_{ij \to H} \ , \tag{72}$$

where the sum goes over all partons i and j of the initial protons and $\hat{\sigma}_{ij \to H}$ represents the cross-section for the hard subprocess.

Alongside μ_F, another scale plays an important role in QCD processes - the renormalisation scale μ_R, which represents the scale at which the QCD running coupling $\alpha_S(\mu_R^2)$ is evaluated. The cross-section for the hard subprocess can be perturbatively expanded into

$$\hat{\sigma}_{ij \to H} = \left(\sigma^0 + \alpha_S(\mu_R^2)\sigma^1 + \dots \right)_{ij \to H} \ . \tag{73}$$

The σ^0 represents the leading order hard scattering cross-section and σ^1 its first order correction, dependent on the strong coupling $\alpha_S(\mu_R^2)$.

Figure 5 illustrates the intermediate steps in the p-p collision. Two partons (a valence quark and a sea gluon) chosen by the PDFs $f(x, Q^2)$ collide in a HS event, generating the final state particles. The final state can also contain other quarks and gluons which were

5 X stands for other collision by-products like quarks, gluons, etc.

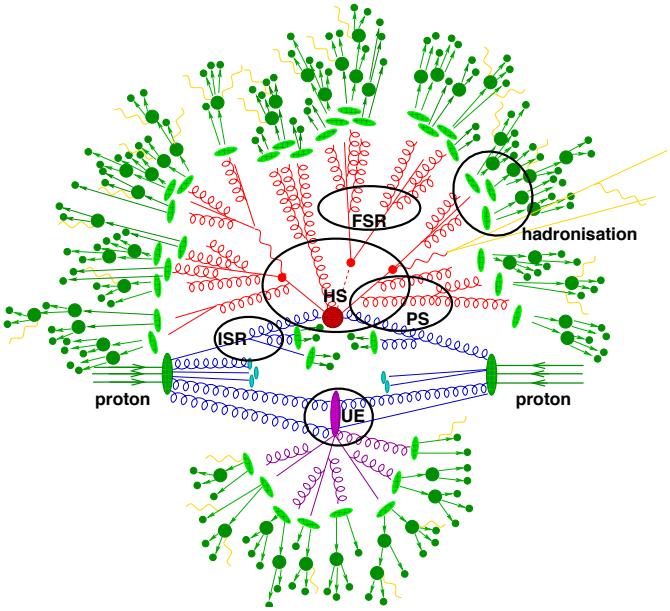

Figure 5.: The structure of a proton-proton collision at the LHC, showing the hard scatter event (HS), initial and final state radiation (ISR/FSR), parton shower (PS), hadronisation and the underlying event (UE). Figure is taken from [28] and modified.

not directly involved in the HS. Quarks and gluons can loose their energy by radiating more gluons which further branch into quark and gluon pairs $(q\bar{q}, gg, gq)$, resulting in a cascade of partons forming a *parton shower* (PS). If the incoming partons radiate gluons before the HS event they produce the *initial state radiation* (ISR) and in case the final partons, after the HS, radiate gluons, they form the *final state radiation* (FSR).

Since quarks and gluons cannot exist as free particles due to color confinement, they undergo the process of *hadronisation*. During the hadronisation they are combined into color neutral hadrons, which through their decay chains form a narrow shower called a *jet*.

Every hard scattering collision is accompanied by an underlying structure (UE) consisting of beam remnants and collisions of partons from the same or the neighbouring bunch crossing which did not participate in the hard subprocess (the minimum bias interaction). These effects are referred as *pileup* (PU).

2.2.2 Higgs production channels

The SM Higgs boson couples to all massive SM particles and the coupling strength depends on the mass of the particle. The coupling strength between the fermions and gauge bosons with the Higgs field is, respectively, linearly and quadratically proportional to their masses;

$$g_{Hff} \propto \frac{m_f}{v}, \quad g_{HVV} \propto \frac{m_V^2}{v}, \quad g_{HHVV} \propto \frac{m_V^2}{v^2}. \tag{74}$$

Hence, the most dominant Higgs production and decay mechanisms involve the $W^{\pm}$ and Z gauge bosons, and the third family of quarks. The Higgs boson couples to massless gluons

and photons as well, but only through one-loop contributions where it couples to virtual $t\bar{t}$ or W^+W^- pairs, respectively.

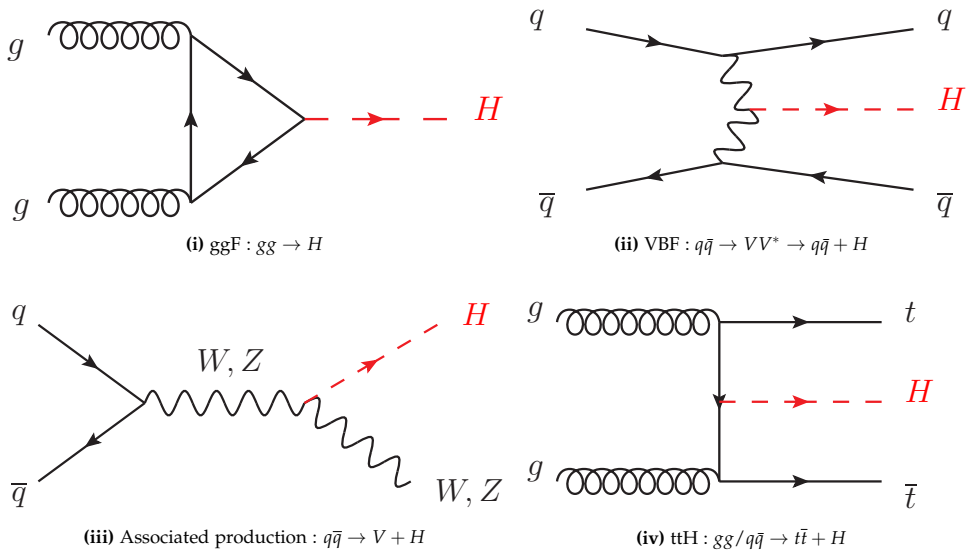

Figure 6.: Feynamn diagrams showing the most dominant Higgs production mechanisms at the LHC [12].

Figure 6 shows the most dominant production mechanisms at the LHC, which are:

i) Gluon Gluon Fusion (ggF) :

At the LHC, ggF is the most dominant production mechanism, controlled by the strong interaction, with the highest production cross-section[6] of 19.3 pb. At the leading order it is mediated by an exchange of virtual heavy quarks, mostly top quarks, since the contribution of lighter quarks is suppressed by m_q^2/m_t^2 due to a smaller Higgs boson coupling. The ggF production directly probes for Higgs boson couplings to heavy quarks.

Radiation from the initial state gluons and from the quark loop represents the higher order corrections. The total ggF cross-section is calculated up to the next-to-next-to-leading order (NNLO) in α_S using the $m_t \to \infty$ approximation, with an effective point-like ggH coupling. Calculations with a finite top mass are computed at the next-to-leading order (NLO) and are included as percent corrections to the NNLO calculation. Both, the NNLO and the NLO ggF cross-section predictions include the resummation of the soft-gluon contributions at the next-to-next-to-leading-logarithmic (NNLL) and next-to-leading-logarithmic (NLL) accuracy, respectively. The NLO electroweak corrections are applied as well. The uncertainty on the total cross-section is 10%.

ii) Vector Boson Fusion (VBF) :

The VBF is the second largest production mechanism at the LHC with the production cross-section of 1.58 pb and a very specific and clean experimental signature, easily distinguishable

6 All production cross-sections in this section are quoted for the Higgs boson with $m_H = 125\,\text{GeV}$ at $\sqrt{s} = 8\,\text{TeV}$ and are taken from [12].

from the QCD background and is in more detail presented in Chapter 5. The VBF production vertex directly couples the Higgs boson and vector bosons and therefore presents a prime opportunity to study the couplings between them.

Total cross-sections include the NNLO QCD corrections and NLO EW contributions.

iii) VH associated production (VH) :

The third biggest production cross-section at the LHC belongs to the associated Higgs production with vector bosons and yields to 0.70 pb for WH and to 0.41 pb for ZH. The QCD corrections to the cross-section are known up to the NNLO and the EW corrections are known up to the NLO. This production mode is one of the cleanest environments to study Higgs decays into bottom quarks.

iv) Top-quark pair associated production (ttH) :

This production mechanism is especially important for measuring the top-Higgs Yukawa coupling and studying the Higgs decay into bottom quarks. The production cross-section is known up to the NLO and yields to 0.13 pb.

A precise measurement of the rate of Higgs events obtained via different production mechanisms is fundamental in order to prove that the observed resonance at 125 GeV is indeed the SM Higgs boson.

The total production cross-section depends on the Higgs mass, and for the Higgs boson with $m_H = 125\,\text{GeV}$ at 8 TeV, it yields[7] to 22.1 pb. Figure 7 shows the inclusive production cross-sections at different Higgs masses at $\sqrt{s} = 8\,\text{TeV}$ and the inclusive production cross-section for the SM Higgs boson with $m_H = 125\,\text{GeV}$ at different center of mass energies.

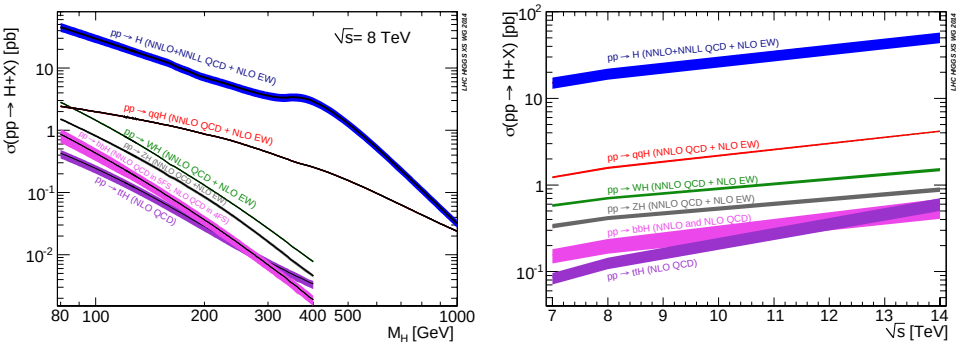

Figure 7.: Total inclusive cross-sections for Higgs boson production mechanisms for different Higgs masses at 8 TeV (left) and for $m_H = 125\,\text{GeV}$ at different center of mass energies $\sqrt{s}$ (right) [29].

2.2.3 Higgs decay channels

For a Higgs boson with $m_H = 125\,\text{GeV}$, the total decay width yields to $\Gamma_H = 4.07 \cdot 10^{-3}\,\text{GeV}$. Due to the nature of the Higgs couplings, the Higgs boson will substantially decay into

7 The cross-section for $m_H = 125\,\text{GeV}$ at 7 TeV is 17.4 pb and 57.0 pb at 14 TeV [12].

heavier particles. Figure 8 shows the branching ratios ($\mathcal{B}$) for the Higgs boson with $m_H = 125\,\text{GeV}$. The most dominant decay mode is to $b\bar{b}$ with $\mathcal{B} = 57.7\%$, followed by the decay to $WW^{(*)}$ with $\mathcal{B} = 21.5\%$. The remaining processes have branching ratios at the percent level; $H \to gg$ with $\mathcal{B} = 8.6\%$, $H \to \tau\tau$ with $\mathcal{B} = 6.3\%$, and $H \to c\bar{c}$ and $H \to ZZ^{(*)}$ with $\mathcal{B} = 2.6\%$. The decay modes with the smallest branching ratios are $H \to \gamma\gamma$, $H \to Z\gamma$ and $H \to \mu\mu$.

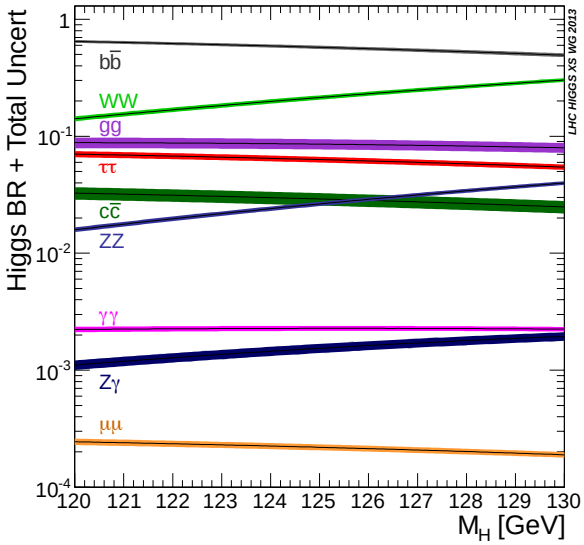

Figure 8.: The branching ratios $\mathcal{B}$ for the main decay channels of the SM Higgs boson for a range of masses close to $m_H = 125\,\text{GeV}$ [29].

The most optimal channels to study the properties of the Higgs boson at the LHC are: $H \to \gamma\gamma$, $H \to ZZ^{(*)}$, $H \to WW^{(*)}$, $H \to b\bar{b}$ and $H \to \tau\tau$. The final state particles in the first two decay chains, $H \to \gamma\gamma$ and $H \to ZZ^* \to 4l$, can be very precisely measured and give a good mass resolution of the reconstructed Higgs, up to 1-2%. The last two decay channels, $H \to b\bar{b}$ and $H \to \tau\tau$, suffer from large background contributions and poor mass resolutions, $\sim$ 10% and $\sim$ 15%, respectively. Since the $H \to WW^{(*)}$ decay channel is one of the main topics of this manuscript, it deserves some special treatment. Its main characteristics are described in more detail in the next section.

2.2.4 The $H \to WW^{(*)} \to \ell^+\nu_\ell\ell^-\bar{\nu}_\ell$ channel

The $H \to WW^{(*)}$ channel has the second largest branching ratio at $m_H = 125\,\text{GeV}$. The only kinematically allowed decay of the Higgs boson with such a mass into two W bosons, is when one of the W bosons is off-shell. Both W bosons can decay hadronically with $\mathcal{B}(W \to qq) = 67.6\%$ or leptonically with $\mathcal{B}(W \to \ell\nu_\ell) = 10.8\%$ [12], giving rise to $qqqq$, $\ell\nu_\ell qq$ and $\ell\nu_\ell\ell\nu_\ell$ final states. The fully leptonic decay, when both Ws decay into a lepton and a corresponding neutrino, reaches the highest purity. Due to the presence of the missing momentum, this channel offers only a poor mass resolution ($\sim$ 20%) and is therefore not considered in the Higgs boson mass measurements.

The Higgs boson searches in the $H \to WW^{(*)}$ channel, presented in this thesis, focus only on the fully leptonic decays of W bosons, probing for ggF and VBF production modes and consequently for Higgs couplings to heavy quarks and vector bosons. The evidence for the Higgs boson decaying into two W bosons was already observed in the 2012 data [30] where most of the signal originated from the ggF production. The VBF production mechanism however, has not been observed yet and the main quest of the data analysis presented in Chapters 5 - 7 of this manuscript is *the search for the VBF production mode*. But before the reader can fully dive into the VBF $H \to WW^{(*)}$ analysis procedure, the LHC and the ATLAS detector and event identification and reconstruction algorithms are presented first, in Chapters 3 and 4, respectively.

3 THE LHC AND THE ATLAS DETECTOR

The discovery of the weak neutral currents in 1973, the discovery of the W and the Z bosons in 1983, the invention of the world wide web in 1989 and finally the discovery of the Higgs boson in 2012 are just a few of the big discoveries made at CERN - the European Organisation for Nuclear Research.

By the end of 1990s, LEP finished its successful operation and in order to push the limits of knowledge even further, a machine was built that would reproduce the conditions which existed one billionth of a second after the Big Bang. This chapter describes the experimental setup and the performance of the worlds largest *laboratory* - the Large Hadron Collider (LHC) [31] and one of its experiments - the ATLAS detector [32].

3.1 The Large Hadron Collider

The Large Hadron Collider is the biggest and the most powerful particle collider ever built. It is located at CERN, at the border between Switzerland and France, near Geneva. The LHC is a two-ring superconducting circular collider, accelerating and colliding protons or heavy ions along its 27 km circumference. It is installed in the existing tunnel that hosted the LEP machine, approximately 100 m below ground. The LHC is designed to operate at the center of mass energy of $\sqrt{s} = 14\,\text{TeV}$ for colliding protons and at $\sqrt{s} = 2.76\,\text{TeV/u}$ for the Pb-Pb collisions.

The LHC physics program is very rich and diverse. The LHC ring hosts 4 major experiments: two general purpose experiments - ATLAS and CMS, and two specialised experiments - LHCb and ALICE. The general purpose experiments are designed to primarily study the nature of the EWSB and the Higgs mechanism, probe for any beyond SM physics and provide precision measurements of the SM parameters. The LHCb is dedicated to study the properties of B-mesons and CP violation in hadronic decays and ALICE is devoted to study the quark-gluon plasma in heavy ion collisions. Additionally, several smaller experiments are placed around the LHC ring, namely MoEDAL, TOTEM and LHCf. The first one searches for magnetic monopoles, the second measures the total p-p cross-section and studies elastic scattering and diffractive dissociation at the LHC, and the last one is dedicated to study the forward production of neutral particles in p-p collisions.

The two proton beams at the LHC travel in opposite directions through two separate beam pipes kept at ultra-high vacuum ($\sim 3 \cdot 10^6$ molecules per cm^3) and intersect at four interaction points (IP) where major LHC experiments are placed. In the design setup, each proton beam is accelerated to 7 TeV through various intermediate steps, as indicated in Figure 9. First, the hydrogen atoms are separated from their valance electrons and the remaining protons are accelerated to 50 MeV in the linear accelerator LINAC2 (the heavy ions are accelerated in LINAC3). The protons are then injected into a series of circular pre-accelerators. The first in line is the Proton Synchrotron Booster (PBS) which accelerates the protons up to 1.4 GeV, followed by the Proton Synchrotron (PS) which pushes the protons up to 25 GeV and the last pre-accelerator is the Super Proton Synchrotron (SPS) that accelerates the protons up to

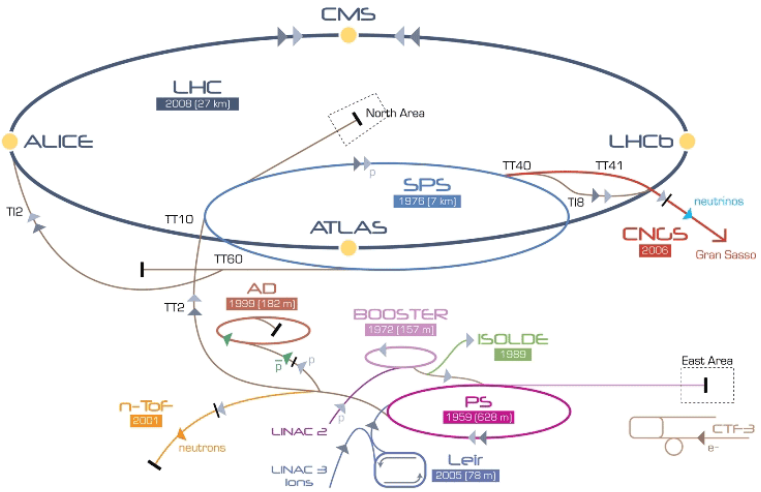

Figure 9.: CERN accelerator complex [33].

450 GeV. Along this series of pre-acceleration steps, the protons are arranged into (nominally) 2080 bunches per beam, each bunch containing $1.1 \cdot 10^{11}$ protons and two consecutive bunches being 25 ns apart. The two proton beams are then injected into to the LHC ring where they are accelerated until they reach their final collision energy. The acceleration takes part in 16 superconductive radio frequency (RF) cavities (8 per beam). The RF cavities boost (and maintain) the energy of the proton beams through the oscillating EM field with the frequency of 400 MHz and each cavity can achieve a maximum voltage of 2 MV and the accelerating field of 5 MV/m.

In order to keep the proton beams confined in the LHC ring a total of $\sim$ 6700 magnets are installed around it. The 1232 superconducting dipole magnets are used to bend the beams around the LHC ring. They are embedded in the superfluidic helium at 1.9 K and operate with a current of 11700 A, producing the 8.4 T magnetic field. The 392 of the magnets are superconducting quadrupole magnets used to focus and stabilise the beams and even higher multipoles are in charge of further corrections to the orbit of the beam.

The Run-1 operation of the LHC started in 2010 and lasted until 2012. During this period, the LHC operated at center of mass-energies of $\sqrt{s} = 7$ TeV and $\sqrt{s} = 8$ TeV. The performance of the LHC and the ATLAS detector during this period is described in Section 3.3.

3.1.1 Luminosity

One of the most important factors to bear in mind concerning the LHC operation, beside the collision energy, is the number of generated events. The LHC is designed to study rare processes with small cross-sections and high masses and such events need to be produced at high rates for a successful detection. Unfortunately, the cross-section of a process cannot be tweaked by ingenious engineers and physicists, as it is an intrinsic property of a process dependent on the collision energy, $\sigma(\sqrt{s})$. On the other hand, the delivered *luminosity* L, in a particle collider can be.

The rate n, at which certain events are generated equals to the product of luminosity and cross-section, $n = L \cdot \sigma(\sqrt{s})$. Consequently, the total number of events generated during the operation time of a collider equals to $N = \mathcal{L} \cdot \sigma(\sqrt{s})$, where $\mathcal{L}$ represents the *integrated*

luminosity $\mathcal{L} = \int L\,dt$, measured in inverse barns ($1b = 10^{-28}$ m^2). The luminosity depends on the beam parameters and is defined as

$$L \propto \frac{f_{rev} n_b N_p^2}{4\pi\sigma_T^2}, \tag{75}$$

where f_{rev} represents the revolution frequency of the beam at the LHC, n_b is the number of bunches per beam, N_p the number of protons per bunch and σ_T^2 the transverse beam size at the interaction point[1].

Events worth studying at the LHC originate from the hard-scattering between two protons, but these events are usually accompanied by the minimum bias, pileup events. The number of pileup[2] events per bunch crossing is described by the Poisson distribution with a mean value μ, estimated as

$$\mu = \frac{L\,\sigma_{inelastic}}{n_b f_{rev}}, \tag{76}$$

where $\sigma_{inelastic}$ represents the inelastic p-p cross-section. The average number of pileup events over all bunch crossings and integrated luminosity is referred as $\langle\mu\rangle$.

3.2 The ATLAS detector

The ATLAS (A Toroidal LHC ApparatuS) detector is one of the two general purpose detectors at the LHC, with a forward-backward symmetry covering a solid angle of almost 4π around the interaction point and so ensuring the detection of all particles produced in the p-p collisions. It consists of several sub-detectors installed in consecutive layers around the IP: the Inner Detector (ID), the Calorimeter System and the Muon Spectrometer (MS). The thin superconducting solenoid surrounds the ID cavity and three large superconducting toroids are placed around the Calorimeter System. The cut-away view of the ATLAS detector and its sub-detectors is shown in Figure 10.

3.2.1 ATLAS coordinate system

The ATLAS detector is built hermetically around the IP which represents the origin of the right-handed coordinate system. The beam line defines the z-axis with the same orientation as the counter-clockwise rotating proton beam. The $x-y$ plane is perpendicular to the z-axis, with the positive x-axis pointing towards the center of the LHC ring and the positive y-axis pointing upwards. The x and y coordinates define the r-axis as $r = \sqrt{x^2+y^2}$. Two angles are additionally used to describe the position in the ATLAS detector: the azimuthal angle $\phi \in [-\pi, \pi]$ is measured from the positive x-axis in the clockwise direction pointing to the positive z-axis and the polar angle $\theta \in [0, \pi]$ that measures the angle with respect to the positive z-axis.

An important quantity in particle physics is the *pseudorapidity* η, defined as $\eta = -\ln\tan(\theta/2)$ and is invariant under the longitudinal boosts in the z-direction. From the perspective of pseudorapidity, the ATLAS detector can be split into two regions: $|\eta| <\sim 1.4$ defines the central or the *barrel* region and the range $1.6 <\sim |\eta| <\sim 2.7$ defines the forward or the *end-cap*

1 Before the collision, the proton bunches are a few centimetres long and squeezed to 16 μm in their transverse direction.

2 There are two kinds of pileup: the *in-time* pileup which corresponds to the minimum bias events from the same bunch crossing as the hard-scatter event and the *out-of-time* pileup which accounts for interactions from the neighbouring bunch crossings.

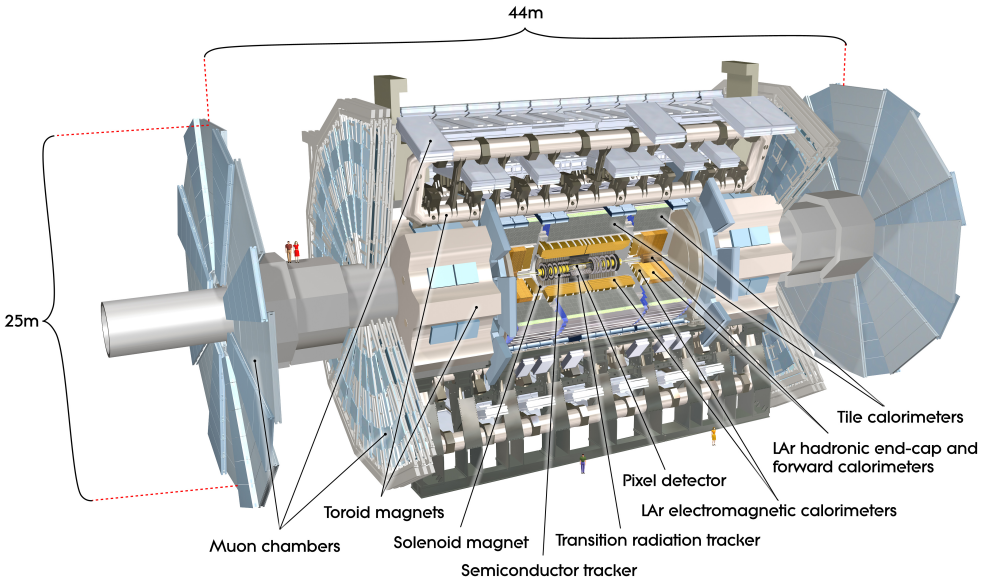

Figure 10.: Cut-away view of the ATLAS detector [34]. The detector is 25 m high and 44 m wide and weighs approximately 7000 tons.

region. Sometimes, for massive objects such as jets, the rapidity $y = 1/2 \ln[(E + p_z)/(E - p_z)]$ is used instead of η.

An opening angle between two trajectories pointing to the IP is expressed as $\Delta R = \sqrt{\Delta\phi^2 + \Delta\eta^2}$.

Several parameters describing the trajectories of traversing particles through the ATLAS detector are defined in the transverse, $x - y$ plane: $p_T (= p \sin\theta)$, E_T and the missing transverse momentum, E_T^{miss}. The transverse and longitudinal impact parameters, d_0 and z_0 respectively, measure the distance of the trajectory's point of the closest approach to the beam line once in the $x - y$ plane (d_0) and once in the $r - z$ plane (z_0).

Before each of the ATLAS sub-detectors is described in detail, a summary of the required (design) resolution for each sub-system, in order to guarantee the desired performance of the ATLAS detector, is shown in Table 4.

3.2.2 Inner Detector

The Inner Detector, as the name suggests, is the innermost sub-detector of the ATLAS detector and is closest to the beam pipe. It is composed of three independent but complementary systems: the Pixel system, the SemiConductor Tracker (SCT) and the Transition Radiation Tracker (TRT), with its cut-view shown in Figure 11. Figure 12 shows the layout of the ID and the structural elements of each of these systems: the barrel region consists of cylindrical and concentric layers while the end-cap region is built from detectors mounted on disks perpendicular to the beam line.

The main purpose of the ID is to provide *tracking information* (precise measurements of the impact parameters, position and momentum, and robust and efficient pattern recognition)

Sub-detector	Resolution	$\lvert\eta\rvert$ coverage Tracking	Trigger
Inner Detector	$\sigma_p/p_T = 0.05\% \cdot p_T \oplus 1\%$	≤ 2.5	-
Electromagnetic Calorimeter	$\sigma_E/E = 10\%/\sqrt{E} \oplus 0.5\%/E \oplus 0.7\%$	≤ 3.2	≤ 2.5
Hadronic Calorimeter (jets):			
barrel and end-cap	$\sigma_E/E = 50\%/\sqrt{E} \oplus 0.3\%$	≤ 3.2	≤ 3.2
forward	$\sigma_E/E = 100\%/\sqrt{E} \oplus 10\%$	$[3.1, 4.9]$	$[3.1, 4.9]$
Muon Spectrometer	$\sigma_p/p_T = 10\%$, at $p_T = 1$ TeV	≤ 2.7	≤ 2.4

Table 4.: The design performance goals of the ATLAS detector [34]. Energy and p_T are measured in GeV. The operator $\oplus$ represents a quadratic sum. The performance of the ATLAS detector during the Run-1 operation is discussed in Chapter 4.

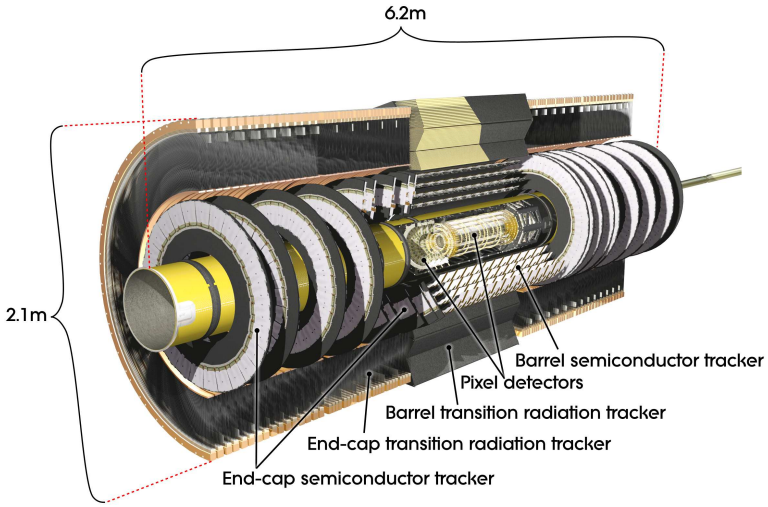

Figure 11.: Cut-away view of the Inner Detector [32].

of traversing charged particles with $p_T > 100$ MeV within $|\eta| < 2.5$. The surrounding superconducting solenoid produces the 2 T magnetic field which bends the trajectories of charged particles when traversing the detector.

The pixel detector and the SCT are both solid-state detectors built out of the high-density doped material. When a charged particle passes through the semiconducting material it ionises it, leaving a trail of electron-hole pairs that travel towards respective electrodes and so producing a signal current. On the other hand, the TRT is a gaseous straw tube detector composed of an anode wire at the center of the tube that is filled with a gas mixture. When a charged particle traverses the TRT it ionises the gas and produces free electrons drifting towards the anode due to a potential difference between the tube and the anode. The measurement of the drift time provides the coordinates of the traversing particle. In addition, the TRT also detects the transition radiation produced when a charged particle passes through the inhomogeneous medium with two different dielectric constants. The intensity of the emitted photons is directly proportional to the γ factor of the relativistic traversing particle

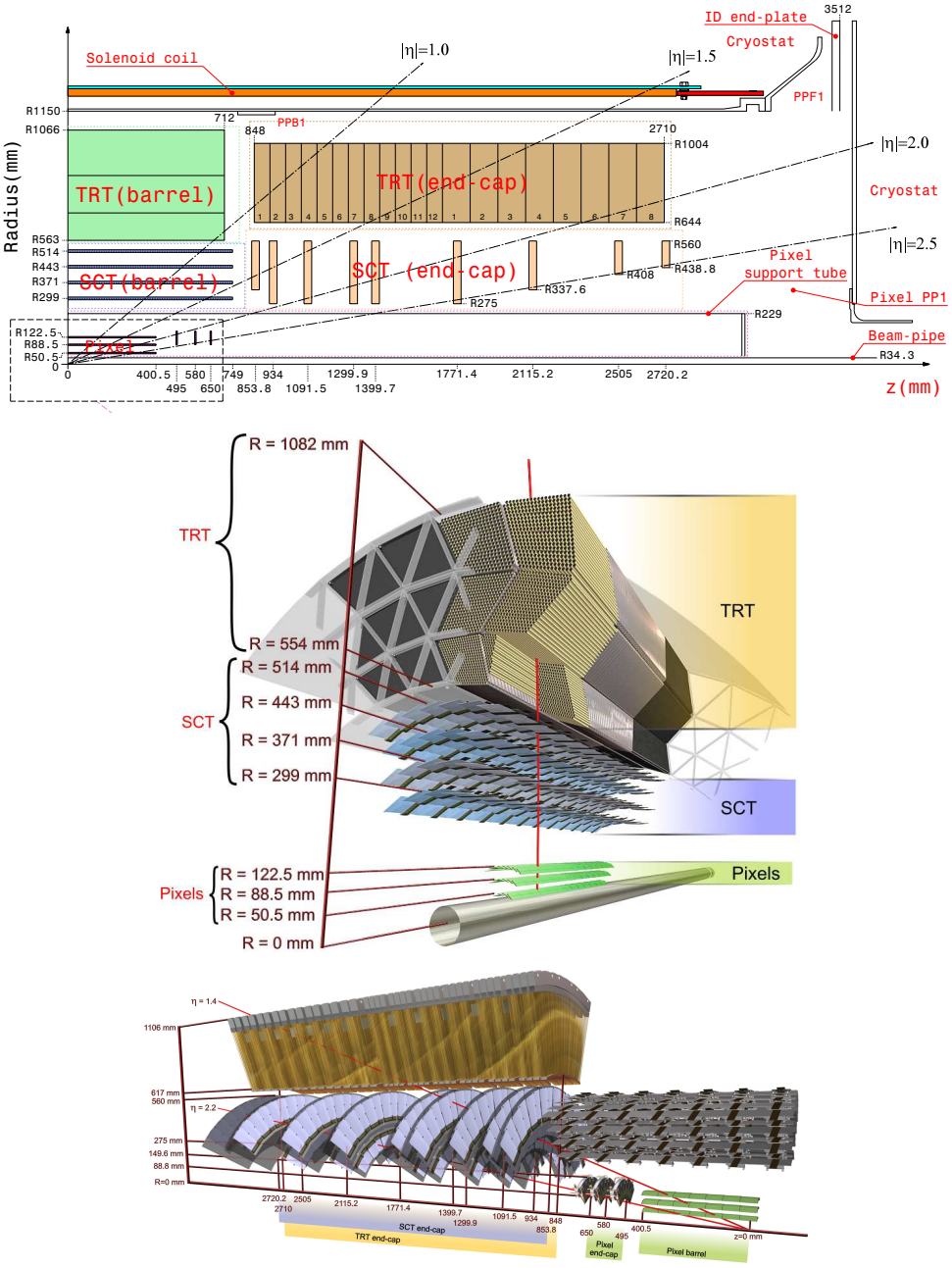

Figure 12.: The complete layout of the ID (top) and the structural elements and sensors in the barrel (middle) and the end-cap (bottom) regions of the ID [32].

and helps to discriminate between electrons and pions. The properties of each individual sub-system are described below:

THE PIXEL DETECTOR: The pixel detector has in total 1744 square-shaped silicon pixel sensors with the minimum pixel size of 50×400 μm^2. It has approximately 80.4 million readout channels and provides an intrinsic resolution of 10 μm in the transverse direction ($r - \phi$) and 115 μm in the longitudinal direction (z in the barrel and r in the end-caps). The sensors are mounted on the support structure arranged in three concentric layers in the barrel and in three disks in the end-cap region. Typically, a charged particle crosses three pixel layers before entering the SCT.

THE SCT: The SCT sensors are also silicon based but have micro-strips instead of pixels. The SCT has in total 4088 modules[3] with approximately 6.3 million readout channels. In the barrel region the sensors are square-shaped with an area of 64.0×63.6 mm^2 and contain 768 of 126.1 mm long and parallel strips with a strip pitch (distance between the centres of two neighbouring strips) of 80 μm. They are mounted on four cylindrical layers surrounding the pixel barrel detector. The end-caps are built out of nine disks and each disk consists of three rings on which wedge-shaped modules are mounted. The modules mounted on the inner, middle and the outer ring have different sizes and are shown in Figure 13. For geometrical

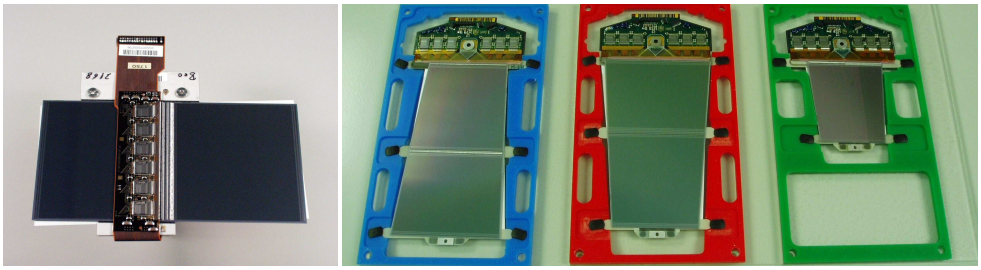

Figure 13.: The SCT silicon strip modules [32]. From left to right: barrel module, outer end-cap module, middle end-cap module and the inner end-cap module.

reasons, disk 9 has only outer modules and disks 1, 7 and 8 have no inner modules[4]. The strips in each module fan radially outwards from the focus-point with a varying strip pitch (from 56.9 μm to 94.2 μm) and length (from 52.5 mm to 119.1 mm). In both SCT regions, modules consist of two pairs of identical sensors glued back-to-back. On one side, the sensors are placed so that the strips are parallel to the beam line (barrel) or span radially outwards from the IP (end-caps). To ensure a high resolution measurement in the direction parallel to the strips, the sensors on the other side of the module are rotated by a stereo angle of 40 mrad, providing a 3D space-point measurement. The intrinsic accuracy per SCT strip module is 17 μm in the transverse direction and 580 μm in the longitudinal direction. All in all, a charged particle crossing the SCT traverses at least 8 strip layers, providing eight 3D coordinates of its trajectory.

THE TRT: The TRT is the outermost layer of the ID, extending up to $|\eta| \leq 2.0$, and is composed of 370000 straw tubes with a 4 mm diameter, embedded in a dielectric material with a varying refractive index. Each tube is filled with a xenon based gas mixture and

3 Two silicon based sensors are glued on a module, one on each side, together with the readout electronics. Modules provide mechanical stability for the sensors and house the services.

4 The disk 8 contains shorter middle modules called the "short middle" module.

equipped with a 31 μm gold plated tungsten anode wire at the center of the tube. In the barrel region the 144 cm long straws are parallel to the beam line and arranged in 73 layers. The end-caps are built out of 37 cm long straws spanning radially outwards and are arranged in 160 layers. The TRT provides the tracking algorithms with a large number of space-points (usually 36), each of them carrying a 2D (r, ϕ) information with an intrinsic accuracy of 130 μm per tube. Even if the TRT provides measurements with a lower precision, the large number of them and consequently a longer measured trajectory length, and the ability to discriminate between the electrons and pions, compensate for this.

3.2.3 The Calorimeter System

The main task of the calorimeter system is to identify and trigger on the traversing charged and neutral particles and measure their energies. The calorimeters are sampling devices built from several alternating layers of an absorbing material and an active medium. When a particle traverses through the dense absorbing material it looses its energy[5] in a cascade of electromagnetic or hadronic particles called a *shower*, which is then measured in the subsequent layer of the active medium. The reconstruction of the shower profile and its depth are used for particle identification.

The calorimeter system is divided into the electromagnetic (ECAL) and hadronic (HCAL) calorimeter, all together covering the range up to $|\eta| < 4.9$. Its cut-away view is shown in Figure 14. Since the electromagnetic showers penetrate through less material before loosing all

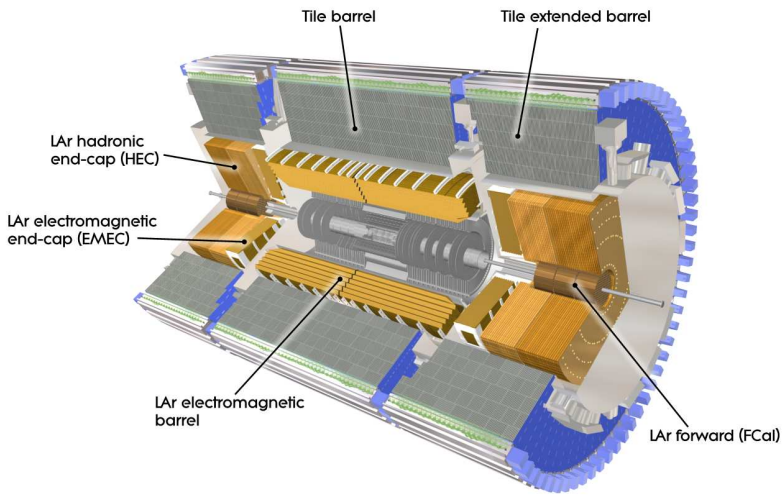

Figure 14.: Cut-away view of the ATLAS Calorimeter system [34].

their energy than the hadronic showers, the ECAL is positioned right after the ID and its solenoid, and the HCAL is placed after the ECAL. The depth of both calorimeters must be sufficient to completely stop and absorb the energy of particle showers in order to prevent any punch-throughs into the surrounding MS system.

5 Electrons loose their energy through photon emission via bremsstrahlung or ionisation and photons loose their energy through e^+e^- production, while hadrons mostly interact hadronically.

The calorimeters are built from two types of technologies; the ECAL uses only liquid argon (LAr) while the HCAL combines the LAr with the Tile Calorimeter. The main features of both calorimeters are described below:

ELECTROMAGNETIC CALORIMETER: The ECAL is a liquid argon detector which uses lead (Pb) plates as an absorber and liquid argon as the active material. The electrodes in the LAr are placed in an accordion geometry, see Figure 15 (left), providing a full ϕ coverage. It is divided into the barrel ($|\eta| < 1.475$) and two end-cap components ($1.375 < |\eta| < 3.2$) with a total thickness of > 22 radiation lengths[6] (X_0) in the barrel region and > 24 X_0 in the end-caps. In the rapidity region that coincides with the ID ($|\eta| < 2.5$), the ECAL has three segments. The innermost segment has the smallest granularity, $\Delta\eta \times \Delta\phi = 0.003 \times 0.1$ and h allows for precision measurements of the energy deposits. The middle section is built out of $\Delta\eta \times \Delta\phi = 0.025 \times 0.025$ towers and contains most of the energy from the showers and the outermost layer has a coarse segmentation and ensures the confinement of the showers. Each end-cap component is divided into two co-axial wheels, further divided into 8 wedge-shaped modules that have the same accordion geometry as in the barrel. Each of them is additionally divided into three longitudinal layers with similar depths as in the barrel.

HADRONIC CALORIMETER: The HCAL consists of three sub-systems: the Tile Calorimeter surrounding the ECAL, the LAr end-cap calorimeter (HEC) and the LAr forward calorimeter (FCal), where the latter provides measurements also for the electromagnetic showers. The Tile Calorimeter uses steal as the absorbing material and scintillating tiles as the active material[7]. It is divided into the barrel ($|\eta| < 1.0$) and two extended barrel ($0.8 < |\eta| < 1.7$) regions, segmented in three layers and divided into 64 modules. The innermost cells have the highest granularity of $\Delta\eta \times \Delta\phi = 0.1 \times 0.1$ and the outermost cells have a coarser granularity with $\Delta\eta \times \Delta\phi = 0.2 \times 0.1$ towers. The total nuclear interaction length[8] (λ) at the outer edge is 9.7 λ at $\eta = 0$. The schematic of the Tile Calorimeter module is shown in Figure 15 (right).

The LAr end-caps consist of two independent wheels per end-cap, built out of 32 wedge-shaped modules, extending between $1.5 < |\eta| < 3.2$. The HEC uses copper as the absorber.

The FCal has two end-caps extending between $3.1 < |\eta| < 4.9$, which are approximately 10 λ deep and divided into three modules per end-cap: the first module measures the electromagnetic showers and the last two the hadronic showers. The absorber material is different between the modules - copper is used in the first module and tungsten in the last two.

3.2.4 The Muon Spectrometer

Muons are minimum ionising particles and traverse the complete ATLAS detector without being stopped in the calorimeters. Therefore, a separate system is built to detect them. The MS surrounds the calorimeter system and with its large volume defines an overall size of the ATLAS detector. Its air-core toroid system consists of a long barrel and two inserted end-cap magnets which generate a strong bending power which is necessary to determine the curvature of highly energetic muons. The MS has an open and light structure, hence minimising the effects of multiple-scattering and provides a standalone reconstruction of muon trajectories with p_T between 3 GeV and 3 TeV within $|\eta| < 2.7$. The muons with smaller

6 The radiation length is the mean length travelled by an electromagnetically-interacting particle until it has only $1/e$ of its original energy left, where e is the base of the natural logarithm equal to $\simeq 2.72$.

7 Particle showers create light when traversing through the scintillating tiles that is multiplied and readout by the photomultiplier tubes.

8 Similar to X_0, the interaction length λ, is the mean path length travelled by a hadronically-interacting particle until it has $1/e$ of its original energy left.

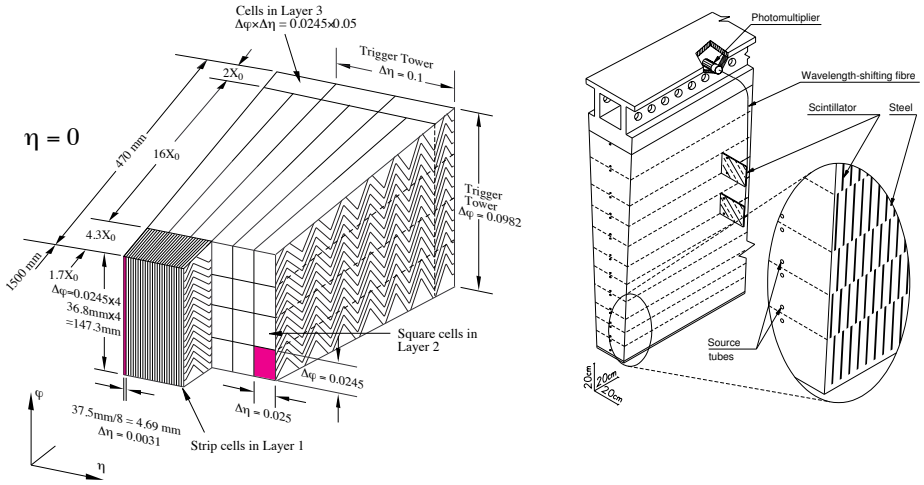

Figure 15.: Schematic view of the LAr barrel module in the ECAL (left) and the Tile Calorimeter module (right) [34].

momenta are identified by the ID since they do not have enough energy to reach the MS. The cut-away view of the MS is shown in Figure 16.

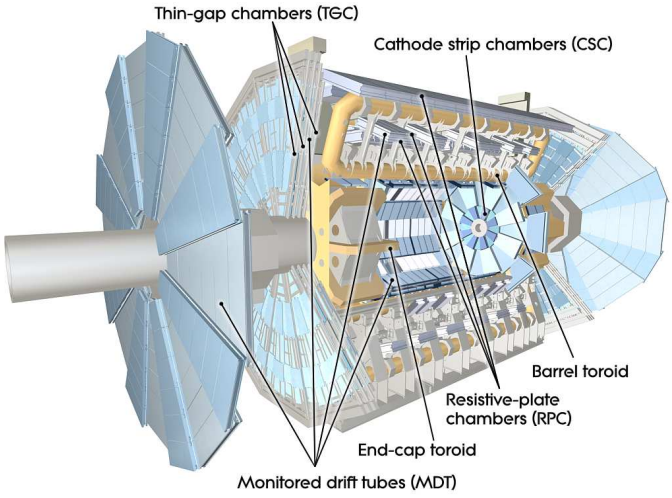

Figure 16.: Cut-away view of the ATLAS Muon Spectrometer [34].

The muon stations which consist of muon detectors are positioned in three concentric layers around the beam line in the barrel region and in four large wheels in the end-cap region. Such a geometry guarantees at least three space-point measurements for the muons originating from the IP, which suffice for an independent measurement of the muon trajectory. The MS incorporates two technologies: the high *precision tracking chambers* and the fast *triggering*

chambers. The former consists of the Monitored Drift Tubes (MDT) and the Cathode Strip Chambers (CSC) and the latter from the Resistive Plate Chambers (RPCs) and the Thin Gap Chambers (TGCs). Both of these technologies are described below:

PRECISION TRACKING CHAMBERS: The MDTs cover the range up to $|\eta| < 2.0$ and consist of up to eight layers of 30 mm wide and 1 - 6 m long drift tubes, achieving an average resolution of 80 μm per tube. The aluminium tubes are filled with a gas mixture and contain a tungsten-rhenium anode in the center of the tube. The MDTs provide a 2D measurement of an angle and the position of the track in the plane perpendicular to the tubes with no measurement of the position along the tube.

The innermost end-cap region, between $2 < |\eta| < 2.7$, is covered with CSCs due to their higher rate capabilities and better time resolution. The CSCs are multi-wire proportional chambers of trapezoidal shape with multiple anode wires, two layers of cathode strips and a gas mixture in between. The strip layers are placed orthogonal with respect to each other to guarantee a 3D space-point measurement. The intrinsic resolution of the CSCs is 40 μm in the bending plane ($r - z$) and $\sim$ 5 mm in the transverse plane due to coarser readout pitch.

TRIGGER CHAMBERS: The muon trigger chambers are a part of the Level-1 ATLAS Trigger System (described in Section 3.2.6) and identify and trigger on muons, provide information about the bunch-crossing and in addition deliver the missing tracking information complementary to the information from the MDT measurements (along the direction of the MDT tubes). The barrel region ($|\eta| < 1.05$) is covered with three cylindrical RPC layers and the end-cap region ($1.05 < |\eta| < 2.4$) is covered by four TGC stations, mounted on two concentric rings. Each RPC consists of two parallel resistive plates with a gaseous mixture between them and the readout copper strips that are installed on the outer faces of plates. The RPCs provide a 2D measurement; one layer provides a measurement of the η coordinate and the other layer of the ϕ coordinate, with a $\sim$ 10 mm spatial resolution and 1.5 ns time resolution. The TGC stations are composed of nine layers of multi-wire proportional chambers similar to CSCs, but with a smaller difference between the wires which allows measurements of drift times shorter than the bunch spacing of 25 ns. The TGCs provide 3D measurements with a spatial resolution of 2-7 mm and a time resolution of 4 ns.

3.2.5 Particle Tracking

When a charged particle traverses the ATLAS detector it leaves a trail of *hits* - charge deposits in points where it passed through the sub-detectors. Such hits are combined into *tracks* (particle trajectories) and are reconstructed from the recorded data in the ID and MS . The curvature of the track in the magnetic field determines the charge, mass and the momentum of the particle. Whether the reconstructed track originates from the *primary vertex* (PV) of the hard *p-p* collision is determined by tracing it back towards the IP. The information about the particle shower profile and depth obtained from the Calorimeter System helps to discriminate between different particles - e and γ are identified by their dense and narrow showers in the ECAL and hadronic particles by their broader showers which penetrate deeply in the HCAL. All in all, each of the stable and detectable particles leaves a specific signature when traversing the ATLAS detector with their trajectories shown in Figure 17. Their main characteristics are:

- **electrons:** tracks in the ID that are associated to the PV and are matched to a shower in the ECAL,
- **muons:** tracks in the MS (+ matching with the tracks in the ID),

- **photons:** showers in the ECAL with no associated tracks in the ID (unconverted photon) or with a displaced vertex in the ID (converted photon),
- **charged hadrons:** broad showers in the HCAL with associated tracks in the ID,
- **neutral hadrons:** broad showers in the HCAL with no associated tracks in the ID.

The τ-leptons have a too short decay time to be directly detected in the detector and are therefore detected through their decay products. The neutrinos only weakly interact with matter and therefore completely traverse the ATLAS detector without leaving a trace. Their presence is determined by evaluating the missing momentum in the transverse plane. The reconstruction algorithms for each of these particles and their performance are described in Chapter 4.

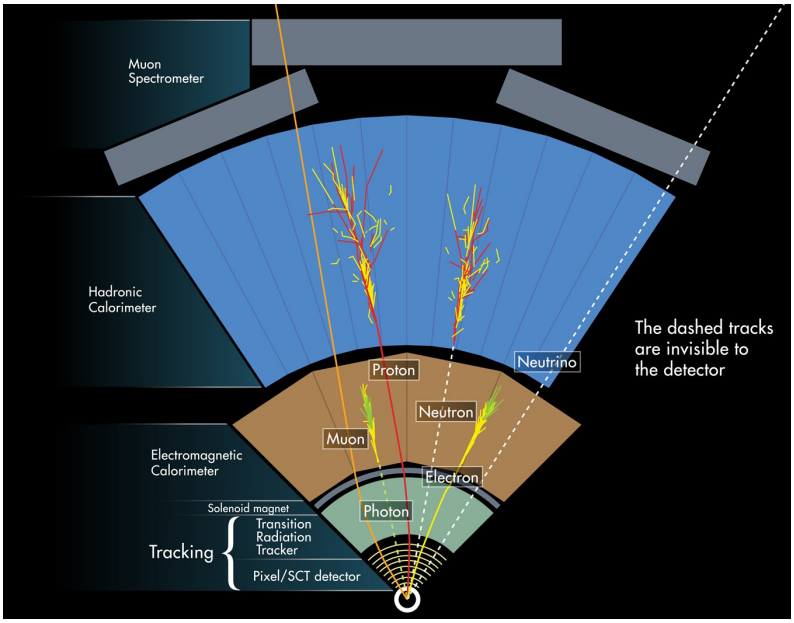

Figure 17.: Schematics of a wedge section of the ATLAS detector with particle tracks [34].

3.2.6 Trigger and Data Acquisition

A fun fact: if all the data at the LHC would be recorded, this would fill up 100000 CDs per second, making a 150 m tall stack of CDs every second, and humanity could finally build its own "stairway to heaven" (reaching the moon twice per year). Bunches of protons at the LHC are designed to collide 40 million times per second, producing 50-60 TB of data each time. These data rates are too large to be stored and even more so to be analysed. In addition, these data consist of interesting events, like the Higgs boson production, but also of minimum bias events and in order to keep only the interesting events, the ATLAS Trigger System is used to reduce the data rate to storable and analysable amounts.

The triggering is performed in three stages: Level-1 trigger, Level-2 trigger and the Event Filter (EF), with the last two trigger stages collectively referred as the High-Level Trigger

(HLT). Each of these stages is based on a fast reconstruction of physics objects like electrons, muons, photons and jets and each stage refines the decision made by the previous stage and significantly reduces the event rate. The Data Acquisition System (DAQ) is responsible for the storage of the recorded data and the schematic of the ATLAS Trigger and the DAQ is shown in Figure 18.

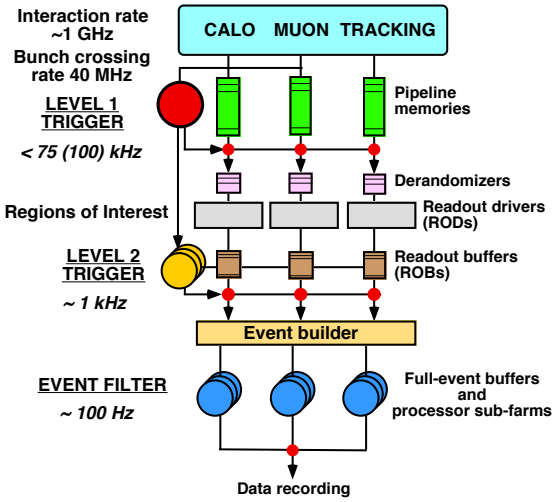

Figure 18.: Block diagram of the ATLAS Trigger and Data Acquisition Systems [35].

The Level-1 trigger is a hardware based trigger that reduces the data rate by a factor of 400, to 75 - 100 kHz, with a latency time of 2.5 μs. It uses the information from the calorimeter system with a reduced granularity to identify high-E_T photons, electrons, jets, E_T^{miss} and hadronically decaying taus, and the MS trigger chambers to identify high-p_{T} muons. The Level-1 trigger defines the Regions of Interest (RoI) corresponding to a cone ($\eta - \phi$ region in the detector) from the IP towards the outer parts of the detector. During the Level-1 trigger decision making, the events are stored in pipeline memories. Those events that pass the Level-1 trigger requirements are stored in the Read-Out-Buffers (ROB) and the information from the RoIs is then fed to the software based Level-2 trigger.

The Level-2 trigger reduces the data rate by a factor of 30, to $\sim$ 3 kHz, with a latency of 40 ms. It analyses the RoI with the full detector granularity within the RoIs and performs a fast event reconstruction. Those events that pass the stricter Level-2 requirements are passed to the Event Builder (EB) and later to the EF, which additionally reduces the data rate to 400 Hz. The EF performs the event reconstruction using the information from the complete detector in its full granularity and uses the offline analyses procedures. The event reconstruction takes approximately 4 s per event. From this point onwards, the data are ready to be stored for the offline analyses.

3.2.7 Simulation of the ATLAS detector

To gain trust in the measured data, the observed results are compared to the theoretical predictions in the form of simulated events. Specific processes from the p-p collisions are generated using the Monte Carlo (MC) methods and consist of simulated hard scattered

events, parton showers, hadronisation, simulations of the underlying event and decays of the outgoing particles. The MC methods use random number generators to simulate the process under consideration according to theoretical prescriptions. The list of MC generators most relevant for the work presented in this thesis is shown in Table 5. The event generation

MC generator	Matrix Element	Functionality
General purpose generators:		
pythia [36, 37]	LO	*PS*, *UE*, *H*, *PU*
herwig [38]	LO	*H*, *PS*, interfaced with jimmy [39] for *UE*
sherpa [28]	LO + multi-leg	*HS*, *PS*, *UE*, *H*
madgraph [40]	LO + multi-leg	*HS*, interfaced with pythia or herwig for *PS*, *UE*, *H*
Matrix Element generators:		
alpgen [41]	LO + multi-leg	*HS*, interfaced with pythia or herwig for *PS*, *UE* and *H*
acermc [42]	LO	*HS*, interfaced with pythia or herwig for *PS*, *UE* and *H*
powheg [43–45]	NLO	*HS*, interfaced with pythia or herwig for *PS*, *UE* and *H*
mc@nlo [46]	NLO	*HS*, interfaced with herwig for *PS*, *UE* and *H*

Table 5.: Overview of the most relevant MC generators used in this thesis. *HS* stands for hard scatter, *PS* for parton shower, *UE* for underlying event, *PU* for pileup and *H* for hadronisation. "Mult-leg" refers to generators that provide additional partons in their matrix element calculation. For further details see [47] and the references within.

produces a list of stable particles and the next step in the verification of the measured results is to precisely simulate the interactions of these particles with the ATLAS detector.

The performance of the ATLAS detector is simulated in the athena framework [48] in four stages [49]: detector geometry construction, detector simulation, digitisation and event reconstruction. In the first stage, each detector component (sensors, support structures, etc.) is described by a basic geometrical shape from the GeoModel library [50] and is placed in the detector volume. The complete geometry is then translated into geant4 [51] - a toolkit simulating the passage of particles through matter, where interactions of the generated MC particles with the detector geometry are recorded in terms of *hits* - energy deposits in the sensitive detector volumes. The digitisation process transforms hits into *digits* - a realistic detector response mimicking the passage of real particles through the detector (voltage or current from a readout channel rising above a specified threshold within a time window). Digits are later translated into Raw Data Objects (RDOs) which include emulated functionality of the readout electronics and are fed into the reconstruction process. Finally, the event reconstruction of the simulated events takes place and follows the same procedure as in the real data (see Chapter 4).

3.3 Performance of the LHC and the ATLAS detector during Run-1

Table 6 shows the design beam parameters and the performance during the Run-1 operation of the LHC. Even if beam parameters were not as high as the designed values between 2010 and 2012 (due to an accident during the initial start-up in 2008), the LHC and the ATLAS detector had an outstanding performance during the Run-1 operation.

In 2011, proton beams were collided at $\sqrt{s} = 7\,\text{TeV}$ with a luminosity of $\sim 3.7 \cdot 10^{33}\,\text{cm}^{-2}\text{s}^{-1}$ and the ATLAS detector recorded in total of 5.3 fb^{-1} of data with in average 9 pileup events per bunch crossing. In 2012, all these numbers increased: the center of mass energy was set to $\sqrt{s} = 8\,\text{TeV}$, the luminosity to $\sim 7.7 \cdot 10^{33}\,\text{cm}^{-2}\text{s}^{-1}$ and the ATLAS detector recorded

Beam Parameter	Design	2010	2011	2012
Center of mass energy, $\sqrt{s}$ [TeV]	14	7	7	8
Peak Luminosity, L [$\cdot 10^{33}$ cm^{-2}s^{-1}]	10	0.21	3.65	7.73
Delivered Integrated Luminosity, $\mathcal{L}$ [fb^{-1}/year]	80-120	0.049	5.6	23.1
Integrated Luminosity recorded by ATLAS [fb^{-1}/year]	-	0.045	5.3	21.7
Maximum number of colliding bunches	2808	348	1854	1380
Number of protons in a bunch [$\cdot 10^{11}$]	1.15	0.9	1.2	1.6
Minimum bunch spacing [ns]	25	150	50	50
Average number of interactions per bunch crossing $\langle\mu\rangle$	19.02	< 3	9.1	20.7

Table 6.: The LHC parameters: the design beam parameters are taken from [31, 52] and the performance measured during the Run-1 operation of the LHC is taken from [53].

21.7 fb^{-1} of data with in average 21 pileup events per bunch crossing. Figure 19 shows the integrated luminosity and the average number of pileup events recorded by the ATLAS detector between 2010 and 2012.

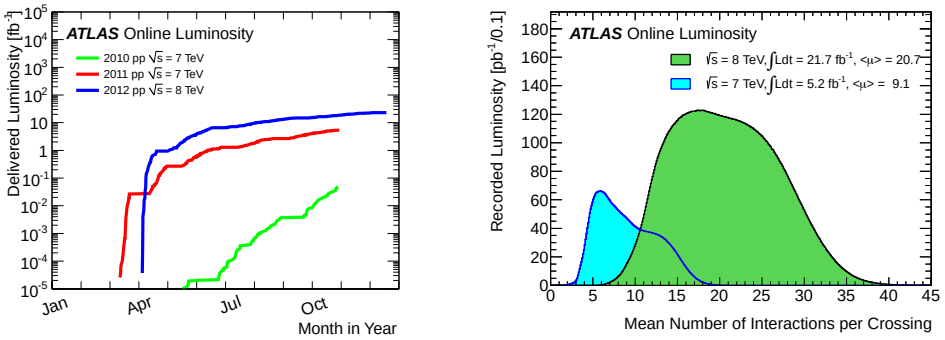

Figure 19.: Integrated luminosity recorded by the ATLAS detector in stable p-p collisions (left) and the average number of collisions per bunch crossing weighted by the integrated luminosity (right) [54].

The increase in luminosity leads to an increase in pileup. In 2012, ATLAS recorded more pileup events per bunch crossing than originally designed. Higher pileup brings higher detector occupancies and higher trigger rates. However, due to an exceptional operation of the ATLAS detector, which recorded data with an average efficiency of 93%, an outstanding performance of its sub-systems, which were recording data in $>$ 99% of the time during stable beams [55] and a great performance of tracking and reconstruction algorithms, the Run-1 operation was a great success for the ATLAS experiment, with the discovery of the Higgs boson as its *cherry-on-top*. The great performance of the tracking algorithms under high pileup conditions and the event reconstruction and identification is the topic of the next chapter.

At the moment of writing this thesis, the second run of the LHC - the Run-2, just started. During 2013 - 2015, the LHC was shut down for upgrades that would allow it to run at its design collision energy of $\sqrt{s} = 14$ TeV and the first collisions at $\sqrt{s} = 13$ TeV have already been recorded earlier this spring.

4 EVENT AND OBJECT RECONSTRUCTION

Several intermediate steps are required to transition from the raw detector signature of the p-p collision products to the final objects used in the analyses. This chapter describes these stages; how the raw data are *reconstructed* into well defined analysis objects and *identified* as electrons, jets or muons. First, a short description of the tracking and vertex reconstruction methods applied in ATLAS is outlined, followed by the reconstruction and identification performance of leptons, jets and the missing transverse momentum. For each of these objects, a set of requirements specific to the identification and reconstruction in the $H \to WW^{(*)}$ analysis [56] is presented.

4.1 Tracks and Vertices

The main role of tracking is to measure the trajectories of charged particles and consequently determine their momenta through the curvature of the track curvature in the magnetic field. Tracking is performed by two algorithms:

i) the *inside-out algorithm:* is responsible for an efficient track reconstruction of the primary charged particles (primaries), i.e. particles which are directly produced in p-p collisions.

ii) the *outside-in algorithm:* is responsible for a track reconstruction of the secondary particles (secondaries), i.e. particles produced in the interactions of primaries.

A tracking algorithm requires a *track seed* in order to reconstruct the trajectory of a particle. A track seed is a collection of *space points*, 3D spatial coordinates (x, y, z), extracted from the raw data (hits) within the complete acceptance ($|\eta| < 2.5$) of the Inner Detector. The inside-out algorithm requires three space points in the separate layers of the pixel and the SCT detectors. Other good quality hits[1] are added to the track candidate along the direction specified by the track seed, moving outwards towards the outer layers of the SCT. Any ambiguities between the track candidates are resolved by a refined fit, based on the pattern recognition of weighted tracks (fake tracks made of purely combinatorial set of hits are assigned a lower weight) and a χ^2 fit [57]. In the final stages, hits from the TRT are also included to the track. The inside-out algorithm requires tracks with $p_T > 400\,\text{MeV}$. Contrary to the inside-out algorithm, the outside-in algorithm starts with the seeds in the TRT and extends inwards toward the SCT and pixel detector.

Once the tracks are reconstructed, both impact parameters, d_0 and z_0, can be obtained. This information is further used in the reconstruction of the primary vertex, i.e. the interaction point and the secondary vertices, i.e. vertices of particle decays. The reconstruction of the primary vertex starts with the *vertex finding algorithm*, which associates all reconstructed tracks, satisfying certain quality requirements (described in detail in [58, 59]), to vertex

1 Hits are classified into three categories: good quality hits, *outliers* which reduce the fit quality of the track, and *holes* which represents hits that are not found but are expected.

candidates inside the interaction region[2]. The *vertex seed* is determined by searching for the most frequently occurring z_0 position of the tracks. Afterwards, the precise position of the vertex is determined by an adaptive *vertex fitting algorithm*, a robust χ^2 fitter [60], which as an input takes the seed position and all the tracks in its vicinity. Tracks not belonging to the vertex (outliers) are assigned a lower weight in the overall vertex χ^2. The tracks which are incompatible with the vertex at more than the 7σ level are used for a new seed and the whole process is repeated until no additional vertices with more than 2 tracks are found. If more than one PV is found, the one with the highest scalar $\sum p_T^2$ of associated tracks is taken to be the PV. In the $H \to WW^{(*)}$ analysis, the PV of each event must have at least three tracks with $p_T > 400\,\text{MeV}$.

The number of simultaneous p-p interactions per bunch crossing (pileup) μ exceeded the design specification of the ID [35, 54] at the end of 2012 data-taking. These increased PU conditions had a great impact on the track and vertex reconstruction. The occupancy of the detector increases with the increasing PU, resulting in a lower efficiency, fake tracks (reconstructed tracks that cannot be matched to a PV nor to a secondary vertex) and vertices. Effects introduced due to the higher PU are minimised by tightening the quality cuts on the reconstructed tracks with a more robust selection criteria. The default quality cuts for the 2011 dataset requested at least 7 hits in the pixel+SCT detectors and at most two holes (missing but expected hits) in the pixel detector, while the 2012 quality cuts only select tracks with at least 9 hits in the pixel+SCT detectors and exactly zero holes in the pixel detector [59].

Figure 20 shows the efficiencies of primary tracks (tracks produced by primary particles) and the number of fake tracks for different PU scenarios in the minimum bias MC samples with the default and robust selection criteria. While the robust criteria decrease the number of fake tracks (right figure) they also lower the overall tracking efficiency by 5%, reaching $\sim 84\%$ (left figure) [59].

The vertex reconstruction efficiency decreases by $\sim 30\%$ with the increasing PU ($\mu = 40$) in the minimum bias MC samples, as is shown on Figure 21. High PU increases the number of fake tracks which result in fake vertices. Applying the robust criteria to the track quality requirements greatly reduces the number of fake vertices (right plot). Even though the vertex efficiency is somewhat lower for the robust criteria at the lower PU than for the default criteria, the efficiencies even out at the higher PU (left plot).

Figure 22 shows the number of reconstructed vertices and tracks for the $\sqrt{s} = 7$ TeV 2011 data samples containing different amounts of pileup. The reconstruction efficiency is stable for $\mu \lesssim 15$, while for the higher pileup $\mu \gtrsim 15$ the efficiency is reduced. Additionally, the average number of reconstructed tracks when using the robust criteria instead of the default one, remains constant for all three pileup scenarios [59].

The vertex and track reconstruction are well understood in the 2011 data and the MC simulation and yield similar results with the increasing PU. On the other hand, for the 2012 data at $\sqrt{s} = 8$ TeV, some discrepancies in the minimum bias vertex multiplicities between the data and the MC appear, and in order to model the pileup effects correctly in simulation a μ-rescaling is applied on the 2012 MC. [61, 62].

2 The interaction region, the beam spot or the collision region is the region where the two proton beams collide.

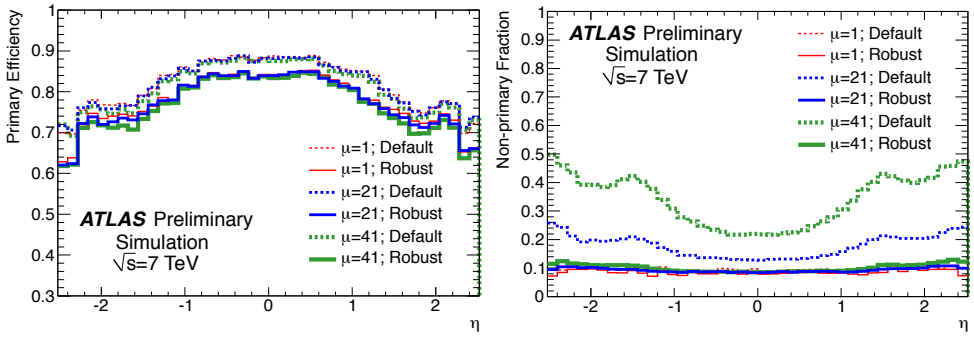

Figure 20.: The primary track reconstruction efficiencies (left) and a fraction of fake tracks (non-primaries) (right) vs. η in the minimum bias MC samples for different pileup scenarios $\mu = 1$, $\mu = 21$ and $\mu = 41$ [59].

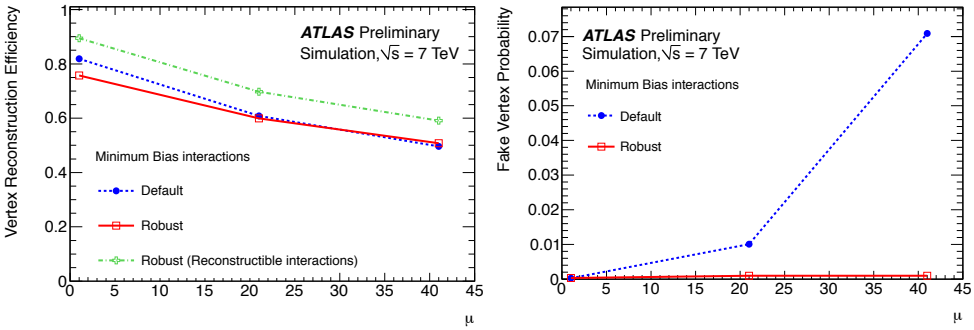

Figure 21.: The vertex reconstruction efficiency (left) and the probability for fake vertices (right) vs. pileup (μ) in the minimum bias MC samples. Reconstructible interactions (appearing in the left plot) are defined as interactions with at least two stable charged primary particles with $|\eta| < 2.5$ and $p_T > 400\,\text{MeV}$ [59].

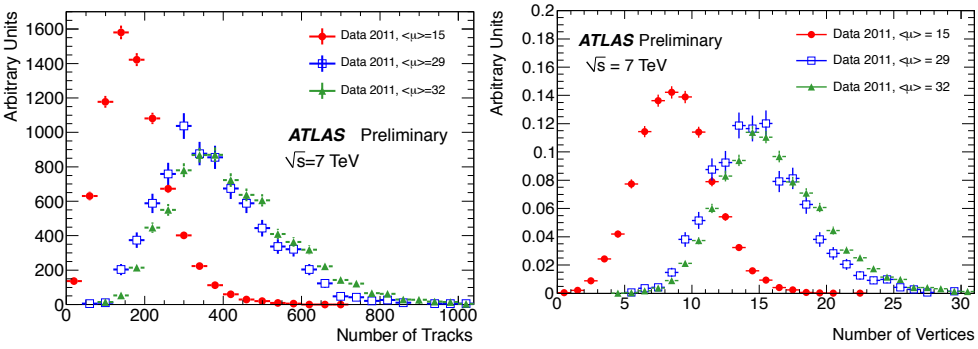

Figure 22.: The number of reconstructed tracks by an inside-out algorithm and the default criteria (left) and the number of reconstructed vertices with the robust track requirements in the 2011 data containing different amounts of pileup μ [59].

4.2 Leptons

Isolated leptons are a very common final state in many analyses at the LHC and their identification and reconstruction is crucial. This section describes the identification and reconstruction of electrons and muons. Since τ leptons are not included in the $H \to WW^{(*)} \to \ell^+\nu_\ell\ell^-\bar{\nu}_\ell$ analysis, they are not described here, but their reconstruction and identification methods can be found in [63–65].

4.2.1 Electrons

Electrons traverse the ATLAS detector leaving a track in the ID until they stop in the electromagnetic calorimeter, where they deposit all their energy.The reconstruction and identification of electrons therefore requires information from both sub-detectors. The *reconstruction* of electrons in the central region ($|\eta| < 2.47$) starts with the *sliding window algorithm* [66, 67] which is a clustering algorithm designed to find seed clusters. The algorithm sums up the energy deposits in the ECAL cells within a fixed size rectangular window (3×5 in units of 0.025×0.025 in $\eta \times \phi$ space) until it finds a local transverse energy maximum above 2.5 GeV in one of such clusters. This cluster becomes a seed and is loosely matched (within a cone of $\Delta\eta < 0.05$) to the tracks extrapolated from their last measuring point in the ID. Due to bremsstrahlung, electrons loose their energy which alters the curvature of their trajectories in the magnetic field. These losses and track alterations are taken into account with the *Gaussian Sum Filter* (GSF) [68]. The GSF approximates the electron trajectories as a weighted sum of Gaussian functions and splits the experimental noise into several Gaussian components. By the end of the 2011 data-taking, all trajectories satisfying standard track requirements ($p_T > 400$ MeV and $|\eta| < 2.5$) have been re-fitted by the GSF and matched to the calorimeter clusters. In 2012, a bremsstrahlung recovery has been added to the initial step of the electron trajectory formation, which improved track reconstruction. The four-momentum of the electron candidate is computed from the cluster energy and the parameters of the track projected to the direction of the track at the interaction point.

Unfortunately, not all objects reconstructed by the electron reconstruction algorithm actually represent real prompt electrons. There are many background objects that mimic them; like hadronic jets faking electrons, photon conversions, electrons originating from decays inside jets (non prompt electrons), and need to be rejected. The *identification* of electrons is based on various discriminating variables, combined into selection criteria, in order to reject as much background as possible while identifying real prompt electrons with high-efficiency. The 2012 identification criteria in the central region are based on the cut-based selection and are divided into three efficiency working points defined with increasing background rejection power [69]:

- *loose:* uses shower shape variables in the first and second layer of the ECAL and hadronic leakage variables. Additional requirements on the track quality and the track-cluster matching are added to improve the rejection of hadronic backgrounds.
- *medium:* uses tighter *loose* selection criteria and requires a hit in the innermost layer of the pixel detector (to reject electrons from photon conversions), a loose selection on the impact parameter, and the extra information from the TRT (to reject charged-hadron background). The background rejection power with respect to the *loose* selection criteria is increased by an order of magnitude.
- *tight:* uses tighter *medium* selection criteria taking into account the ratio of cluster energy to track momentum (E/p) and applies a veto on reconstructed photon conversion

vertices associated with the cluster. The background rejection power is increased by a factor of two compared to the *medium* selection.

More details about the 2011 and 2012 identification criteria can be found in [67] and [70], respectively.

In order to cope with higher number of pileup interactions in the 2012 data-taking, the identification criteria have been re-optimised and a likelihood-based method (LH) has been added to improve the background rejection. The LH method, which is a multivariate technique, allows a combined evaluation of several different discriminating variables [70]. The LH uses the signal and the background probability density functions (PDFs) of discriminating variables. Based on the PDFs, which are obtained from the data, LH evaluates an overall probability whether a given object represents a signal or a background object. The LH selection is also split into three parts: LOOSE, MEDIUM and VERY TIGHT, which roughly match the *medium* and *tight* cut-based selection criteria with a better background rejection. A data-driven estimate [70] of the background rejection efficiency for various identification criteria is shown on Figure 23. The LH selections offer approximately twice as much background rejection compared to the cut-based ones.

Before using the reconstructed and identified electrons in the physics analyses, inefficiencies arising due to trigger, reconstruction and identification algorithms must be accounted for. Electron selection efficiencies are determined directly from the data using the tag-and-probe (TAP) method [67] on clean and unbiased electron samples, like $Z \to ee$, $W \to e\nu$ and $J/\psi \to ee$. The TAP method uses strict selection criteria to select one electron (*tag*) while the second electron (*probe)*, identified with the looser criteria, is used to measure the efficiency of the selection criteria. The measured efficiencies in the MC usually differ from TAP results on the data and are corrected for by a *scale factor* (SF), a data-to-MC ratio. The combined reconstruction and identification efficiencies for different cut-based and LH identification criteria are shown on Figure 24. Even though the combined reconstruction and identification efficiencies are rather similar between the LH and cut-based selections, the LH identification criteria reject more background, as is shown on Figure 23.

The $H \to WW^{(*)}$ analysis uses the following identification criteria:

- in the low E_T region ($10 - 25\,\text{GeV}$) the VERY TIGHT LH requirement is used, which reduces backgrounds from light-flavour jets and photon conversions by 35% compared to the cut-based selection with the same signal efficiency.
- in the high E_T region ($> 25\,\text{GeV}$) where misidentification backgrounds are less important, a cut-based *medium* selection is used. It increases the electron identification efficiency by about 11% compared to the *tight* cut-based selection.

4.2.2 Muons

Muons are minimum ionising particles and therefore traverse the ATLAS detector without being stopped by the calorimeter system. Their reconstruction and identification therefore largely relies on the ID and the Muon Spectrometer subsystems, and in a lesser extent also from the calorimeters. All muon reconstruction algorithms exploit the independent momentum measurements from the ID and the MS. Furthermore, the use of such a combination reduces the muon misidentification rate. Depending on the available information for the muon reconstruction (the ID, the MS or the calorimeters), the muon identification follows various reconstruction criteria:

- **Stand-alone muons (SA):** The muon trajectory is reconstructed only from the segments found in the MS (tracks traversing at least two layers of the MS chambers) and

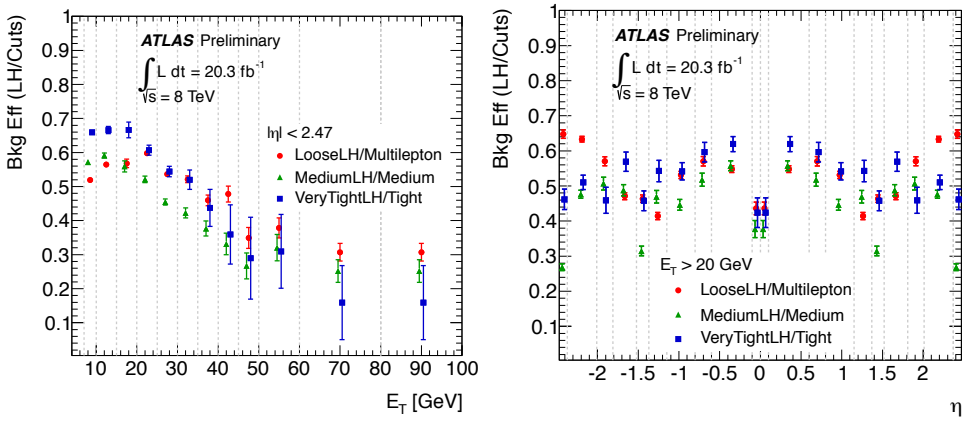

Figure 23.: Ratio of background efficiencies between a LH selection and the closest (efficiency wise) cut-based selection as a function of E_T and η [70].

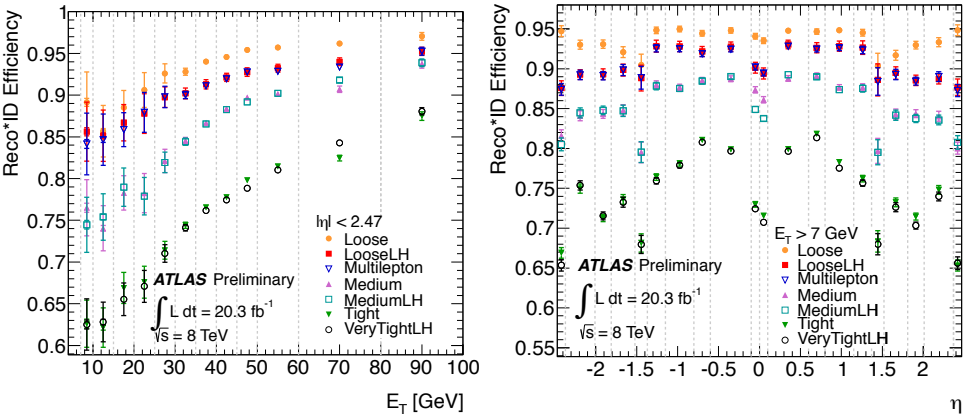

Figure 24.: Combined electron reconstruction and identification efficiencies for cut-based and likelihood identification criteria as a function of E_T (left) and η for $E_T > 7$ GeV (right). The data efficiencies are derived from the measured data-to-MC efficiency ratios (SF) and the MC prediction from $Z \to ee$ decays in 2012 dataset [70].

provides a base for the momentum measurement. Tracks are extrapolated to the beam line, including corrections due to energy loss and multiple scattering of muons in the calorimeter. Tracks of the SA muons have in general a greater pseudorapidity coverage, up to $|\eta| < 2.7$, compared to $|\eta| < 2.5$ for the tracks in the ID. Very low momentum tracks (~ 1 GeV) are difficult to reconstruct as a SA muon since they do not penetrate to the outer most MS stations.

- **Combined muons (CB):** the CB muons have the highest purity. Track reconstruction is performed independently in the ID and the MS. The track quality is determined by a χ^2 test, defined as a difference between the outer and inner track vectors, weighted by their combined covariance matrix. The muon trajectory in the ID relates the muon trajectory in the MS to the primary vertex.

- **Segment-tagged muons (ST):** the ID tracks with a sufficient momentum are propagated to the first MS station where a search for nearby segments begins. In case such a segment is close enough to the predicted track position, the track in the ID is tagged as a muon track and is used to evaluate muon kinematics. The ST muons are used to increase the detector acceptance (in case of low-p_T muon which cross only one layer of the MS chambers or muons travelling through holes in the η coverage).

- **Calorimeter-tagged muons (CaloTag):** If an energy deposit in the calorimeter of a track coming from the ID is compatible to an energy deposit of a minimum ionizing particle, it is tagged as a muon. These muons have the lowest purity but recover the acceptance for low-p_T muons at $\eta \approx 0$, where the MS has a gap in coverage.

The muon reconstruction is performed using two independent reconstruction algorithms:

- **Staco** or **Chain 1:** performs a statistical combination of the ID and the MS track parameters using the corresponding covariance matrices [71].

- **Muid** or **Chain 2:** performs a global re-fit of muon tracks using hits from the ID and the MS [72].

For the reconstruction of the 2012 data a unified algorithm, **Chain 3**, incorporating the best features of Chain 1 and Chain 2, is used in parallel with the Chain 1 and Chain 2 algorithms. All three chains have very similar performances [73].

The reconstruction efficiency of various muon types is composed of three different contributions: the reconstruction efficiency in the ID, the reconstruction efficiency in the MS and the efficiency of the matching between the ID and the MS contributions. Tag-and-probe methods, where probes represent a sample of muons reconstructed by either ID or MS, are used to test the reconstruction efficiency of the other system (MS or ID). In the central region ($|\eta| < 2.5$), the reconstruction efficiencies are estimated using $Z \to \mu\mu$ and $J/\psi \to \mu\mu$ (for low-p_T muons) samples.

There are two areas in the ATLAS detector with lower reconstruction efficiency due to acceptance losses; near $\eta \approx 0$, where the MS is only partially equipped with muon chambers due to the ID and calorimeter services, and close to $\eta \approx 1.2$, which is the transition between the barrel and the end-cap regions with only one layer of the MS chambers. Figure 25 shows the muon reconstruction efficiencies in the ID as a function of η for different muon types as measured in $Z \to \mu\mu$ events for the 2011 and the 2012 datasets. A combination of all muon types (CB, ST and CaloTag) gives approximately 99% efficiency across all the ID regions for the 2012 data. The use of the ST muons allows the recovery of lost efficiency in the region $1.2 < |\eta| < 1.3$ and the CaloTag muons recover the lost efficiency at $\eta \approx 0$. The scale factors (data/MC) obtained from TAP method, are within 1% with the largest differences observed for the CB muons. The efficiencies for the 2011 period are generally lower than for the 2012[3], especially for the CB muons at $|\eta| \simeq 1.2$.

Muons arising from heavy particle decay inside jets are rejected by a set of isolation criteria, discussed in the next section, but their contamination of the prompt muons is less than 1% for the $H \to WW^{(*)}$ analysis described in this thesis. The isolation criteria represent an additional selection for muons, similar to electron identification criteria.

Muons in the $H \to WW^{(*)}$ analysis are reconstructed by the Staco (Chain 1) algorithm using the combined information from the ID and the MS for tracks with $|\eta| \leq 2.5$.

3 Between the 2011 and the 2012 data-taking periods additional MS layers have been installed at $\eta = -1.2$ and partially also at $\eta = +1.2$.

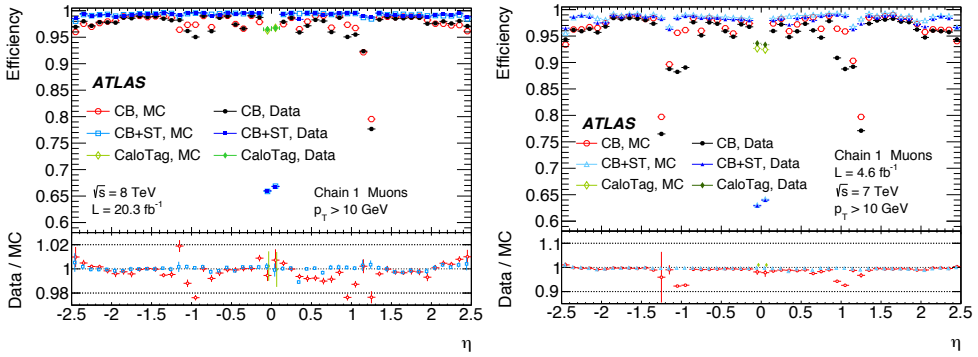

Figure 25.: Muon reconstruction efficiency as a function of η for different muon types reconstructed by Chain 1 algorithm for the 2012 data (left) and the 2011 data (right). The efficiency is measured in $Z \to \mu\mu$ events for muons with $p_T > 10\,\text{GeV}$ [73].

4.2.3 Lepton Isolation

In order to reject jets incorrectly reconstructed as prompt leptons, further requirements are imposed on the lepton impact parameters and on the *isolation* of reconstructed and identified lepton candidates. The lepton isolation is evaluated by two criteria:

- *calorimeter based isolation*: the calorimetric isolation variable is defined as the ratio of the scalar sum $\sum E_T$ deposited in the calorimeter cells[4] in a cone of ΔR around the candidate and divided by the candidate's E_T (p_T). It is additionally corrected for the energy leakage from the candidate to the isolation cone and for the pileup effects.
- *track-based isolation*: the track isolation variable represents the ratio of the scalar sum $\sum p_T$ of tracks with a minimum p_T (specified below) within a cone of ΔR around the candidate, excluding the track of the candidate itself, and divided by the candidate's E_T (p_T). The considered tracks must be of good quality and originate from the PV associated with the candidate's track [70].

In the $H \to WW^{(*)}$ analysis the transverse impact parameter d_0 and its estimated uncertainty σ_{d_0} must satisfy $|d_0|/\sigma_{d_0} < 0.3$ for both electrons and muons. The longitudinal impact parameter $z_0 \sin\theta$ must be less than 0.4 mm for electrons and less than 1.0 mm for muons.

The electron track isolation criteria in the $H \to WW^{(*)}$ analysis is based on the $\sum p_T$ of all tracks with $p_T > 400$ MeV ($p_T > 900$ MeV for 2011 analysis) within a cone of $\Delta R = 0.4$ for $p_T < 15\,\text{GeV}$, and $\Delta R = 0.3$ for $p_T > 15\,\text{GeV}$ tracks coming from the PV. Additionally, the track isolation requires the ratio $\sum p_T / E_T^{\text{electron}} < 0.06$ for the lower E_T range ($10 - 15\,\text{GeV}$) and less than 0.10 for the higher E_T range ($> 25\,\text{GeV}$). The calorimeter isolation evaluates the ratio of $\sum E_T / E_T^{\text{electron}}$ in a cone of $\Delta R = 0.3$ around the electron candidate cluster. The cells within 0.125×0.175 in $\eta \times \phi$ space around the center of the electron's energy deposit are excluded from the sum. The electrons relative calorimetric isolation criteria varies monotonically, depending on the electron's E_T. The lower bound is 0.20 for $10 < E_T < 15\,\text{GeV}$ and the upper bound is 0.28 for $E_T > 25\,\text{GeV}$. Applying electron isolation criteria reduces background contamination from 3% to 0.5%.

For muons, the track isolation criteria in the $H \to WW^{(*)}$ analysis consider all tracks with $p_T > 1\,\text{GeV}$ within the same cone sizes as for electrons. The ratio $\sum p_T / p_T^{\text{muon}}$ ought to

4 In 2012 analysis a cell-based algorithm is replaced by topological cluster algorithm, which is more robust against pileup [66].

be less than 0.06 for the low-p_T ($10 - 15\,\text{GeV}$) muon candidates, and less than 0.12 for the high-p_T muons ($> 25\,\text{GeV}$). The relative calorimetric isolation criteria is calculated as the $\sum E_T / p_T^{\text{muon}}$ from calorimeter cells for muon candidates within $\Delta R = 0.3$. All calorimeter cells within $\Delta R < 0.05$ of the muon candidate are excluded from the E_T. The muon's relative calorimetric isolation also varies monotonically from 0.06 for $10 < p_T < 15\,\text{GeV}$ muons, to 0.28 for $p_T > 25\,\text{GeV}$ muons. The muon calorimeter isolation, while it should be linearly dependent on the pileup, shows a non-linear nature and additional quadratic corrections are applied on the measured isolation energy. The quadratic corrections are smaller for 2012 analysis than for 2011 analysis, due to better noise suppression in the calorimeter cells for the 2012 data-taking. The differences in isolation efficiencies between the data and the MC are considered in the applied scale factors.

The electron and muon isolation efficiencies, obtained through TAP methods using $Z \to ee$ and $Z \to \mu\mu$ samples respectively, are well modelled in the MC, with scale factors $\lesssim 2\%$ for electrons and $\lesssim 5\%$ for muons.

4.2.4 Lepton Triggers

Due to limitations in data storage capacities and detector readout, not all collision events can be recorded. Requirements at the trigger level are used to identify events of interest while maintaining the recording rate within the allotted limits. This section offers a summary of trigger requirements used specifically in the $H \to WW^{(*)}$ analysis.

The $H \to WW^{(*)}$ analysis searches for events with high-p_{T} leptons by triggering either on a single lepton (single lepton trigger) *or* two leptons (dilepton triggers) in the event. The single lepton triggers use tighter lepton identification criteria and have higher p_{T} thresholds compared to dilepton triggers. The combination (*or*) of dilepton and single lepton triggers helps to recover the lost efficiency for lower p_T leptons and allows the selection of leading leptons with lower p_{T}.

In the 8 TeV $H \to WW^{(*)}$ analysis, the minimum p_T requirement for single electron triggers is either 60 GeV or $24i$ GeV, where i stands for a trigger-level isolation requirement, which is less stringent than the one used offline[5] and 12 GeV for the double electron triggers. The minimum p_T requirement for the single and double muon trigger is 36 GeV or $24i$ GeV and 18 GeV respectively, and 12 GeV for the double $e\mu$ trigger. Table 7 summarises all the triggers used in the 8 TeV $H \to WW^{(*)}$ analysis.

ee	single-lepton triggers dilepton trigger	`EF_e60_medium1` *or* `EF_e24vhi_medium1` *or* `EF_2e12Tvh_loose1` *or* `EF_2e12Tvh_loose1_L2StarB`
μ	single-lepton trigger dilepton trigger	`EF_mu24vh_tight` *or* `EF_mu36_tight` *or* `EF_mu18_tight_EFFS`
$e\mu$	single-lepton trigger dilepton trigger	all single lepton triggers in used ee and $\mu\mu$ channel *or* `EF_e12Tvh_medium1_mu8`

Table 7.: Single and double lepton triggers used in the 8 TeV $H \to WW^{(*)}$ analysis. The `EF` refers to event filter, `e` signifies an electron and `mu` a muon. The number following the lepton flavour is the p_{T} threshold. The `vh` indicates the calorimeter isolation and `i` the track isolation with `loose`, `medium` or `tight` identification criteria. Other remaining notations refer to the trigger chains.

5 The offline selection selects two leptons, ee, $\mu\mu$ or $e\mu$, with opposite charges. The leading lepton in terms of p_{T} must have $p_{\text{T}} \geq 22\,\text{GeV}$ and the subleading must have $p_{\text{T}} \geq 10\,\text{GeV}$. More details about the offline selection can be found in Chapter 5.

The trigger efficiencies are measured by a TAP method with a $Z/\gamma^* \to ee, \mu\mu$ data sample. For electrons, the efficiency of the single lepton trigger increases with p_T and in average yields 90% efficiency. The single muon trigger efficiency varies with η and is approximately 70% (90%) in the $|\eta| < 1.05$ ($|\eta| > 1.05$) region. The dilepton triggers increase the signal acceptance and the signal efficiency gain varies between $\sim 2\%$ and $\sim 18\%$.

4.3 Jets

Due to the color confinement quarks and gluons fragment and *hadronise*, forming a collimated shower of energetic hadrons - *jets*, which are produced in abundance in high energy p-p collisions. Jets are detected through the energy deposits of their constituent hadrons in the ATLAS calorimeter systems. These energy deposits are summed and grouped together by a topological clustering algorithm[6] [66]. Topological clusters represents clusters of energy deposits, built from topologically connected calorimeter cells, which contain a sufficient signal-to-noise ratio. They represent an input for *jet finding algorithms*[7].

The most commonly used jet finding algorithm in ATLAS is the *anti-k_T* clustering algorithm [75] and belongs to the family of *sequential recombination algorithms*, where the input objects are iteratively grouped together depending on the distance between them d_{ij}, and the distance to the beam line d_{iB};

$$d_{ij} = \min(k_T^{i\,2p}, k_T^{j\,2p}) \frac{\Delta R_{ij}^2}{R^2}, \qquad d_{iB} = k_T^{i\,2p}. \tag{77}$$

The k_T^i, k_T^j represent the transverse momentum of objects i and j, respectively. The ΔR_{ij} is defined as $\Delta R_{ij}^2 = (y_i - y_j)^2 + (\phi_i - \phi_j)^2$, where $y_{i,j}$ and $\phi_{i,j}$ represent the rapidity and azimuthal angle of the i-th and j-th object. The parameters p and R depend on the specific algorithm. For the anti-k$_T$ algorithm p has a value of -1 which results in the clustering beginning with the highest k_T object, e.g. the object i. The distances between the other objects in the vicinity of the object i, d_{ij}, are compared to d_{iB}. In case $d_{ij} < d_{iB}$, i and j are recombined into a new object k, otherwise the object i is defined as a *jet* and is removed from the list of objects before searching for other jets.

The calorimeter jets are built from topological clusters with positive energy and are calibrated using the MC simulation. Jets are initially reconstructed at the electromagnetic (EM) scale, which correctly measures the energy deposits of particles producing electromagnetic showers (electrons and photons), but not for hadrons. The *local cell signal weighting* (LCW) calibration method [76] calibrates the topo-clusters to obtain the correct response to hadrons. It classifies the topo-clusters as either electromagnetic or hadronic based on their shape, and applies an energy correction derived from the MC simulation. The LCW calibration addresses the calorimeter non-compensation and energy losses (e.g. due to detector dead material). After the calibration, an additional *jet energy scale* (JES) correction is applied to account for further differences between truth-level jets and reconstructed jets, which are not taken into account by the cluster-based corrections. The LCW + JES calibration applies a correction to the energy offset due to the pileup interactions (for both in-time pileup and out-of-time pileup), corrects the jet direction so that it points to the PV instead of the nominal center of the ATLAS detector, calibrates the jets to the hadronic energy scale using p_T- and η-dependent correction

6 A topological clustering algorithm sums up the energy deposits in a group of cells, starting with a seed cell with a high energy deposit. It iteratively adds neighbouring cells if their energy exceeds the low energy threshold.

7 Jet finding algorithms attempt to reconstruct the partonic initial state by grouping calorimeter energy deposits. In order for such algorithms to perform optimally, they are required to be both infra-red and collinear safe [74].

factors determined from the MC and the data, and lastly applies *in situ* corrections [76, 77]. Figure 26 compares the responses of EM+JES and LCW+JES calibration methods.

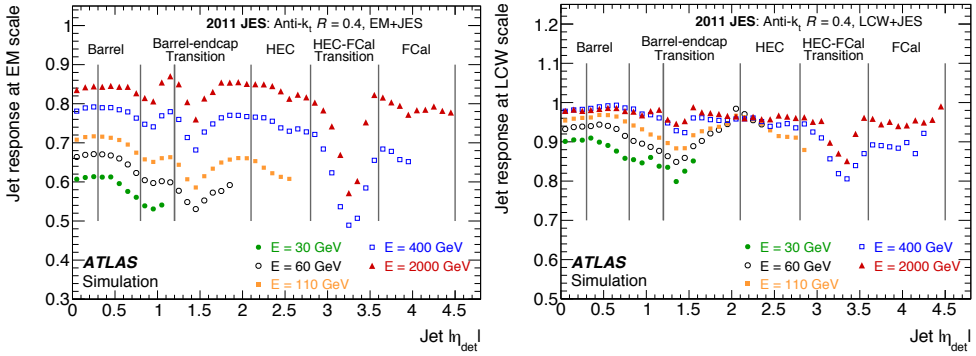

Figure 26.: The average energy response defined as $\mathcal{R}^{\mathrm{EM(LCW)}} = E_{\mathrm{jet}}^{\mathrm{EM(LCW)}} / E_{\mathrm{jet}}^{\mathrm{truth}}$ from simulated topo-cluster jets for EM+JES (left) and LCW+JES calibration (right) at various truth-jet energies as a function of η. The inverse of $\mathcal{R}^{\mathrm{EM(LCW)}}$ corresponds to the average jet energy scale corrections for EM or LCW calibrations. [76]

Jets play a very important role in the $H \to WW^{(*)}$ analysis and are identified using the anti-k$_T$ algorithm with $R = 0.4$ and LCW+JES calibration. In order to classify events in the appropriate jet categories within the $H \to WW^{(*)}$ analysis, and thus defining specific event selections (more in Chapter 5), jets must have $p_{\mathrm{T}} > 25\,\mathrm{GeV}$ for $|\eta| < 2.4$ and $p_{\mathrm{T}} > 30\,\mathrm{GeV}$ for $2.4 < |\eta| < 4.5$ region. The increased p_{T} threshold in the forward region suppresses pileup jets. Jets which are used in other selections, like the ones used for central jets rejection in the VBF analysis, or jets used in the b-jet identification, have lower p_{T} thresholds, $p_{\mathrm{T}} > 20\,\mathrm{GeV}$.

In order to identify whether a calorimeter jet originated from the hard scatter, the *jet vertex fraction* (JVF) variable is used. The JVF variable is defined as the fraction of the scalar $\sum p_T$ of the tracks in a jet originating from the selected hard scatter PV. JVF values approaching 1 indicate a hard-scatter jet, those approaching 0, a pileup jet, and the case JVF $= -1$ indicates no tracks have been assigned to the jet (mostly forwards jets).

In MC truth-level studies, the hard-scatter and the pileup jets are distinguished by the ΔR matching to the truth jets. If a calorimeter jet is within $\Delta R \leq 0.4$ to the truth jet, then it is tagged as a true jet, else it is tagged as a pileup jet.

Figure 27 shows the great discriminating power of the JVF variable between the hard scatter and the pileup jets from a simulated Z + jets sample. The application of the JVF also ensures the stability of the mean jet multiplicity against pileup [78].

In the $H \to WW^{(*)}$ analysis, the jets with $p_T < 50\,\mathrm{GeV}$ and $|\eta| < 2.4$ must have more than 50% of the summed scalar p_T of their tracks within $\Delta R = 0.4$ around the jet axis associated to the PV (JVF > 0.5).

4.3.1 Identification of b-jets

As it will be seen in Chapter 5, events containing top quarks, which further decay to Wb, with $\mathcal{B}(t \to Wb) \approx 100\%$, represent one of the largest backgrounds in the VBF $H \to WW^{(*)}$ analysis and in order to reduce it, a good b-jet identification and reconstruction technique is crucial. The b-jets can be identified through various algorithms based on impact parameters or secondary vertices, and those more complex even exploit the topologies of the b-jet and

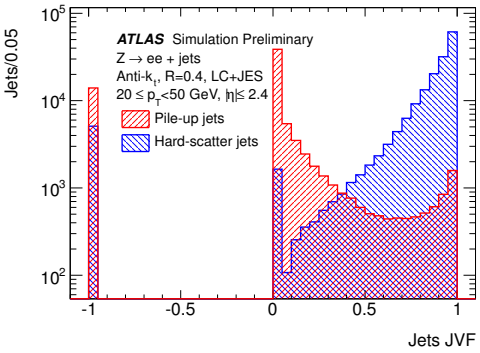

Figure 27.: The JVF distribution of hard scatter and pileup jets with $20 < p_T < 50\,\text{GeV}$ in $|\eta| < 2.5$ in simulated $Z \to ee +$ jets [78].

c-jet weak decays. All these discriminating variables are used as an input to a multivariate algorithm, called the MV1 [79], which returns a tag weight for a *b*-jet, a *c*-jet or a light-jet (*u*,*d*,*s*). A cut on the tag weight defines a *working point* of the *b*-tagging algorithm and different working points represent different *b*-jet tagging and light-jet rejection efficiencies as shown in Figure 28.

The performance of the MV1 *b*-tagging algorithm is measured in a $t\bar{t}$ data sample, considering only jets with $p_T > 20\,\text{GeV}$ in the limited acceptance of the ID ($|\eta| < 2.5$) [80, 81]. The *b*-tagging performance is estimated as a *b*-tagging efficiency (fraction of correctly tagged *b*-jets) with respect to the mistagging rate (fraction of incorrectly tagged light or *c*-jets). Figure 29 shows the efficiencies of the MV1 algorithm to select *b*-jet, *c*-jets and light jets for the 70% working point.

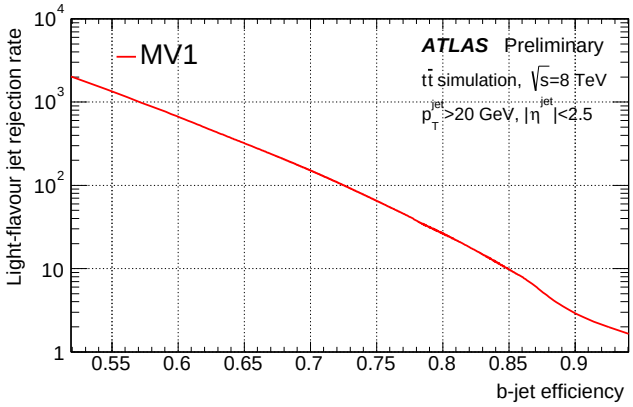

Figure 28.: Light-jet rejection versus *b*-jet tagging efficiency for the MV1 algorithm. Jets are selected from the simulated $t\bar{t}$ sample with $p_T > 20\,\text{GeV}$ and $|\eta| < 2.5$ [80].

The MV1 algorithm, being the most common *b*-tagging algorithm in ATLAS, is also used in $H \to WW^{(*)}$ analysis where a 85% working point is chosen (allowing the highest top background rejection) with 10.3% probability to misidentify the light-jets with *b*-jets.

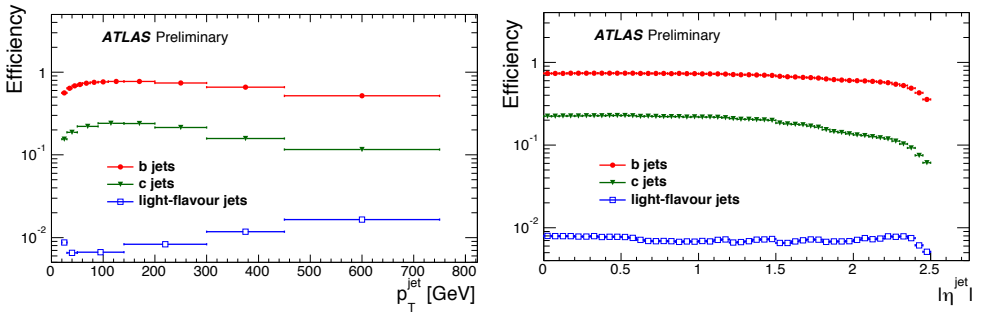

Figure 29.: The efficiency of MV1 b-tagger to select b-jet, c-jets or light flavour jets as a function of p_T (left) and η (right) for the 70% working point. Jets are selected from simulated $t\bar{t}$ sample at $\sqrt{s} = 8\,\text{TeV}$ with $p_T > 20\,\text{GeV}$ and $|\eta| < 2.5$ [80].

4.4 Overlap between objects

Reconstructed leptons and/or jets can sometimes overlap in the (η, ϕ) space. The $H \to WW^{(*)}$ analysis takes the following steps to resolve any such overlaps:

- Electrons with tracks extending to the MS are removed.
- If a muon and an electron candidate are separated by $\Delta R < 0.1$, the electron is removed since these cases usually indicate a muon undergoing a bremsstrahlung in the ID or the calorimeter.
- If an electron is within $\Delta R < 0.05$ of any muon in the event collection, the event is removed.
- A high-p_T electron is always reconstructed as a jet, and if a jet and an electron object are separated by $\Delta R < 0.3$, the jet is removed.
- If a muon object is separated by $\Delta R < 0.3$ from the jet, the muon is removed, since it most probably comes from a heavy flavour decay.
- In case two electron objects are separated by less than $\Delta R = 0.1$, the electron with a larger E_T is retained.

4.5 Missing Transverse Momentum

Neutrinos do not interact with matter and cannot be directly detected by particle detectors. Their presence however, can be distinguished as a momentum imbalance in the transverse plane where momentum conservation is expected. The *missing transverse momentum* is defined as a negative sum in the transverse plane of all reconstructed and calibrated objects such as leptons, jets and photons (hard objects), including also the remaining low-p_T *soft* objects

$$\mathbf{E}_\mathbf{T}^{\text{miss}} = -\left(\sum_{\substack{\text{identified} \\ \text{objects}}} \mathbf{p}_\text{T} + \sum_{\text{soft}} \mathbf{p}_\text{T} \right). \tag{78}$$

The identification, reconstruction and calibration of the soft objects and leptons, jets and photons differ between different methods of evaluating the missing transverse momentum. The $H \to WW^{(*)}$ analysis uses three methods to reconstruct missing transverse momentum[8]:

Calorimeter based reconstruction, $\mathbf{E_T^{miss}}$: Reconstruction of the missing transverse momentum is based on the energy deposits in the calorimeter and reconstructed muons from the MS and the ID (in regions with compromised MS coverage). Calorimeter energy deposits are linked to a high-p_T parent object in a specific order to avoid double counting: electrons, photons, hadronically decaying taus, jets, low-p_T objects and finally muons [82];

$$\mathbf{E_T^{miss}} = -\left(\sum_{e}\mathbf{p}_T + \sum_{\gamma}\mathbf{p}_T + \sum_{\tau}\mathbf{p}_T + \sum_{\text{jets}}\mathbf{p}_T + \sum_{\text{soft}}\mathbf{p}_T + \sum_{\mu}\mathbf{p}_T\right). \tag{79}$$

The leptons used in $\mathbf{E_T^{miss}}$ are defined as described in section 4.2, and photons and jets ought to have $E_T > 20\,\text{GeV}$. Muons' energy loss when traversing through the calorimeter is accounted for in the $\mathbf{E_T^{miss}}$ calculation. The transverse momentum of the remaining low-p_T objects is determined by the calibrated calorimeter energy deposits from topological clusters. The calorimeter based reconstruction of the missing transverse momentum is highly dependent on pileup, since the calorimeter energy deposits cannot be easily associated to the PV.

Track-based reconstruction, $\mathbf{p_T^{miss\,(trk)}}$: Reconstructing the missing transverse momentum from the tracks of fully reconstructed leptons, jets and photons highly reduces the pileup dependence, since the tracks can be directly associated with the PV. The tracks used in track-based missing transverse momentum calculation $\mathbf{p_T^{miss\,(trk)}}$ must have $p_T > 0.5\,\text{GeV}$ and originate from the PV. Poorly reconstructed tracks (isolated tracks which are not matched to any reconstructed object with $p_T > 100\,\text{GeV}$) which greatly impact the $\mathbf{p_T^{miss\,(trk)}}$ calculation, are removed. Since the track-based missing transverse momentum reconstruction does not include any information about neutral hadrons, its resolution is worse than E_T^{miss}, especially when jets are present in the final state.

Combined calorimeter and track-based reconstruction, $\mathbf{p_T^{miss,\,jet\text{-}corr}}$: This type of missing transverse momentum reconstruction uses tracks of reconstructed particles as well, with the exception of jets, for which the energy is reconstructed by the calorimeter. Jets used in $\mathbf{p_T^{miss,\,jet\text{-}corr}}$ calculation must have $p_T > 25(30)\,\text{GeV}$ for $|\eta| < 2.4(> 2.4)$ and $|JVF| > 0.5$ for $p_T < 50\,\text{GeV}$ in $|\eta| < 2.4$.

Figure 30 shows the comparison of all three varieties of missing transverse momentum reconstruction used in the $H \to WW^{(*)}$ analysis, as a function of pileup. The $p_T^{\text{miss (trk)}}$ is the most stable with increasing pileup but has the worst resolution, while $p_T^{\text{miss, jet-corr}}$ recovers the lost resolution and retains a small pileup dependence. Therefore, the $\mathbf{p_T^{miss,\,jet\text{-}corr}}$ is chosen as the reconstruction method in the $H \to WW^{(*)}$ analysis.

8 Quantities in bold represents vectors, like $\mathbf{E_T^{miss}}$, while quantities in normal text represent magnitudes of the vectors, like E_T^{miss}.

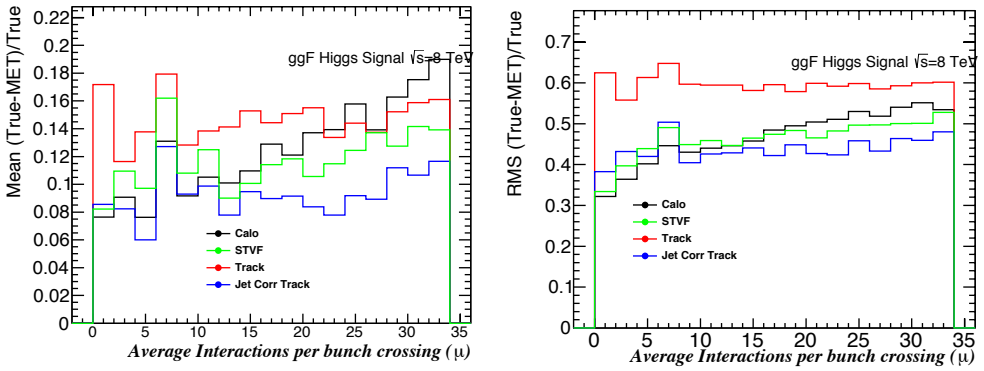

Figure 30.: The mean (left) and root-mean-square (right) of the resolution (True - E_T^{miss})/True) for all varieties of transverse missing transverse momentum calculation used in $H \to WW^{(*)}$ analysis as a function of pileup. The missing transverse momentum is evaluated in the ggF Higgs signal sample with 1 additional jet. Results are shown for calorimeter based E_T^{miss} (black), track-based $p_T^{\text{miss (trk)}}$ (red) and jet-corrected track-based $p_T^{\text{miss, jet-corr}}$ (blue) method. The green curve represents a variety of calorimeter based E_T^{miss} with pileup suppression (Soft Term Vertex Fraction - STVF), which has not been used in the $H \to WW^{(*)}$ analysis.

Each of these missing transverse momentum definitions can be used as a magnitude, a vector or a projection onto the axis defined by the nearest lepton or a jet, $E_{T,\text{rel}}^{\text{miss}}$. The relative quantity $E_{T,\text{rel}}^{\text{miss}}$ is defined as

$$E_{T,\text{rel}}^{\text{miss}} = \begin{cases} E_T^{\text{miss}} \sin \Delta\phi_{\text{near}} & \text{if } \phi_{\text{near}} < \pi/2 \\ E_T^{\text{miss}} & \text{otherwise,} \end{cases} \tag{80}$$

where ϕ_{near} is the angle between the E_T^{miss} and the nearest lepton or a jet. More details about the missing transverse momentum reconstruction can be found in [56, 82, 83].

The response of the ATLAS detector is well understood. The final-state objects that are important for the $H \to WW^{(*)}$ searches, like jets, electrons, muons and the missing transverse momentum are extracted from the raw data obtained in p-p collisions through the algorithms and procedures outlined in this chapter. The search for the VBF $H \to WW^{(*)}$ production mode can therefore begin and is presented in the next three chapters; Chapters 5 to 7.

5 VBF $H \to WW^{(*)}$ ANALYSIS

The decay of the Higgs boson into two W bosons, its high production cross-section via ggF and VBF, and the large branching ratio of the Higgs boson to WW^* in the low Higgs boson mass region, make the $H \to WW^{(*)}$ channel one of the most sensitive channels in the SM Higgs boson searches.

The $H \to WW^{(*)}$ analysis has been present from the beginning of the Higgs searches with the ATLAS detector. A combination of the most sensitive Higgs channels ($H \to WW^*/ZZ/\gamma\gamma$) based on the full 2011 dataset recorded at $\sqrt{s} = 7\,\text{TeV}$ [84] and part of the 2012 dataset recorded at $\sqrt{s} = 8\,\text{TeV}$, reported an excess of observed Higgs events around $m_H = 125\,\text{GeV}$, with $5.9\,\sigma$ significance [9]. At $\sqrt{s} = 7\,\text{TeV}$ [85] the $H \to WW^{(*)}$ channel did not observe any significant excess in data, while at $\sqrt{s} = 8\,\text{TeV}$ and 5.8 fb^{-1} an evidence of the Higgs signal has been reported with $3.2\,\sigma$ [30]. The analysis [86] of the combined $8 + 7\,\text{TeV}$ datasets, which preceded the analysis described in this thesis, observed $3.8\,\sigma$ for the combined ggF+VBF Higgs signal and $2.5\,\sigma$ for the VBF production alone. Even though those past analyses provided the evidence for the Higgs boson decay into two W bosons, none of them observed any relevant excess in data originating solely from the VBF production mode. In order to determine whether the discovered Higgs boson is indeed the SM one or whether it is the first direct detection of some New Physics, all its production and decay modes, its couplings and other properties have to be precisely measured. One of the missing pieces to achieve this goal is the detection of the VBF production mode in the $H \to WW^{(*)}$ channel and is the main focus of the analysis presented in this thesis.

The description of the experimental search for the Higgs boson produced through VBF and decaying into WW^* using the complete 2012 dataset of 20.3 fb^{-1}, is split into three main parts, each written in its own chapter: this chapter provides an overview and outlines the event selection for the VBF $H \to WW^*$ analysis, Chapter 6 is dedicated to one of its largest backgrounds - the *top-quark background*, and Chapter 7 describes the statistical treatment of the data and presents the measurements of the signal strength and Higgs boson couplings to vector bosons and fermions.

5.1 Overview of the $H \to WW^{(*)}$ analysis

The general strategy of the 2012 data analysis is to focus on the mass region around $m_H = 125\,\text{GeV}$ and identify *signal regions* (SRs), which maximise the sensitivity of the $H \to WW^{(*)} \to \ell^+\nu_\ell\ell^-\bar{\nu}_\ell$ analysis and separate the signal from the background. Dedicated *control regions* (CR) are built to estimate the backgrounds in the SRs. The CRs are defined to be orthogonal to the SRs and at the same time as similar as possible to the SR selection, in order to reduce the theoretical and experimental uncertainties in the background predictions. Whenever possible, backgrounds are normalised to the data within the corresponding CRs.

The $H \to WW^{(*)}$ analysis considers the two largest Higgs production mechanisms; the ggF - probing the Higgs boson couplings with heavy quarks, and the VBF - probing direct

couplings of the Higgs boson with vector bosons. The VH production is also considered, but due to its small cross-section it is not treated separately as the VBF or the ggF. The small contribution from VH is added to the VBF signal, unless stated otherwise.

One of the main differences between the ggF and VBF production modes is the number of jets accompanying final state leptons and is the basis for the definition of the SRs. Events are divided into *jet categories*; $n_j = 0$, $n_j = 1$ and $n_j \geq 2$, each representing its own SR, probing ggF ($n_j \leq 1$) or VBF ($n_j \geq 2$) production modes. Even though the $n_j \geq 2$ category mostly probes the VBF production, the ggF also contributes ($\sim 20\%$ at the beginning of the selection enhancing the VBF topology) and is therefore treated as a background in the VBF category. As already mentioned, this thesis focuses only on the VBF production mode, although final results, discussed in Chapter 7, include the contributions from ggF channels as well.

The 2012 VBF analysis is split into two independent analyses carried out in parallel; the *cut-based* analysis and a multivariate analysis (MVA) based on the boosted decision tree (BDT) algorithm [87]. The cut-based analysis is based on a consecutive set of selection criteria and is in detail described in this thesis. All the previous $H \to WW^{(*)}$ publications are based on the cut-based method as well, which is by now very well understood. However, since the MVA method resulted in a higher expected signal significance it represents the *nominal* VBF analysis for the 2012 dataset. Both methods have been developing in parallel, where the cut-based method provided a sanity check to the MVA method.

From this point on, the term "VBF analysis" will represent only the analysis done with the cut-based method, unless stated otherwise.

5.1.1 The $H \to WW^{(*)}$ signal topology

The $H \to WW^{(*)}$ decay can be better discriminated from the backgrounds when both W bosons decay leptonically to a lepton $\ell = e, \mu$ and a corresponding neutrino. The fully leptonic final state signature is also searched for in the analysis presented in this thesis and consists of two isolated, oppositely charged leptons with high-p_{T}, and a large amount of missing transverse momentum. Due to the presence of neutrinos in the final state, the invariant mass of the final state products cannot be fully reconstructed. The *transverse mass* however, can be evaluated without the unknown longitudinal neutrino momenta, and is defined as

$$m_T = \sqrt{(E_{\mathrm{T}}^{\ell\ell} + p_{\mathrm{T}}^{\nu\nu})^2 - |\mathbf{p}_{\mathrm{T}}^{\ell\ell} + \mathbf{p}_{\mathrm{T}}{}^{\nu\nu}|^2}, \tag{81}$$

where $E_{\mathrm{T}}^{\ell\ell}$ represents the transverse energy of the two final state leptons, $E_{\mathrm{T}}^{\ell\ell} = \sqrt{(p_{\mathrm{T}}^{\ell\ell})^2 + (m_{\ell\ell})^2}$ and $\mathbf{p}_{\mathrm{T}}^{\ell\ell}$ the vector sum of their transverse momenta. $\mathbf{p}_{\mathrm{T}}{}^{\nu\nu}$ represents the vector sum of transverse momenta of the final state neutrinos. The m_T distribution peaks just below the Higgs boson mass and effectively reduces some of the backgrounds.

The spin-0 Higgs boson decays into two spin-1 W bosons with anti-aligned spins, as is indicated in Figure 31. Due to the angular momentum conservation, almost massless neutrinos, and the V-A nature of the weak interaction, the two final state leptons have aligned spins and roughly emerge in the same direction from the interaction point, having a small opening angle, $\Delta\phi_{\ell\ell}$, between them. Consequently, their invariant mass $m_{\ell\ell}^2 \simeq E_{\ell 1} E_{\ell 2}(1 - \cos\Delta\phi_{\ell\ell})$, is also small and a large missing transverse momentum is expected to balance the transverse momenta of the two leptons. The small invariant mass and the small opening angle are also used to discriminate between the Higgs signal and various backgrounds.

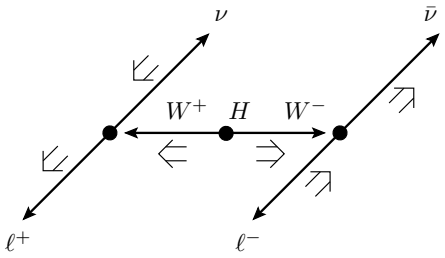

Figure 31.: Schematics of the $H \to WW^{(*)}$ decay. Smaller arrows indicate the direction of particles and the larger ones their spins projections.

5.1.2 Vector Boson Fusion topology

Final states of the Higgs boson decay, produced through the vector boson fusion, have a very specific and distinguishable experimental signature with the Feynamn diagram shown in Figure 32. Two incoming quarks from the initial protons scatter at very small angles, radiating two virtual vector bosons, a W or a Z, which subsequently annihilate, forming a Higgs boson. The two scattered quarks hadronise into two highly energetic forward jets[1], the

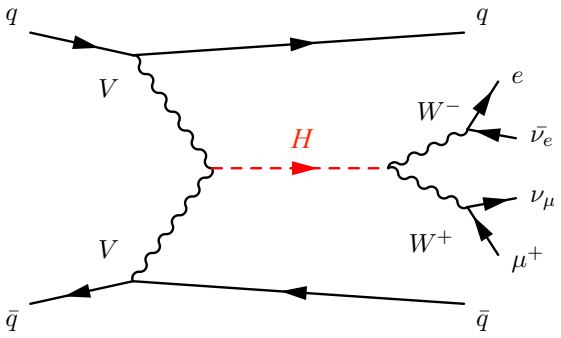

Figure 32.: The Feynman diagram of the Higgs boson produced through VBF in the $H \to WW^{(*)} \to \ell^+\nu_\ell\ell^-\bar{\nu}_\ell$ channel.

tag jets, with a very large rapidity gap between them, $\Delta y_{jj} = |y_{j1} - y_{j2}|$ and a large invariant mass, m_{jj}.

The VBF production is purely an electroweak process and therefore absent from any color exchange between the two scattering quarks. Hence, no additional jets appear in the rapidity region between the two tag jets, Δy_{jj}. In addition, the Higgs boson tends to be produced centrally, forcing its decay products in the rapidity region between the two tag jets. All these experimental features are shown in Figure 33, representing the ATLAS event display of a Higgs boson candidate produced through the VBF and decaying into two W bosons.

1 The two jets are in the forward and backward direction, respectively. The product of their rapidities is negative; $y_j^1 \cdot y_j^2 < 0$.

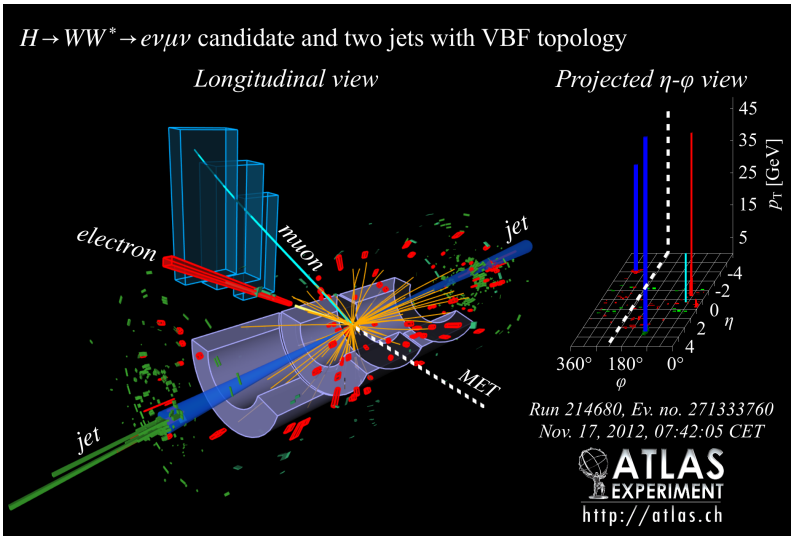

Figure 33.: The ATLAS event display for a VBF $H \to WW^{(*)} \to \ell^+\nu_\ell\ell^-\bar{\nu}_\ell$ candidate, recorded in the 2012 dataset.

5.1.3 Backgrounds in the $H \to WW^{(*)}$ analysis

Various physics processes mimic the final state of the $H \to WW^{(*)}$ decay - two energetic leptons with the opposite electric charge and a large missing transverse momentum:

- **The irreducible non-resonant SM WW production:** This is one of the largest backgrounds when both Ws decay leptonically to $\ell\nu_\ell\ell\nu_\ell$ and mostly dominates in the $n_j = 0$ category. It is greatly reduced by considering the properties of the W decay and the spin-0 nature of the Higgs boson. Requiring a small opening angle and a small invariant mass of the final state leptons largely separates the Higgs signal from the non-resonant WW decay.

- **Top-quark decays:** The top quark decays to a W and a b-jet ($t \to Wb$). When a W decays leptonically $W \to \ell\nu$, the final states mimic the $H \to WW^{(*)} \to \ell^+\nu_\ell\ell^-\bar{\nu}_\ell$ final states, with an exception of highly energetic b-jets. Due to inefficiencies in b-jet identification algorithms, the $t\bar{t}$ and single-top decays remain a large background, especially in the $n_j \geq 1$ categories, even after requiring a veto on b-jets in the signal selection.

- **Drell-Yan (DY):** The decays of Z/γ^* to ee, $\mu\mu$ and $\tau\tau \to \ell\nu\nu\ell\nu\nu$ final states contaminate the signal when there is a mismeasurement of the transverse particle momentum p_T, causing a fake E_T^{miss} measurement. The DY background is particularity large in signal events with leptons of the same flavour ($ee/\mu\mu$) and can be reduced through various E_T^{miss} requirements. On the other hand, in the events with different flavoured final state leptons ($e\mu/\mu e$), the DY background has a smaller contribution, coming only from the fully leptonic τ decays which have a small branching ratio. In case Z/γ^* is accompanied by jets and jets are misidentified as leptons, the Z/γ^*+jets background also contaminates the signal. Contributions from $Z/\gamma^* \to ee, \mu\mu, \tau\tau$ decays and Z/γ^*+jets background are combined.

- **Misidentified leptons**: The W+jets and multijet production contaminate the signal when jets are being misidentified as leptons and in the case of the multijet production, when they are also accompanied by the mismeasured E_T^{miss}. The misidentified leptons may originate from leptonic decays of heavy quarks (non prompt leptons) or from hadronic showers that mimic electromagnetic showers (fake leptons).

- **Other diboson backgrounds** ($VV = W\gamma, W\gamma^* / WZ, Z\gamma$ and $ZZ \to \ell\ell\ell\ell$ or $ZZ \to \ell\ell\nu\nu$) : When a vector boson is accompanied by a photon, the photon can get misreconstructed as a lepton, or in the case of an off-shell photon γ^*, low mass lepton pairs are produced and one of these leptons is not reconstructed. The $ZZ \to \ell\ell\nu\nu$ decays represent an irreducible background and $ZZ \to \ell\ell\ell\ell$ contaminates the signal whenever two of the leptons are misidentified or lost.

The impact of these backgrounds differs between events with *different* or *same* flavour final state leptons, $e\mu / \mu e$ or $ee / \mu\mu$, respectively (e.g. DY background). Splitting each jet category by the final state lepton flavour, therefore helps to remove their contributions more effectively.

5.2 Data and Monte Carlo samples

Data

This analysis considers 20.3 fb^{-1} of the data recorded in 2012 at the center of mass energy of $\sqrt{s} = 8$ TeV. The data have to fulfil quality requirements: events recorded when relevant detector components were not operating correctly are rejected.

In the final results presented in Chapter 7, the 2012 dataset is combined with 4.5 fb^{-1} of data recorded during the 2011 data-taking at $\sqrt{s} = 7$ TeV.

Monte Carlo samples

The specific MC samples are generated for all of the signal and background processes, with the exception of W + jets and multijet backgrounds, which are estimated using data. Table 8 summarises all MC generators and the cross-section times branching ratios for all signal and background processes used in the $H \to WW^{(*)}$ analysis.

The hard scattering event in most processes is generated by the POWHEG MC generator, including corrections up to the NLO in α_S. In processes where multi-partonic final states are required, ALPGEN or SHERPA MC generators provide merged calculations at the LO in α_S, with up to five additional partons. For some of the background processes only the LO hard scatter calculations exist, and such processes are simulated using ACERMC or GG2VV [88]. The parton distributions functions (PDF) are taken from CT10 [89] for POWHEG and SHERPA samples, while CTEQ6L1 [90] is used in ALPGEN+HERWIG and ACERMC samples.

The modelling of parton showers, hadronisation and the underlying event is done by HERWIG (interfaced with JIMMY for the modelling of the underlying event), PYTHIA or SHERPA. Pileup interactions are modelled by PYTHIA8.

The $H \to WW^{(*)}$ signal is modelled by POWHEG+PYTHIA8 and includes the VBF, ggF and VH production modes[2]. The modelling of the ggF production mode by POWHEG is corrected for by HRES2.1 [91] to match higher order calculations of the Higgs boson p_T distribution. For

2 The heavy quark associated production is neglected in the $H \to WW^{(*)}$ analysis due to its negligible contribution.

Process		MC generator	$\sigma \cdot \mathcal{B}$ (pb)
Signal			
ggF	$H \to WW^{(*)}$	POWHEG+PYTHIA8	0.435
VBF	$H \to WW^{(*)}$	POWHEG+PYTHIA8	0.0356
VH	$H \to WW^{(*)}$	PYTHIA8	0.0253
WW			
$q\bar{q} \to WW$ and $qg \to WW$		POWHEG+PYTHIA6	5.68
$gg \to WW$		GG2VV+HERWIG	0.196
$(q\bar{q} \to W) + (q\bar{q} \to W)$		PYTHIA8	0.480
$q\bar{q} \to WW$		SHERPA	5.68
VBS $WW+2$ jets		SHERPA	0.0397
Top quarks			
$t\bar{t}$		POWHEG+PYTHIA6	26.6
Wt		POWHEG+PYTHIA6	2.35
$tq\bar{b}$		ACERMC+PYTHIA6	28.4
$t\bar{b}$		POWHEG+PYTHIA6	1.82
Other dibosons (VV)			
$W\gamma$	($p_{\mathrm{T}}^{\gamma} > 8\,\mathrm{GeV}$)	ALPGEN+HERWIG	369
$W\gamma^*$	($m_{\ell\ell} \leq 7\,\mathrm{GeV}$)	SHERPA	12.2
WZ	($m_{\ell\ell} > 7\,\mathrm{GeV}$)	POWHEG+PYTHIA8	12.7
VBS $WZ+2$ jets	($m_{\ell\ell} > 7\,\mathrm{GeV}$)	SHERPA	0.0126
$Z\gamma$	($p_{\mathrm{T}}^{\gamma} > 8\,\mathrm{GeV}$)	SHERPA	163
$Z\gamma^*$	(min. $m_{\ell\ell} \leq 4\,\mathrm{GeV}$)	SHERPA	7.31
ZZ	($m_{\ell\ell} > 4\,\mathrm{GeV}$)	POWHEG+PYTHIA8	0.733
$ZZ \to \ell\ell\nu\nu$	($m_{\ell\ell} > 4\,\mathrm{GeV}$)	POWHEG+PYTHIA8	0.504
Drell-Yan			
Z	($m_{\ell\ell} > 10\,\mathrm{GeV}$)	ALPGEN+HERWIG	16500
$Z+2$ jets (VBF)	($m_{\ell\ell} > 7\,\mathrm{GeV}$)	SHERPA	5.36

Table 8.: Monte Carlo samples used in the modelling of the signal and background process in the $H \to WW^{(*)}$ analysis. The cross sections multiplied with the branching ratio $\sigma \cdot \mathcal{B}$ are quoted at $\sqrt{s} = 8\,\mathrm{TeV}$ and $m_H = 125.36\,\mathrm{GeV}$ for the signal. Here ℓ refers to e, μ and τ. The branching fractions include the decays of $t \to Wb$, $W \to \ell\nu$ and $Z \to \ell\ell$ ($ZZ \to \ell\ell\nu\nu$ includes the $\ell\ell$ and $\nu\nu$ branching fractions). For more information see [56].

completeness, the modelling of the $H \to \tau\tau$ (using POWHEG+PYTHIA8) is also included in the signal modelling, but its contribution is negligible and therefore left out from Table 8.

The $H \to WW^{(*)}$ analysis considers only dileptonic final states $H \to WW^{(*)} \to \ell^+\nu_\ell\ell^-\bar{\nu}_\ell$, with ℓ being mostly e or μ, with a small contribution from the leptonic τ decays. The branching fractions for the $H \to WW^{(*)} \to \ell^+\nu_\ell\ell^-\bar{\nu}_\ell$ decay as a function of m_H are taken from PROPHECY4f [92] and HDECAY [93].

The cross-section for the inclusive WW production is calculated at the NLO with MCFM [94] and the non-resonant gluon fusion (quark box) is modelled by GG2VV up to the LO, including WW and ZZ productions and their interference. The kinematics of the WW decay are modelled by POWHEG+PYTHIA8 for the $n_j \leq 1$ categories and with the merged multi-leg SHERPA generator for the $n_j \geq 2$ category. The double parton interaction process $(q\bar{q} \to W) + (q\bar{q} \to W)$ is modelled by PYTHIA8. The WW, WZ and ZZ states produced by the non-resonant vector boson scattering (VBS) are also modelled by SHERPA providing the LO cross-sections and the event modelling[3].

Top quark decays are modelled by POWHEG+PYTHIA8. The $t\bar{t}$ production is normalised to the NNLO in α_S with resummation of higher order terms up to the NNLL evaluated with TOP++2.0 [95]. The single-top processes; Wt, $tq\bar{b}$ and $t\bar{b}$ are normalised to NNLL, following the calculations from [96–98]. The dilepton filter is applied on $t\bar{t}$ and Wt (diagram-removal scheme) samples to increase the statistics, and only leptonic decays in the $tq\bar{b}$ and $t\bar{b}$ are considered.

The Drell-Yan and $W\gamma$ samples are simulated with ALPGEN+HERWIG with merged LO calculations and up to five additional jets. The $W\gamma$ merged sample is generated requiring $p_{\mathrm{T}}^{\gamma} > 8\,\mathrm{GeV}$ and $\Delta R(\gamma, \ell) > 0.25$ and is normalised to the NLO MCFM calculation. The Drell-Yan sample is generated with a dilepton mass greater than 10 GeV and is normalised to the DYNNLO [99, 100] NNLO calculation. The Z/γ^* sample is reweighed to the MRSTmcal PDF set [101]. In the case events from the Drell-Yan ALPGEN+HERWIG sample overlap with $Z(\to \ell\ell)\gamma$ SHERPA sample, they are removed.

The $W\gamma^*$ process is defined as an associated $W + Z\gamma^*$ production with an opposite-charge same-flavour lepton pair. Depending on the invariant mass of the lepton pair, the $W\gamma^*$ process is produced by two different generators. For the low $m_{\ell\ell}$ range, $m_{\ell\ell} < 7\,\mathrm{GeV}$, the $W\gamma^*$ is modelled by SHERPA with up to one additional parton, while for the high $m_{\ell\ell}$ range, $m_{\ell\ell} > 7\,\mathrm{GeV}$, it is modelled by POWHEG+PYTHIA8 and normalised to the cross-section from POWHEG. The jet multiplicity is corrected by the SHERPA sample generated with $0.5 < m_{\ell\ell} < 7\,\mathrm{GeV}$ with up to two additional partons, while the total cross-section is corrected using the ratio of MCFM NLO to SHERPA LO calculations in the same mass range. Similarly, the modelling of the $Z\gamma^*$, defined as $Z\gamma^*$ pair-production with one same-flavour opposite-charge lepton, is split into two mass regions; $m_{\ell\ell} \leq 4\,\mathrm{GeV}$ and $m_{\ell\ell} > 4\,\mathrm{GeV}$. The lower mass range is modelled by SHERPA while the higher mass range is modelled by POWHEG+PYTHIA8.

The $Z(\to \ell\ell)\gamma$ process is simulated by SHERPA requiring $p_{\mathrm{T}}^{\gamma} > 8\,\mathrm{GeV}$, $\Delta R(\gamma, \ell) > 0.1$ and $m_{\ell\ell} > 10\,\mathrm{GeV}$. Its cross-section is normalised to the NLO using MCFM calculation.

A more detailed description of all MC samples used in the $H \to WW^{(*)}$ analysis can be found in [56].

5.3 Event Selection

After reconstruction and identification (see Chapter 4) of all relevant final state objects for the $H \to WW^{(*)}$ analysis: electrons, muons, jets and the missing transverse momentum,

3 For completeness, the VBS ZZ process is also included in the background modelling but due to its small contribution is left out of Table 8.

a specific set of consecutive selection criteria (cuts) is chosen to reject the backgrounds and enhance the VBF signal. This section describes this selection. Starting with a set of *preselection* criteria, common to all jet categories, that is designed to select events with two oppositely charged leptons, the description focuses on the event selection specific for the VBF category. The event selection for the BDT VBF analysis and the ggF channels can be found in the Appendix, Section A.

5.3.1 Preselection

The $H \to WW^{(*)}$ selection begins by choosing events with exactly two identified and isolated high-p_{T} leptons. Selected leptons must have opposite electric charge and the leading lepton in p_{T} must have $p_{\mathrm{T}}^{\mathrm{lead}} > 22\,\mathrm{GeV}$, while the subleading lepton is required to have $p_{\mathrm{T}}^{\mathrm{sublead}} > 10\,\mathrm{GeV}$. At this stage of preselection, final state leptons are split into $e\mu/\mu e$ and $ee/\mu\mu$ channels. The background composition differs between the two channels; the $e\mu/\mu e$ is composed of mostly DY ($Z/\gamma^* \to \tau\tau$) and top-quark decays, while the $ee/\mu\mu$ is highly dominated by the $Z/\gamma^* \to ee/\mu\mu$ decays.

The next criterion selects events with the invariant mass of the final state leptons, $m_{\ell\ell}$, to be greater than 10 GeV (12 GeV) for the $e\mu/\mu e$ ($ee/\mu\mu$) final states, and reduces the contamination from the low-mass Drell-Yan events and hadronic resonances (e.g. J/Ψ, Y). A large contamination of Z/γ^* events in the $ee/\mu\mu$ channel is additionally reduced by removing events in the Z-boson mass window, $|m_{\ell\ell} - m_Z| > 15\,\mathrm{GeV}$ - the *Z-veto*.

After the Z-veto, the remaining events are split into different signal regions based on jet categories; $n_j = 0$, $n_j = 1$ and $n_j \geq 2$. Next, selection criteria targeting the missing transverse momentum is applied in each jet category. In the VBF category, $E_T^{\mathrm{miss}} > 55\,\mathrm{GeV}$ and $p_T^{\mathrm{miss,\,jet\text{-}corr}} > 50\,\mathrm{GeV}$ criteria are applied in the $ee/\mu\mu$ channel, while no missing transverse momentum requirement is imposed in the $e\mu/\mu e$ channel since the contamination from Drell-Yan events is smaller and by dropping this criterion the statistics of the signal increase. Figure 34 shows the E_T^{miss} and $p_T^{\mathrm{miss,\,jet\text{-}corr}}$ distributions after the Z-veto for the $ee/\mu\mu$ final states in the VBF category.

Figure 35 shows the backgrounds composition in each jet category for $e\mu/\mu e$ and $ee/\mu\mu$ final states at the end of the preselection. The top-quark background is the dominant background in the $n_j \geq 2$ category, for both $e\mu/\mu e$ and $ee/\mu\mu$ final states.

5.3.2 The VBF Event Selection

The VBF production mechanism has a distinguishable experimental signature featuring two energetic, forward jets. Jets are required to have $p_{\mathrm{T}} > 25\,\mathrm{GeV}$ within $|\eta| < 2.4$ and $p_{\mathrm{T}} > 30\,\mathrm{GeV}$ at $2.4 < |\eta| < 4.5$. Since the $n_j \geq 2$ category is mostly dominated by the top-quark decays, imposing a veto on b-jets ($n_b = 0$ with $p_{\mathrm{T}} > 20\,\mathrm{GeV}$) reduces the top-quark background contamination. Figure 36 (left) shows the number of b-jets in the $n_j \geq 2$ channel.

Even after the b-jet veto, a large fraction of the top-quark background remains in the signal region due to the limited η coverage of the Inner Detector. The top-quark decays are further reduced through the cut on the vector sum of the final state objects, $\mathbf{p}_{\mathrm{T}}^{\mathrm{sum}} = \mathbf{p}_{\mathrm{T}}^{\ell\ell} + \mathbf{p}_{\mathbf{T}}^{\mathrm{miss,\,jet\text{-}corr}} + \sum \mathbf{p}_{\mathrm{T}}^{\mathbf{j}}$, where the last term represents a vector sum of transverse momenta of all jets in the event. The top quarks are created mostly through the gluon-gluon annihilation and are accompanied by more QCD radiation than the VBF Higgs production and therefore have a higher jet multiplicity (see Figure 35). In addition, the VBF Higgs production is in itself an electroweak process where additional QCD radiation arises only due to the initial

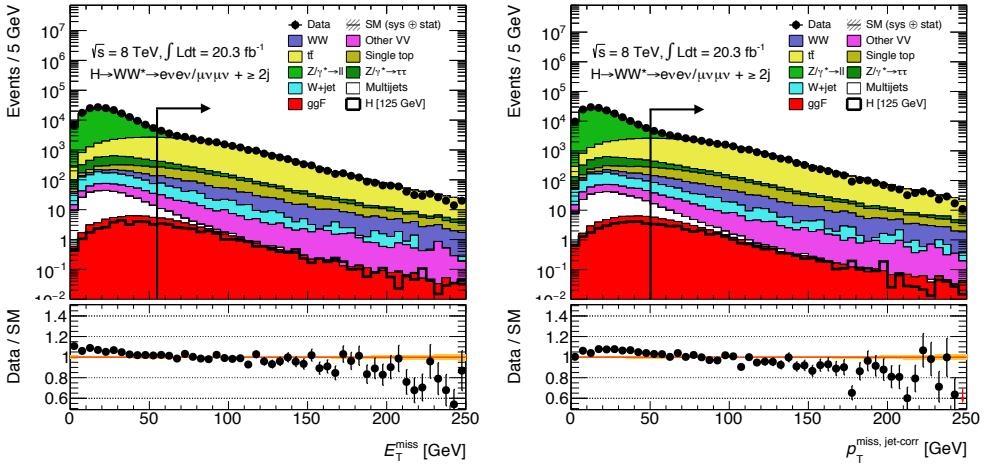

Figure 34.: Missing transverse momentum E_T^{miss} (left) and $p_T^{\text{miss, jet-corr}}$ (right) for $ee/\mu\mu$ final states after the Z-veto. The lower part of the plot represents the data/MC ratio and the yellow band represents the combined (in quadrature) systematics and statistical uncertainties. The Higgs signal is overlaid on top of the background contributions. The black arrow indicates the VBF SR.

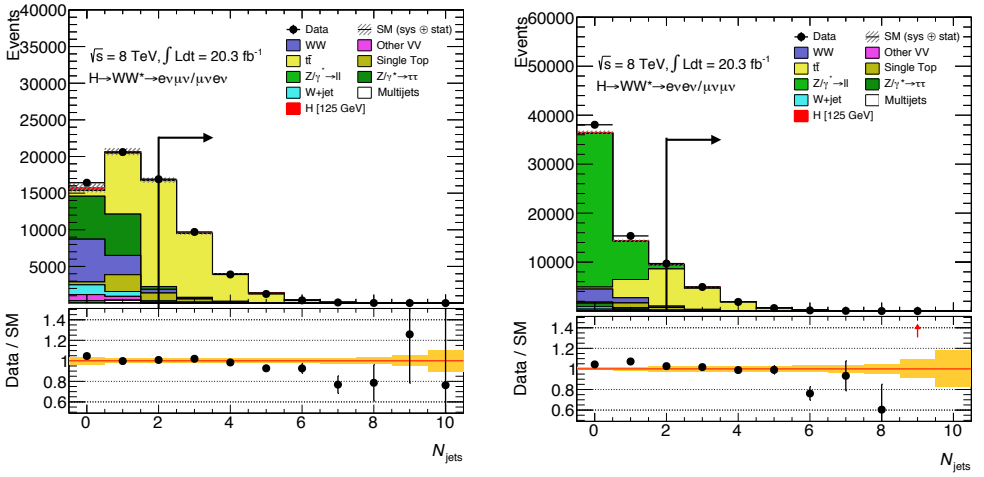

Figure 35.: Jet multiplicities for $e\mu/\mu e$ (left) and $ee/\mu\mu$ (right) final states after the missing transverse momentum requirements. The lower part of each plot represents the data/MC ratio and the yellow band represents the combined (in quadrature) systematics and statistical uncertainties. The Higgs signal is stacked on top of the background contributions. The black arrow indicates the VBF SR.

and final state radiation. Since the top-quark background is accompanied by more jets than the VBF Higgs signal, the $\mathbf{p}_{\text{T}}^{\text{sum}} < 15\,\text{GeV}$ represents a good discriminant between the VBF signal and the top-quark background, shown in Figure 36 (right).

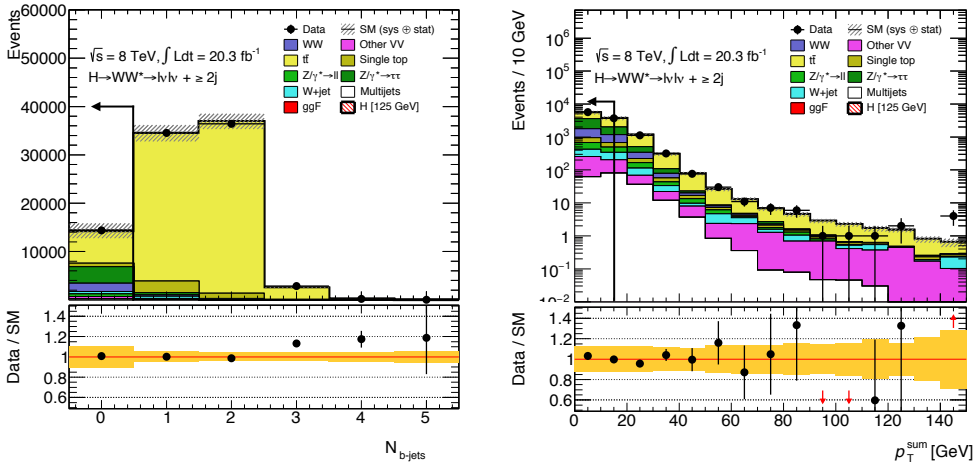

Figure 36.: The distribution of b-jets after selecting events with $\geq$ 2 jets (left) and $p_{\mathrm{T}}^{\mathrm{sum}}$ distribution after the b-veto vet (right). The lower part of each plot represents the data/MC ratio and the yellow band represents the combined (in quadrature) systematics and statistical uncertainties. The VBF Higgs signal is stacked on top of the background contributions. The black arrow indicates the VBF SR.

The second largest background in the VBF signal region is due to $Z/\gamma^* \to \tau\tau$ decays and is reduced by requiring $m_{\tau\tau} < m_Z - 25\,\mathrm{GeV}$, called hereafter the $Z \to \tau\tau$-veto, where $m_{\tau\tau}$ represents the invariant mass of the two τ leptons. Both τ leptons are usually produced back-to-back and are highly boosted. The reconstruction of $m_{\tau\tau}$ proceeds under the *collinear approximation* assuming that the visible τ decay products ($\ell = e, \mu$) are collinear to the invisible τ decay products (ν_τ, ν_ℓ) due to the strong boost of τ leptons. This approximation ensures that the missing transverse momentum from both τ decays is accounted for, making it possible to determine their four-momenta and consequently reconstruct their invariant mass. Figure 37 shows the $m_{\tau\tau}$ distribution for the $e\mu/\mu e$ and $ee/\mu\mu$ final states.

The two selection criteria enhancing the VBF signal topology, the m_{jj} and Δy_{jj}, follow the $Z \to \tau\tau$-veto. The invariant mass of the two tag jets is required to be more than 600 GeV and their rapidity gap ought to be larger than 3.6. Both distributions are shown in Figure 38.

Since the VBF production is an electroweak process, there is no hadronic activity expected in the rapidity region between the two tag jets. The number of additional jets represents such a hadronic activity and requiring no additional jets between the two tag jets, further carves the VBF phase space. The absence of additional jets with $p_{\mathrm{T}} > 20\,\mathrm{GeV}$ in the Δy_{jj} gap is called the *central jet veto* (CJV) [102], and suppresses all processes with jets produced through QCD. Figure 39 (left) shows the p_{T} distribution of central additional jets.

The Higgs boson and its decay products tend to be produced centrally, in the rapidity region between the two tag jet. Therefore, requiring a veto on leptons produced outside of the Δy_{jj} gap - the *outside lepton veto* (OLV), suppresses non-Higgs events and is shown in Figure 39 (right).

After the OLV requirement, the $H \to WW^{(*)}$ decay topology is imposed by requesting: $\Delta\phi_{\ell\ell} < 1.8$, $m_{\ell\ell} < 50\,\mathrm{GeV}$ and $m_T < 130\,\mathrm{GeV}$. Table 9 shows the event yields in the VBF SR.

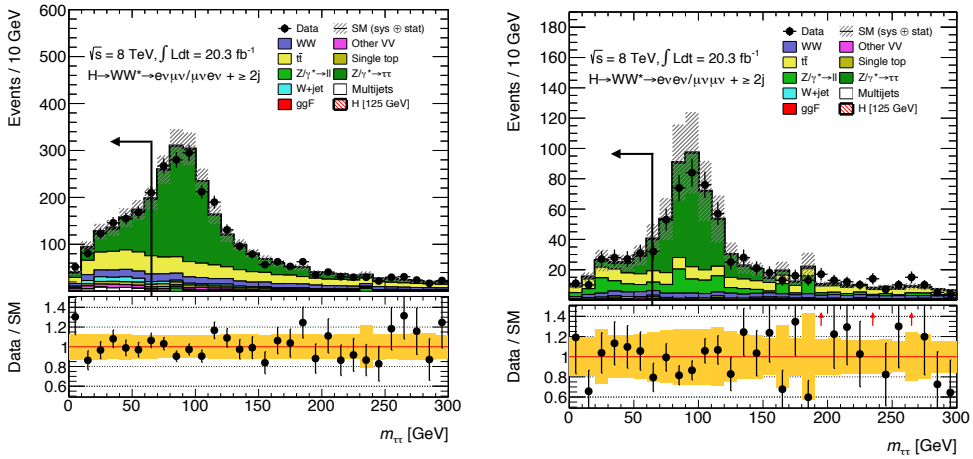

Figure 37.: The $m_{\tau\tau}$ distribution after the $p_{\mathrm{T}}^{\mathrm{sum}}$ selection for $e\mu/\mu e$ (left) and $ee/\mu\mu$ (right) final states. The lower part of each plot represents the data/MC ratio and the yellow band represents the combined (in quadrature) systematics and statistical uncertainties. The VBF Higgs signal is stacked on top of the background contributions. The black arrow indicates the VBF SR.

	Summary						Composition of N_{bkg}									
Selection	$N_{\mathrm{obs}}/N_{\mathrm{bkg}}$	N_{obs}	N_{bkg}	N_{signal}			N_{WW}		N_{top}		N_{misid}		N_{VV}	N_{DY}		
$n_j \geq 2$	$\pm$			N_{ggF}	N_{VBF}	N_{VH}	N_{WW}^{QCD}	N_{WW}^{EW}	$N_{t\bar{t}}$	N_t	N_{Wj}	N_{jj}		$N_{\ell\ell}$	$N_{\tau\tau}^{QCD}$	$N_{\tau\tau}^{EW}$
$e\mu/\mu e$ channel	1.00 ± 0.00	61434	61180	85	32	26	1350	68	51810	2970	847	308	380	51	3260	46
$n_b = 0$	1.02 ± 0.01	7818	7700	63	26	16	993	43	3000	367	313	193	273	35	2400	29
$p_{\mathrm{T}}^{\mathrm{sum}} < 15$	1.03 ± 0.01	5787	5630	46	23	13	781	38	1910	270	216	107	201	27	2010	23
$m_{\tau\tau} < m_Z - 25$	1.05 ± 0.02	3129	2970	40	20	9.9	484	22	1270	177	141	66	132	7.6	627	5.8
$m_{jj} > 600$	1.31 ± 0.12	131	100	2.3	8.2	-	18	8.9	40	5.3	1.8	2.4	5.1	0.1	15	1.0
$\Delta y_{jj} > 3.6$	1.33 ± 0.13	107	80	2.1	7.9	-	11.7	6.9	35	5.0	1.6	2.3	3.3	-	11.6	0.8
CJV > 1	1.36 ± 0.18	58	43	1.3	6.6	-	6.9	5.6	14	3.0	1.3	1.3	2.0	-	6.8	0.6
OLV	1.42 ± 0.20	51	36	1.2	6.4	-	5.9	5.2	10.8	2.5	1.3	1.3	1.6	-	5.7	0.6
$m_{\ell\ell}, \Delta\phi_{\ell\ell}, m_{\mathrm{T}}$	2.53 ± 0.71	14	5.5	0.8	4.7	-	1.0	0.5	1.1	0.3	0.3	0.3	0.6	-	0.5	0.2
$ee/\mu\mu$ channel	0.99 ± 0.01	26949	27190	31	14	10.1	594	37	23440	1320	230	8.6	137	690	679	16
$n_b, p_{\mathrm{T}}^{\mathrm{sum}}, m_{\tau\tau}$	1.03 ± 0.03	1344	1310	13	8.0	4.0	229	12.0	633	86	26	0.9	45	187	76	1.5
$m_{jj}, \Delta y_{jj}$, CJV, OLV	1.39 ± 0.28	26	19	0.4	2.9	0.0	3.1	3.1	5.5	1.0	0.2	0.0	0.7	3.8	0.7	0.1
$m_{\ell\ell}, \Delta\phi_{\ell\ell}, m_{\mathrm{T}}$	1.63 ± 0.69	6	3.7	0.3	2.2	0.0	0.4	0.2	0.6	0.2	0.2	0.0	0.1	1.5	0.3	0.1

Table 9.: Event yields in the VBF SR for $e\mu/\mu e$ and $ee/\mu\mu$ final states. The expected signal yield is split into N_{ggF}, N_{VBF}, and N_{VH} contributions. The N_{ggF} is treated as a background in the VBF analysis and is included in N_{bkg}. The expected yields of the dominant backgrounds are normalized as described in Chapter 6. The selection criteria are imposed sequentially from top to bottom, excluding preselection. Entries 0.0 (-) indicate less than 0.1 (0.01) events. All energy-related units are given in GeV.

5.3.3 Summary of the VBF $H \to WW^{(*)}$ Event Selection

The summary of all requirements defining the signal region of the (cut-based) VBF $H \to WW^{(*)}$ analysis is presented in Table 10. The m_T distribution represents the VBF signal discriminant in the final fit (described in Chapter 7) and is shown in Figure 40.

At the end of the event selection, the VBF signal region is further divided into two m_{jj} regions: the low m_{jj} region - $600\,\mathrm{GeV} < m_{jj} < 1\,\mathrm{TeV}$ and the high m_{jj} region - $m_{jj} > 1\,\mathrm{TeV}$. This split improves the expected signal significance by $\mathcal{O}(5\%)$ due to a longer m_{jj} tail in the VBF signal with respect to the backgrounds. The VBF analysis reaches the highest sensitivity

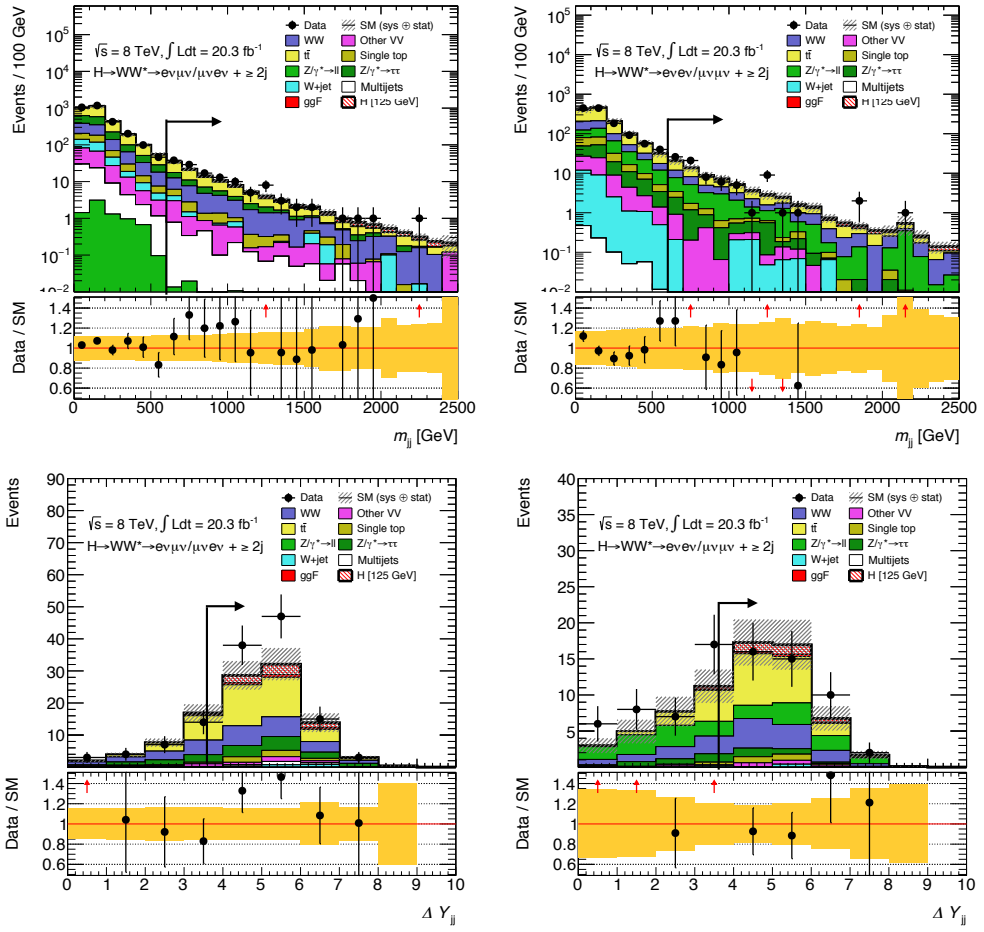

Figure 38.: Top row shows the invariant mass of the two tag jets (m_{jj}) for $e\mu/\mu e$ (left) and $ee/\mu\mu$ (right) final states, after the $Z \to \tau\tau$-veto. The bottom row shows the rapidity gap between the two tag jets (Δy_{jj}) for $e\mu/\mu e$ (left) and $ee/\mu\mu$ (right) final states after the m_{jj} selection. The lower part of each plot represents the data/MC ratio and the yellow band represents the combined (in quadrature) systematics and statistical uncertainties. The VBF Higgs signal is stacked on top of the background contributions. The black arrow indicates the VBF SR.

in the $e\mu/\mu e$ channel.

In order to enhance the sensitivity of the (VBF) searches it is not simply enough to design SRs with a high signal-to-background ratio. For a correct interpretation of the observed data, an accurate estimation of each of the background processes in the SR is just as important.

Table 11 shows the background and signal fractions in the VBF SR. How to tame the backgrounds and how to evaluate the uncertainties on their estimation is the topic of the next chapter, which is in particular dedicated to one of the largest backgrounds in the most sensitive $e\mu/\mu e$ channel - the top-quark decays.

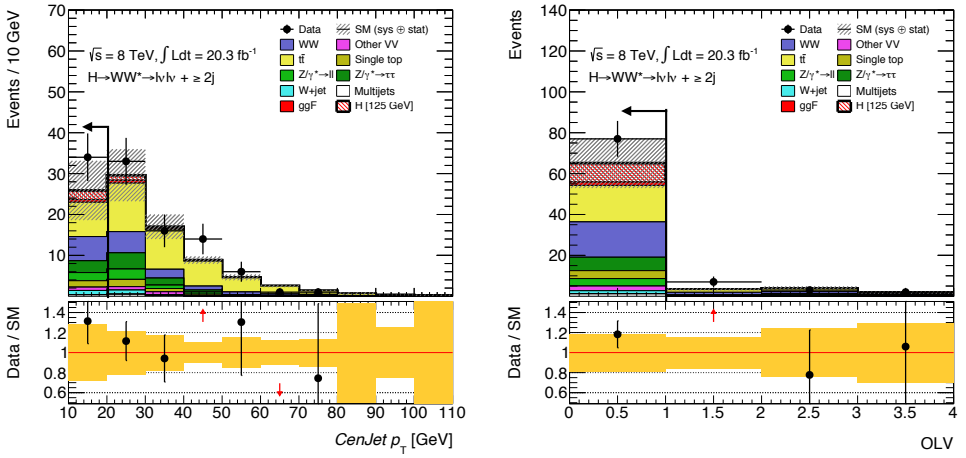

Figure 39.: Central (third) jet p_{T} distribution after the Δy_{jj} selection (left) and the OLV after the central jet veto (right). The first bin in the OLV histogram is filled if both leptons are inside the tag jet rapidity gap, the second and third bin are filled if one of the leptons is outside of the tag jet rapidity gap, and the forth bin is filled if both leptons are outside the tag jet rapidity gap. The lower part of each plot represents the data/MC ratio and the yellow band represents the combined (in quadrature) systematics and statistical uncertainties. The VBF Higgs signal is stacked on top of the background contributions. The black arrow indicates the VBF SR.

VBF $H \to WW^{(*)}$ selection criteria: $n_j \geq 2$	
Preselection	Two isolated leptons ($\ell = e, \mu$) $p_{\mathrm{T}}^{\mathrm{lead}} > 22$ for the leading leptons $p_{\mathrm{T}}^{\mathrm{sublead}} > 10$ for the subleading leptons Opposite-charge leptons $m_{\ell\ell} > 10\,(12)$ for $e\mu/\mu e$ ($ee/\mu\mu$) $\lvert m_{\ell\ell} - m_Z \rvert > 15\,(12)$ for $ee/\mu\mu$
Background rejection	$E_T^{\mathrm{miss}} > 55$ for $ee/\mu\mu$ $p_T^{\mathrm{miss,\,jet\text{-}corr}} > 50$ for $ee/\mu\mu$ $m_{\tau\tau} < m_Z - 25$ $n_b = 0$ $p_{\mathrm{T}}^{\mathrm{sum}} < 15$
VBF topology	$m_{jj} > 600$ $\Delta y_{jj} > 3.6$ central jet veto - CJV ($p_{\mathrm{T}} > 20$) no leptons outside tag jets - OLV
$H \to WW^{(*)} \to \ell^+\nu_\ell\ell^-\bar{\nu}_\ell$ topology	$m_{\ell\ell} < 50$ $\Delta\phi_{\ell\ell} < 1.8$ $m_T < 130$

Table 10.: Event selection in the cut-based VBF $H \to WW^{(*)} \to \ell^+\nu_\ell\ell^-\bar{\nu}_\ell$ analysis. Requirements apply for both $e\mu/\mu e$ and $ee/\mu\mu$ channels, unless specified otherwise. All energy-related units are given in GeV.

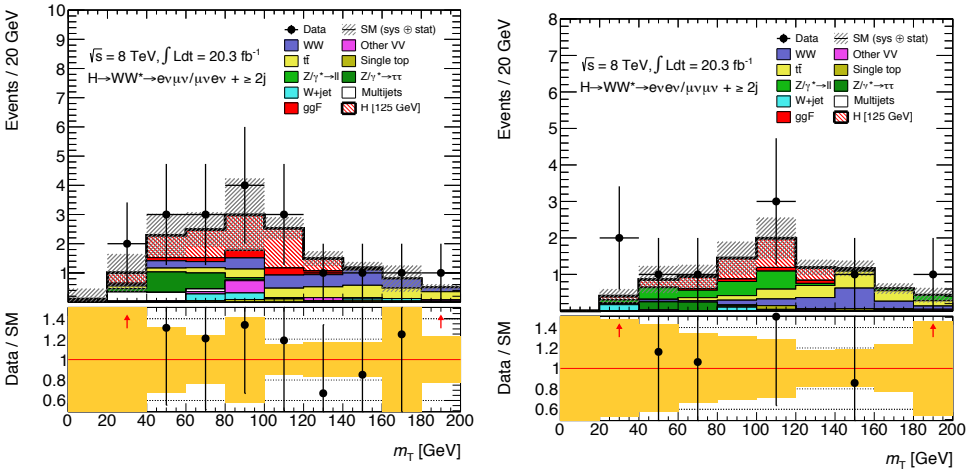

Figure 40.: The m_T distribution in the $n_j \geq 2$ VBF category for $e\mu/\mu e$ (left) and $ee/\mu\mu$ (right) final states, shown before the m_T selection. The lower part of the plot represents the data/MC ratio and the yellow band represents the combined (in quadrature) systematics and statistical uncertainties. The VBF Higgs signal is stacked on top of the background contributions.

	N_{signal}	N_{top}	N_{WW}	N_{DY}	N_{ggF}	N_{misid}	N_{VV}
$e\mu/\mu e$, $m_T < 130$							
$m_{jj} < 1000$	36%	17%	14%	8%	9%	6%	9%
$m_{jj} > 1000$	62%	8%	15%	5%	8%	3%	–
$ee/\mu\mu$, $m_T < 130$	37%	14%	8%	32%	5%	2%	2%

Table 11.: Background and signal fractions ($S + B = 100\%$) in the VBF SR after $m_T < 130\,\text{GeV}$ requirement. All energy-related units are given in GeV.

6 THE TOP BACKGROUND

Decays of top-quarks, hereafter referred as the *top background*, represent one of the most dominant backgrounds in the VBF SR (see Table 11) due to their large production cross-section at the LHC. The top background consists of two contributions; $t\bar{t}$ decays and single-top decays, with their Feynman diagrams shown in Figure 41. The $t\bar{t}$ events are mostly produced

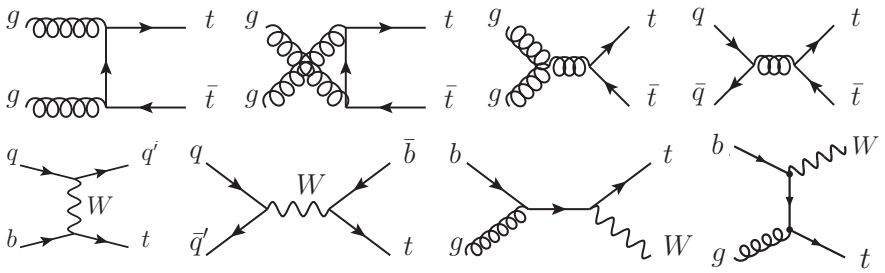

Figure 41.: Leading order Feynman diagrams for the top-quark production. Top row indicates top quark pair production ($t\bar{t}$) and the bottom row indicates single-top quark production [103].

by gg or qq fusion, while the single-top is produced through EW interaction (t-channel ($tq\bar{b}$) or s-channel ($t\bar{b}$) contributions) and through Wtb vertex. The leptonic decays of top-quarks, $t \to Wb \to \ell\nu b$, lead to a final state with two leptons, missing transverse momentum and two (one) b-jets in the $t\bar{t}$ (Wt) process. The s- and t-channel single-top final states contain one lepton, one b-jet and missing transverse momentum and represent a background for the $H \to WW^{(*)}$ analysis only when a jet is misidentified as a (second) lepton. The single-top decays give a smaller contribution to the total top background compared to the $t\bar{t}$ events; in the VBF SR after the b-jet veto, only 10% of events come from single-top decays.

This chapter describes the methods used to estimate background contributions in the VBF SR and their uncertainties (the impact of systematic uncertainties on the final results is presented in Chapter 7). Starting with the top background, the description of its control region and estimation of its systematic uncertainties is followed by a summary of all other *non-top* backgrounds and their uncertainties. At the end of this chapter, the experimental uncertainties and the theoretical uncertainties on the VBF signal are summarised as well.

6.1 Top Control Region

Whenever possible, the background contribution in the SR is estimated by a data-driven method using a dedicated control region. The *top control region* describes a region of phase space orthogonal to the VBF SR selection, that contains mostly events from top-quark decays, but at the same time keeps as many similarities with the VBF SR as possible.

The orthogonality of the control region with respect to the SR is achieved by reverting targeted criteria defining the SR. In case of the top CR, this is achieved by reverting a criterion which removes all events containing a b-jet from the VBF SR - the b-jet veto.

Even though all events containing a b-jet are rejected in the VBF SR, the top-quark decays still greatly contaminate the VBF SR. A truth-level study of $t\bar{t}$ events in the VBF SR, passing the b-jet veto and VBF topological selection, revealed that the two leading jets in these events are mostly (in 65%) composed of a *light-jet* (most likely coming from the initial and/or final state radiation) and a b-jet, and *not* from two b-jets as intuitively expected. Additionally, in 33% of such events both leading jets originate from light jets, and in only 1% from the two b-jets. The missing second b-jet is either not identified by the b-tagging algorithm due to the b-tagging inefficiency[1] or due to the limited acceptance of the ID ($|\eta| < 2.5$). Another possibility is that the light-flavoured jet is harder than the second b-jet and replaces the b-jet as the subleading jet. Since the remaining top-quark events in the VBF SR after the b-jet veto, consist mostly of events where only one leading jet originates from a b-jet, the top CR is defined by requiring *exactly one* b-tagged jet, $n_b = 1$.

The complete definition of the top CR begins with the same preselection criteria as in the VBF SR, described in Section 5.3.1. After selecting ≥ 2 jets, the top CR distinguishes from the VBF SR by accepting only events with exactly one b-jet, $n_b = 1$. The remaining selection criteria closely follow the VBF SR selection summarised in Table 10: (in consecutive order) $p_{\mathrm{T}}^{\mathrm{sum}} < 15\,\mathrm{GeV}$, $Z \to \tau\tau$-veto and VBF topological cuts: $m_{jj} > 600\,\mathrm{GeV}$, $\Delta y_{jj} > 3.6$, CJV (central jet veto) and OLV (outside lepton veto). This event selection guarantees that the top CR contains mostly top events (92%) and only minor contributions from signal and other backgrounds, like $Z/\gamma^* \to \tau\tau$ (3%) and W+jets (1%) which are reduced to less than a percent level towards the end of the top CR selection. Figure 42 shows the m_{jj} and m_T distributions in the top CR after selecting $n_b = 1$, and after requiring $\Delta y_{jj} > 3.6$.

The number of top background events in the VBF SR ($N_{\mathrm{top}}^{\mathrm{SR,\,est}}$) is estimated through the top background event yields in the top CR. It is defined as the number of top-quark events in the SR estimated from MC ($N_{\mathrm{top}}^{\mathrm{SR,\,MC}}$) and corrected for by the *normalisation factor* $\mathrm{NF_{top}}$;

$$
\begin{aligned}
N_{\mathrm{top}}^{\mathrm{SR,\,est}} &= N_{\mathrm{top}}^{\mathrm{SR,\,MC}} \cdot \underbrace{\frac{N_{\mathrm{data}}^{\mathrm{CR}} - N_{\mathrm{other\ bkg}}^{\mathrm{CR}}}{N_{\mathrm{top}}^{\mathrm{CR,\,MC}}}}_{\mathrm{NF_{top}}} \\
&= \underbrace{\frac{N_{\mathrm{top}}^{\mathrm{SR,\,MC}}}{N_{\mathrm{top}}^{\mathrm{CR,\,MC}}}}_{\alpha_{\mathrm{top}}\text{: CR to SR extrapolation}} \cdot \left(N_{\mathrm{data}}^{\mathrm{CR}} - N_{\mathrm{other\ bkg}}^{\mathrm{CR}}\right). \qquad (82)
\end{aligned}
$$

The normalisation factor represents the *data-to-MC* ratio of the *observed* top events in the top CR with respect to the number of expected top events from MC, $N_{\mathrm{top}}^{\mathrm{CR,\,MC}}$. The observed top background event yields are obtained by subtracting *other* background contributions (all non-top contributions, including the Higgs signal) from the data, $N_{\mathrm{data}}^{\mathrm{CR}} - N_{\mathrm{other\ bkg}}^{\mathrm{CR}}$. The non-top backgrounds are discussed in more detail in Section 6.5, but an overview of the methods used to estimate them is presented in Table 12.

The $\mathrm{NF_{top}}$ indicates how well the top MC describes the data in the top CR and adjusts its normalisation. Table 13 shows the evolution of data-driven top normalisation factors and

1 In the $H \to WW^{(*)}$ analysis, the b-tagging is performed by the MV1 algorithm with a 85% working point for jets with $p_{\mathrm{T}} > 20\,\mathrm{GeV}$ and a 10% misidentification rate (light jets). Almost all $t\bar{t}$ events have at least one b-jet above $p_{\mathrm{T}} > 20\,\mathrm{GeV}$ and the p_{T} threshold in the b-tagging algorithm has a negligible effect.

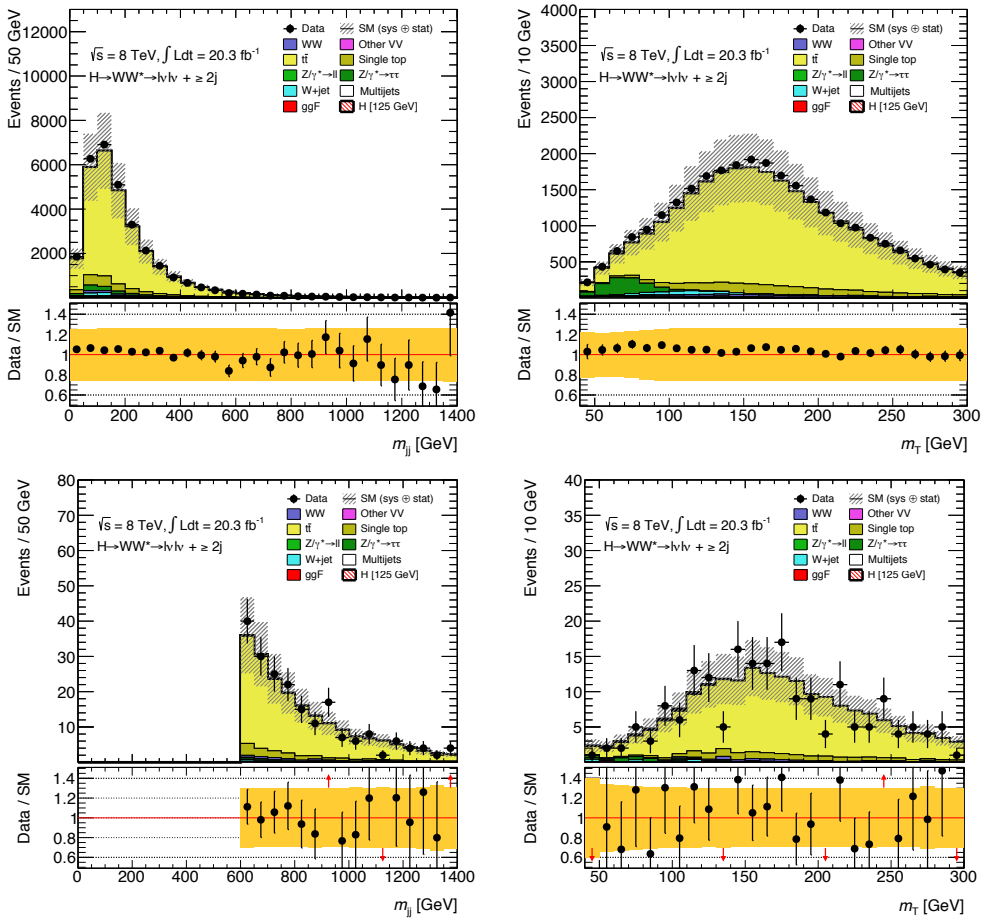

Figure 42.: The invariant mass of the two tag jets m_{jj} (left) and the transverse mass of all final state particles m_T (right). Distributions are shown in the top CR, after requiring $n_b = 1$ (top) and after selecting $\Delta y_{jj} > 3.6$ (bottom). The lower part in each plot represents the data/MC ratio and the yellow band represents the combined (in quadrature) systematics and statistical uncertainties. Normalisation factors are applied.

Background	data-driven	MC
top	√	√
WW	–	√
Drell-Yan	√	√
ggF	–	√
Misidentified leptons	√	–
VV	–	√

Table 12.: Summary of background estimation methods in the VBF SR.

event yields, throughout the top CR selection criteria for the combined $e\mu/\mu e + ee/\mu\mu$ final

states. The final NF_{top} is estimated after the last selection criterion, the OLV requirement and amounts to 1.04 ± 0.19, indicating a good agreement between the top MC and the data.

Selection stage in top CR	NF_{top}	N_{top}	N_{obs}	$N_{other\ bkg}$	(Z/γ^*)	N_{VBF}
$n_b = 1$	1.041 ± 0.007	27081	30519	2353	(954)	19
$p_T^{sum} < 15$	1.048 ± 0.008	17920	20454	1683	(766)	16
$m_{\tau\tau} < m_Z - 25$	1.06 ± 0.01	12129	13643	811	(224)	13
$m_{jj} > 600$	0.97 ± 0.06	310	332	34	(7)	2
$\Delta y_{jj} > 3.6$	1.03 ± 0.08	197	215	14	(2)	1
CJV	1.14 ± 0.16	52	63	5	(1)	1
OLV	1.04 ± 0.19	32	34	5	(-)	1

Table 13.: Evolution of normalization factors NF_{top} and (rounded) event yields throughout top CR selection criteria. The selection criteria are imposed sequentially, from top to bottom, excluding preselection. The values are shown for the combined $e\mu/\mu e$ and $ee/\mu\mu$ final states, assuming the VBF criteria are flavour agnostic. The NF_{top} values include only statistical uncertainties. $N_{other\ bkg}$ represent all non top backgrounds, including the VBF signal. The Z/γ^* ($Z/\gamma^* \to \tau\tau$) and VBF event yields are shown separately as well, but their values are included in $N_{other\ bkg}$. The value of NF_{top} at the OLV stage is within the $t\bar{t}$ (6%) and Wt (7%) cross-section uncertainties. All energy-related units are given in GeV.

The second part of Equation 82 defines the *extrapolation factor* α_{top} from top CR to VBF SR, defined as the ratio of top background event yields estimated by MC in the VBF SR with respect to the top CR. The extrapolation factor estimates top background events in the SR with a smaller uncertainty - the large theoretical uncertainties arising when estimating $N_{top}^{SR,\,est}$ directly from the MC simulation are replaced by two smaller contributions (provided a sufficient number of top events); the statistical uncertainty on $N_{data}^{CR} - N_{other\ bkg}^{CR}$ and the systematic uncertainty on α_{top}. Thus, the final systematic uncertainty on the top background estimation in the VBF SR is defined as the *theoretical* uncertainty on the extrapolation factor α_{top} and is discussed in more details in Section 6.4.

The definition of the top CR went through several changes and optimisations in the course of the VBF analysis. Two of such optimisations are described in the following sections; the change of the nominal $t\bar{t}$ MC generator from MC@NLO to POWHEG and an optimisation of the top CR definition excluding the CJV requirement.

6.2 Change of the Top MC Generator

The previously published VBF analysis [86] used the MC@NLO MC generator, showered with HERWIG, as the default $t\bar{t}$ generator. Even though MC@NLO predicted higher rates than the data in the VBF top CR, making its normalisation factor equal to 0.59 ± 0.07, and even if it exhibited poor modelling of the m_{jj} distribution, it still remained the default $t\bar{t}$ MC generator since it was, at that time, the best known $t\bar{t}$ MC generator with the highest available statistics.

A possible explanation for these discrepancies observed in top background modelling when using a MC@NLO+HERWIG generator is believed to come from the known faulty behaviour of central jets [104–107]. The left plot in Figure 43 shows the rapidity distribution of the highest-p_T jet in $t\bar{t}$ events, comparing the ALPGEN and MC@NLO generators, both showered with HERWIG. On the right plot of the same figure a rapidity distance between the Higgs boson and the highest-p_T jet is shown, comparing POWHEG and MC@NLO generators. The same

effect is observed in many other processes as well; MC@NLO showered with HERWIG has a dip at $y \approx 0$ in the rapidity distribution of the highest-p_T jet.

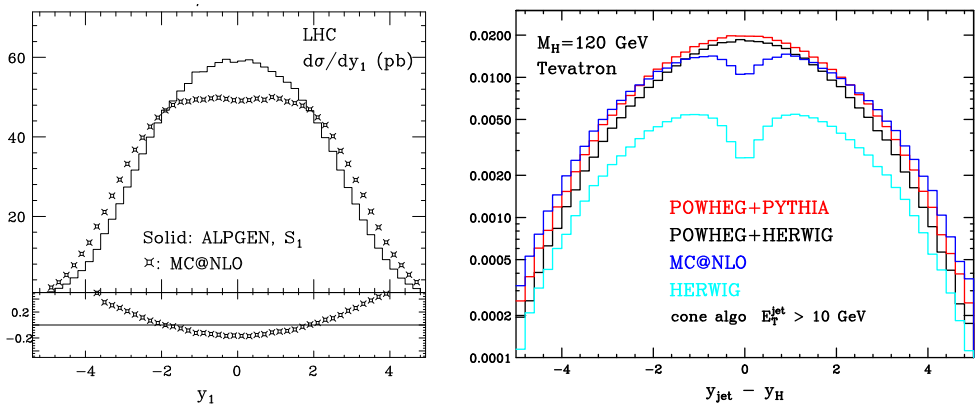

Figure 43.: The rapidity of the highest-p_T jet in generated $t\bar{t}$ events [106] (left) and the rapidity distance between the Higgs boson and the highest-p_T jet, for a generated Higgs boson through ggF [107] (right). Various MC generators are compared.

The dip at zero rapidity in MC@NLO is a feature related to its matching with HERWIG. The showering algorithm implemented in HERWIG generates the dip at $y \approx 0$ (related to the showering of the hardest radiation) that MC@NLO cannot compensate for, while POWHEG and ALPGEN can.

Due to all MC@NLO-related challenges described above and because other $t\bar{t}$ MC generators have become available with increased statistics, the VBF $H \to WW^{(*)}$ analysis agreed to revisit the choice of the default $t\bar{t}$ generator.

Three $t\bar{t}$ NLO MC generators are considered and compared between each other[2]; MC@NLO+HERWIG, POWHEG+PYTHIA6 and POWHEG+HERWIG. Table 14 summarises the key differences between the considered MC generators and Table 15 compares the normalisation factors between them.

The normalisation factor obtained with MC@NLO+HERWIG shows large discrepancies from unity after the m_{jj} selection, which is due to the already known poor modelling of the m_{jj} distribution. The POWHEG+PYTHIA6 generator provides an NF_{top} closest to unity compared to the other two generators, and has a smaller statistical uncertainty compared to POWHEG+HERWIG. In addition, it also provides a better Data/MC shape description for both VBF specific variables compared to MC@NLO and POWHEG+HERWIG, as shown in Figure 44.

In order to completely exclude systematic effects in the MC@NLO+HERWIG shape discrepancies, a combined uncertainty due to jet energy scale (JES) and jet energy resolution (JER) is added to the statistical uncertainties, but it does not cover the observed shape discrepancies. Thus, POWHEG+PYTHIA replaced MC@NLO+HERWIG as the default $t\bar{t}$ MC generator in the $H \to WW^{(*)}$ analysis.

2 Each $t\bar{t}$ generator is accompanied by associated single-top MC generators. For the MC@NLO+HERWIG $t\bar{t}$ sample, the single-top events are produced either by ACERMC ($tq\bar{b}$) or MC@NLO ($t\bar{b}$, Wt), both showered with HERWIG. The POWHEG+PYTHIA6 $t\bar{t}$ sample is accompanied with single-top samples produced by ACERMC+ PYTHIA ($tq\bar{b}$) and POWHEG+PYTHIA6 ($t\bar{b}$ and Wt processes) and the POWHEG+HERWIG $t\bar{t}$ sample has the Wt process simulated by POWHEG+HERWIG, POWHEG+PYTHIA6 is used for $t\bar{b}$, and ACERMC+PYTHIA for $tq\bar{b}$.

MC generator	Description
NLO ME	MC@NLO and POWHEG are two methods developed to avoid double-counting of NLO ME and PS emissions:
• MC@NLO:	- using the modified subtraction scheme to remove from NLO expressions those terms that will be generated by PS - presence of negative event weights - can be matched to only specific PS (HERWIG)
• POWHEG:	- generates the hardest emission first and then combines with PS - generally positive weights - interfaced with any PS
Parton Shower	
• PYTHIA:	- offers p_{T} (first emission the hardest) and virtuality ordering - for hadronisation uses string fragmentation model
• HERWIG:	- angular ordering (first emission not necessarily the hardest but rather at the widest angle) - for hadronisation uses cluster fragmentation model

Table 14.: Summary of the key differences between NLO ME and PS generators. For further details refer to [47], [105] and the references within.

Selection stage	$\mathrm{NF}_{\mathrm{top}}^{\mathrm{POWHEG+PYTHIA6}}$	Δ	$\mathrm{NF}_{\mathrm{top}}^{\mathrm{MC@NLO+HERWIG}}$	Δ	$\mathrm{NF}_{\mathrm{top}}^{\mathrm{POWHEG+HERWIG}}$	Δ
$n_b = 1$	1.025 ± 0.006	3%	1.005 ± 0.006	1%	1.050 ± 0.007	5%
$p_T^{\ell\ell,\mathrm{jets}} > 25$	1.025 ± 0.006	3%	1.005 ± 0.006	1%	1.050 ± 0.007	5%
$p_{\mathrm{T}}^{\mathrm{sum}} < 15$	1.031 ± 0.007	3%	1.006 ± 0.007	1%	1.057 ± 0.007	6%
$m_{jj} > 600$	0.935 ± 0.038	7%	0.742 ± 0.030	25%	1.018 ± 0.042	2%
f_{recoil}	0.947 ± 0.040	5%	0.747 ± 0.032	25%	1.031 ± 0.045	3%
$\Delta y_{jj} > 3.6$	1.005 ± 0.054	1%	0.716 ± 0.039	28%	1.113 ± 0.062	11%
OLV	0.992 ± 0.063	1%	0.706 ± 0.045	29%	1.094 ± 0.071	9%
$m_{\tau\tau} < m_Z - 25$	0.974 ± 0.064	2%	0.693 ± 0.046	31%	1.080 ± 0.073	8%

Table 15.: Evolution of normalization factors $\mathrm{NF}_{\mathrm{top}}$ throughout the topCR selection criteria, comparing all three considered $t\bar{t}$ MC generators; MC@NLO+HERWIG, POWHEG+PYTHIA6 and POWHEG+HERWIG. The selection criteria are imposed sequentially, from top to bottom, excluding preselection and belong to at an earlier stage of the VBF analysis but the conclusions do not change. The $p_T^{\ell\ell,\mathrm{jets}}$ and f_{recoil} (defined in Appendix, Section A.2) have been replaced in the final top CR (Section 6.1) by the $p_T^{\mathrm{miss,\,jet\text{-}corr}}$ criterion at the preselection stage (see Section 5.3.1). Symbol Δ represents the difference between $\mathrm{NF}_{\mathrm{top}}$ and unity. All energy-related units are given in GeV.

6.3 Optimisation of the Top CR

The leading jets in $t\bar{t}$ events are usually b-jets and are rejected in the VBF SR. However, the b-tagging algorithm operates only in the central rapidity region $|\eta| < 2.5$, enhancing the number of remaining $t\bar{t}$ events (after the b-jet veto) with a leading jet towards higher rapidities (forward rapidity region). This introduces a bump at $|\eta| \approx 2.5$ in the VBF SR, as shown in Figure 45, which is even more pronounced after the VBF topological selection.

Vetoing all central b-jets in the VBF SR changes the flavour composition of the leading jets in $t\bar{t}$ events (see discussion in Section 6.1). Consequently, $t\bar{t}$ events in the VBF SR have more events with light jets as leading jets with respect to $t\bar{t}$ events in the top CR, where leading jets are still mostly b-jets.

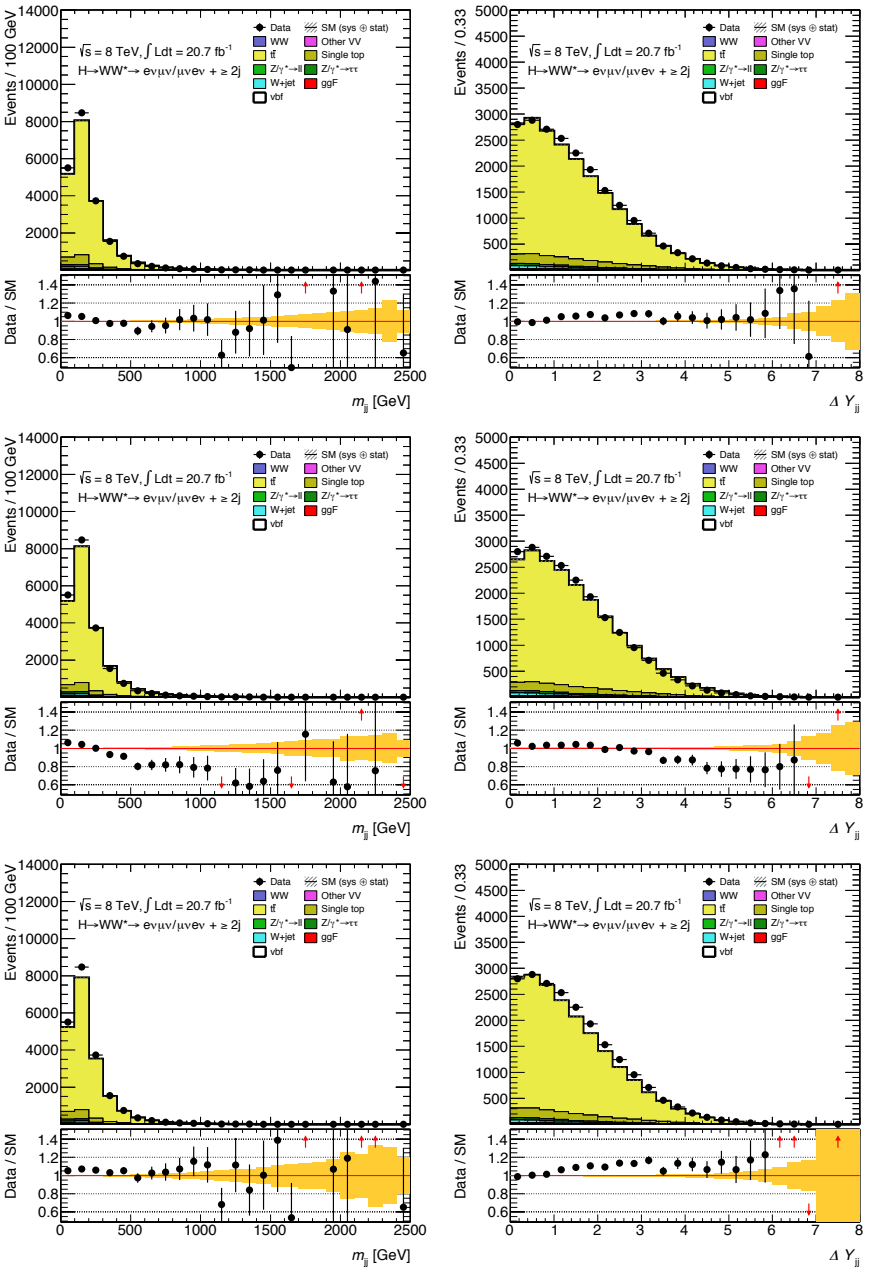

Figure 44.: The invariant mass of the two tag jets m_{jj} (left) and the rapidity gap between them Δy_{jj} (right), for all three considered $t\bar{t}$ MC generators in the top CR: POWHEG+PYTHIA6 (top), MC@NLO+HERWIG (middle) and POWHEG+HERWIG (bottom), shown before the m_{jj} selection. The top CR is defined by consecutive criteria specified in Table 15. The $\mathrm{NF_{top}}$ are applied in order to enhance the shape comparisons between the three MC generators. The yellow band in the Data/MC ratio plots includes only statistical uncertainties.

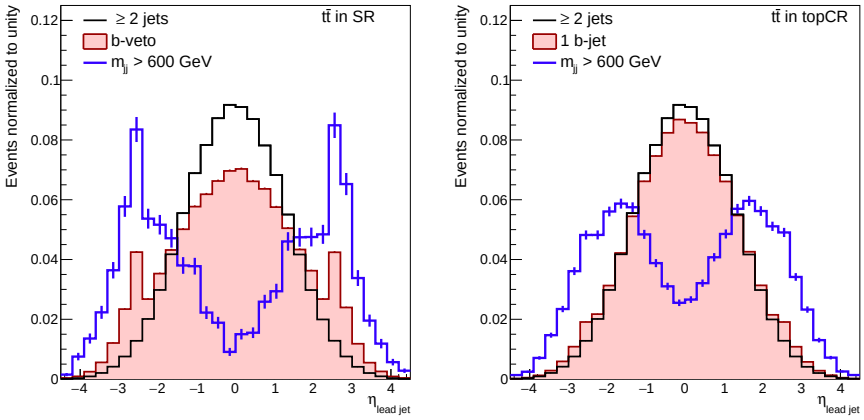

Figure 45.: Rapidity of the leading jet in the $t\bar{t}$ MC events in the VBF SR, $n_b = 0$ (left) and top CR, $n_b = 1$ (right) after selecting $\geq$ 2jets, b-jet requirement and $m_{jj} > 600\,\text{GeV}$ selection.

The top CR selects events with one b-tagged jet with 85% efficiency. This working point carries a non-negligible probability ($\approx 10\%$) of mis-tagging a light jet for a b-jet in the central rapidity region. The $t\bar{t}$ events with a mis-tagged b-jet, most likely have a real b-jet in the forward rapidity region, mimicking the event topology from the VBF SR, where b-jets are mostly forward. Including the *central jet veto* in the top CR would therefore veto all such events and reduce kinematic similarities between the VBF SR and the top CR. Hence, removing a CJV requirement from the top CR definition, but keeping it in the VBF SR, has been considered. Figure 46 shows various distributions in the VBF SR and in the top CR, with and without the CJV requirement. Distributions without the central jet veto are more similar to the distributions in the SR.

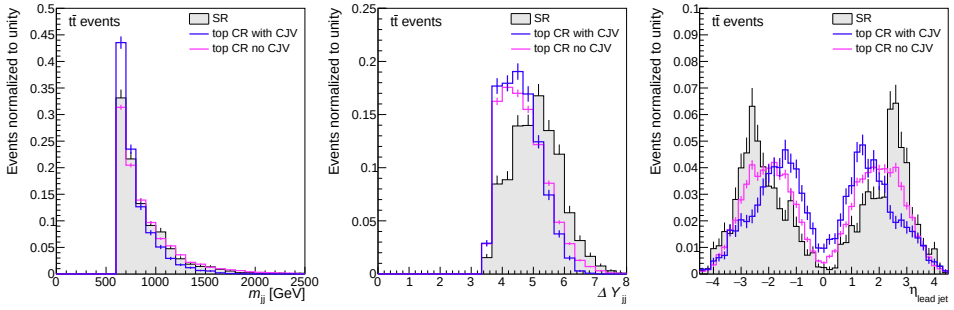

Figure 46.: Shape comparison between m_{jj} (left), Δy_{jj} (middle) and η_j^{lead} (right) distributions between the VBF SR and top CR, with and without the central jet veto.

In order to test the effects of the CJV criterion further, an additional study is performed comparing extrapolation factors α_{top} between various MC generators, with and without the CJV requirement applied in the top CR. For this particular study, a special set of generator level samples with increased statistics (up to 25 times the statistics of the official samples) has been produced. The generator level samples have been properly validated to the official samples with the full ATLAS detector simulation, and all distributions resemble closely.

Table 16 shows the evaluation of extrapolation factors at (consecutive) selection stages, with and without the CJV requirement.

Selection stage	POWHEG	MC@NLO	ALPGEN
$p_{\mathrm{T}}^{\mathrm{sum}} < 15$	0.025 ± 0.000	0.025 ± 0.000	0.024 ± 0.000
$m_{jj} > 600$	0.027 ± 0.000	0.029 ± 0.000	0.022 ± 0.001
$\Delta y_{jj} > 3.6$	0.035 ± 0.001	0.037 ± 0.001	0.030 ± 0.001
CJV (not applied in top CR)	0.011 ± 0.000	0.015 ± 0.000	0.007 ± 0.000
OLV	0.013 ± 0.000	0.018 ± 0.001	0.008 ± 0.001
CJV (applied in top CR)	0.051 ± 0.002	0.052 ± 0.002	0.043 ± 0.002
OLV	0.071 ± 0.003	0.076 ± 0.003	0.059 ± 0.003

Table 16.: Evolution of extrapolation factors $\alpha_{\mathrm{top}} = N_{\mathrm{top}}^{\mathrm{SR,\,MC}} / N_{\mathrm{top}}^{\mathrm{CR,\,MC}}$ for various $t\bar{t}$ MC generators; POWHEG, MC@NLO and ALPGEN, all showered with HERWIG. The statistical error is coming only from the number of events in the MC. All energy-related units are given in GeV.

Removing the CJV from the top CR increases the statistics in the top CR and therefore decreases the statistical uncertainty on α_{top}. In addition, the shapes of the m_{jj} and Δy_{jj} distributions look more alike between the SR and top CR for all $t\bar{t}$ MC generators, as is shown in Figure 47; the ratio between distributions in the VBF SR and top CR is flatter and closer to unity for all MC generators when the CJV requirement is removed from the top CR.

However, the theoretical uncertainties on the top background estimation increase considerably when the CJV is not applied in the top CR. As is discussed in Section 6.4, one of the largest contributions to the theoretical uncertainty on the top background estimation is due to the *MC generator modelling*, which considers relative differences in α_{top} between various MC generators. The relative differences in α_{top} between generators increase when the CJV requirement is removed from the top CR, especially for the MC@NLO, as is shown in Table 17. These effects are observed also in the BDT VBF analysis, and since the increase in kinematic similarities and statistics between the top CR and VBF SR does not compensate for the large increase in relative differences in α_{top}, and consequently in theoretical uncertainties on the top background estimation in case the CJV requirement is removed from the top CR, the central jet veto *remained* in the top CR.

Selection stage in top CR	$\frac{\text{POWHEG - MC@NLO}}{\text{POWHEG}}$	$\frac{\text{POWHEG - ALPGEN}}{\text{POWHEG}}$	$\frac{\text{MC@NLO - ALPGEN}}{\text{MC@NLO}}$
CJV *not* applied in top CR	38%	38%	56%
CJV applied in top CR	7%	17%	22%

Table 17.: Relative differences in extrapolation factor $\alpha_{\mathrm{top}} = N_{\mathrm{top}}^{\mathrm{SR,\,MC}} / N_{\mathrm{top}}^{\mathrm{CR,\,MC}}$ throughout the (consecutive) top CR selection criteria between considered MC generators at the end of the top CR selection (OLV stage).

A possible explanation for such large relative discrepancies in α_{top} when the CJV is not included in the top CR, especially when comparing to MC@NLO, is related to the faulty behaviour of central jets in MC@NLO+HERWIG, discussed in Section 6.2 and Figure 43. Unfortunately, the VBF analyses has been rushing towards publication and this study ran out of time

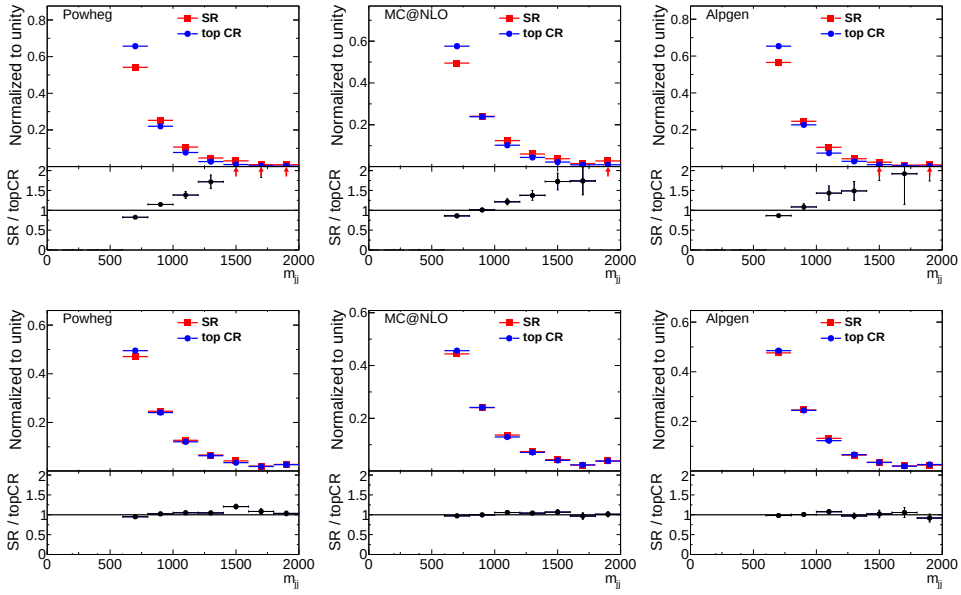

Figure 47.: The m_{jj} distribution for $t\bar{t}$ events; POWHEG (left), MC@NLO (middle) and ALPGEN (right), all showered with HERWIG, for $e\mu/\mu e$ + $ee/\mu\mu$ final states. Figures are shown before the final (OLV) criterion . The upper row indicates the top CR with the CJV criterion, while the bottom row indicates the top CR without the CJV criterion. Blue histograms represent the top CR and red histograms the SR, both normalized to unit area.

for any further investigations. However, a deeper understanding of jet kinematics, jet flavour composition and jet modelling between various MC generators, and the impact of the central jet veto on the VBF analysis, represent possible improvements for the future VBF analyses.

6.4 Systematic uncertainties on the Top Background

A precise estimate of background contributions in the SR is important for the final interpretation of the data (see Chapter 7). The theoretical uncertainties on the top background estimation are evaluated through α_{top} - any variation in α_{top} is equivalent to the fluctuations in the estimated number of top events in the SR. They are split into four contributions, following the prescription from [108]:

- **Generator modelling uncertainty:** comparing α_{top} for three different MC generators; ALPGEN, MC@NLO and POWHEG, all showered with HERWIG.
- **QCD scale uncertainty:** differences in α_{top} due to the choice of the QCD scale used in MC generation, estimated by varying the renormalisation (μ_R) and factorisation (μ_F) scales by a factor of two up and down.
- **PDF uncertainty:** variations in α_{top} due to different PDF sets.
- **Parton Shower and Underlying Event (PS/UE) uncertainties:** comparing α_{top} between $t\bar{t}$ events produced by POWHEG and showered either with PYTHIA or HERWIG.

The impact on the shapes of relevant distributions (e.g. m_T, m_{jj}) is also investigated for all these sources. In addition to the four contributions outlined above, another source is included in the overall theoretical uncertainty on the $t\bar{t}$ events - the *uncertainty due to the initial and final state radiation* - ISR/FSR. Even though the top background theoretical uncertainty is evaluated on $t\bar{t}$ events, it is applied on the complete top background, including single-top events. Each of the five sources is described in details below.

6.4.1 Generator modelling uncertainty

The generator modelling uncertainty accounts for discrepancies in different matrix element (ME) calculations, between the default NLO $t\bar{t}$ MC generator - POWHEG and alternative generators ALPGEN or MC@NLO. All three generators are showered with HERWIG to exclude possible uncertainties due to PS/UE. POWHEG is compared to the multi-leg ALPGEN generator in order to test for possible discrepancies in the modelling of additional jets, particularly important due to the CJV requirement in top CR, while the comparison between POWHEG and MC@NLO probes for differences in NLO ME calculations.

The generator modelling uncertainty is evaluated by taking the largest observed discrepancy in α_{top} between two of the three considered MC generators. Table 18 summarises the extrapolation factors and Table 19 shows their relative differences.

Selection stage in top CR	POWHEG	MC@NLO	ALPGEN
$p_{\text{T}}^{\text{sum}} < 15$	0.025 ± 0.000	0.025 ± 0.000	0.024 ± 0.000
$m_{jj} > 600$	0.027 ± 0.000	0.029 ± 0.000	0.022 ± 0.001
$\Delta y_{jj} > 3.6$	0.035 ± 0.001	0.037 ± 0.001	0.030 ± 0.001
CJV	0.051 ± 0.002	0.052 ± 0.002	0.043 ± 0.002
OLV	0.071 ± 0.003	0.076 ± 0.003	0.059 ± 0.003
$m_{jj} < 1000$	0.065 ± 0.003	0.070 ± 0.003	0.055 ± 0.004
$m_{jj} > 1000$	0.114 ± 0.009	0.099 ± 0.007	0.087 ± 0.012

Table 18.: Evolution of extrapolation factors from top CR to SR, $\alpha_{\text{top}} = N_{\text{top}}^{\text{SR, MC}} / N_{\text{top}}^{\text{CR, MC}}$, throughout the top CR selection criteria, for various $t\bar{t}$ MC generators; POWHEG, MC@NLO and ALPGEN, all showered with HERWIG. The selection criteria are imposed sequentially from top to bottom, excluding preselection. The statistical error is coming only from the number of events in the MC. All energy-related units are given in GeV.

Selection stage in top CR	$\frac{\text{POWHEG - MC@NLO}}{\text{POWHEG}}$	$\frac{\text{POWHEG - ALPGEN}}{\text{POWHEG}}$	$\frac{\text{MC@NLO - ALPGEN}}{\text{MC@NLO}}$
OLV	$6.2 \pm 0.3\%$	$17 \pm 1\%$	$22 \pm 1\%$
$m_{jj} < 1000$	$8.2 \pm 0.5\%$	$15 \pm 1\%$	$22 \pm 2\%$
$m_{jj} > 1000$	$13 \pm 1\%$	$24 \pm 4\%$	$12 \pm 2\%$

Table 19.: Relative difference in $\alpha_{\text{top}} = N_{\text{top}}^{\text{SR, MC}} / N_{\text{top}}^{\text{CR, MC}}$ between two of the three considered MC generators; POWHEG, MC@NLO and ALPGEN, all showered with HERWIG. The results are shown at the end of the top CR selection, at the OLV criterion. All energy-related units are given in GeV.

The largest discrepancy in α_{top} occurs between MC@NLO and ALPGEN, with an overall generator modelling uncertainty of 22%, or 22% and 12% including the split into the low and high m_{jj} region, respectively.

The differences in the shape of the m_T distribution between the generators are within MC statistical uncertainties.

6.4.2 QCD scale uncertainty

The differences in the extrapolation factor due to different QCD renormalisation and factorisation scales, are estimated by independently varying both scales up and down by a factor of two with respect to the nominal set ($\mu_r = \mu_f = 1.0$); from ($\mu_r = 0.5, \mu_f = 0.5$) to ($\mu_r = 2.0, \mu_f = 2.0$). The QCD scale uncertainty is quoted as the maximum variation in α_{top} with respect to the nominal set. The maximum variation yields 10% after the OLV requirement, and 10% and 23% for the low and high m_{jj} region, respectively.

A possible impact of various QCD scales on the shape of the m_T distribution has been also considered, but all variations are well within MC statistical uncertainties.

6.4.3 PDF uncertainty

The PDF uncertainty is estimated following the procedure described in [109]. The final uncertainty is evaluated as a fluctuation in α_{top} in the m_T distribution due to the variations in the default PDF set CT10 and due to its reweighing to an alternative PDF set, NNPDF10 [110].

The overall PDF uncertainty on α_{top} for both sources, combined in quadrature, is comparable to statistical uncertainties and reaches at most 10%.

6.4.4 Parton Shower and Underlying Event uncertainties

Comparing the default $t\bar{t}$ NLO MC generator POWHEG, once showered with PYTHIA and once with HERWIG, accounts for the uncertainties due to different evaluation of the underlying event (contributions of the spectator quarks in the final state) and parton showering model (branching and hadronisation of the hard process particles).

For both considered parton shower models the extrapolation factor α_{top} is compared throughout the top CR selection and is shown in Table 20. The differences in α_{top} reach at most 17% and lie well within statistical uncertainties, with the statistical significance equal to $\sim 1.2\,\sigma$.

A possible systematic uncertainty due to shape discrepancies in various distributions is also considered. Different PS/UE models mostly affect additional jets, and any difference between PYTHIA and HERWIG would be the most prominent in $p_{\text{T}}^{\text{sum}}$ and N_{jets} distributions. Figure 48 shows the $p_{\text{T}}^{\text{sum}}$ and m_T distributions, with all the differences well within statistical uncertainties.

The systematic uncertainty due to the different parton shower and underlying event modelling can therefore be *neglected*, since it is smaller than the statistical uncertainties.

6.4.5 Initial and Final State Radiation uncertainties

After the *b*-jet veto, the majority of top background events has at least one light jet as a leading jet (see discussion in Section 6.1). Since the light jets most likely originate from the higher order QCD processes, like *initial* or *final state radiation*, the estimation of the top background is therefore sensitive to the modelling of additional jets and to QCD radiation.

Selection stage in top CR	POWHEG+PYTHIA	POWHEG+HERWIG	Δ
$p_{\mathrm{T}}^{\mathrm{sum}} > 15$	0.0365 ± 0.0002	$0.03620.0004$	$0.89\,\sigma$
$m_{jj} > 600$	0.041 ± 0.001	0.043 ± 0.002	$0.71\,\sigma$
$\Delta y_{jj} > 3.6$	0.054 ± 0.002	0.055 ± 0.004	$0.32\,\sigma$
OLV	0.016 ± 0.001	0.019 ± 0.002	$1.18\,\sigma$
$m_{\tau\tau} < m_Z - 25$	0.017 ± 0.001	0.020 ± 0.003	$1.17\,\sigma$

Table 20.: Evolution of extrapolation factors from the top CR to VBF SR for POWHEG+PYTHIA and POWHEG+HERWIG $t\bar{t}$ samples in different flavour final states, throughout the top CR selection criteria. The selection criteria are imposed sequentially from top to bottom, excluding preselection and belong to an an earlier stage of the top CR definition (at that point CJV criterion has been removed). With the CJV included in the top CR, the differences reach at most $1.9\,\sigma$. The symbol Δ represents the difference between the two samples. All energy-related units are given in GeV.

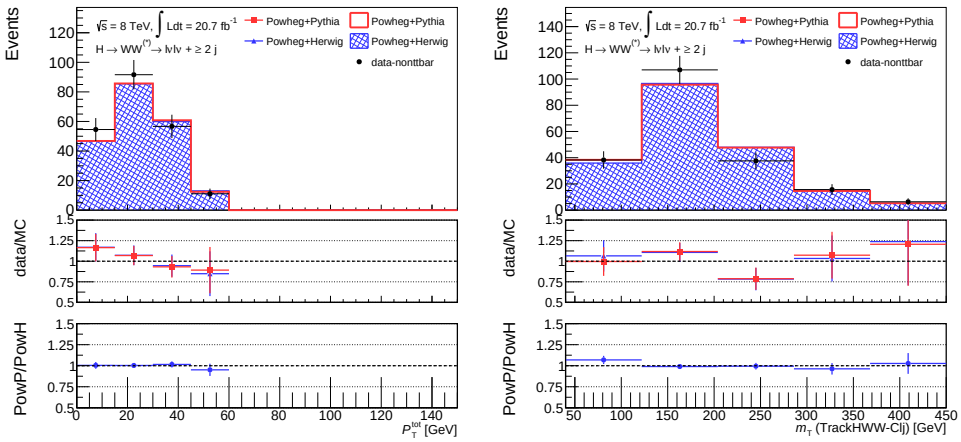

Figure 48.: The $p_{\mathrm{T}}^{\mathrm{sum}}$ (left) and m_T (right) distributions comparing POWHEG+PYTHIA and POWHEG+HERWIG $t\bar{t}$ samples for $e\mu/\mu e$, shown after the OLV requirement. The top CR is defined as specified in Table 20. The normalisation factors are applied in the top CR in order to enhance any differences in shapes between the two samples. The top part of each plot shows the shape comparison between the two showering samples, the middle part shows the data-to-MC ratio and the bottom part shows the POWHEG+PYTHIA vs. POWHEG+HERWIG ratio.

The understanding of the impact of the ISR and FSR uncertainties on the analysis is therefore very important.

Gluons radiated before (ISR) or after (FSR) the hard scatter event lead to parton showers, by additionally splitting into more gluons or quark-antiquark pairs. These parton showers have low energies and are therefore not well described by the perturbative regime of QCD, but are rather evaluated through an approximation scheme assuming collinear parton splitting (low-energy gluon emissions). Parton shower MC generators, like PYTHIA and HERWIG, use parton splitting functions to describe the probability of a parton splitting into two additional partons, DGLAP [111–113] evolution equations and Sudakov form factors [114] to properly evaluate the collinear and low energetic radiation. The NLO generators, like POWHEG or MC@NLO, already describe one additional (light) jet through their next-to-leading order matrix element

calculations. However, the second or third, etc. additional jets are generated purely by the parton shower model, which is less reliable for high-p_T jets.

Two methods for estimating the ISR/FSR systematics are considered in this thesis: the benchmark ATLAS method and an independent truth-level MC study. Both of them are described in the following.

THE BENCHMARK ATLAS RECOMMENDATION: The benchmark ATLAS recommendation for the evaluation of ISR/FSR uncertainties in $t\bar{t}$ events, is based on the data-driven *gap fraction analysis* method using dilepton $t\bar{t}$ events [115]. The gap fraction f_{gap}, represents a vetoed fraction of $t\bar{t}$ events which do not contain any additional jets in the specified rapidity region with p_T greater than the threshold value Q_0. It is related to the probability of no additional jets being produced in a rapidity region as a function of p_T (Q_0) of the highest-p_T additional jet. Two $t\bar{t}$ samples are generated with an increased and decreased radiation (how are they generated is described below) using the LO ACERMC+PYTHIA6 generator and are labelled as MORE PS and LESS PS, respectively. The systematic uncertainty assigned due to the ISR/FSR is estimated as half of the difference between the two samples,

$$\Delta_{\text{ISR/FSR}} = \frac{1}{2} \cdot (\text{MORE PS} - \text{LESS PS}) \,. \tag{83}$$

Following this proceduce, a 28% systematic uncertainty due to ISR/FSR is evaluated on the top background estimation in the VBF $H \to WW^{(*)}$ analysis[3].

The MORE PS and LESS PS samples have a LO ME and their increased and decreased radiation levels are controlled by *tuning* certain parameters in PYTHIA6[4] which control the renormalisation scales and consequently the amount of ISR and FSR. The values of these parameters are chosen such that the variations between MORE PS and LESS PS samples *bracket* the observed $t\bar{t}$ data from the gap fraction analysis [116]. Figure 49 shows the gap fraction for the default LO ACERMC+PYTHIA6 MORE PS and LESS PS samples and a possible improvement in the ISR/FSR systematic estimation using the NLO POWHEG generator. Samples with increased and decreased radiation generated by POWHEG+PYTHIA6 are produced by varying the renormalisation and factorisation scales in POWHEG together with varying parton showering parameters in PYTHIA6[5] and are labelled SCALE + RADHI and SCALE + RADLO, respectively.

Two main conclusions can be drawn from Figure 49:

- The parameters in PYTHIA6 defining MORE PS and LESS PS samples are chosen so that both variations bracket the experimental data. Hence, the value of the systematic uncertainty due to the initial and final state radiation, estimated by Equation 83, is *limited* by the uncertainty of the data-driven gap fraction analysis.

- The spread between the increased and decreased radiation samples in case of a LO generator (left plot of Figure 49) is $\approx 10\%$. Using an NLO generator (right plot of Figure 49), which already includes the modelling of one additional parton in the ME, the spread between the increased and decreased radiation samples decreases to only a few

3 This uncertainty is estimated as $\alpha_{\text{top}}^{\text{NOMINAL}} \pm \alpha_{\text{top}}^{\text{ISR/FSR}}$ and is evaluated at the m_{jj} stage due to lower statistics at later stages.

4 The samples with increased and decreased radiation are generated by tuning the `PARP(61)` and `PARP(72)` parameters which correspond to changing the QCD scale used in the running strong coupling in ISR and FSR respectively, `PARP(64)` controlling the renormalisation scale in ISR, `PARP(67)` controlling the high-p_T ISR branchings, and `PARJ(82)` controlling the low-p_T cutoff in FSR [36].

5 In this case, the ISR and FSR are controlled by `radHi` and `radLo` Perugia 2012 tunes [117], which besides the default PYTHIA6 parameters controlling the renormalisation scales of ISR/FSR (`PARP(67)`, `PARP(64)`, `PARP(72)`) include also variations in infra-red cutoffs of both ISR (`PARP(62)`) and FSR (`PARJ(82)`) and parameters controlling the underlying event activity (`PARP(82)`, `PARP(90)`).

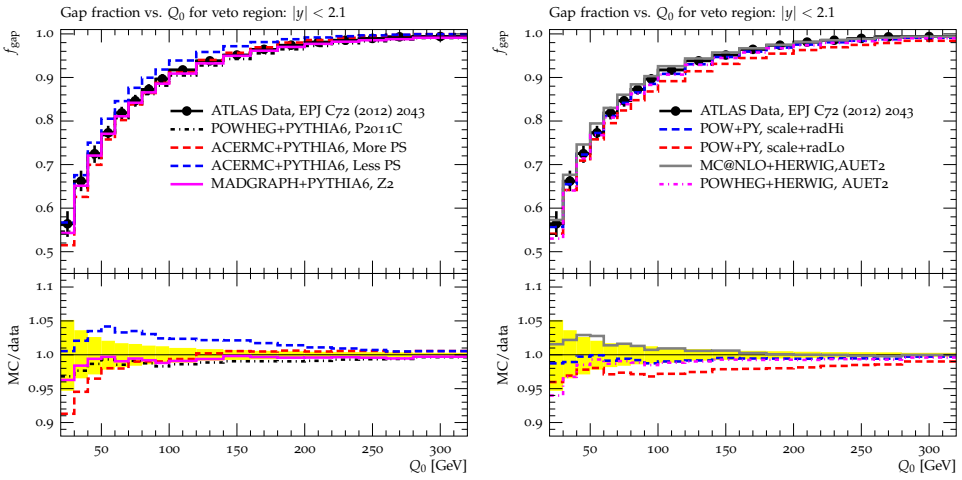

Figure 49.: The gap fraction analysis comparing two samples with increased and decreased radiation produced by the LO generator ACERMC+PYTHIA6 (left) and by the NLO generator POWHEG+PYTHIA6 (right) [116]. The yellow band represents the total experimental uncertainty on the data (statistical and systematic). The experimental data are taken from [115].

percent, indicating that the ISR/FSR effects depend mostly on the first additional jet, which is present in LO generators only through the parton showering model.

The main contributions to the systematic uncertainty of the data-driven gap fraction analysis are due to JER, JES, JVF and the *b*-tagging, as shown in Figure 50. Most of these contributions are already separately included in the VBF $H \to WW^{(*)}$ analysis (see Section 6.6). In

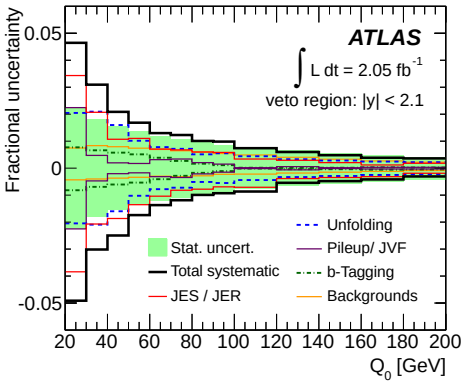

Figure 50.: The breakdown of the systematic uncertainties in the gap fraction analysis [115].

addition, the systematic uncertainty on the top background estimation already includes uncertainties due to various QCD scales, PDFs and different parton showering models and all of these contributions indirectly include also the uncertainty due to ISR/FSR. Therefore, using the gap fraction envelope, based on a LO generator, which results in the 28% uncertainty due to ISR/FSR, is an *overestimation*, even if it is mainly driven by the experimental results

obtained from the data. In addition, it leads to *double counting* of systematic uncertainties already included in the VFB $H \to WW^{(*)}$ analysis.

The truth-level MC study: An additional truth-level MC study is performed in order to confidently discard the systematic uncertainty due to ISR and FSR in the top background estimation. The $t\bar{t}$ events are produced by the MC@NLO+HERWIG NLO generator at $\sqrt{s} = 8\,\text{TeV}$, including only dileptonic decays.

The amount of initial and final state radiation in HERWIG is controlled by the parameter SCALUP, which vetos the emissions in parton showers with p_T greater than SCALUP. The parameter SCALUP can be modified through two additional parameters ISCA and XSCA[6] affecting both ISR and FSR, and effectively controlling the scale at which parton showering starts. The parameter ISCA controls the functional form of the shower and has two options, while parameter XSCA is a multiplicative factor and controls the scale of the veto of the emissions:

$$\begin{aligned} \texttt{ISCA} = 0 &\longrightarrow \texttt{SCALUP} = \texttt{ECM} - 2\texttt{PTR} \;\; [\texttt{default}], \\ \texttt{ISCA} = 1 &\longrightarrow \texttt{SCALUP} = \texttt{ECM}, \\ \texttt{XSCA} \in [0.3, 3.0] &\longrightarrow \texttt{SCALUP} = \texttt{SCALUP} \cdot \texttt{XSCA}\ . \end{aligned} \tag{84}$$

Parameters ECM and PTR represent the center of mass energy for a subprocess and p_T of hard emissions in the collider frame, respectively. The allowed values of the XSCA parameter are only in the range $[0.3, 3.0]$[7]. Effectively, events with XSCA $= 3.0$ have more emissions, meaning more ISR and FSR than events with XSCA $= 0.3$, which have less radiation. Any variation in the SCALUP parameter is expected to be small from the start, since the SCALUP parameter affects only the parton showering part of the MC@NLO+HERWIG generation, so only events which already have one real emission in the NLO part (produced by a NLO matrix element). Therefore, changes in ISR/FSR are only a *beyond* next-to-leading order effect, which has already been observed in Figure 49.

A set of cuts was applied on the truth level MC@NLO+HERWIG sample, mimicking the VBF $H \to WW^{(*)}$ preselection:

- Lepton selection: $|\eta| < 2.5$, $p_T^{\text{lead}} > 22\,\text{GeV}$, $p_T^{\text{sublead}} > 15\,\text{GeV}$,
- Jet selection: anti-k$_T$ clustering algorithm with $R = 0.4$ and $p_T > 25\,\text{GeV}$, ≥ 2 jets with $p_T > 25(30)\,\text{GeV}$ for jets in $|\eta| < 2.4(\geq 2.4)$.

Figure 51 shows the p_T and η distributions of the third (additional) jet in the $t\bar{t}$ events, and Figure 52 shows the N_{jets} and m_{jj} distributions for various configurations of XSCA and ISCA parameters. The discrepancies between the different amounts of ISR/FSR are all *at the percent level* or within statistical uncertainties.

To sum up, due to the possible overestimation and double counting of the systematic uncertainties using the benchmark recommendation with a LO generator, and since the truth-level study, using an NLO generator, revealed that the ISR/FSR systematic results only in the percent level effects, the ISR/FSR uncertainty on the top background estimation is *not included* in the VBF analysis, as summarised in Table 21.

6 Several new options controlling the SCALUP parameter were implemented by Prof. Dr. Bryan Webber, particularly for this study, using fortran HERWIG6.

7 Prof. Dr. Bryan Webber, private communications. Setting XSCA > 3 has no impact since HERWIG automatically brings the value back to 3, and setting XSCA < 0.3 makes the SCALUP parameter too small and contradicts previously established theoretical assumptions in HERWIG.

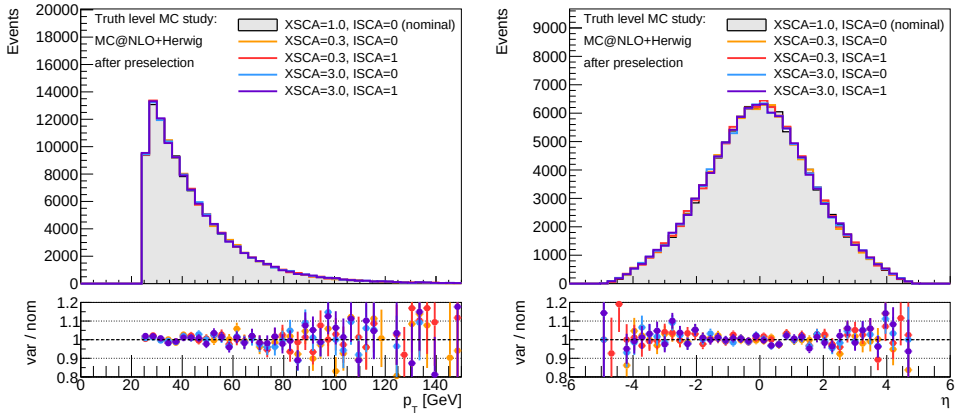

Figure 51.: The p_{T} (left) and η (right) distributions of the third jet in dileptonic $t\bar{t}$ events for various values of `XSCA` and `ISCA` parameters. Since the variations of `XSCA` and `ISCA` parameters affect only the showering stage, the same event file generated by NLO ME is used for all variations.

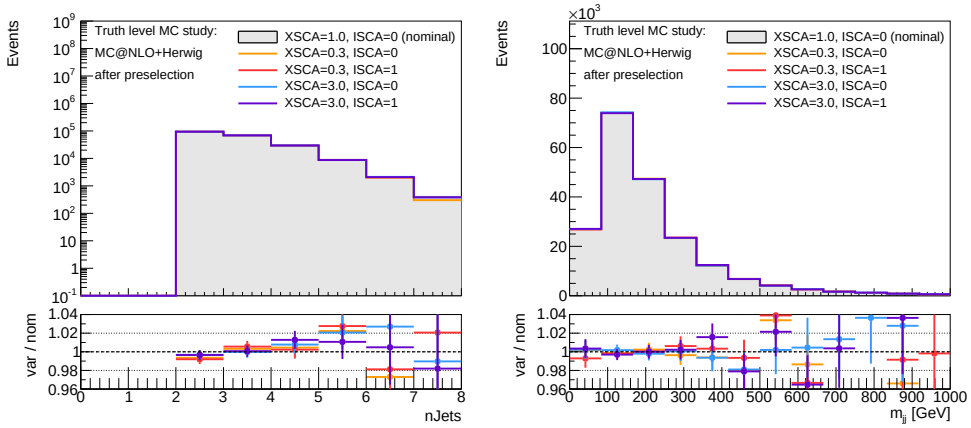

Figure 52.: Number of jets (left) and m_{jj} (right) distributions for various values of `XSCA` and `ISCA` parameters in dileptonic $t\bar{t}$ events. Since the variations of `XSCA` and `ISCA` parameters affect only the showering stage, the same event file generated by NLO ME is used for all variations.

ISR/FSR systematic	Value
benchmark recommendation	28%
truth level MC study	negligible

Table 21.: Summary of the ISR/FSR systematic uncertainties on the top background estimation.

6.4.6 Summary of systematic uncertainties on the top background estimation in VBF $H \to WW^{(*)}$ analysis

Table 22 summarises all theoretical systematic uncertainties on the top background estimation. The systematic uncertainties due to parton showering and underlying event and

ISR/FSR are neglected, all the other contributions are independently included in the final fit, and in total result to 26.2% uncertainty.

Uncertainty	Value
Generator modelling	22%
QCD scale variations	10%
PDF variations	10%
PE/UE	neglected
ISR/FSR	neglected
TOTAL	26.2%

Table 22.: Summary of all considered theoretical uncertainties on α_{top} for the top background estimation in the VBF SR.

6.5 Other backgrounds and their systematic uncertainties

The top background is one of the most dominant backgrounds in the VBF SR and even if the uncertainties on its estimation might carry the biggest impact on the statistical interpretation of the data, the uncertainties of other, non-top backgrounds are just as important for the correct interpretation of the results. The remaining backgrounds and their MC generators have already been discussed in Chapter 5. This section reviews the impact of the non-top backgrounds in the VBF SR, their estimation methods and their systematic uncertainties.

6.5.1 WW + 2 jets background

The decay of the non-resonant WW production has two well separated charged leptons in the final state, just like $H \to WW^{(*)} \to \ell^+\nu_\ell\ell^-\bar{\nu}_\ell$. The invariant mass of the two final state leptons $m_{\ell\ell}$, and the opening angle between them $\Delta\phi_{\ell\ell}$, represent good discriminating variables between the Higgs signal and the WW background. The WW production contaminates the VBF signal region only when the two vector bosons are associated with two jets and is one of the largest backgrounds in the VBF SR.

The definition of the $WW + 2$ jets control region is challenging due to a large top background contamination, hence the WW estimation in the VBF SR relies completely on MC predictions.

The $WW + 2$ jets events are divided into two categories, depending on whether they contain only electroweak vertices (EW $WW + 2$ jets) or also QCD vertices (QCD $WW + 2$ jets). Four standard types of theoretical uncertainties (introduced in Section 6.4) are associated to the WW background prediction, separately evaluated for the EW and QCD vertices[8]. The largest uncertainty comes from higher order QCD corrections and yields 10% for EW and 34% for QCD vertices. The generator modelling uncertainty and the uncertainty due to UE and PS are evaluated together by comparing SHERPA and MADGRAPH MC generators, resulting in 8% and 3% uncertainty for QCD and EW vertices, respectively. The PDF uncertainty is estimated to 2%-4%.

8 The uncertainties due to the interference between QCD and EW diagrams are at the percent level.

6.5.2 Drell-Yan background

Even after cutting on the missing transverse momentum and $m_{\tau\tau}$, the DY background still significantly contributes to the VBF SR. The DY process has two oppositely charged leptons in the final state and a substantial amount of missing transverse momentum. In case of $Z/\gamma^* \to \tau\tau$ decays, the E_T^{miss} is reconstructed due to neutrinos in the final state, while for $Z/\gamma^* \to \ell\ell$, $\ell = e, \mu$, it is mostly due to the degraded detector resolution, which is not well modelled in the MC. Both of these two contributions are discussed separately below.

- **$Z/\gamma^* \to \tau\tau$ BACKGROUND:** The $Z/\gamma^* \to \tau\tau$ events mostly dominate in the $e\mu/\mu e$ channel. The DY events in the VBF SR are corrected by a data-driven normalisation factor $NF_{\tau\tau}$ (obtained through a dedicated $Z/\gamma^* \to \tau\tau$ control region) and multiplied by a *correction factor* $CF_{\tau\tau}$ that corrects for the inefficiencies due to VBF selection criteria.

The $Z/\gamma^* \to \tau\tau$ control region is defined by requiring $m_{\ell\ell} < 80\,\text{GeV}$, $|m_{\tau\tau} - m_Z| < 25\,\text{GeV}$ and $p_{\text{T}}^{\text{sum}} < 15\,\text{GeV}$ after the $\geq$ 2-jets preselection and b-veto are applied. Due to the large top background contamination in the $Z/\gamma^* \to \tau\tau$ CR ($\sim 10\%$), a top normalisation factor derived in the top CR after the $p_{\text{T}}^{\text{sum}} < 15\,\text{GeV}$ selection, is applied to correct the top-quark contribution in the $Z/\gamma^* \to \tau\tau$ CR.

The normalisation factor $NF_{\tau\tau}$ is evaluated as a ratio between the difference in the data and non-$\tau\tau$ backgrounds with respect to the MC prediction (see Equation 82). The correction factor $CF_{\tau\tau}$ is defined as a double ratio of data/MC, before and after VBF selection:

$$CF_{\tau\tau} = \frac{\text{data/MC} \quad (\text{after VBF cuts})}{\text{data/MC} \quad (\text{before VBF cuts})}. \tag{85}$$

The $CF_{\tau\tau}$ is estimated in the Z - CR (defined by the inverted Z-veto, $\geq$ 2-jets preselection and the VBF topological selection) in the $ee/\mu\mu$ channel[9]. The final normalisation factor, corrected for the VBF selection inefficiency, is evaluated at the OLV stage, and results to $NF_{\tau\tau} \cdot CF_{\tau\tau} = 1.17 \pm 0.03$.

The uncertainty on the $Z/\gamma^* \to \tau\tau$ background estimation is evaluated by comparing the correction factor $CF_{\tau\tau}$ with an alternative correction factor estimated in an alternative low-E_T^{miss} Z - CR. The differences between both correction factors are at the percent level and well within statistical uncertainties. Therefore, the systematic uncertainty on the $Z/\gamma^* \to \tau\tau$ background is neglected.

- **$Z/\gamma^* \to ee/\mu\mu$ BACKGROUND:** The $Z/\gamma^* \to ee/\mu\mu$ background contribution in the VBF SR is estimated by a data-driven ABCD method, defined in the $E_T^{\text{miss}} - m_{\ell\ell}$ plane. After the preselection criteria[10], the phase space is split into four regions:
  - **A** (signal-like region, low $m_{\ell\ell}$): $m_{\ell\ell} < 50\,\text{GeV}$, $E_T^{\text{miss}} > 55\,\text{GeV}$,
  - **B** (Z-peak CR): $|m_{\ell\ell} - m_Z| < 15\,\text{GeV}$, $E_T^{\text{miss}} > 55\,\text{GeV}$,
  - **C** (low $m_{\ell\ell}$ CR): $m_{\ell\ell} < 50\,\text{GeV}$, $20 < E_T^{\text{miss}} < 55\,\text{GeV}$,
  - **D** (Z-peak CR): $|m_{\ell\ell} - m_Z| < 15\,\text{GeV}$, $20 < E_T^{\text{miss}} < 55\,\text{GeV}$.

9 The VBF selection criteria target mostly dijet variables, and the $Z/\gamma^* \to \tau\tau$ and the $Z/\gamma^* \to \ell\ell$ events have the same jet production process. Additionally, since the $ee/\mu\mu$ $Z/\gamma^* \to \ell\ell$ has a greater purity and statistics, and since the VBF selection criteria are lepton flavour agnostic, the $Z/\gamma^* \to \ell\ell$ (Z - CR) is chosen as the sample where the correction factor is evaluated.

10 The preselection criteria for $Z/\gamma^* \to ee/\mu\mu$ ABCD method are: $\geq$ 2-jets, b-veto, $p_{\text{T}}^{\text{sum}} < 15\,\text{GeV}$, $Z/\gamma^* \to \tau\tau$-veto, $p_T^{\text{miss, jet-corr}} > 50\,\text{GeV}$ and $m_{jj} > 600\,\text{GeV}$.

The normalisation factor is calculated in region A and is defined as

$$NF_{Z/\gamma^* \to ee/\mu\mu} = \frac{A_{\text{data}}}{A_{\text{MC}}} = \frac{B_{\text{data}} \frac{C_{\text{data}}}{D_{\text{data}}}}{B_{\text{MC}} \frac{C_{\text{MC}}}{D_{\text{MC}}}} = f_{\text{corr}} \frac{B_{\text{data}} \frac{C_{\text{data}}}{D_{\text{data}}}}{A_{\text{MC}}}, \tag{86}$$

where $f_{\text{corr}} = \frac{A_{\text{MC}}/B_{\text{MC}}}{C_{\text{MC}}/D_{\text{MC}}}$ represents a MC-based "non-closure" term which accounts for possible correlations between the $m_{\ell\ell}$ and E_T^{miss} variables in the MC. The value of f_{corr} equals to 0.96 ± 0.31, indicating almost no correlation between the $m_{\ell\ell}$ and E_T^{miss} distributions. The final normalisation factor is corrected for the VBF selection inefficiencies, estimated in the same way as in the $Z/\gamma^* \to \tau\tau$ case and equals to 1.02 ± 0.25.

The systematic uncertainty on the $Z/\gamma^* \to ee/\mu\mu$ background estimation is evaluated as the uncertainty on the ABCD method. The estimated MC non-closure factor is compared to the data-driven evaluation of f_{corr} (data - non-$Z/\gamma^* \to ee/\mu\mu$ MC). The largest discrepancy between the two is 41% and represents the final systematic uncertainty on the ABCD method.

6.5.3 ggF + 2 jets background

When the ggF production of the Higgs boson is associated with 2 or more jets and passes the VBF selection, it contaminates the VBF SR and is considered as a background in the VBF analysis. The uncertainties on the ggF estimation in the VBF SR are based on two contributions: QCD scale variations and PS/UE uncertainty.

The uncertainty due to different QCD scales is evaluated by varying the renormalisation and factorisation scales in POWHEG+MINLO MC. It is includes the effects coming from the $\geq$ 2-jets selection and VBF topological selection, considering the effects of the CJV requirement as well. The total uncertainty is evaluated by taking the largest difference in the acceptance due to QCD scale variations relative to the central value, and it is found to be 47% (71%) for the low (high) m_{jj} region.

The second contribution to the uncertainty on the ggF estimation is due to PS/UE and is evaluated by comparing POWHEG+PYTHIA and POWHEG+HERWIG ggF+2 jets MC samples. The final uncertainty on the acceptance due to different PS/UE models is 28%, with negligible differences in the shapes of the m_T distribution.

6.5.4 Misidentified leptons

If a W boson is produced in an association with one or more jets, it is considered a possible background for the $H \to WW^{(*)}$ signal, whenever jets get misidentified as leptons. Likewise, multijet production also contaminates the signal whenever two jets are misreconstructed as leptons and have misreconstructed E_T^{miss}.

The W+jets and multijets backgrounds are estimated through two control regions that use an alternative lepton definition, enhanced in jets misidentified as leptons, and contain data events with one *anti-identified* leading or subleading lepton for the W+jets CR, and with two *anti-identified* leading leptons for the multijets CR. The anti-identified leptons are reconstructed leptons which pass a *looser* identification and isolation criteria than the analysis leptons, and would therefore fail the VBF SR selection. The events in both CRs are required to satisfy all the remaining VFB SR criteria. The SR and both CRs contain contributions from W+jets, multijets and from prompt leptons coming from hard scatter or photon conversions, and when predicting the W+jets or multijet background in the SR, the contaminations from other contributions are subtracted.

The estimate of the W+jets or multijets background in the VBF SR is obtained by scaling the number of events in the suitable control region by an extrapolation factor, called the *fake factor*, which is defined as the ratio of identified to anti-identified leptons, and is usually measured in bins of lepton p_{T} and η. The fake factor measures the rate at which misidentified jets pass the full lepton identification with respect to the rate they pass the anti-identification requirement, and is obtained in a data-derived Z+jets or dijets samples, separately for different and same flavour final states.

- **W+JETS:** The estimate of W+jets in the VBF SR is obtained in the W+jets CR with the fake factor evaluated in the Z+jets data sample. The systematic uncertainty on the W+jets estimation is evaluated as the systematic uncertainty on the Z+jets fake factor method, with contributions coming from the MC-based correction factor that accounts for any differences in flavour composition and jet kinematics between the W+jets and Z+jets samples, and from estimating EW contamination in the Z+jets sample (e.g. prompt leptons from WZ, ZZ). The total systematic uncertainty depends on p_{T} of the anti-identified leptons and results in 29%-61% (32%-63%) for anti-identified electrons and 25%-46% (37%-53%) for anti-identified muons with the opposite (same) charge.

- **MULTJETS:** The multijet contribution to the VBF SR and W+jets CR is estimated in the multijet CR. The fake factor is evaluated in the dijet data sample, applied for every misidentified object and corrected for its dependence on the jet flavour composition due to the presence of an additional identified or anti-identified lepton. In addition, contributions from prompt leptons in W or Z events are subtracted from the dijet sample and represent the dominant source of the systematic uncertainty on the multijet background estimation. The total systematic uncertainty depends on the lepton flavour and ranges between 30% and 50%.

Even though, W+jets and multijets backgrounds have relatively large systematic uncertainties, they do not greatly affect the VBF signal due to their small (a few percent) contribution in the VBF SR at the end of the event selection (see Table 11).

6.5.5 Di-boson background

The di-boson background includes all events originating from two vector bosons other than WW, e.g. $W\gamma$, $W\gamma^*$, WZ and ZZ. Their contribution is much more important in $n_j \leq 1$ SR than in the VBF analysis, where their contribution is only a few percent, and has therefore a negligible effect on the signal estimation.

An overview of all dominant systematic uncertainties in the VBF analysis, including all discussed background theoretical uncertainties, is presented in the next section in Table 23. Other sources contributing to the overall uncertainty that have not been described so far are described next.

6.6 REMAINING SYSTEMATIC UNCERTAINTIES

The systematic uncertainties are divided into two main contributions; *experimental uncertainties* and *theoretical uncertainties*. Theoretical uncertainties on the background estimation in the VBF SR have already been discussed in Sections 6.4 and 6.5. This section summarises all the remaining contributions; the theoretical uncertainties on the VBF signal and the experimental

uncertainties. The impact of the systematic uncertainties on the final results is discussed in Chapter 7.

6.6.1 Theoretical uncertainties

Theoretical Uncertainties on the VBF signal

The theoretical uncertainties on the VBF signal are estimated for various sources; missing electroweak corrections, different PDF sets, efficiency of VBF criteria, PS/UE and ME modelling and the missing higher order QCD effects.

The VBF Higgs production contains only electroweak vertices and is well described already by the LO matrix element. The default VBF signal MC generator is POWHEG which includes the NLO QCD effects but does not account for the NLO EW effects, that can represent significant alterations to Higgs p_T spectrum [118]. The uncertainty due to the missing EW terms is explicitly evaluated in the BDT analysis and is found to be negligible. The same result is also assumed for the cut-based analysis.

The uncertainty due to different PDF sets and the uncertainty on the efficiency of the VBF selection criteria (termed CJV), have been already estimated in previous studies [118] and both amount to 4%.

The rest of the systematic uncertainties are estimated for the nominal VBF selection (see Table 10) with the Higgs topological cuts placed right after the preselection and the b-jet veto removed in order to increase statistics. The uncertainty due to PS/UE modelling is estimated by comparing POWHEG+PYTHIA and POWHEG+HERWIG MC VBF signal samples. The uncertainty on the acceptance at the end of the event selection yields to 8%. Shape discrepancies in kinematic distributions between the two MC samples have been considered as well, but their differences are reduced to the percent level at the end of event selection.

The uncertainty due to higher order QCD corrections is evaluated as discrepancies in the acceptance due to the upward and downward variations of the QCD scales in POWHEG+PYTHIA VBF signal samples with respect to the nominal values. The largest discrepancy amounts to 3.6%. Shape discrepancies have been considered as well with the largest deviations being less than 10%.

The uncertainty due to different ME calculations is estimated by comparing event yields in POWHEG+HERWIG and AMC@NLO [119]+HERWIG normalised to the default POWHEG+PYTHIA sample, after the preselection stage. The relative difference in the acceptance between the two samples amounts to 0.2% and can be neglected compared to other contributions. However, the discrepancy in the cross-sections between AMC@NLO and POWHEG is larger, up to 2.4%, and is therefore quoted as the ME uncertainty. No significant discrepancy in the shapes of the distributions is observed.

Summary of Theoretical Uncertainties

Table 23 summarises all significant theoretical uncertainties in the VBF $H \to WW^{(*)}$ analysis. Theoretical uncertainties on W+jets and multijets estimation and di-boson backgrounds are not included due to their small (a few percent) contributions in the VBF SR.

One last theoretical systematic uncertainty which has not been yet discussed is the uncertainty on the branching ratio of the $H \to WW^{(*)}$ and arises due to the higher order calculations and uncertainties in the input parameters, like α_S and m_T. The uncertainty is evaluated in [118] and yields to 4.3%.

Source	VBF signal	Backgrounds				
		Top	WW + 2 jets EW	WW + 2 jets QCD	Drell-Yan	ggF
QCD scale	3.6%	10%	10%	34%	-	48% (71%)
PDF	4%	10%	2-4%		-	-
Generator modelling	2.4%	22%	3%	8%	-	-
PS/UE	8%	-			-	28%
ISR/FSR	-	-	-	-	-	-
CJV	4%	-	-	-	-	-
DY ABCD ($ee/\mu\mu$ only)	-	-	-	-	41%	-
TOTAL	10.7%	26.2%	10.9%	35.1%	41%	55% (76%)
Statistical						
$e\mu/\mu e$	2%	7%	6%		22%	3%
$ee/\mu\mu$	3%	11%	8%		24%	6%

Table 23.: Summary of theoretical systematic uncertainties for the VBF signal and background samples. The row 'TOTAL' represents the total theoretical systematic uncertainty evaluated by quadratically summing up all contributions. In the ggF column, the value in brackets represents the value of the systematic uncertainty for the $m_{jj} > 1\,\text{TeV}$ region. The statistical uncertainties represent the MC statistical uncertainties obtained before the final m_T selection in the VBF SR.

6.6.2 Experimental uncertainties

Experimental uncertainties arise from the limited detector response and inefficiencies in the reconstruction and identification of analysis objects. They are split into several categories discussed below.

Jet Energy Scale and Resolution

The systematic uncertainty due to the jet energy scale (JES) calibration (introduced in Section 4.3) consists of various contributions. Among others are the modelling and statistical uncertainties on the jet calibration from the central region - "η intercalibration", pile-up and calorimeter response on jet flavour composition. The total uncertainty due to JES is less than 7%.

The uncertainty on jet energy resolution (JER) is determined from in situ measurements as a function of p_{T} and η and is included as a separate systematic. The uncertainty due to JER varies between 2% - 40%.

Both JER and JES uncertainties are the dominant experimental uncertainties for the signal and background processes. They affect the VBF phase space through the $n_j \geq 2$ selection, dijet variables and indirectly also through E_T^{miss} measurement.

Jet Vertex Fraction

The systematic uncertainty due to the jet vertex fraction is found to be negligible for the signal and background samples. The most sensitive selection criterion on the JVF is the central jet veto and reveals only a minor effect of 0.5%.

Jet b-tagging

The systematic uncertainties on the b-jet tagging arise from the identification efficiencies and misidentification rates, where c- or light-jets are identified as b-jets (see Section 4.3.1). The uncertainty due to the identification efficiencies is at most 7.8%. The uncertainty due to the misidentification rate for light-jets (depending on p_{T} and η) varies between 9% - 19%, and for c-jets (depending on p_{T}) between 6% - 14%.

The greatest impact of the b-tagging uncertainties in the VBF $H \to WW^{(*)}$ analysis is on the top background estimation due to different b-jet requirements in the VBF SR and top CR.

Lepton reconstruction and Trigger efficiencies

Lepton reconstruction, identification and isolation uncertainties are estimated through the tag-and-probe methods (described in Sections 4.2.1 and 4.2.2). The lepton efficiencies are evaluated to be $< 3\%$ and $< 0.5\%$ for electrons and muons, respectively. The uncertainties due to lepton energy scale and resolution depend on $p_{\mathrm{T}}(E_T)$ and η and are $\leq 1\%$. These uncertainties have only a small effect on the signal and background event yields.

The systematic uncertainty due to trigger efficiencies is less than 1%.

Missing transverse momentum

All experimental systematic uncertainties affecting leptons and jets are also propagated to the uncertainties on E_T^{miss} and $p_T^{\mathrm{miss,\,jet\text{-}corr}}$ since their evaluation depends on all reconstructed objects. The uncertainty on E_T^{miss} additionally accounts for uncertainties due to the soft-term contributions (see Section 4.5) and $p_T^{\mathrm{miss,\,jet\text{-}corr}}$ accounts for the p_{T} imbalance between tracks not associated with charged particles. The mean of longitudinal components varies between 0.2 GeV - 0.3 GeV (0.3 GeV - 1.4 GeV) for the E_T^{miss} soft-term ($p_T^{\mathrm{miss,\,jet\text{-}corr}}$ contributions). The resolution of longitudinal and perpendicular terms varies between 1% - 4% (1.5 GeV - 3.3 GeV) for the E_T^{miss} soft-term ($p_T^{\mathrm{miss,\,jet\text{-}corr}}$ contributions).

Pile-up

Pile-up impacts the jet energy calibration and can introduce additional hard jets which can migrate between different jet bins in the $H \to WW^{(*)}$ analysis. The effect of pile-up impacts JES only at the percent level. Migrations between jet bins produce additional jets between the tag jets in the VBF category, and amount to a systematic of at most 1%. Additionally, the μ-rescaling parameter (see Section 4.1) has been varied from the nominal value 0.9 by ± 0.1, and an effect of at most 2% (4%) was observed on the signal (background) event yields.

Luminosity

The systematic uncertainty on the luminosity measurement yields 2.8% for the $\sqrt{s} = 8\,\mathrm{TeV}$ dataset.

The VBF SR has been defined and the event yields measured (see Tables 9 and 10 in Chapter 5). The background contributions in the VBF SR are well understood and modelled and the systematic uncertainties on their modelling have been estimated. The next step is the statistical treatment of the observed event yields and their comparison with the theoretical

predictions is main topic of the next chapter, where the fitting procedure applied in the $H \to WW^{(*)}$ analysis and the final results are described.

7 STATISTICAL TREATMENT OF THE VBF $H \to WW^{(*)}$ DATA

Finding the Higgs boson candidate, produced through vector boson fusion and decaying into two W bosons, is a challenging task. Out of one billion collisions produced per second at the LHC, only those satisfying the $H \to WW^{(*)}$ event selection are of interest for this analysis. After the final requirement on m_T has been applied in the VBF SR, only $\mathcal{O}(10)$ events remain and in order to give an accurate statistical interpretation of such an observation, a precise prediction of the signal and background event yields and a reliable response of the ATLAS detector are crucial.

The VBF $H \to WW^{(*)}$ event selection has been already described in Chapter 5 and the estimation of signal and background yields and their systematic uncertainties in Chapter 6. This chapter describes the statistical interpretation of the recorded VBF $H \to WW^{(*)}$ data during the 2012 data-taking. The likelihood function and the test statistic used in the final fitting procedure are presented in Section 7.1. The measurements of the VBF $H \to WW^{(*)}$ signal strength and Higgs boson couplings are presented in Section 7.2, including the results of the combined ggF+VBF analysis as well.

7.1 Fitting Procedure

The fitting procedure includes events selected by the selection criteria summarised in Table 10, with the $e\mu/\mu e$ final states additionally split into the high and low m_{jj} region at 1 TeV. The final criterion on $m_T < 130$ GeV is excluded from the event selection, since the m_T distribution is used as the discriminant in the final fit.

The m_T distribution is split into three bins with boundaries[1]

$$[0, 80], \quad [80, 130], \quad [130, \infty] \qquad \text{(units in GeV)},$$

in order to maximise the expected signal significance. The bin boundaries are chosen such that statistical fluctuations associated to the background subtraction are stable and the event yields are approximately constant in each bin. In addition to the event yields, the fitting procedure includes background normalisation factors and systematic (and statistical) uncertainties discussed in Chapter 6. In order to evaluate the significance of the measured signal events, the likelihood function has to be built first and it is described next.

7.1.1 Likelihood function

The likelihood function $\mathcal{L}$, expresses the *probability* of the observed data under a hypothesis. The $\mathcal{L}(\mu, \boldsymbol{\theta}|\mathbf{N})$ is a function of the *signal strength* parameter μ and of a set of *nuisance parameters*

1 Previous VBF results [86] showed that the VBF analysis is dominated by the lack of statistic. Therefore, an optimisation of the number of bins used in the final fit has been performed, where a smaller number of bins is preferred, in order to avoid any possible background shape systematic.

$\boldsymbol{\theta} = \{\theta_a, \theta_b, ...\}$, given that a set of $\mathbf{N}$ events is observed, $\mathbf{N} = \{N_a, N_b, ...\}$. The signal strength is the parameter of interest in the $H \to WW^{(*)}$ analysis and is defined as the ratio of observed signal events with respect to the number of events predicted by the SM:

$$\mu = \frac{\sigma^{\text{obs}}}{\sigma^{\text{SM}}}. \tag{87}$$

A value of $\mu = 1$ indicates that the observed signal yields agree with the SM prediction and corresponds to the *signal-over-background* hypothesis, while $\mu = 0$ indicates that no signal has been observed and corresponds to the *background-only* hypothesis. The nuisance parameters represent all parameters which are not known a priori, but are fitted from the data (e.g. background normalisation factors).

The likelihood function can be separated into three contributions; the probability distribution of observing $\mathbf{N^{SR}}$ events in the SR, the probability distribution of observing $\mathbf{N^{CR}}$ events in all considered control regions, and the probability distribution of the considered systematic uncertainties;

$$\begin{aligned}\mathcal{L}(\mu, \boldsymbol{\theta}|\mathbf{N}) = & \\ = \prod_{c}^{DF,SF} f_{SR}(\mathbf{N_c^{SR}} \,|\, \mu, \boldsymbol{\theta}) \cdot & \prod_{c'}^{DF,SF} f_{CR}(\mathbf{N_{c'}^{CR}} \,|\, \mu, \boldsymbol{\theta}) \cdot \prod_{n}^{syst.} g(\vartheta_n \,|\, \theta_n),\end{aligned} \tag{88}$$

where the products over c, c' consider $e\mu/\mu e$ and $ee/\mu\mu$ final states. The SR has been defined in Chapter 5 and the CRs in Chapter 6.

The first term is a *Poisson* distribution,

$$\text{Poiss}(N_c^{SR}|\lambda) = e^{-\lambda}\lambda^{N^{SR_c}}/N^{SR_c}!\,, \tag{89}$$

describing the probability of observing $\mathbf{N^{SR}}$ events in the SR if λ events are expected from the SM. The expected number of events is actually a sum of expected signal S^{SR} and background $\sum_i B_i^{SR}$ contributions in the SR, where the sum over i goes through all considered backgrounds. The expected signal events S^{SR} are additionally multiplied by the signal strength μ (the parameter of interest); $\lambda = \mu \cdot S^{SR} + \sum_i B_i^{SR}$ and $f_{SR}(\mathbf{N_c^{SR}} \,|\, \mu, \boldsymbol{\theta})$ is defined as:

$$f_{SR}(\mathbf{N_c^{SR}} \,|\, \mu, \boldsymbol{\theta}) = \prod_{b \in m_T bins} \text{Poiss}\left(N_{c,b}^{obs,SR} \,\middle|\, \mu \cdot S_{c,b}^{SR}(\boldsymbol{\theta}) + \sum_i \text{NF}_i\, B_{c,b,i}^{SR}(\boldsymbol{\theta})\right), \tag{90}$$

where the product goes over bins in the m_T distribution[2], and the background events are multiplied by their normalisation factors NF_i. The expected background and signal events are estimated either by the data-driven techniques or MC and are therefore both functions of nuisance parameters $\boldsymbol{\theta}$.

The second term in Equation 88 represents the probability of observing $\mathbf{N_{c'}^{CR}}$ events in considered control regions, described again by the Poisson distribution. For each control region j, the Poisson function is defined as $\text{Poiss}(\mathbf{N_{c',j}^{CR}}|\lambda_j)$, where $\mathbf{N_{c',j}^{CR}}$ is the number of observed events in the control region j, and $\lambda_j = \mu \cdot S^{CR\,j} + \text{NF}_j B_j^{CR\,j} + \sum_{i \neq j} \text{NF}_i B_i^{CR\,j}$ represents the sum of expected signal events $S^{CR\,j}$ in j^{th} CR, expected background events B_j in the j^{th} CR

2 If there is more than one SR, an additional product over all considered SRs is included.

and, whenever the j^{th} CR is contaminated by other backgrounds $i \neq j$, their contributions are also included,

$$f_{CR}(\mathbf{N}_{\mathbf{c'}}^{\mathbf{CR}} \mid \mu, \boldsymbol{\theta}) = \tag{91}$$
$$= \prod_{j \in CRs} \text{Poiss}\left(N_{c'}^{obs,\,CR\,j} \,\middle|\, \mu \cdot S_{c'}^{CR\,j}(\boldsymbol{\theta}) + \text{NF}_j B_{c'}^{CR\,j}(\boldsymbol{\theta}) + \sum_{i \neq j} \text{NF}_i \, B_{i,c'}^{CR\,j}(\boldsymbol{\theta}) \right).$$

The third component in Equation 88 constrains all nuisance parameters with a *Gaussian* term $g(\vartheta_n, \theta_n) = e^{-(\vartheta_n - \theta_n)^2/2}/\sqrt{2\pi}$, where the parameter ϑ_n represents the central value of the measured systematic uncertainty n and θ_n its associated nuisance parameter. The impact of systematic uncertainties on the expected event yields in Equations 90 and 91 is evaluated through the response functions ν which parametrise the impact of the nuisance parameters θ,

$$S(\boldsymbol{\theta}) = S(\vartheta) \cdot \prod_{ns} \nu_{ns}(\theta_{ns}), \tag{92}$$
$$B_i(\boldsymbol{\theta}) = B_i(\vartheta) \cdot \prod_{nb} \nu_{nb,i}(\theta_{nb}).$$

Some systematic uncertainties affect only background processes while others affect both signal and background event yield. Additionally, some systematics are correlated among m_T bins (e.g. normalisation uncertainties) while others are not, and the response functions are defined accordingly.

The statistical uncertainties due to the finite size of MC samples, are also included in the likelihood. Their nuisance parameters are constrained by a Poisson distribution.

Finally, in order to determine the observed signal strength μ^{obs}, $\mathcal{L}$ is maximized with respect to its arguments (μ and $\boldsymbol{\theta} = \{\text{NF}, \theta_n\}$) and evaluated at $\vartheta_n = 0$.

7.1.2 Test statistic and p-values

Testing whether a background-only or a signal-over-background hypothesis agrees with the observed data is done through a *profile likelihood ratio* $\lambda(\mu)$, defined as

$$\lambda(\mu) = \begin{cases} \dfrac{\mathcal{L}(\mu, \hat{\hat{\boldsymbol{\theta}}}(\mu))}{\mathcal{L}(\hat{\mu}, \hat{\boldsymbol{\theta}})} & \text{if } \hat{\mu} \geq 0, \\ \dfrac{\mathcal{L}(\mu, \hat{\hat{\boldsymbol{\theta}}}(\mu))}{\mathcal{L}(0, \hat{\boldsymbol{\theta}}(0))} & \text{if } \hat{\mu} < 0. \end{cases} \tag{93}$$

The parameter values $\hat{\mu}$ and $\hat{\boldsymbol{\theta}}$ represent the parameters that maximise the likelihood and the parameter $\hat{\hat{\boldsymbol{\theta}}}(\mu)$ represents the value of $\boldsymbol{\theta}$ that maximises the likelihood for a specific value of μ. The hypotheses with $\hat{\mu} \geq 0$ are physical, while hypotheses with $\hat{\mu} < 0$ are not and represent a downward fluctuation of the background (lack of observed data with respect to the expected backgrounds).

The two-sided test statistic q_μ, is used to test the compatibility between the observed data and the tested hypothesis μ and is defined as

$$q_\mu = -2 \ln \lambda(\mu). \tag{94}$$

The higher the value of q_μ, the larger is the incompatibility between the observed data and the tested hypothesis. The absolute minimum, $q_\mu = 0$, represents the best agreement between the data and the tested hypothesis and is reached at $\mu = \hat{\mu}$.

The order of agreement between the observed data and the tested hypothesis is quantified by *p-values*. The *p*-value is defined as an integrated probability density function of the test statistic q_μ;

$$p_\mu = \int_{q_\mu^{\rm obs}}^{\infty} f(q_\mu \mid \mu, \hat{\hat{\boldsymbol{\theta}}}(\mu)) dq_\mu \ , \tag{95}$$

and represents the probability that the tested hypothesis μ agrees with the observed or higher values of q_μ. The *p*-value is evaluated using asymptotic formulae described in [120].

Whenever an explicit value of the signal strength is to be measured, the test statistic from Equation 94 is evaluated assuming a signal-over-background hypothesis. In addition, a 68% confidence level (C.L.) intervals, set by the values of μ satisfying $p_\mu = 0.16$, are evaluated as well. For the measurement of the Higgs boson signal strength, the mass of Higgs boson needs to be specified.

In case no signal is present in the observed data, or when an observed signal is confirmed with 5 standard deviations with respect to background-only hypothesis, one-sided test statistics are built in order to evaluate the *exclusion limits* or claim the *discovery* of the signal, and are discussed below.

Exclusion Limits

An exclusion limit is placed when no signal is observed in the data. A one-sided test statistic, defined as

$$\tilde{q}_\mu = \begin{cases} -2 \ln \lambda(\mu) & \text{if } \hat{\mu} \leq \mu, \\ 0 & \text{if } \hat{\mu} > \mu \ , \end{cases} \tag{96}$$

is used to test the signal-over-background hypothesis and determine upper limits on the signal strength. The restriction $\hat{\mu} \leq \mu$ prevents incompatibilities of the tested hypothesis and the observed data for any upward fluctuation of the data. In order to additionally prevent any effects of downward fluctuation in the data, an alternative *p*-value is defined as the *conditional probability* $\mathrm{CL_s}$, using the modified frequentist technique [121]

$$\mathrm{CL_s} = \frac{p_\mu}{1 - p_b}, \tag{97}$$

where p_b is defined as

$$p_b = \int_{-\infty}^{\tilde{q}_\mu^{\rm obs}} f(\tilde{q}_\mu \mid 0, \hat{\hat{\boldsymbol{\theta}}}(0)) d\tilde{q}_\mu, \tag{98}$$

and p_μ is defined in Equation 95 with q_μ replaced by $\tilde{q}_\mu$. The value $1 - p_b$ represents the probability that the observed data agree with the background-only hypothesis. Finally, the 95% exclusion limit on μ is determined as the largest value of μ ($\mu_{\rm max}$) satisfying $\mathrm{CL_s} \geq 0.05$. In the case $\mu < 1$ and $\mathrm{CL_s} = 0.05$, the signal-over-background hypothesis is *excluded* at 95% C.L.. The sensitivity of this measurement is obtained by comparing it to the expected upper limit $\mu_{\rm max}$, assuming a background-only hypothesis.

Discovery and Signal Significance

In an attempt to confirm a tested hypothesis as a *discovery*, the background-only hypothesis must be rejected by more than five standard deviations. A one-sided test statistic is constructed assuming a background-only hypothesis,

$$q_0 = \begin{cases} -2\ln\lambda(0) & \text{if } \hat{\mu} \geq 0, \\ 0 & \text{if } \hat{\mu} < 0. \end{cases} \tag{99}$$

The level of agreement between the data and the tested hypothesis is estimated by the p_0-value,

$$p_0 = \int_{q_0^{\text{obs}}}^{\infty} f(q_0 \,|\, 0, \hat{\hat{\boldsymbol{\theta}}}(0))\, dq_0 \,. \tag{100}$$

The p_0-value represents the probability that an excess, at least as large as it is observed in the data, is actually produced only due to the background fluctuations.

The signal significance Z, can be extracted from the p_0-value as

$$Z = \Phi^{-1}(1 - p_0), \tag{101}$$

where Φ represents the cumulative probability function of the standard Gaussian function. A *discovery* of the signal is confirmed whenever the background-only hypothesis is rejected by more than five standard deviations, $Z \geq 5\sigma$, or equivalently $p_0 < 2.9 \cdot 10^{-7}$ and an *evidence* of the signal is confirmed if $Z \geq 3\sigma$ or $p_0 < 1.5 \cdot 10^{-3}$. The sensitivity of this calculation is estimated by comparing the results to the p_0-value evaluated assuming a signal-over-background hypothesis.

7.1.3 Assumptions in the VBF fit model

The previously published VBF $H \to WW^{(*)}$ analysis [86], observed that the accuracy of the VBF signal strength measurement is mostly affected by the statistical uncertainty of the observed data. The systematic uncertainties evaluated in this analysis are therefore expected to have only a secondary effect on the measured signal strength. Any systematic uncertainty resulting in a 5% effect or less is consequently not included in the final fit. The following list summarises the remaining assumptions in the VBF cut-based fit model:

- Most of the systematic uncertainties are separately evaluated for the low and high m_{jj} region. However, the only contribution with differences between the two m_{jj} regions that actually impacts the total uncertainty, is due to the QCD scale variations in the ggF+2jets background (see Table 23). Consequently, it is the only systematic uncertainty included in the fit with separate contributions for the low and the high m_{jj} region.
- The only uncertainties impacting the signal strength measurement are uncertainties on the acceptance. Shape uncertainties in the m_T distribution have a negligible effect due to the crude binning in the m_T distribution, and are therefore not included in the fit.
- The ggF Higgs boson production is considered as a background in the VBF analyses, and its expected yields are predicted by the SM.
- Two control regions are included in fit - the $Z/\gamma^* \to ee/\mu\mu$ CR and the top CR (for their definition see Chapter 6).
- Normalisation factors from the top and the Drell-Yan background are included in the final fit. The $NF_{Z/\gamma^* \to \ell\ell}$ and NF_{top} are extracted from the fit, while the $NF_{Z/\gamma^* \to \tau\tau}$

is simply hardcoded in the fit model. The final normalisation factors are summarised in Table 24.

NF	Value	Δ
top	1.02 ± 0.20	20%
$Z/\gamma^* \to \ell\ell$	0.94 ± 0.26	28%
$Z/\gamma^* \to \tau\tau$	1.17 ± 0.03	3%

Table 24.: The normalisation factors for the top and Drell-Yan backgrounds and their relative statistical uncertainties, Δ. The $NF_{Z/\gamma^* \to \ell\ell}$ and NF_{top} are extracted from the fit.

7.2 Experimental Results

This section presents the final experimental results of the $H \to WW^{(*)}$ analysis. First, the measurement of the signal strength in the VBF Higgs production and the impact of various systematic uncertainties on the measured μ_{VBF} are outlined. The results obtained from the VBF BDT analysis and the combination with the ggF channels, including 8 TeV and 7 TeV data, are presented next.

The excess in the data is described by the SM Higgs boson signal hypothesis. The results are quoted for $m_H = 125.36 \pm 0.41$ GeV as obtained from the combined mass measurement in $H \to ZZ$ and $H \to \gamma\gamma$ channels [122].

7.2.1 Observation of the VBF Higgs production mode in the $H \to WW^{(*)} \to \ell^+\nu_\ell\ell^-\bar{\nu}_\ell$ channel

Table 25 shows the expected and observed event yields, and the signal and background composition at the end of the VBF event selection. The final number of expected signal and

Final Cut	N_{obs}	N_{sig}	N_{bkg}	$N_{\text{obs}}/N_{\text{bkg}}$
$e\mu/\mu e$				
$m_{jj} < 1000$	8	2.3	4.1	1.98 ± 0.73
$m_{jj} > 1000$	6	2.4	1.6	3.87 ± 1.65
$ee/\mu\mu$	6	2.2	3.7	1.63 ± 0.69
TOTAL	20	6.9	9.4	2.17 ± 0.62

Table 25.: The observed (N_{obs}) and expected signal (N_{sig}) and background (N_{bkg}) event yields at the end of the VBF event selection (see Chapter 5, Tables 9 and 10) and their fractions ($S + B = 100\%$). The cut on m_T is not applied in the fit. The split in high and low m_{jj} region is applied only in the $e\mu/\mu e$ final state, since the $ee/\mu\mu$ has lower statistics. All energy-related units are in GeV.

backgrounds events for the combined $e\mu/\mu e$ and $ee/\mu\mu$ final states is 6.9 and 9.4 respectively, while 20 events have been observed, resulting in an approximately 2 times more of the observed data events than the background events. The transverse mass distribution used in the final fit has been already presented in Figure 40.

The expected and observed signal strength, $\hat{\mu}_{\text{VBF}}$ and the associated signal significance Z_{VBF}, are presented in Table 26. The observed signal strength for the combined $e\mu/\mu e$ and $ee/\mu\mu$ final states is $\hat{\mu}^{\text{obs}}_{\text{VBF}} = 1.66^{+0.78}_{-0.67}$ and agrees with the SM predictions within uncertainties. Equivalently, the observed signal significance is 3.2 standard deviations, where $2.0\,\sigma$ is expected. Since $Z^{\text{obs}}_{\text{VBF}} \geq 3\,\sigma$, an *evidence* for the VBF Higgs production in the $H \to WW^{(*)} \to \ell^+\nu_\ell\ell^-\bar{\nu}_\ell$ decay is observed *for the first time*. Figure 53 shows the final, post-fit m_T distribution for the combined $e\mu/\mu e$ and $ee/\mu\mu$ final states.

	$\hat{\mu}^{\text{exp}}_{\text{VBF}}$	$\hat{\mu}^{\text{obs}}_{\text{VBF}}$	$Z^{\text{exp}}_{\text{VBF}}$	$Z^{\text{obs}}_{\text{VBF}}$
$e\mu/\mu e$	$1^{+0.75}_{-0.64}$	$1.85^{+0.89}_{-0.78}$	1.8	3.1
$ee/\mu\mu$	$1^{+1.36}_{-1.15}$	$0.76^{+1.35}_{-1.05}$	0.9	0.7
Combined	$1^{+0.67}_{-0.58}$	$1.66^{+0.78}_{-0.67}$	2.0	**3.2**

Table 26.: Expected and observed signal strengths and associated significances for $e\mu/\mu e$, $ee/\mu\mu$ and combined $e\mu/\mu e$ + $ee/\mu\mu$ final states in the VBF analysis. The ggF signal is considered as a background to the VBF signal and its prediction is taken from the SM.

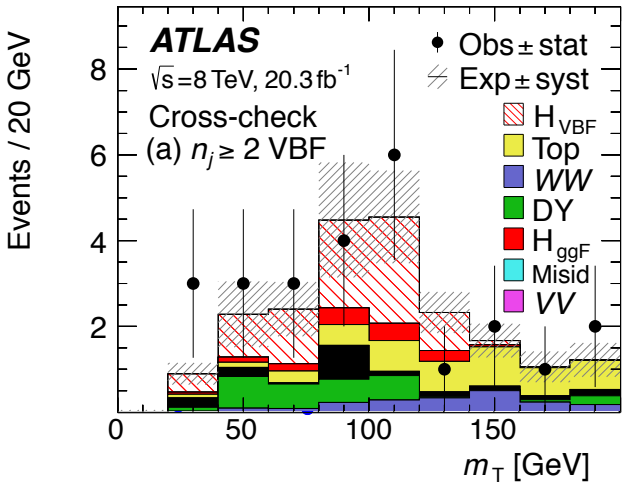

Figure 53.: The post-fit m_T distribution in the VBF analysis for the combined $e\mu/\mu e$ and $ee/\mu\mu$ final states.

The impact of the statistical and systematic uncertainties on the observed signal strength is presented in Table 27. The measurement of $\hat{\mu}^{\text{obs}}_{\text{VBF}}$ is mostly dominated by the statistical uncertainty (77%).

Table 28 shows the composition of the systematic uncertainties and their impact on the observed signal strength. The largest contribution from experimental systematic uncertainties is due to JES and JER. The largest impact of the theoretical uncertainties is due to PS/UE modelling in the VBF signal. The uncertainties on the top background have a smaller effect on the observed signal strength, with the largest contribution coming from the generator modelling uncertainties, as discussed in the previous chapter, resulting in the 6% uncertainty.

	$\hat{\mu}^{\text{obs}}_{\text{VBF}}$	σ^{syst}		σ^{stat}	
$e\mu/\mu e$	$1.85^{+0.89}_{-0.78}$	$^{+0.38}_{-0.30}$	[17%]	$^{+0.80}_{-0.72}$	[83%]
$ee/\mu\mu$	$0.76^{+1.35}_{-1.05}$	$^{+0.61}_{-0.43}$	[19%]	$^{+1.2}_{-0.96}$	[81%]
Combined	$1.66^{+0.78}_{-0.67}$	$^{+0.39}_{-0.29}$	[23%]	$^{+0.67}_{-0.60}$	[77%]

Table 27.: Observed signal strength and its total systematic and statistical uncertainties for $e\mu/\mu e$, $ee/\mu\mu$ and the combined final states in the VBF analysis. The ggF signal is considered as a background to the VBF signal and its prediction is taken from the SM.

7.2.2 Impact of top systematics on $Z^{\text{exp}}_{\text{VBF}}$

The VBF signal strength is highly dominated by the statistical uncertainties. The evaluated systematic uncertainties on the top background are; 22% from the generator modelling, 10% from QCD scale variations, and 10% from PDF sets variations. They are independently included in the final fit and their impact on the signal strength measurement is 6%, 3% and 3%, respectively.

The contributions to the top background uncertainty have been extensively studied in this manuscript in order to improve and reduce the total systematic uncertainty on the signal strength measurement. Table 29 shows what would be the impact on the expected signal significance for all the discussed, but at the end not included, contributions of top background systematic uncertainties.

The generator modelling uncertainty is the largest contribution of top systematic uncertainties and is estimated as the largest discrepancy between two of the three considered MC generators, resulting in $\Delta(\text{ALPGEN}, \text{MC@NLO}) = 22\%$. Removing the CJV requirement from the top CR increases the generator modelling uncertainty, from the nominal 22% to 53% and consequently almost doubles the impact on the $Z^{\text{exp}}_{\text{VBF}}$, from 6% to 11%. Additionally, if the remaining two generator modelling contributions, $\Delta(\text{ALPGEN}, \text{POWHEG})$ and $\Delta(\text{POWHEG}, \text{MC@NLO})$, would be included, the generator modelling uncertainty would increases to 28% with the CJV requirement and to 74% if the CJV is not included in the top CR (see Table 17). The impact on $Z^{\text{exp}}_{\text{VBF}}$ would increase from 7% to 14%, with and without CJV requirement, respectively.

The systematic uncertainty due to the PS/UE modelling is not included in the final fit because the observed uncertainty due to different showering models is smaller than statistical uncertainties. If this would not be the case and the systematic uncertainty of 17% would have been assigned on the PS/UE modelling (estimated as the difference in the event yields between the two showering models at the $Z \to \tau\tau$-veto stage, see Table 20) and included in the final fit, it would represent a 4% impact on $Z^{\text{exp}}_{\text{VBF}}$.

The systematic uncertainty due to ISR/FSR is also neglected in the final fit (see discussion in Section 6.4.5). If however, the ISR/FSR systematic would have been estimated by the benchmark ATLAS recommendation (see Section 6.4.5) and a 28% uncertainty (see Table 21) would be included in the fit, this would cause a 7% impact on the $Z^{\text{exp}}_{\text{VBF}}$.

Table 30 shows the impact on the expected significance if all discussed contributions from Table 29 would be quadratically combined with the nominal top background systematic uncertainty, considering both scenarios - with and without the CJV in the top CR. The removal of the CJV requirement from the top CR definition doubles the impact of the total top systematic uncertainty on the expected significance, from 7% to 12% and reduces the

Source	Error +	Error −	$\frac{\Delta\hat{\mu}_{\mathrm{VBF}}}{\hat{\mu}_{\mathrm{VBF}}}$
Experimental			
• Jet Energy Scale			
Eta Modelling	0.17	0.15	20%
Flavour Composition	0.09	0.07	9%
2012 Modelling	0.06	0.05	7%
Flavour Response	0.04	0.03	4%
• Jet Energy Resolution	0.12	0.08	12%
• E_T^{miss}			
Resolution of Soft terms	0.06	0.05	7%
Scale of Soft terms	0.04	0.04	5%
Theory			
• VBF signal			
PS/UE	0.16	0.10	16%
PDF	0.08	0.05	8%
CJV	0.08	0.05	8%
QCD scale	0.08	0.05	7%
ME	0.05	0.03	5%
• ggF + 2 jets			
QCD scale	0.07	0.07	8%
PS/UE	0.04	0.04	5%
• Top background			
Generator Modelling	0.05	0.05	6%
QCD scale	0.02	0.03	3%
PDF	0.02	0.03	3%
• WW QCD			
QCD scale	0.06	0.06	7%
ME modelling	0.02	0.02	2%
• DY			
ABCD	0.05	0.05	6%
• $BR(H \to WW^{(*)})$	0.10	0.06	9%
Top NF	0.06	0.04	6%
DY NF	0.02	0.02	3%
Statistical uncertainty	0.67	0.60	77%
TOTAL	0.78	0.678	87%

Table 28.: Impact of the systematic uncertainties (absolute and relative) on the observed signal strength $\hat{\mu}_{\mathrm{VBF}}^{\mathrm{obs}} = 1.66$, for the combined $e\mu/\mu e$ and $ee/\mu\mu$ final states.

Top syst. uncertainty contribution	$Z_{\text{VBF}}^{\text{exp}}$	$\Delta Z_{\text{VBF}}^{\text{exp}}$		$\Delta Z_{\text{VBF}}^{\text{exp}} / Z_{\text{VBF}}^{\text{exp}}$	Δ_Z
Nominal (quadratic sum of generator modelling, QCD and PDF uncertainties)					
• 26%	1.996	$+0.065$	-0.066	7%	-
Generator modelling:					
Including only Δ(ALPGEN, MC@NLO)					
• 53% no CJV in top CR	1.964	$+0.111$	-0.114	11%	1.6%
• 22% with CJV in top CR	1.999	$+0.057$	-0.057	6%	0.2%
Including all Δ MC contributions, quadratically summed up (see Table 17)					
• 74% no CJV in top CR	1.940	$+0.136$	-0.141	14%	2.8%
• 28% with CJV in top CR	1.993	$+0.069$	-0.070	7%	0.1%
Parton Shower and Underlying Event modelling:					
• 17% at $Z \to \tau\tau$-veto (Table 20)	2.005	$+0.040$	-0.041	4%	0.5%
ISR/FSR:					
• 28% at m_{jj} stage (Table 21)	1.994	$+0.069$	-0.070	7%	0.1%

Table 29.: Impact of various contributions of top systematic uncertainties on the expected VBF signal significance ($Z_{\text{VBF}}^{\text{exp}}$), extracted from the final fit model in combined $e\mu/\mu e$ and $ee/\mu\mu$ final states, for the $m_H = 125.36\,\text{GeV}$ Higgs boson mass hypothesis. In this case "Nominal" uncertainty refers to the quadratic sum of generator modelling, QCD and PDF uncertainties (see Table 22) and results in $Z_{\text{nom}}^{\text{exp}} = 1.996$. The symbol Δ_Z is defined as $\frac{|Z_{\text{VBF}}^{\text{exp}} - Z_{\text{nom}}^{\text{exp}}|}{Z_{\text{nom}}^{\text{exp}}}$. The "Nominal "top background uncertainty is not included in the fit when the impact of other contributions is tested.

value $Z_{\text{VBF}}^{\text{exp}}$ for $\approx 2\%$. Combining the uncertainties due to PS/UE and ISR/FSR with the nominal top systematic uncertainty increases the impact on $Z_{\text{VBF}}^{\text{exp}}$ from 7% to 10%.

7.2.3 The VBF production mode in the VBF BDT analysis

The nominal $H \to WW^{(*)}$ VBF analysis is based on the boosted decision tree. A decision tree is a collection of cuts defined to classify events as signal-like or background-like. The output of the decision tree training is the BDT score, which yields $+1$ if the events are 100% signal-like, -1 if the events are 100% background-like, and zero if the events are not classified. Events which are misidentified after the first tree is grown are fed into the second tree. This proceeds iteratively until thousand trees are grown through the process known as *boosting*. A weighted average of all BDT scores, $\mathcal{O}_{\text{BDT}}$, is taken as the final output of the BDT VBF analysis and is required to be greater than -0.48. The event selection for the VBF BDT analysis can be found in Appendix, Section A.

The statistical fit is performed on the BDT response distribution, which summarises the separation power of all BDT input variables. In order to fully benefit from the BDT separation power, the number of bins in the $\mathcal{O}_{\text{BDT}}$ distribution has been optimised and the boundaries of the three bins are

$$\mathcal{O}_{\text{BDT}}: \quad [-0.48, 0.3],\ [0.3, 0.78],\ [0.78, 1.0].$$

The signal region in the VBF BDT analysis is split by lepton flavour and further divided according to the BDT bin boundaries, in total yielding six signal regions. The background normalisation in the SRs is using MC expectations, except for the top and Drell-Yan backgrounds, where data-driven techniques are used. Figure 54 shows the $\mathcal{O}_{\text{BDT}}$ and m_T distributions for the VBF BDT analysis.

Total top syst. uncertainty	$Z_{\mathrm{VBF}}^{\mathrm{exp}}$	$\Delta Z_{\mathrm{VBF}}^{\mathrm{exp}}$		$\Delta Z_{\mathrm{VBF}}^{\mathrm{exp}} / Z_{\mathrm{VBF}}^{\mathrm{exp}}$	Δ_Z
with CJV in top CR:					
Nominal					
• $(22\%, 10\%, 10\%) = 26\%$	1.996	$+0.065$	-0.066	7%	0.1%
Nominal, including all Δ MC contributions					
• $(28\%, 10\%, 10\%) = 31\%$	1.991	$+0.075$	-0.077	8%	0.2%
Nominal + PS					
• $(22\%, 10\%, 10\%, 17\%) = 31\%$	1.991	$+0.075$	-0.077	8%	0.2%
Nominal + ISR/FSR					
• $(22\%, 10\%, 10\%, 28\%) = 38\%$	1.983	$+0.088$	-0.090	9%	0.6%
Nominal + PS + ISR/FSR					
• $(22\%, 10\%, 10\%, 17\%, 28\%) = 42\%$	1.978	$+0.095$	-0.097	10%	0.9%
no CJV in top CR:					
Nominal					
• $(53\%, 10\%, 10\%) = 55\%$	1.962	$+0.114$	-0.117	12%	1.7%
Nominal, including all Δ MC contributions					
• $(74\%, 10\%, 10\%) = 75\%$	1.939	$+0.137$	-0.142	14%	2.8%

Table 30.: Impact of the total top systematic uncertainty on the expected VBF signal significance $Z_{\mathrm{VBF}}^{\mathrm{exp}}$, extracted from the final fit model in combined $e\mu/\mu e$ and $ee/\mu\mu$ final states, for the $m_H = 125.36\,\mathrm{GeV}$ Higgs boson mass hypothesis. In this case "Nominal" uncertainty refers to the quadratic sum of generator modelling, QCD and PDF uncertainties (see Table 22) and results in $Z_{\mathrm{nom}}^{\mathrm{exp}} = 1.996$. The symbol Δ_Z is defined as $\frac{|Z_{\mathrm{VBF}}^{\mathrm{exp}} - Z_{\mathrm{nom}}^{\mathrm{exp}}|}{Z_{\mathrm{nom}}^{\mathrm{exp}}}$. The symbol Δ MC refers to all considered generator modelling uncertainties (see Table 19).

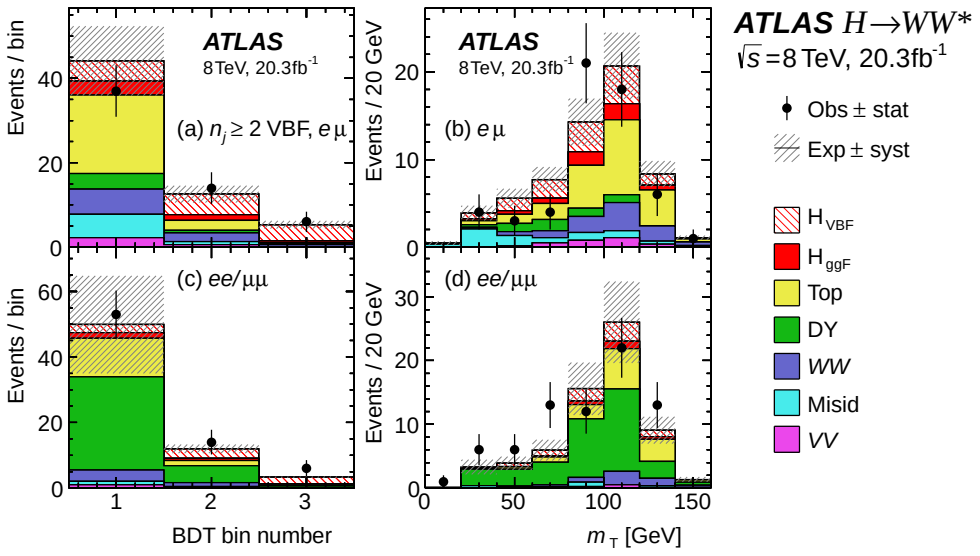

Figure 54.: The post-fit $\mathcal{O}_{\mathrm{BDT}}$ distribution (left) and m_T distribution (right) for $e\mu/\mu e$ (top) and $ee/\mu\mu$ (bottom) final states in the VBF BDT analysis.

The ggF background prediction is profiled from the global fit (different to the cut-based VBF results, where the ggF contribution is taken from the SM) combining ggF and VBF analyses together with the extraction of the signal strength for the VBF production. Figure 55 shows the global likelihood function for the combined 2011+2012 dataset, evaluated as a function of the $\mu_{\mathrm{VBF}}/\mu_{\mathrm{ggF}}$ ratio where both signal strengths are varied independently. The best fit value for the $\mu_{\mathrm{VBF}}/\mu_{\mathrm{ggF}}$ ratio at $m_H = 125.36\,\mathrm{GeV}$, is

$$\frac{\mu_{\mathrm{VBF}}}{\mu_{\mathrm{ggF}}} = 1.26\,^{+0.61}_{-0.45}\ (\mathrm{stat.})\ ^{+0.50}_{-0.26}\ (\mathrm{syst.}) = 1.26^{+0.79}_{-0.53}. \tag{102}$$

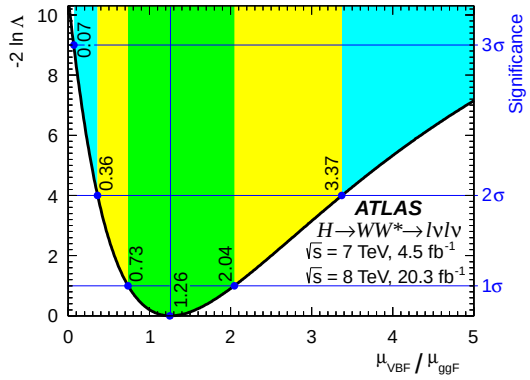

Figure 55.: The global likelihood scan as a function of the $\mu_{\mathrm{VBF}}/\mu_{\mathrm{ggF}}$ ratio for $m_H = 125.36\,\mathrm{GeV}$. The green (yellow) (blue) band represents one (two) (three) standard deviation uncertainty around the central value. The observed signal significance is evaluated for $\mu_{\mathrm{VBF}}/\mu_{\mathrm{ggF}} = 0$ and yields to $3.2\,\sigma$.

The expected significance for the VBF Higgs production process, as observed in the BDT analysis, is $2.7\,\sigma$ and the observed significance[3] results in 3.2 standard deviations, confirming the *evidence* for the VBF production mode in the $H \to WW^{(*)} \to \ell^+\nu_\ell\ell^-\bar{\nu}_\ell$ channel.

Both, the cut-based and the BDT, VBF analyses confirm the evidence for the VBF production in the $H \to WW^{(*)} \to \ell^+\nu_\ell\ell^-\bar{\nu}_\ell$ channel, which has never been observed before. Table 31 shows the comparison between the expected and observed significances for the cut-based and BDT VBF analyses as obtained from the combined fit. The BDT analysis improves the sensitivity of the expected results by $\approx 30\%$ with respect to the cut-based result, and by $\approx 60\%$ with respect to the previously published VBF results [86, 123]. The improvement of the BDT analysis over the cut-based analysis for the observed signal significance is $\approx 6\%$.

The compatibility between the cut-based and BDT analyses is checked with pseudo-experiments, and the differences in the $Z^{\mathrm{obs}}_{\mathrm{VBF}}$ between the two analyses in pseudo-experiments are in 79% larger than the differences observed between the cut-based and the BDT data analysis, establishing a good agreement between the two analyses.

3 The observed significance is evaluated at $\mu_{\mathrm{VBF}}/\mu_{\mathrm{ggF}} = 0$, which is equivalent to the significance measurement assuming the background-only hypothesis ($\mu_{\mathrm{VBF}} = 0$) and proves that a fraction of events is indeed produced through VBF. The advantage of this procedure is the cancellation of the Higgs branching fraction in the $\mu_{\mathrm{VBF}}/\mu_{\mathrm{ggF}}$ ratio.

VBF analysis	$Z_{\mathrm{VBF}}^{\mathrm{exp}}$	$Z_{\mathrm{VBF}}^{\mathrm{obs}}$
cut-based	2.1	3.0
BDT	2.7	3.2
cut-based [86]	1.6	2.5

Table 31.: Comparison of the expected and observed signal significances in both VBF analyses; the nominal BDT analysis and the cross-check cut-based analysis for the $m_H = 125.36\,\mathrm{GeV}$, obtained from the combined fit, including 2011+2012 datasets. The expected ggF event yields were obtained from the fit. The value from the previously published (cut-based) VBF analysis [86] is also included for comparison.

7.2.4 Combined VBF and ggF Experimental Results

The $H \to WW^{(*)}$ analysis probes for the ggF production mode in the $n_j = 0$ and $n_j = 1$ channels. In addition, a non-negligible contribution of the ggF events is found in the $n_j \geq 2$ category as well and in order to fully exploit the signal significance measurement, an analysis focusing on ggF+2jets events in $e\mu/\mu e$ channel is also performed, where this time VBF production is considered as a background. All analyses are cut-based. The ggF event selection in all three jet categories is described in Appendix, Section A.

The combined results contain 2011 and 2012 datasets in all $H \to WW^{(*)}$ categories; ggF production for $n_j = 0, 1, \geq 2$ channels and the VBF (BDT) production in $n_j \geq 2$ channel. This combination improves the sensitivity of the expected significance by $\approx 50\%$, with respect to the previously published results [123].

All jet categories probing for the ggF production mode use the m_T distribution as the final discriminant in the fit. Figure 56 shows the m_T distribution for ggF analysis in $n_j \leq 1$ and $n_j \geq 2$ categories.

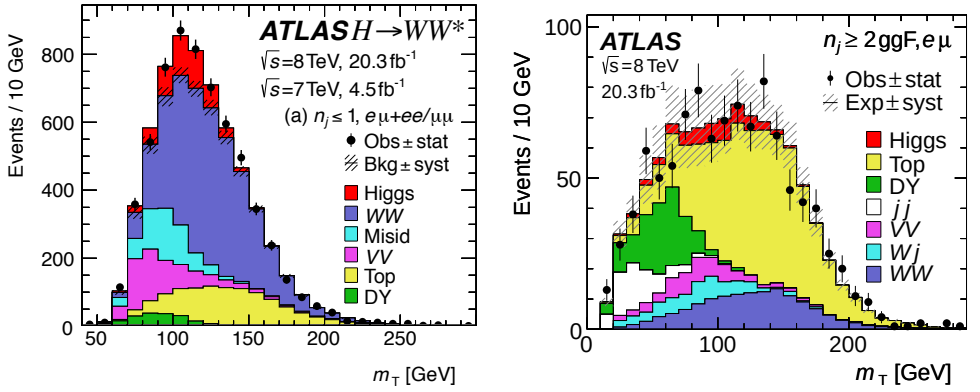

Figure 56.: The m_T distribution in channels probing the ggF produciton mode: in the combined $e\mu/\mu e + ee/\mu\mu$, $n_j \leq 1$ channel for $8 + 7\,\mathrm{TeV}$ data (left) and in the $e\mu/\mu e$ $n_j \geq 2$ channel for $8\,\mathrm{TeV}$ data (right).

The significance of the observed excess in data is evaluated by the profile likelihood fit, combining all lepton flavours and all jet categories. Figure 57 shows the local p_0-value as a function of m_H with a minimum around $m_H \approx 130\,\mathrm{GeV}$. This corresponds to the observed

signal significance of 6.1 σ, where 5.8 σ is expected, establishing a *discovery* of the Higgs boson signal in the $H \to WW^{(*)} \to \ell^+\nu_\ell\ell^-\bar{\nu}_\ell$ channel alone.

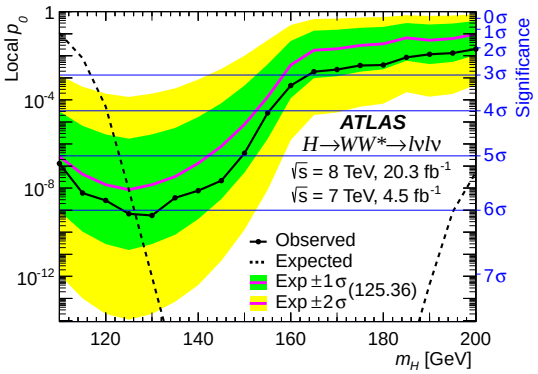

Figure 57.: The expected (dashed line) and observed (solid line) local p_0 value as a function of m_H. The magenta solid line represents the expected p_0 for $m_H = 125.36\,\text{GeV}$.

Figure 58 (left) shows the observed *best-fit* signal strength $\hat{\mu}$ as a function of m_H. In this case, m_H is also included as a parameter of interest in the fit, alongside $\hat{\mu}$, testing which combination of $\hat{\mu}$ and m_H are the most favoured by the data. The observed $\hat{\mu}$ is close to zero for $m_H > 160\,\text{GeV}$, and equals to one around $m_H \approx 125\,\text{GeV}$. The increase in $\hat{\mu}$ for lower Higgs masses is due to the poor mass resolution in the $\ell\nu\ell\nu$ channel and a lower branching ratio for the $H \to WW^*$ at lower m_H and does not indicate that the observed signal is 5× the SM prediction for $m_H = 115\,\text{GeV}$. The best-fit values for $\hat{\mu}$ and m_H are $\hat{\mu} = 0.94$ at $m_H = 128\,\text{GeV}$. Figure 58 (right) shows a 2D likelihood contour plot portraying the observed signal strength μ as a function of m_H. The expected SM signal strength ($\mu = 1$) at $m_H = 125.36$ lies well within the 68% C.L. of the observed best-fit values, pointing to a great compatibility between the observed values and the SM prediction.

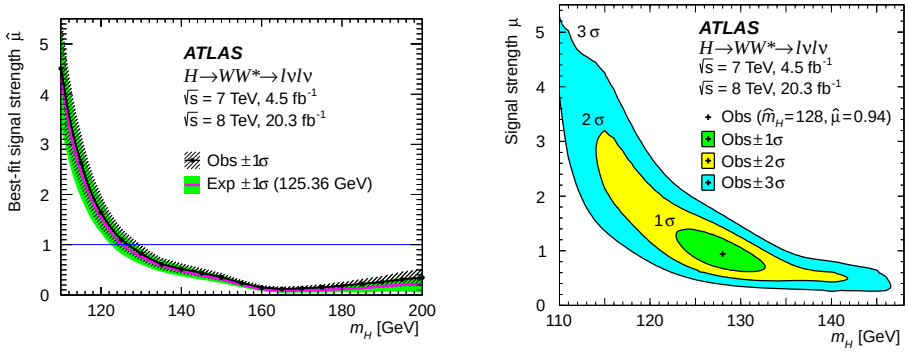

Figure 58.: The best-fit signal strength $\hat{\mu}$ as a function of m_H (left) and a 2D likelihood contour plot showing μ as a function of m_H (right) with respect to the best-fit value $\hat{\mu} = 0.94$ at $m_H = 128\,\text{GeV}$.

The signal strength for the combined 2011 and 2012, ggF and VBF data at $m_H = 125.36\,\text{GeV}$, is

$$\mu = 1.09\,^{+0.16}_{-0.15}\,(\text{stat.})\,^{+0.17}_{-0.14}\,(\text{syst.}) = 1.09\,^{+0.23}_{-0.21}\,. \tag{103}$$

In this case, the systematic and statistical uncertainties have similar impacts. Since the ggF and VBF production modes are sensitive in different signal regions, they can be independently and simultaneously obtained through the combined fit. Their values at $m_H = 125.36\,\text{GeV}$ are

$$\begin{aligned} \mu_{\text{VBF}} &= 1.27\,^{+0.44}_{-0.41}\,(\text{stat.})\,^{+0.30}_{-0.21}\,(\text{syst.}) = 1.27\,^{+0.53}_{-0.45}\,, \\ \mu_{\text{ggF}} &= 1.02 \pm 0.19\,(\text{stat.})\,^{+0.22}_{-0.18}\,(\text{syst.}) = 1.02\,^{+0.29}_{-0.26}\,. \end{aligned} \tag{104}$$

The μ_{VBF} is mostly dominated by its statistical uncertainties, while the ggF production mode has systematic and statistical uncertainties of the same order. Figure 59 shows their 2D likelihood contour.

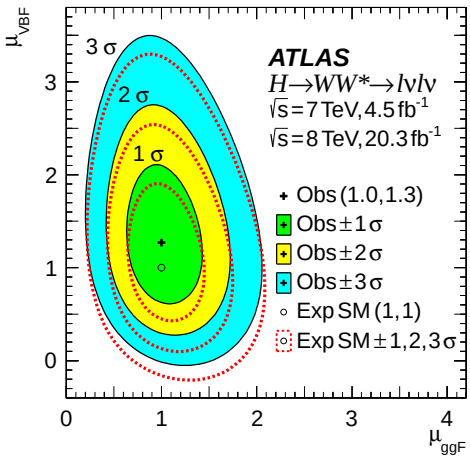

Figure 59.: A 2D likelihood contour of μ_{VBF} versus μ_{ggF} comparing observed and expected values. The best-fit observed value is presented by a cross symbol while the open circle represents the SM expected value.

7.2.5 Couplings of the Higgs boson with vector bosons and fermions

The measurement of the signal strength is model dependent and assumes specific production cross-sections and decay branching ratios for the Higgs boson. Possible deviations between the discovered Higgs boson particle and the SM predictions can be observed through the *couplings* of the Higgs boson with individual SM particles in a model independent way. The method estimating the compatibility of measured signal strengths with the SM predictions

is described in [124]. The parametrisation[4] from [124] introduces *coupling scale factors* κ, for each Higgs production/decay process

$$\kappa_i^2 = \frac{\sigma_{ii}}{\sigma_{ii}^{SM}} = \frac{\Gamma_{ii}}{\Gamma_{ii}^{SM}}, \tag{105}$$

where i indicates each SM particle that couples to the Higgs boson. If a Higgs coupling with the SM particle agrees with the SM prediction, its coupling scale factor κ_i equals one.

The $H \to WW^{(*)}$ analysis probes Higgs couplings to fermions and vector bosons. A scale factor is applied to each coupling respectively; κ_F is applied to all fermionic couplings and κ_V to all bosonic couplings. Following [124], the ggF and VBF signal strengths are proportional to

$$\begin{aligned} \mu_{\text{VBF}} &\propto \frac{\kappa_V^4}{(\mathcal{B}_{H\to f\bar{f}} + \mathcal{B}_{H\to gg})\kappa_F^2 + (\mathcal{B}_{H\to VV})\kappa_V^2}, \\ \mu_{\text{ggF}} &\propto \frac{\kappa_F^2 \cdot \kappa_V^2}{(\mathcal{B}_{H\to f\bar{f}} + \mathcal{B}_{H\to gg})\kappa_F^2 + (\mathcal{B}_{H\to VV})\kappa_V^2}. \end{aligned} \tag{106}$$

The ggF $H \to WW^{(*)}$ signal strength probes both couplings; κ_F through heavy quark loops in the production vertex and κ_V through Higgs boson decay to WW in the decay vertex, while the VBF production only probes κ_V. Both denominators in Equation 106 represent the total SM decay width of the Higgs boson, considering only fermionic and bosonic decays[5]. Since $(\mathcal{B}_{H\to f\bar{f}} + \mathcal{B}_{H\to gg}) \approx 0.75$, the κ_F^2 factor in the denominator prevails over κ_V^2 (for $\kappa_V^2 \lesssim 3\kappa_F^2$), almost cancelling the κ_F^2 contribution from μ_{ggF} and making the μ_{VBF} the main contribution for estimating the coupling of the Higgs boson to fermions. Additionally, since both signal strengths are proportional to κ^2, the $H \to WW^{(*)}$ decay is not sensitive to the sign of κ, but only on its magnitude.

Figure 60 shows a likelihood scan for both coupling scale factors, with the best-fit values equal to

$$\begin{aligned} \kappa_F &= 0.93^{+0.24}_{-0.18}\,(\text{stat.})\,^{+0.21}_{-0.14}\,(\text{syst.}) = 0.93\,^{+0.32}_{-0.23}\,, \\ \kappa_V &= 1.04^{+0.07}_{-0.08}\,(\text{stat.})\,^{+0.07}_{-0.08}\,(\text{syst.}) = 1.04 \pm 0.11\,. \end{aligned}$$

Both scale factors are equal to unity within the uncertainties, indicating a good agreement with the SM prediction.

7.3 Conclusions

The $H \to WW^{(*)}$ analysis, described in this thesis, delivered several "discoveries". First and foremost, the evidence for the production of the Higgs particle via vector boson fusion in the $H \to WW^{(*)}$ channel has been observed for the first time with $3.2\,\sigma$ and $3.0\,\sigma$ for the BDT and cut-based VBF analyses, respectively. Second, the Higgs boson with $m_H \approx 130\,\text{GeV}$ has

4 This method uses the following approximations: All the signal originates from a single resonance with $m_H = 125\,\text{GeV}$ and a negligible width so that the production and decay process are independent and can be factorised. The Higgs boson is a CP-even scalar as predicted by the SM and only absolute values of the couplings are taken into account, while their tensor structure is assumed to be the same as in SM.

5 The small contribution to $H \to \gamma\gamma$ depends on both κ_F and κ_V but is not explicitly shown in Equation 106 [124].

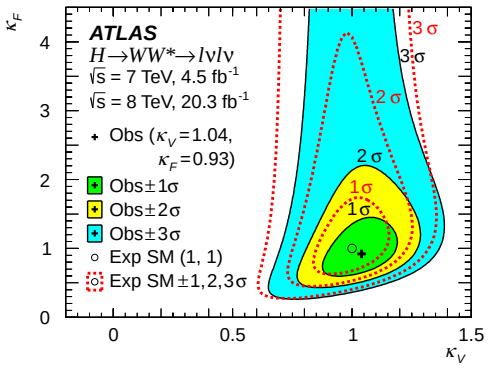

Figure 60.: A 2D likelihood scan as a function of κ_F and κ_V. The cross symbol indicates the observed best fit value, and the open circle indicates the SM prediction.

been discovered with $6.1\,\sigma$ in the $H \to WW^{(*)} \to \ell^+\nu_\ell\ell^-\bar{\nu}_\ell$ channel alone. Finally, all the measurements of the signal strengths and Higgs couplings to vector bosons and fermions agree with the SM predictions within uncertainties.

In current measurements, the results are still largely dominated by the statistical uncertainties, in particular for the VBF production mode. However, in the next decade, the ATLAS detector and the LHC accelerator will undergo various upgrades in order to prolong and improve their performance for the higher luminosity scenarios, which are described in the next chapter, Chapter 8. Future runs will bring more data and consequently reduce the currently limiting statistical uncertainties. It is thus extremely important to understand and reduce all sources of systematic uncertainties on the background predictions and of the detector response, so that future analyses can test the presence of New Physics with higher sensitivities.

Several feasibility studies have been performed to study the improvements in the sensitivity of various measurements at the upgraded ATLAS detector. One of such studies has been performed under the scope of the European Committee for Future Accelerators (ECFA), studying the improvements in the $H \to WW^{(*)}$ signal strength measurement at 300 fb^{-1} and 3000 fb^{-1} with the upgraded ATLAS detector, and is presented in Chapter 9.

Part II.

FUTURE RUNS AT THE LHC

8 UPGRADE OF THE ATLAS DETECTOR

By the end of spring 2015, the first long shut down (LS1) of the LHC was successfully concluded and the first collisions at $\sqrt{s} = 13\,\text{TeV}$ are being recorded. During the LS1, among other procedures, the interconnections between the superconducting magnets at the LHC were consolidated, the PS and SPS were upgraded and additional protective shielding was added to the electronic equipment. These upgrades allow the LHC to continue its operation near its design parameters: $\sqrt{s} = 13\text{-}14\,\text{TeV}$, 25 ns bunch spacing and luminosity up to $1 \cdot 10^{34}\,\text{cm}^{-2}\text{s}^{-1}$, which will deliver approximately 150 fb^{-1} by the end of the Run-2 (2019).

The ATLAS detector used the LS1 to replace the beam pipe and add an additional pixel layer around it - the insertable B layer (IBL). Other major upgrades include the installation of the missing MS components, upgrade of luminosity monitors (DBM) and other consolidation works (new ID cooling, upgraded magnet cryogenics, etc.)

In order to extend the operation of the LHC even further, strengthen our knowledge of the SM and expand the searches for New Physics, two additional upgrade stages are planned for the next decade, with the schedule shown in Figure 61. The LS2 starting in 2019 will

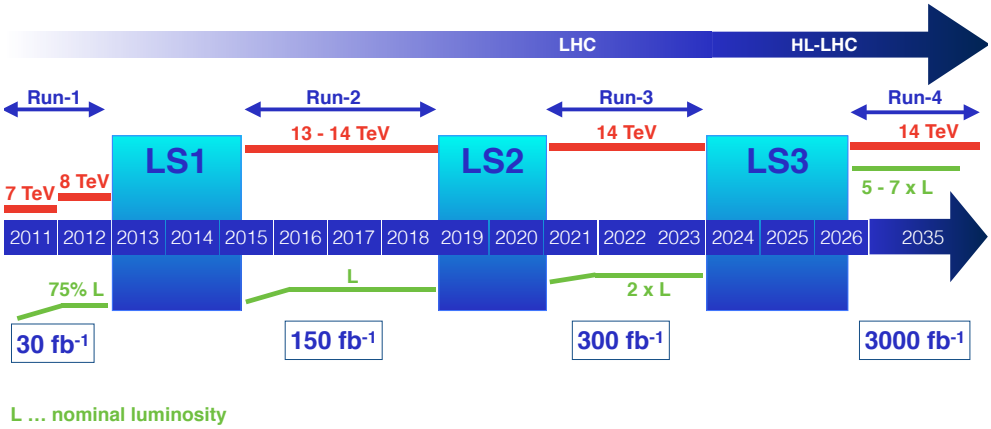

Figure 61.: The time-line of the scheduled upgrades at the LHC [125]. The schematic was adapted from [126].

prepare the LHC and its experiments for luminosities up to $300\,\text{fb}^{-1}$ and the LS3, starting in 2024, will push the LHC into the so-called High-Luminosity phase (HL-LHC), in which luminosities up to $3000\,\text{fb}^{-1}$ could be recorded. To bring these numbers into perspective: all the hadron colliders in the world before the start of the LHC recorded $\approx 10\,\text{fb}^{-1}$, while the LHC delivered almost three times more in the first two years of its operations and it plans to deliver up to three hundred times more by 2035.

This chapter describes the upgrades of the ATLAS detector: Section 8.2 summarises the key improvements during the Phase-I and Phase-II upgrades, Section 8.3 is dedicated to the

upgrade of the Inner Detector during LS3, and Section 8.4 to a possible upgrade scenario where the ATLAS tracking capabilities are extended up to $|\eta| \leq 4.0$.

8.1 Motivation for upgrades

The SM came out triumphant in the Run-1 data-taking - all the analyses done with the 7 TeV and 8 TeV data point to the fact that the discovered Higgs boson is indeed the SM one. Unfortunately (or fortunately for us physicists) the SM Higgs boson at $m_H = 126.5\,\text{GeV}$ does not answer all the fundamental questions, like: Why is the Higgs boson so light? What is dark matter? How does gravity fit in with the remaining forces?...

The main motivation for the HL-LHC is of course looking for answers on these questions. Running the accelerator with its design luminosity will give only marginal statistical gain after 2019[1] and in order to find these answers a substantial increase in luminosity is required. The following list presents some of the interesting processes which cannot be studied without the planned upgrades:

- The HL-LHC will be a Higgs factory, producing over a million of non-hadronically decaying Higgs bosons ($\approx$1500 Higgs events were recorded during Run-1) and allowing for precision measurements of its properties (mass, width, spin and CP), self-couplings and couplings to the other SM particles, where discrepancies from the SM predictions can point to contributions from New Physics.
- Rare Higgs boson decays, like $H \to \mu\mu$, where a $5\,\sigma$ discovery can be reached only with $3000\,\text{fb}^{-1}$ [127].
- Exploring the TeV scale for new particles, like Z'.
- Studying the longitudinal vector boson scattering (VBS) at higher energies which is one of the key processes towards a deeper understanding of the EWSB.
- An increased sensitivity for direct searches of New Physics, e.g. with 3000 fb^{-1} top-squark searches increase their sensitivity by 20% [128].

Various studies explored the prospects of the upgraded ATLAS detector and two of them are explicitly described in this thesis. Chapter 9 is dedicated to the VBF $H \to WW^{(*)}$ measurement at the HL-LHC and Chapter 10 describes the benefits of the extended tracking for an analysis studying the WW scattering.

8.2 ATLAS detector upgrades

Table 32 summarises the main characteristics of the Phase-I and Phase-II upgrades compared to the design LHC parameters and Run-1 values.

An increase in luminosity causes an increase in the average number of interactions per bunch crossing, higher event rates and detector occupancies, and harsher radiation environment especially for the detector components closest to the beam pipe. These are the challenges that the ATLAS detector will need to address in order to continue its operation. In addition, the most intriguing physics processes require similar (or better) detector performance as in the Run-1, even under such conditions: among others are low-p_{T} (20 GeV) single

1 After 2019, running the LHC with $1 \cdot 10^{34}$ fb^{-1} will require more than 10 years to halve the statistical uncertainties.

	LHC design	Run-1	Run-2	Run-3	Run-4
Center of mass energy [TeV]	14	$7-8$	$13-14$	14	14
Integrated Luminosity during operation time [fb^{-1}]	~ 500	~ 27	150	300	3000
Luminosity [$10^{34}\,\mathrm{cm}^{-2}\mathrm{s}^{-1}$]	1	< 0.7	1	2 - 3	5 - 7
Pileup $\langle\mu\rangle$	19	< 21	~ 30	50 - 80	140 - 200
Bunch Spacing [ns]	25	150, 50	25	25	25

Table 32.: Design specifications of the LHC [52], parameters obtained during the Run-1 operation [53], projections for the Run-2 (2016) operation [125] and the foreseen LHC parameters for the Run-3 [129] and Run-4 [130] operations.

isolated lepton triggers, good lepton momentum resolution up to high p_T and a good identification of heavy flavours, multi-jets and E_T^{miss} signatures.

The changes in the ATLAS detector towards the HL-LHC will come gradually; the Phase-1 upgrade will mostly focus on upgrading the trigger (Level-1) and muon systems, while the main challenge of the Phase-2 upgrade is the replacement of the Inner Detector. Both phases are described below and summarise the main upgrades as described in their Letters of Intent (LoI) [129, 130] and from the available Technical Design Reports (TDR) [131–133].

8.2.1 Phase-I upgrade

In 2019, the LHC will undergo the second long shut-down in order to prepare the accelerator and its experiments for the Run-3 data-taking. The upgrades of the LHC include the integration of Linac4 into the injector complex, energy increase of the PS Booster, reduction in the beam emittance and upgrade of the collimation system [129]. These procedures will allow for the experiments to reach luminosities up to $2\text{-}3 \cdot 10^{34}\,\mathrm{cm}^{-2}\mathrm{s}^{-1}$, with $\langle\mu\rangle = 50-80$ interactions per bunch crossing, and by the end of the Run-3 operation (2022), collect up to $300\,\mathrm{fb}^{-1}$ of integrated luminosity. The ATLAS detector will adjust to these conditions by upgrading its hardware (Level-1) trigger through the upgrades described in the following paragraphs.

Upgrades of the Muon Spectrometer:

The performance of the muon tracking chambers degrades at higher luminosities, especially in the end-cap region, due to higher background fluxes. In order to cope with such conditions and maintain the current performance, the first end-cap station of the MS (muon small wheels) will be replaced with the New Small Wheel (NSW). The NSW will incorporate two chamber technologies: small-strip TGCs which will integrate the NSW into the Level-1 trigger system and MicroMegas (MM) detectors for precision tracking. The sTGCs will perform a real-time segment reconstruction at every bunch crossing and provide precise track positions and angular resolutions. The MMs will help maintain the current ATLAS muon p_T resolution even at higher luminosities.

Upgrades of the Calorimeter System:

Increasing the granularity of the LAr Level-1 Trigger will improve its performance at higher luminosities. The 10-fold increase in granularity will be achieved by digitising the currently analogue trigger readout scheme. This will improve trigger energy resolution and object selection efficiencies, provide a better discrimination against backgrounds, improve the E_T^{miss} resolution and allow for electron shower shape analyses.

Fast TracK Trigger (FTK):

The FTK is an electronic system that will be able to perform global track finding and reconstruction for events passing the Level-1 trigger and provide an early access of tracking information (with resolutions close to the off-line ones) to the Level-2 trigger. Through its powerful parallel processing, the FTK will release the current Level-2 CPU constraints and consequently allocate more resources for the more advanced selection algorithms which will improve the heavy flavour tagging.

Upgrades of the Trigger and Data Acquisition systems:

The upgrades of the MS and LAr will improve the performance of the Level-1 trigger, which will still operate within the current detector latency (2.5 μs) and trigger rate (up to 100 kHz). The High-Level Trigger (HLT) selection software will be upgraded to minimize the average per-event processing time and avoid long execution times. No bigger changes are proposed for the Data Acquisition architecture but an increase in its bandwidth may be necessary to include the information from the NSW, upgraded LAr and the FTK.

8.2.2 Phase-II upgrade

During the 10 year long Run-4, the LHC will deliver up to 3000 fb^{-1}. In order to achieve such a high integrated luminosity, all the LHC's components damaged by the radiation will be replaced and stronger (up to 13 T) focusing magnets will be installed at the ATLAS and CMS interaction points. Additionally, in order to deliver maximal possible luminosities during the HL-LHC run-time, crab cavities (ensuring quasi-head-on bunch collision at the IP) and luminosity levelling will be applied (for further details see [134] and references within).

The increase in luminosity to $7 \cdot 10^{34}\,\text{cm}^{-2}\text{s}^{-1}$ will result in $\langle\mu\rangle = 140 - 200$ pileup events and the HL-LHC requires a detector that is capable of operating in conditions with such large particle fluxes and deliver the required performance. The Phase-II upgrade procedures will prepare the ATLAS detector for the HL-LHC conditions and are described below.

Upgrades of the Trigger System:

Several upgrades of the Trigger system are envisioned, the main one being the split of the hardware trigger (Level-1 at Phase-I) to the Level-0 and Level-1 triggers. The Level-0 trigger will accept event rates from the calorimeter and MS at 500 kHz, within a latency of 6 μs, and will also incorporate topological triggering capabilities. Its functionality is the same as the Phase-I Level-1 trigger. The Phase-II Level-1 trigger will reduce the Level-0 trigger rate[2] to 200 kHz within the latency of 14 μs. Such a reduction in the triggering rate is made possible by introducing track information within a Region-of-interest (RoI), full calorimeter granularity within the same RoI and a refined muon selection. The trigger electronics in the MS and calorimeters will need to be upgraded as well to face such high trigger rates. Upgrades of the Data Acquisition architecture and development of a new HLT selection software are under consideration.

2 The performance assumptions for the ATLAS detector at the HL-LHC are not yet final and several changes were already made to the baseline LoI features. One of them is doubling the Level-0 and Level-1 trigger rates to 1 MHz and 400 kHz, respectively.

Upgrades of the Calorimeter System:

Due to the radiation damage and higher trigger rates at the HL-LHC, the LAr and Tile Calorimeter electronics will have to be completely replaced[3]. Two scenarios are additionally considered for the upgrade of the FCal: either completely replacing the FCal with the higher-granularity sFCal, or installing a MiniFCal calorimeter in front of the current FCal, to reduce the particle fluxes on it and keep its performance at desired levels. Adding a precision timing detector (tens of ps) in front of the LAr end-cap that would measure arrival times of charged particle tracks, will allow ATLAS to develop algorithms for local pile-up subtraction on an event-by-event basis.

Upgrades of the Muon System:

The upgrade of the MDT readout system and muon trigger electronics is foreseen in order to maintain desired spatial resolution, tracking efficiency and selectivity for high-p_T tracks.

Upgrades of the ATLAS Software:

The biggest challenge so far is to integrate the simulation of the Phase-II upgrades into the existing framework. In addition, the ATLAS simulation at the HL-LHC will be more memory and CPU demanding and will have to perform under an increased event complexity. Therefore, optimisations of the current software and changes in computing architectures are under study.

Replacement of the Inner Detector:

The Inner Detector was designed with a life expectancy of 10 years for an operation at $\sqrt{s} = 14\,\text{TeV}$ with a peak luminosity of $1 \cdot 10^{34}\,\text{cm}^{-2}\text{s}^{-1}$. The electronics were designed to cope with up to 100 kHz hardware trigger rate and the detector elements were designed to sustain an integrated luminosity of $700\,\text{fb}^{-1}$. Even though the ID performed extremely well during the Run-1 of the ATLAS data-taking (and will continue its excellent operation also during the Run-2 and Run-3), it would not sustain the environment at the HL-LHC and is therefore going to be completely replaced by a new, all-silicon based[4] tracking system, which is described in the next section.

8.3 The new Inner TracKer

The new Inner TracKer (ITk) consists of pixel layers (placed at inner radii) that are surrounded by a strip detector. Its baseline LoI layout is shown in Figure 62. In the central region, the sensors are arranged in cylinders with 4 pixel layers followed by 3 short-strip (23.8 mm) layers and 2 long-strip (47.8 mm) layers. The short "stub" layer is placed between the last two long-strip layers to cover the loss in acceptance at the transition towards the end-caps. The forward region is covered by 6 pixel disks and 7 strip disks. This layout guarantees at least 11 hits per track at $|\eta| \leq 2.5$, less than 1% channel occupancy at $\langle\mu\rangle = 200$ and less material (a factor 5 reduction compared to the ID). Due to the increased granularity (smaller pixel sensors and short inner strips) the ITk provides a better two-particle separation and fake-track rejection and a better signal-to-noise ratio. A slightly larger outer active radius

3 Except for the HEC cold electronics which are not foreseen to be replaced.

4 The occupancies in the TRT will reach very high levels at the HL-LHC, which would severely compromise the tracking performance, therefore the TRT will be removed from the ATLAS detector during the LS3 and its functionality will be partially covered by the silicon based strip detector.

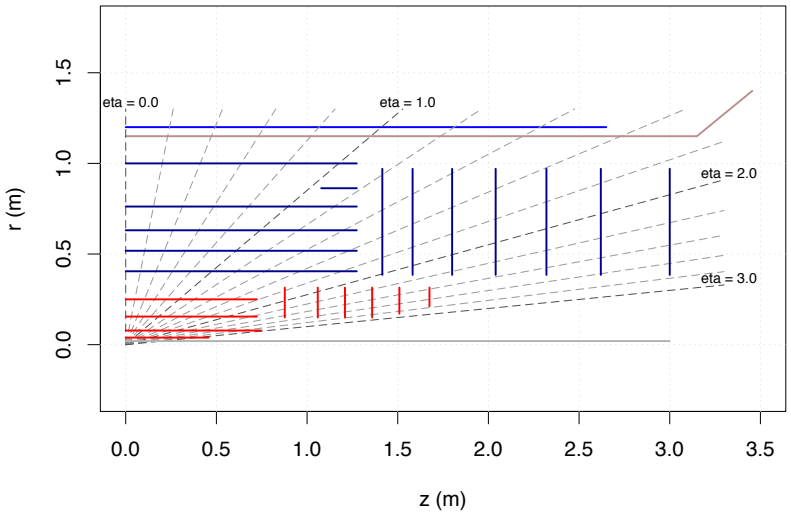

Figure 62.: The ITk baseline LoI layout [130]; the pixel system is shown in red and the strip tracker in blue. The gaps between sub-detectors are there for services and support structures.

improves the momentum resolution and more evenly spaced silicon layers, especially in the forward region, improve the track reconstruction.

Current performance studies of the ITk LoI layout show very encouraging results: the light-jet rejection rates at $\langle\mu\rangle = 140$ are comparable to the rejection rates of the ID+IBL at zero pileup [130], the simulated tracking efficiencies show a significant improvement with respect to the ID [135] and in addition, tracking and vertexing is stable with increasing pileup [130, 133].

8.3.1 Pixels at the ITk

The pixel system in the ITk LoI layout is composed of four barrel layers with radii from 39 mm up to 250 mm, and six end-cap disks with z-coordinates from $\pm$877 mm up to $\pm$1675 mm. The pixel sensors are less than 150 μm thick. The two innermost layers have smaller pixels with 25×150 μm^2 granularity and the remaining barrel layers and the end-cap disks have a larger granularity of 50×250 μm^2, in total resulting in 8.2 m^2 of active silicon pixel area with 638 million readout channels.

The baseline ITk LoI layout has some shortcomings related to the routing of the services for the pixel detector and several modifications are under study. Figure 63 shows a few alternatives: the Pixel Ring layout solves the problem by replacing solid pixel disks with open pixel rings. In the Conical layout, the mechanical support on which the barrel pixel sensors are mounted is bent inwards towards the beam pipe, changing the position and orientation of the pixel modules which allows for a larger spacing between the barrel and end-cap pixel systems. In the Alpine layout, the pixel sensors are placed at an increasing inclination angle above $|\eta| \sim 2.25$, which results in an ideal sensor orientation where each sensor is perpendicular to the direction of the incoming particles and less material.

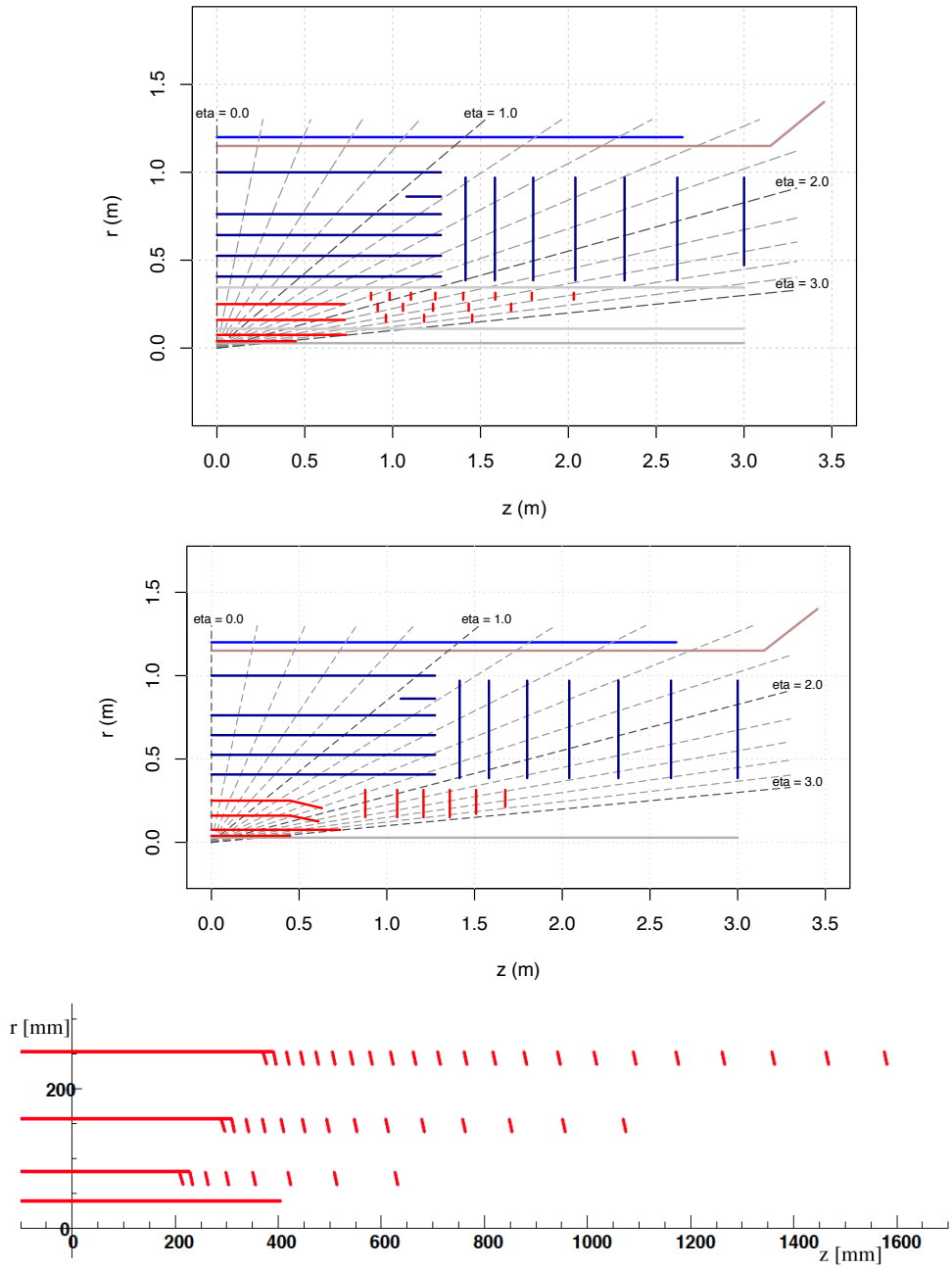

Figure 63.: Various ITk layouts under study: Pixel Ring layout (top), Conical layout (middle) and the Alpine layout (bottom) [130].

8.3.2 Strips at the ITk

The ITk strip detector consists of a central barrel region and two end-caps, totalling 193 m^2 of active silicon strip area with 74 million readout channels.

Strip Barrel

In the ITk LoI layout, the strip barrel covers the region up to $|\eta| <\sim 1.1$ and consists of five full-length cylinders (2.6 m) with radii between 405 mm and 1000 mm and a short "stub" layer ($\sim$ 195 mm), placed between the last two cylinders, to cover the gap in acceptance between the barrel and the end-caps. Barrel layers consist of 472 full-length staves and each stave has 26 modules[5], 13 on each face. The stave is a basic mechanical structure and is shown in Figure 64. It provides rigidity and support for the modules and houses the services.

The barrel strip sensors are square-shaped with an area of 97.54×97.54 mm^2 and a thickness of 320 ± 15 μm. There are 1280 readout strips across each sensor, giving a strip pitch of 74.6 μm. The strips are parallel to each other and to the edges of the sensor. The strips on one face of a stave have an axial geometry, while a 40 mrad stereo angle between the strips is incorporated by rotating the modules on the other face of a stave.

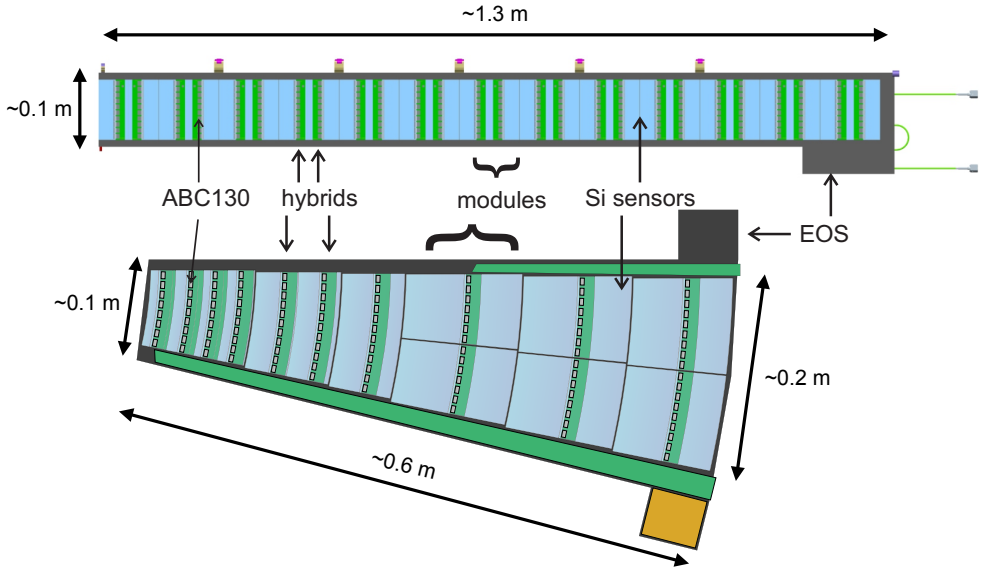

Figure 64.: The barrel stave structure (top) and the end-cap petal structure (bottom) for the ITk strip detector [130].

Strip End-caps

The ITk LoI strip detector has two identical end-caps, rotated by 180° with respect to each other, and covers the region between $1.2 \leq |\eta| \leq 2.7$. Each end-cap consists of 7 disks between $z = \pm 1415$ mm and $z = \pm 3000$ mm and each disk is built out of 32 identical

5 A module is a basic unit on a stave. Front-end readout chips (ABC130) are mounted on kapton circuits to make a readout hybrid and one or two hybrids are glued to the surface of a single-sided silicon sensor to form a module.

petals. The petal, shown in Figure 64, is a double-sided, wedge-shaped, mechanical structure (analogous to the stave) that spans from the inner to outer radius of the end-cap disk. Neighbouring petals are castellated in z. The petal has 6 rows of modules on each face: the first three rows have one module and the last three rows have two modules side by side, for a total of 9 modules of 6 different types.

In order to give an accurate measurement of the $r\phi$ coordinate, the strips on one side of the petal should have a radial geometry (pointing towards the beam line) and the strips on the other side should have a stereo geometry (rotated by a stereo angle). This supposes a *wedge-like* shape of the sensor. However, placing simple, symmetric trapezoidal modules (like in the SCT) on the petal structure and rotating them by a stereo angle would cause clashes at the corners of the neighbouring modules. The design, developed at Nikef [136], that circumvents these problems is the *N*-sensor and its cartoon is shown in Figure 65. The shape of the *N*-sensor is complex - it has two straight and tilted side edges and two curved edges.

The strips inside the *N*-sensor are implanted under a stereo angle of $+20$ mrad with respect to the radial direction (their focus is slightly displaced from the beam line - $\mathcal{O}(10$ mm$)$) and fan radially outwards between the two straight edges. Cutting the straight edges parallel to the strips guarantees the same focus point for the edges and the strips and avoids any clashes at the corners of the modules. In addition, since the sensors on the other side of the petal are rotated by 180° this automatically creates a 40 mrad stereo angle (strips on the other side of the petal are rotated by -20 mrad) and neither the petals nor the sensors need to be rotated any further. The curved *N*-sensor edges guarantee a uniform gap between consecutive modules, which is especially important at the transition from one to two modules per row[6]. Finally, the combination of the curved and straight edges parallel to the strips ensures the same length for all the strips and therefore the same noise and performance. This simplifies the bonding of the strips as well and avoids any dead areas inside the sensor.

As opposed to the current SCT sensor that has only one row of strips, the *N*-sensor is segmented into several rows of strips, depending on its type. The parameters of each sensor type are presented in Table 33.

Sensor type	R_i [mm]	R_o [mm]	Length [mm]	w_i [mm]	w_o [mm]	Number of Segments	Number of strips	Strip Length [mm]
1	384	489	105	77	98	4	1026, 1154	19, 24, 29 32,
2	489	575	86	98	115	4	1282, 1410	18, 27, 24, 15
3	575	638	63	115	127	2	1538	31, 31
4	638	756	118	64	75	4	898, 898	32, 26, 26, 32
5	756	867	111	76	87	2	1026	55, 55
6	867	968	101	87	97	2	1154	40, 60

Table 33.: Parameters for the six *N*-sensor types taken from [138]. Sensor type indicates in which petal row the sensor is positioned. R_i and R_o represent the inner and outer radii measured from the beam line and w_i and w_o the widths of the sensor at R_i and R_o, respectively. Length represents the difference between R_i and R_o. Number of segments refers to the minimum number of rows of strips in one sensor for the desired occupancy. The Number of Strips is quoted for consecutive pairs of rows of strips and the length of strips is quoted for consecutive rows. Each sensor is 320 μm thick.

The 1% strip occupancy and bonding requirements (e.g. hybrid spacing and bond pitch) specify the number of rows in each sensor and the lengths of strips in each row. For example,

6 Without the circular edges an additional pentagonal-shaped sensor would be needed at the transition from one to two sensors per row, complicating the simulation and digitization of the strip end-cap sensors.

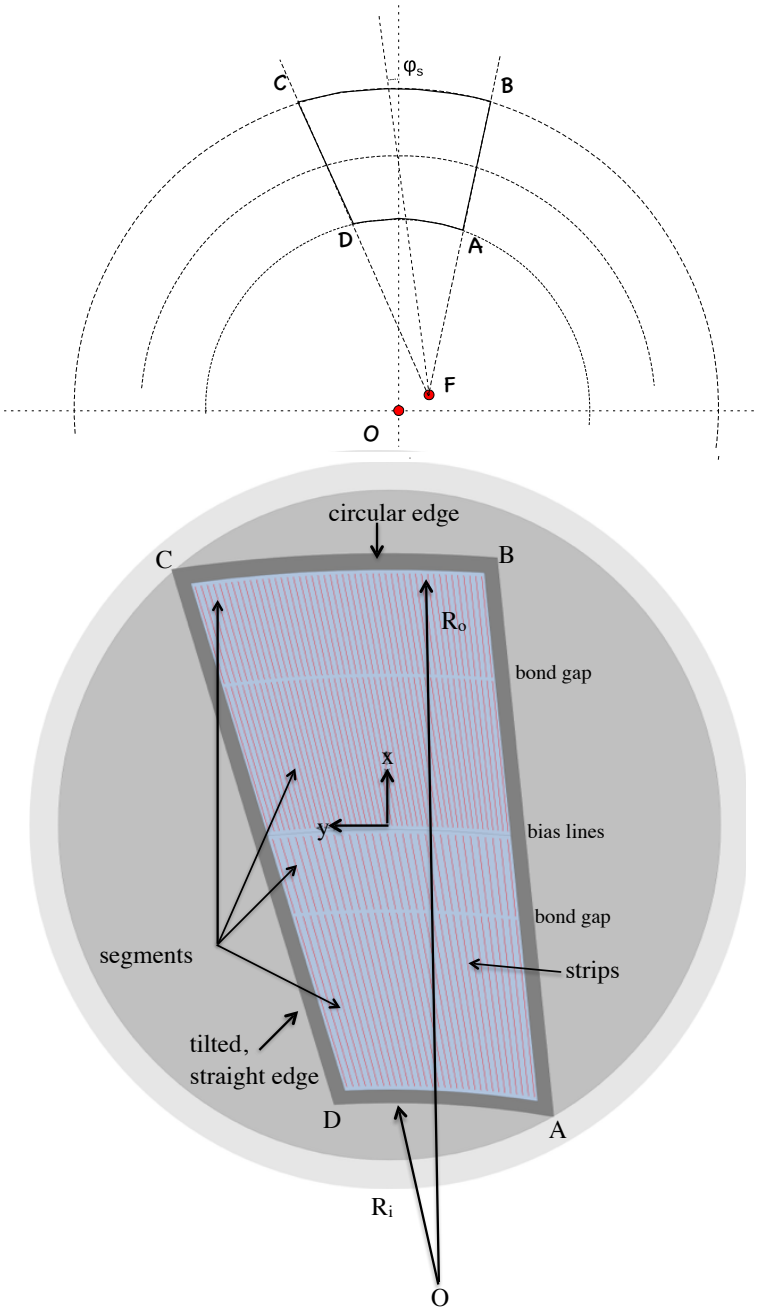

Figure 65.: The schematics of the end-cap strip sensor - the *N*-sensor. Top sketch shows the N-sensor geometry - curved edges are concentric arcs of circles centred at the beam line while the two straight edges are rotated by the stereo angle φ_S and focus away from the beam-line. The bottom plot shows an exaggerated cartoon of the N-sensor. Blue color inside the sensor indicates the active silicon area and the red lines indicate the strips. Grey circles represent the original silicon wafer ($R = 70$ mm). The cartoon shows an *N*-sensor segmented in four rows of strips, where pairs of rows are bonded to the same readout chip and have the same number of strips [137]. The dimension of each sensor type are presented in Table 33.

the sensor of type one is the closest to the beam-pipe and requires shorter strips to cope with higher track density and radiation damage. The strip pitch between the rows of strips varies but it is between ≈ 70 μm and ≈ 80 μm, similar to the barrel strip pitch.

The current ITk simulation uses an approximate description of the strip end-cap sensors that is based on the current SCT simulation. This approximation gives sensible results and models the position and the length of the strips and the material distribution reasonably well. However, details such as the gaps between the sensors and petals are not modelled correctly, and for the future detailed simulations (and eventually comparisons with the HL-LHC data) it is essential to describe the ITk layout and the detector elements much better.

8.3.3 Implementation of the *N*-sensor shape in the ATLAS simulation

In order to study the performance of the strip end-caps and the whole ITk, the *N*-sensor needs to be properly implemented in the ATLAS simulation. The first step is describing it in GeoModel. However, the shape of the *N*-sensor is complex and the GeoModel library lacked a method that would create it automatically. Hence, three different methods of building the *N*-sensor shape were first tested in a simple standalone GEANT4 simulation and compared in terms of accuracy of constructed shape and the computing time needed for particle transport in GEANT4. The three considered methods are:

- `G4GenericTrap`: creates a generic trapezoid. This method was used for a simplified version of the *N*-sensor shape with all straight edges,
- `G4ExtrudedSolid`: approximates the round edges of the *N*-sensor by several linear segments,
- `G4BooleanSolid`: constructs volumes from a boolean operation (intersection, union) between two other geometrical volume.

Figure 66 shows the constructed sensor shapes. An *intersection* between a cylindrical band (`G4Tubs`) and an enlarged trapezoid (`G4GenericTrap`) constructs the desired shape of the *N*-sensor (two right most plots in the top row of Figure 66). The sensors were placed in the petal without any overlaps or clashes (bottom plot on Figure 66).

The computing time for a particle transport in a boolean solid is proportional to the number of constituent solids [139] and since the *N*-sensor shape is most accurately described by a boolean solid, it is important to test how this choice influences the computing time. Table 34 shows the average CPU time needed for 10^6 particles to traverse the sensor volume comparing the three methods. The computing time in a boolean volume is only slightly longer than

GEANT4 method	mean CPU time [μs]
`G4GenericTrap`	70
`G4BooleanSolid`	74
`G4ExtrudedSolid` - 5 segments	112
`G4ExtrudedSolid` - 10 segments	161
`G4ExtrudedSolid` - 20 segments	249

Table 34.: The mean CPU time needed for 10^6 particles to traverse the sensor volume in a standalone GEANT4 simulation comparing various methods of sensor shape construction.

in a simple volume (`G4GenericTrap`) and since the `G4BooleanSolid` method constructs the

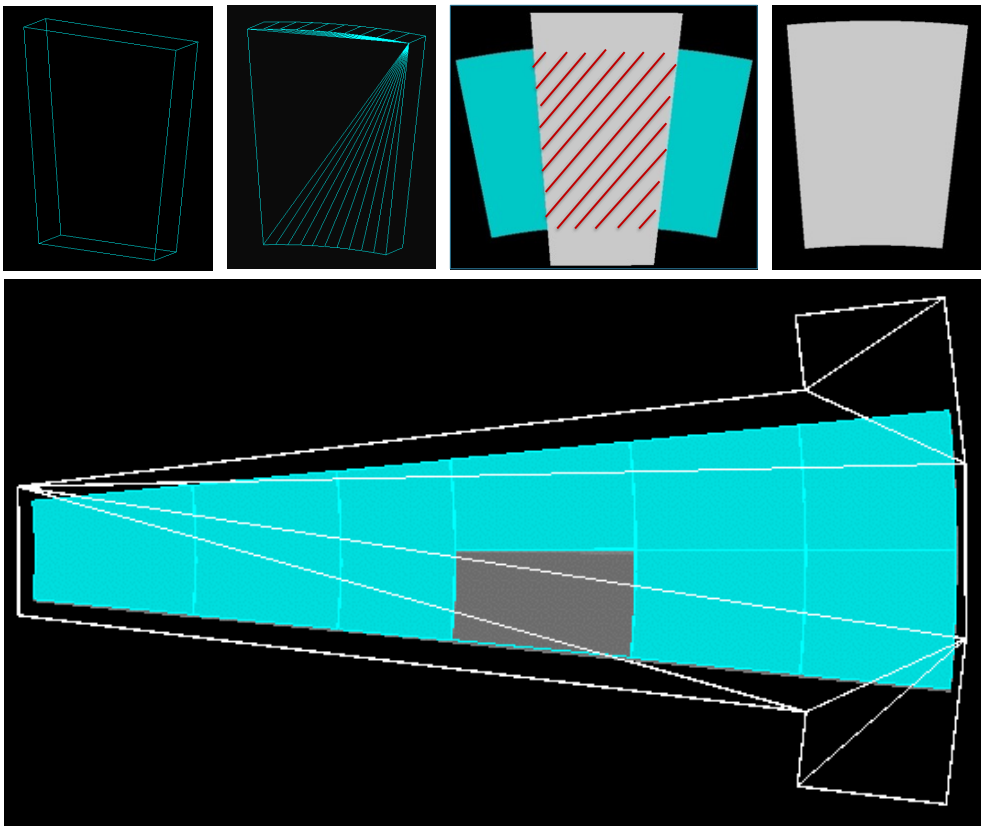

Figure 66.: Top row: The *N*-sensor shapes built in a standalone GEANT4 simulation. From left to right: `G4GenericTrap`, `G4ExtrudedSolid` with 10 linear segments, `G4BooleanSolid` showing an intersection between `G4Tubs` and `G4GenericTrap` and the resulting shape with two straight and two round edges. Bottom row: The two-sided petal structure with boolean *N*-sensor shape. The blue color indicates the front side of a sensor and the grey color the back side. The lines inside the `G4ExtrudedSolid` sensor and the petal structure are a consequence of the GEANT4 visualization.

exact shape of the *N*-sensor it has been chosen as the optimal method to be implemented in the ATLAS simulation.

The GEOMODEL developers then added an equivalent of the `G4GenericTrap` method to the GEOMODEL software which allowed for the end-cap geometry to be correctly implemented with the GEOMODEL in the ATHENA framework. The correct ITk geometry was implemented in the layout that preceded the LoI layout - the so-called "Utopia layout" [140]. Figure 67 shows global *hit rz*-coordinates, once with the simplified *N*-sensor shape (sensor description from the SCT - a simple trapezoid with all straight edges) and once with the realistic *N*-sensor shape built by `G4BooleanSolid`. Hits produced in the *N*-sensors precisely coincide with the hit map produced with a simplified sensor shape (previously validated), proving that the petals and the *N*-sensors are properly constructed and placed into the ITk. In addition, two ITk displays with the *N*-sensors are shown in Figure 68. Unfortunately, due to a known issue in the VP1 display [141], the round edges of boolean solids are not visualized properly.

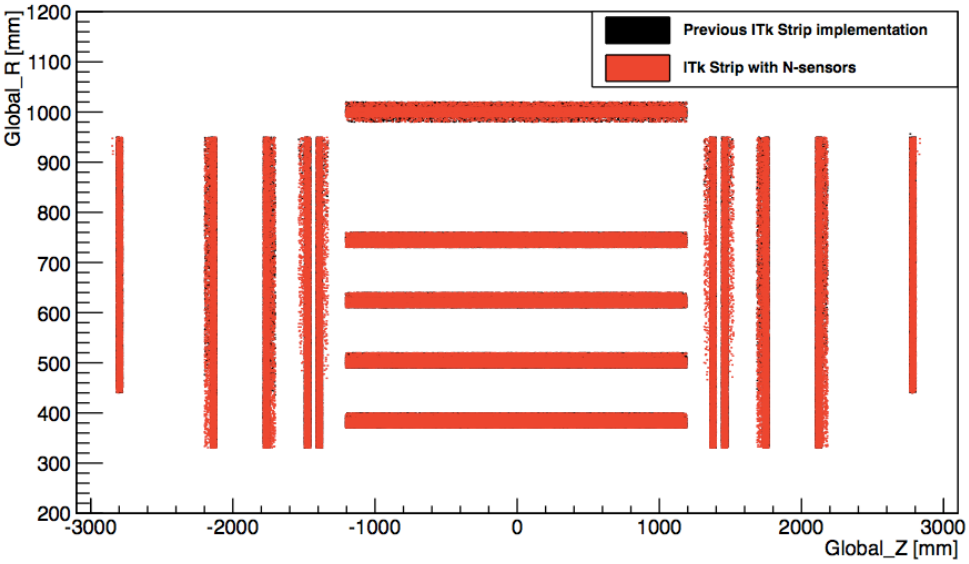

Figure 67.: The hit map showing global *rz*-coordinates of the hit. Black points represent the Utopia layout [140] where the *N*-sensor shape is approximated by an SCT sensor geometry (simple trapezoids with straight edges), and red points represent a realistic *N*-sensor shape constructed as a boolean solid. The hit map was made with a sample of muons produced at 14 TeV. The red points lie on top of the black points, which hardly show, indicating correct implementation of the *N*-sensors.

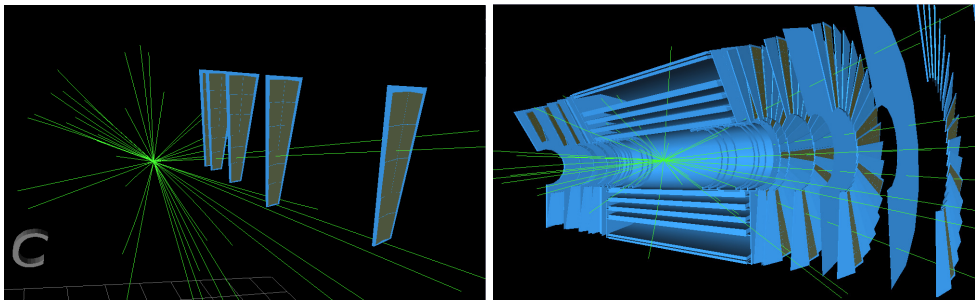

Figure 68.: The VP1 display of the ITk layout which preceded the baseline LoI layout [140]. The brown color indicates the sensitive material and the green lines indicate the muon tracks.

The ongoing work

The next step in the ATLAS simulation is digitization and particle tracking. The digitization procedure of the *N*-sensors is more complex and requires some changes to the existing digitization code. For example, the ITk strip end-cap sensors have many rows of strips, with varying number of strips (per row and per sensor), as opposed to the current SCT end-cap sensor. Therefore, the identifier scheme in the current simulation needs to be updated to include an additional parameter enumerating the row of strips in an *N*-sensor. In addition, the current ATLAS simulation code is too complex and difficult to maintain and various efforts

are put into optimizing and simplifying the code. One of such attempts is translating the code responsible to build the ATLAS detector geometry from the current `C++` based code to `xml` based code [142]. First results with the `xml` geometry description and the first complete digitization of the ITk LoI layout with a correct implementation of the *N*-sensor geometry are available at [143] and [144], respectively. The next step along a complete LoI ITk simulation is tracking.

The final layout of the ITk strip detector is still under discussion. At the moment, various studies are dedicated to estimate the impact on the performance (and costs) of the ITk with one less strip barrel layer and having instead one extra (fifth) pixel layer [133].

8.4 Extended Tracker coverage

One of the possible improvements of the ITk is extending its coverage to $|\eta| \leq 4.0$. Many physics channels would benefit from an increased signal acceptance in the forward region, especially those with forward jets, like VBF Higgs production processes or vector boson scattering. The biggest improvement in performance of an extended tracker is believed to come from the ability to tag forward jets (e.g. signal jets in VBF or VBS), better pileup rejection and heavy-flavour tagging in the forward region.

Tracking at high η is more challenging due to the weaker B field, shorter lever-arm that impacts p_T measurements and due to a larger amount of material that particles need to traverse. The Large Eta Task Force (LETF) studied various ITk layouts with the extended pseudorapidity coverage and their impacts on the physics performance. Two of the considered ITk layouts are shown in Figure 69. In addition to the extended tracking of the ITk, the LETF studied, among others, the benefits of extending the MS coverage and improving the calorimeter performance. The final report of the LETF can be found in [145].

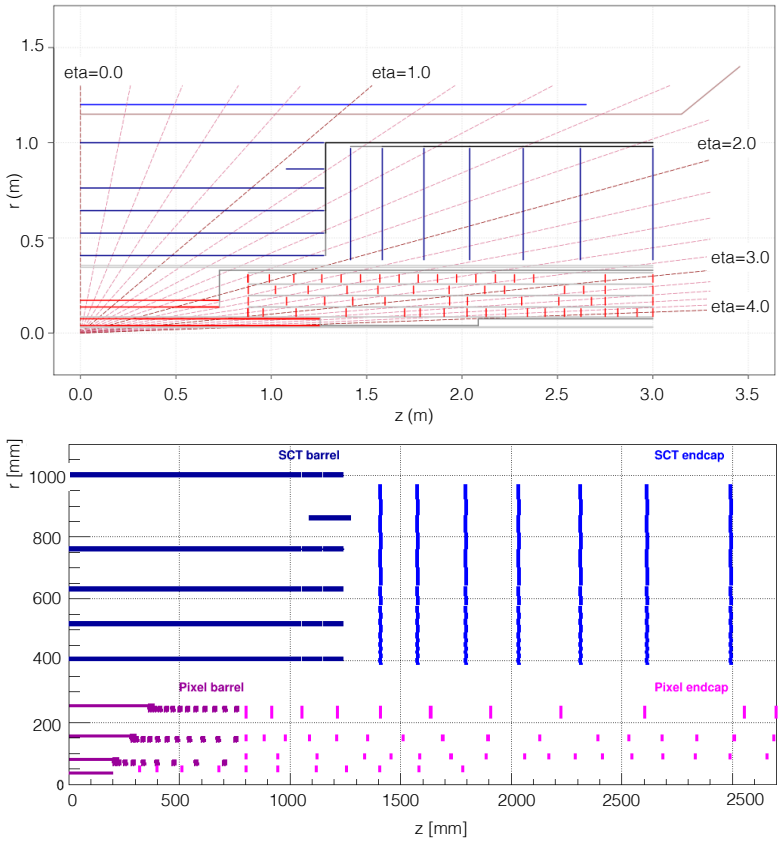

Figure 69.: Two ITk layouts with an extended coverage; extending the coverage of the inner pixel barrel layers and adding more pixel rings (top) and the Alpine-VF layout with an extended coverage (bottom) [145].

9 VBF $H \to WW^{(*)}$ ANALYSIS AT THE HL-LHC

In the next decades, the LHC and its experiments will undergo various upgrades (described in Chapter 8) in order to reach up to 3000 fb^{-1} of integrated luminosity. One of the main motivations for these upgrades is to obtain more precise measurements of the Higgs boson properties and various analyses are dedicated to study the *prospects* of these measurements and to estimate what precision can be reached with increased datasets.

This chapter summarizes the feasibility study for projections of the $H \to WW^{(*)} \to \ell^+\nu_\ell\ell^-\bar{\nu}_\ell$ analysis during Run-3 and Run-4 (see Figure 61) of the ATLAS data-taking, focusing on the VBF production. This study has been done under the scope of the European Committee for Future Accelerators (ECFA) [146] and is documented in [127]. The starting point for this analysis is based on the cut-based $H \to WW^{(*)}$ analysis concluded in 2013 [86], hereafter referred as the *Run-1 baseline analysis*, that preceded the $H \to WW^{(*)}$ analysis described in Chapters 5 - 7. The Run-1 baseline analysis observed the VBF production mode with a significance of 2.5 σ, resulting in the signal strength of $\hat{\mu}^{\text{obs}}_{\text{VBF}} = 1.66 \pm 0.67$ (stat.) ± 0.42 (syst.). The combined ggF+VBF signal was observed with 3.8 σ with the signal strength $\hat{\mu}^{\text{obs}}_{\text{ggF+VBF}}$ equal to 1.01 ± 0.21 (stat.) ± 0.23 (syst.). The improvements in precision of the signal strength measurement, due to the increase in luminosity and center of mass energy at the upgraded LHC, are presented in the following sections.

9.1 Analysis Strategy

The prospects of the $H \to WW^{(*)}$ analysis at $\sqrt{s} = 14$ TeV and 300 fb^{-1} or 3000 fb^{-1} consider the ggF and VBF Higgs production modes (no VH) for the Higgs boson with $m_H = 125$ GeV. Only leptonic W decays ($W \to \ell\nu$ with $\ell = e, \mu$) into different flavour ($e\mu/\mu e$) final states are considered. The events are split into three jets categories; $n_j = 0$, $n_j = 1$ and $n_j \geq 2$, the first two probing the ggF production mode and the $n_j \geq 2$ channel probing the VBF production mode.

Rather than using only a few generator level MC samples generated at 14 TeV, this analysis uses all the available signal and background *fully reconstructed* MC samples at 8 TeV. This guarantees higher statistics and includes *all* the signal and background processes used in the Run-1 baseline analysis. The reconstructed 8 TeV MC samples are extrapolated to 14 TeV by reweighing the PDFs and emulating any difference in performance due to higher pileup at future LHC runs. The PDF reweighing procedure has been validated where only a handful of events have been found to carry large weights which would point to an underpopulated phase space.

9.1.1 MC samples

Table 35 summaries all MC samples used in this prospects study, including their 14 TeV cross-sections. In the case the cross-section at 14 TeV has not yet been computed for a certain

process, a scaling derived from the increase in the cross-section from similar processes is applied: $W\gamma^{(*)}$ (2.2), tW (3.7), tb (2.2), tqb (2.9) and a factor of 2.7 for the electroweak di-boson processes.

All the considered background processes, except for W+jets, are normalized to their MC predictions. The W+jets background is estimated using the data-driven dijet fake factor method, based on the Run-1 baseline analysis (similar to the method described in Section 6.5.4), scaled by 1.81 - a factor which corresponds to the increase in the inclusive W+jets production from 8 TeV to 14 TeV.

Process	MC generator	$\sigma \cdot \mathcal{B}$ (pb)	$\sigma_{14\,\text{TeV}}/\sigma_{8\,\text{TeV}}$
Signal			
ggF	POWHEG+PYTHIA8	1.2	2.7
VBF	POWHEG+PYTHIA8	0.10	2.7
VH	PYTHIA8	0.056	2.3
Background			
$gg \to WW$	GG2WW3.1.2+HERWIG	0.49	2.3
$gg \to ZZ$	GG2ZZ 2.0+HERWIG	0.055	16.5
$q\bar{q}, gq \to WW$	POWHEG+PYTHIA6	12	2.2
$t\bar{t}$	MC@NLO+HERWIG	978	4.1
Single top: tW, tb	MC@NLO+HERWIG	96	3.4, 2
Single top: tqb	ACERMC+PYTHIA6	258	2.7
Z/γ^*, inclusive	ALPGEN+HERWIG	29666	2.2
$Z^{(*)} \to \ell\ell + 2j$	SHERPA processes up to $\mathcal{O}(\alpha_s)$	3.2	2.7
$Z^{(*)}Z^{(*)} \to 4\ell$ / $2\ell\,2\nu$, $m_{\ell\ell} \geq 4\,\text{GeV}$	POWHEG+PYTHIA8	2.6	2.2
$Z^{(*)}Z^{(*)} \to 4\ell$ / $2\ell\,2\nu + 2j$	SHERPA with no $\mathcal{O}(\alpha_s)$ terms	0.0054	2.7
$WZ/W\gamma^*$	POWHEG+PYTHIA8	5.0	2.2
$WZ \to 3\ell\nu + 2j$	SHERPA with no $\mathcal{O}(\alpha_s)$ terms	0.034	2.7
$W\gamma^*, m_{\gamma^*} \leq 7\,\text{GeV}$	SHERPA	17.6	2.2
$W\gamma$	ALPGEN+HERWIG	705	2.2
$WW \to 2\ell\,2\nu + 2j$	SHERPA with no $\mathcal{O}(\alpha_s)$ terms	0.107	2.7

Table 35.: MC generators used to model the $H \to WW^{(*)}$ signal at $m_H = 125\,\text{GeV}$ and all background processes in the prospects of the $H \to WW^{(*)}$ analysis at $\sqrt{s} = 14\,\text{TeV}$. The decay channels of the W and Z are included in the product of the cross section (σ) and branching fraction ($\mathcal{B}$). For the VH process, $\sigma \cdot \mathcal{B}$ only includes leptonic decays and for single-top processes inclusive cross sections are taken. The last column shows the ratio between the 14 TeV and 8 TeV cross-sections.

The cross-section for the Higgs signal at 14 TeV increases by a factor of 2.7 with respect to 8 TeV, while the cross-section for the $t\bar{t}$ production increases by a factor of 4. This could represent a challenge for the future $H \to WW^{(*)}$ analyses.

9.2 Performance Assumptions

Since the exact design of the upgraded ATLAS detector is yet unknown, several performance assumptions have to be made. Assumptions on the jet and missing transverse momentum performance are based on the studies using $\langle\mu\rangle = 80$ MC samples and the results are extrapolated to $\langle\mu\rangle = 50$ or $\langle\mu\rangle = 140$.

9.2.1 Leptons

Specifications for the lepton isolation and reconstruction are the same as are used on the Run-1 data. Any degradation in performance and efficiencies of the identification and reconstruction algorithms due to higher pileup conditions is assumed to be compensated by various detector upgrades (e.g. ITk, NSW) and refined techniques (e.g. improved electron identification using the likelihood method).

In order to keep lepton p_{T} thresholds at 15 GeV also at higher pileup, the single lepton triggers used in the Run-1 baseline analysis have to be replaced by the dilepton (or topological) triggers. This change causes a 6% loss in the triggering efficiency in the $e\mu/\mu e$ channel and is emulated in this analysis.

9.2.2 Jets

To account for higher pileup conditions, the 8 TeV reconstructed jets are appropriately smeared. First, the 8 TeV truth jets are smeared using the η-dependent truth-jet-p_{T}-smearing parametrisation at 14 TeV and $\langle\mu\rangle = 50$ or $\langle\mu\rangle = 140$, derived from [147]. The p_{T} resolution of the 8 TeV reconstructed jets is then matched to the p_{T} resolution of the smeared truth jets, as shown in Figure 70. The blue curve represents the p_{T} resolution of the 8 TeV reconstructed jets, smeared to match the p_{T} resolution at higher pileup conditions.

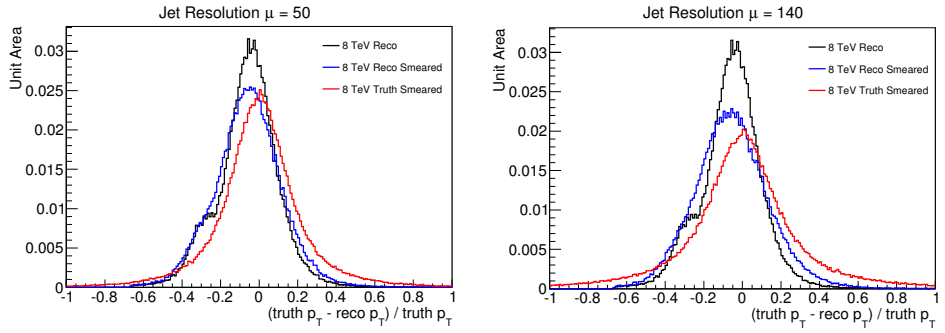

Figure 70.: Comparison between jet p_{T} resolution for 8 TeV reconstructed jets (black), 8 TeV smeared truth jets (red) and 8 TeV smeared reconstructed jets (blue) in $|\eta_{jet}| < 0.8$ region for $\langle\mu\rangle = 50$ (left) and $\langle\mu\rangle = 140$ (right). The truth and reconstructed jets are matched if the following conditions are fulfilled: $p_{\mathrm{T}}^{\mathrm{jet}} > 10\,(20)$ GeV for truth (reco) jets, reco-p_{T}/truth-$p_{\mathrm{T}} < 3$, Δ(truth, reco)< 0.4 and in case jets overlap with electrons they are removed.

The pileup jets are removed from the event by increasing the jet p_{T} threshold and by applying the JVF criterion. The JVF requirement is refined from the baseline selection to target the high-p_{T} jets as well; $|\mathrm{JVF}| > 0.5$ for jets with $p_{\mathrm{T}} < 50$ GeV (baseline) and $|\mathrm{JVF}| > 0.1$ for jets with $50\,\mathrm{GeV} < p_{\mathrm{T}} < 80\,\mathrm{GeV}$. In the Run-1 baseline analysis, the jet p_{T} thresholds are set to 25 GeV in the central rapidity region and to 30 GeV in the forward region. By raising these thresholds to 30 GeV and 35 GeV across the entire rapidity range for $\langle\mu\rangle = 50$ and $\langle\mu\rangle = 140$ respectively, the average number of pileup jets per event reduces to 0.3 and 0.8 respectively, as is shown in Figure 71 (left). By additionally applying the JVF criterion, 95% of all pileup jets are removed from the event. The remaining 5% are added to the 8 TeV MC samples according to the rates from Figure 71 (left), with their p_{T} and η sampled from a simulated pileup jets sample at $\langle\mu\rangle = 80$. The right plot in Figure 71 shows the resulting

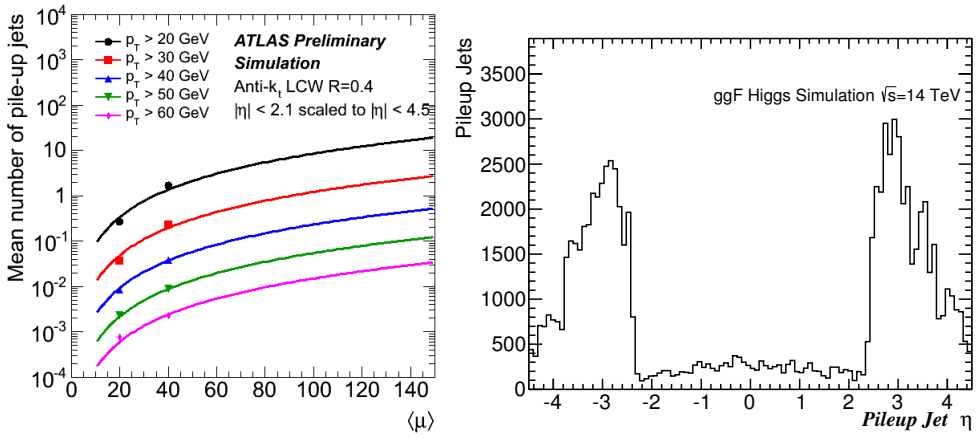

Figure 71.: Average number of pileup jets as a function of $\langle\mu\rangle$ for various jet p_T thresholds (left) and the distribution of pileup jets at $\langle\mu\rangle = 140$ versus η in the ggF signal sample at the beginning of the analysis selection (right).

pileup jet η distribution in the ggF signal sample at $\langle\mu\rangle = 140$, where the large majority of pileup jets dwells outside of the tracker acceptance, $|\eta| \geq 2.5$.

For identifying the b-jets, the MV1 b-tagging algorithm is used with the 85% working point, where the probability for a pileup jet being mistagged as a b-jet is found to be $\approx 20\%$ (evaluated in $Z/\gamma^* \to \ell\ell$+jets sample at $\langle\mu\rangle = 80$). Combining the b-tagging algorithm with the JVF criterion reduces this probability to the percent level.

9.2.3 Missing transverse momentum

Due to a more stable performance with the increasing pileup, the calorimeter based evaluation of the missing transverse momentum (E_T^{miss}) is replaced by the evaluation including information from tracks associated to jets - $p_T^{\text{miss, jet-corr}}$ (see Section 4.5). The use of $p_T^{\text{miss, jet-corr}}$ increases the rejection of the Drell-Yan and multi-jets backgrounds at higher pileup with respect to E_T^{miss}.

The resolution of the soft terms is smeared by 33 MeV per unit of $\langle\mu\rangle$, derived from the high pileup Z samples. Figure 72 shows the resolution of the smeared $p_T^{\text{miss, jet-corr}}$ for the 8 TeV conditions and both higher pileup conditions.

9.3 Object and Event Selection

The object and event selection closely follow the selection from the Run-1 baseline analysis and is in fact not so different from the event selection described in Chapter 5. The key differences between the Run-1 and 14 TeV selections are in requiring higher p_T thresholds for leptons ($p_T > 25\,(15)$ GeV for the leading (subleading) lepton) and jets (selected by the anti-k_T algorithm with $R = 0.4$), use of the refined JVF criterion, and using $p_T^{\text{miss, jet-corr}}$ instead of E_T^{miss} ($p_T^{\text{miss, jet-corr}} > 20$ GeV).

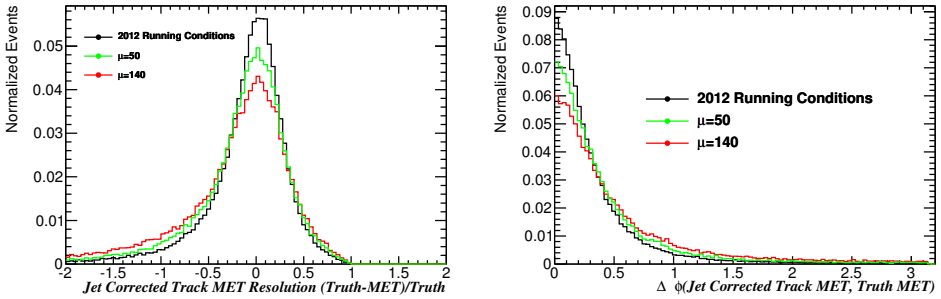

Figure 72.: The $p_T^{\text{miss, jet-corr}}$ resolution (left) and ϕ resolution (right) for the ggF signal sample including the 2012 data conditions (black) and both high pileup conditions; $\langle\mu\rangle = 50$ (green) and $\langle\mu\rangle = 140$ (red).

The VBF SR is additionally optimized to reduce the effects of the increased pileup and higher top-quark production cross-section. The following VBF SR selection criteria are changed with respect to the Run-1 baseline event selection (shown in brackets):

- $m_{jj} > 1.25\,\text{TeV}$ $(500\,\text{GeV})$,
- $|\eta_j| > 2.0$ for tag jets in opposite hemispheres $(\Delta y_{jj} > 2.8)$,
- $p_{\text{T}}^{\text{sum}} < 20\,\text{GeV}$ $(45\,\text{GeV})$,
- the CJV threshold is raised to include jets with $p_{\text{T}} > 30\,\text{GeV}$ $(20\,\text{GeV})$,
- $p_{\text{T}}^{\text{jet}} > 45\,\text{GeV}$ $(25, 30\,\text{GeV})$.

Increasing the m_{jj} threshold and requiring jets in opposite hemispheres with pseudorapidity larger than 2.0 reduces the large amount of $t\bar{t}$ contamination and removes $t\bar{t}$ events with a hard central jet and one forward ISR or pileup jet. The $p_{\text{T}}^{\text{sum}}$ requirement is tightened to match the efficiency from the Run-1 baseline selection, which uses E_T^{miss} in the $p_{\text{T}}^{\text{sum}}$ definition, and the $p_{\text{T}}^{\text{jet}}$ threshold is additionally raised to 45 GeV to remove pileup-dependent backgrounds like $Z \to \tau\tau$. Additionally, a higher jet p_{T} threshold is used in the b-tagging algorithm at $\langle\mu\rangle = 140$, $p_{\text{T}} > 25\,\text{GeV}$ (for $\langle\mu\rangle = 50$, $p_{\text{T}} > 20\,\text{GeV}$).

The benefits of the optimized VBF SR criteria are seen in the increased separation between the VBF signal and the $t\bar{t}$ background, as shown in Figure 73. The m_{jj} and $p_{\text{T}}^{\text{sum}}$ distributions are shown in Figure 74 and Table 36 summarizes the final event selection used in this analysis.

9.4 SYSTEMATIC UNCERTAINTIES

The precision on the Run-1 VBF $H \to WW^{(*)}$ signal strength measurement is mostly dominated by the statistical uncertainties. Up to a hundred times larger integrated luminosity at the HL-LHC will provide enough data to reduce the statistical uncertainties and consequently the dominant experimental uncertainties, like JER, JES and the b-tagging efficiency. The higher MC and data statistics in the dedicated control regions and more refined data-driven estimates will also improve the modelling of the backgrounds and reduce their uncertainties. Moreover, more data will allow definitions of additional CRs which were not possible at the

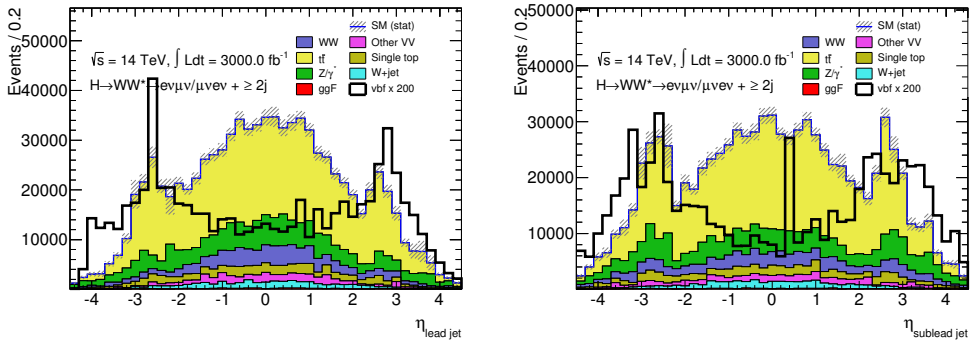

Figure 73.: The η distribution for a leading (left) and subleading (right) tag jet in the VBF SR before the m_{jj} selection at 14 TeV and 3000 fb^{-1}. The VBF signal is scaled by a factor of 200.

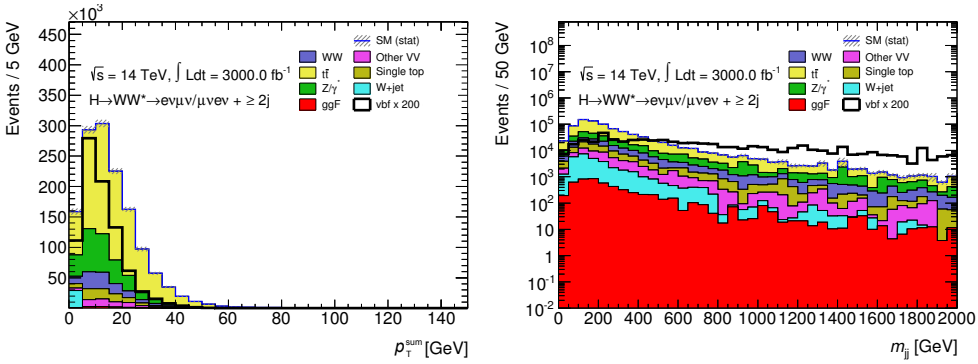

Figure 74.: The $p_{\mathrm{T}}^{\mathrm{sum}}$ (left) and m_{jj} (right) distributions in the VBF SR at 14 TeV and 3000 fb^{-1}. The $p_{\mathrm{T}}^{\mathrm{sum}}$ distribution is shown after the b-jet veto and m_{jj} is shown after the $Z \to \tau\tau$-veto. The VBF signal is scaled by a factor of 200.

Run-1 due to the low statistics (e.g. same-sign lepton selection for estimation of the di-boson background).

The assumed systematic uncertainties on the background estimation for this prospect study are summarized in Table 37. In the Run-1 baseline analysis, the top background is estimated using a dedicated control region where the largest impact on its estimation comes from the experimental uncertainty on the b-tagging efficiency. With an increased statistics in the future runs, the modelling of the top background will improve. This analysis assumes a total systematic uncertainty of 10% on the top background estimation, assuming a $\sim$ 30% reduction on its baseline Run-1 experimental uncertainty and a $\sim$ 50% reduction on its baseline Run-1 theoretical uncertainty.

The main source of systematic uncertainties on the $WW + 2$ jets background estimation in the Run-1 baseline analysis comes from its QCD contributions. At 14 TeV, the EW $WW +$ 2 jets contribution will increase .Since their theoretical uncertainties are up to four times smaller with respect to the QCD contributions, this analysis assumes a reduction in the total systematic uncertainty on the $WW + 2$ jets background to 10%.

VBF $H \to WW^{(*)}$ selection criteria:	
Preselection	Two isolated leptons ($\ell = e, \mu$) with opposite charge $p_{\mathrm{T}}^{\mathrm{lead}} > 25$, $p_{\mathrm{T}}^{\mathrm{sublead}} > 15$ $m_{\ell\ell} > 10$ $p_T^{\mathrm{miss,\,jet\text{-}corr}} > 20$
General selection	$n_j \geq 2$ $p_T^{\mathrm{jet}} > 45$ $n_b = 0$ $p_{\mathrm{T}}^{\mathrm{sum}} < 20$ $Z \to \tau\tau$ veto
VBF topology	$m_{jj} > 1250$ $\lvert\eta_j\rvert > 2.0$, tag jets in opposite hemisphere CJV ($p_{\mathrm{T}} > 30$) OLV
$H \to WW^{(*)} \to \ell^+\nu_\ell\ell^-\bar{\nu}_\ell$ topology	$m_{\ell\ell} < 60$ $\Delta\phi_{\ell\ell} < 1.8$ $m_T < 1.07 \cdot m_H$

Table 36.: Selection criteria used in the 14 TeV VBF $H \to WW^{(*)}$ analysis. All energy-related units are given in GeV.

	14 TeV	8 TeV
WW	$10 = 9 \oplus 5$	30
top	$10 = 8 \oplus 8$	$33 = 15 \oplus 29$
VV	10	20
Z+jets	10	20
W+jets	20	30

Table 37.: The total background systematic uncertainty (in %) used in the prospects for the VBF $H \to WW^{(*)}$ analysis at 14 TeV, compared to the uncertainties used in the Run-1 baseline analysis [86]. The WW and top background contributions are split into their theoretical $\oplus$ experimental contributions. The uncertainties on other backgrounds are purely experimental. The symbol $\oplus$ indicates a quadratic sum.

For the remaining backgrounds this analysis assumes only experimental systematic uncertainties: for the di-boson background the experimental uncertainties are halved to 10%, assuming a possibility of a new control region with the same-sign lepton selection. The uncertainties on the Z+jets background are also halved to 10%, where an increase in the statistics in the dedicated control region offers a better understanding of the Z+jets modelling. The estimation of the W+jets background is data-driven and the increase in statistics will reduce its experimental uncertainties as well. However, since the W+jets background estimation is more complex than of the other backgrounds, only a reduction for one-third with respect to the Run-1 baseline uncertainty is assumed. A 3% uncertainty on the luminosity and the uncertainty on the $H \to WW^{(*)}$ branching ratio are also included in the analysis.

The theoretical uncertainties on the VBF and ggF (treated as a background in the VBF analysis) $H \to WW^{(*)}$ signal are one of the leading systematic uncertainties on the expected event yields in the Run-1 baseline analysis. In order to estimate their impact on the signal strength measurement at 300 fb^{-1} and 3000 fb^{-1}, two scenarios are considered: a more con-

servative one where theoretical uncertainties are the same as in the Run-1 baseline analysis and are presented in Table 38, and a more optimistic scenario where these uncertainties are reduced by 50%.

	QCD	PDF	UE/PS	TOTAL
VBF signal	$1 \oplus 4$	3	3	6
ggF signal	$43 \oplus 4$	8	9	44

Table 38.: The ggF and VBF signal theoretical uncertainties (in %) used in the prospects for the VBF $H \to WW^{(*)}$ analysis. These uncertainties are the same as the Run-1 baseline signal theoretical uncertainties. The ggF signal is considered as a background in the VBF analysis. The QCD uncertainties are split into uncertainties on the QCD scale $\oplus$ QCD acceptance. The operator $\oplus$ represents a quadratic sum.

9.5 RESULTS

The expected precision on the signal strength measurement is obtained by fitting the m_T distribution. The uncertainties due to the limited MC sample size are neglected and a smoothing algorithm is applied on the m_T distribution.

A possible improvement for future VBF $H \to WW^{(*)}$ analyses would be a fit on one of the variables enhancing the VBF topology, like m_{jj}, to even further discriminate between the signal and backgrounds and reduce the uncertainties.

9.5.1 VBF production mode at the HL-LHC

Table 39 shows the expected event yields at future LHC runs. Due to the higher pileup, the signal-to-background ratio is larger at 300 fb^{-1} than at 3000 fb^{-1}.

	N_{bkg}	N_{signal}	S/B	N_{VBF}	N_{ggF}	N_{WW}	N_{VV}	N_{top}	$N_{Z+\text{jets}}$	$N_{W+\text{jets}}$
300 fb^{-1}, $\langle\mu\rangle = 50$										
before m_T	101	62	0.6	57	5	12	4	65	12	8
after m_T	51	56	1.1	52	4	6	1	24	12	8
3000 fb^{-1}, $\langle\mu\rangle = 140$										
before m_T	1825	590	0.3	500	90	300	120	990	335	80
after m_T	995	503	0.5	436	67	110	65	405	335	80

Table 39.: The expected signal and background event yields in the VBF $H \to WW^{(*)}$ analysis at 14 TeV.

The expected precision on the signal strength is evaluated from the shape of the m_T distribution shown in Figure 75 and is presented in Table 40. Two scenarios are considered: the signal theoretical uncertainties are either taken from Table 38 (kept the same as in the Run-1 baseline analysis) or they are reduced by a half. The precision of the VBF signal strength, with the same signal theoretical uncertainties as in the Run-1 baseline analysis, substantially improves with the increased dataset; from 48% at Run-1 to 25% at 300 fb^{-1}, and even further, to 15% at 3000 fb^{-1}. At 300 fb^{-1}, the $\Delta\hat{\mu}_{\text{VBF}}$ is still limited by the statistical uncertainties. Reducing the signal theoretical uncertainties by a half improves $\Delta\hat{\mu}_{\text{VBF}}$ at the percent level for both upgrade scenarios.

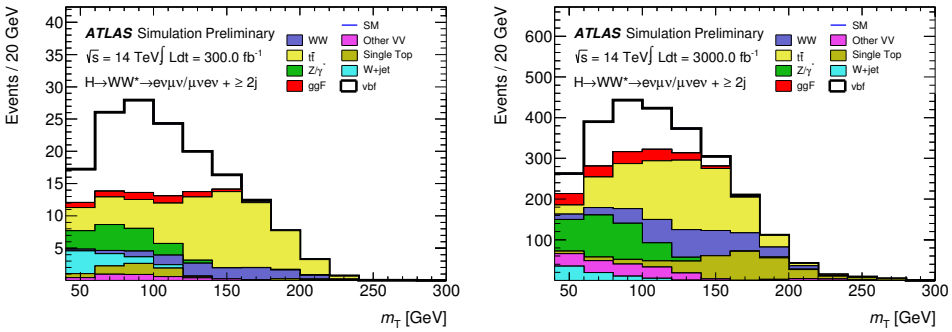

Figure 75.: The m_T distribution in the VBF $H \to WW^{(*)}$ analysis before the final m_T requirement for $\langle\mu\rangle = 50$ and 300 fb^{-1} (left) and for $\langle\mu\rangle = 140$ and 3000 fb^{-1} (right).

	$\Delta\hat{\mu}_{\text{VBF}}$		Δ [%]
no reduction			
300 fb^{-1}	$+0.25$	-0.22	$\sim 25\%$
3000 fb^{-1}	$+0.15$	-0.15	$\sim 15\%$
50% reduction			
300 fb^{-1}	$+0.24$	-0.21	$\sim 24\%$
3000 fb^{-1}	$+0.13$	-0.12	$\sim 13\%$
$\hat{\mu}^{\text{obs}}_{\text{Run-1}}$ (2013) [86]	$1.66 \pm 0.67(\text{stat.}) \pm 0.42(\text{syst.})$		$\sim 48\%$

Table 40.: Projections for the precision on the expected VBF signal strength measurement for 300 fb^{-1} and 3000 fb^{-1}, once with no reduction in the signal theoretical uncertainties (see Table 38) and once with 50% reduction. For comparison, the observed signal strength measurement in the Run-1 baseline analysis [86] is shown as well.

9.5.2 Combined VBF+ggF at the HL-LHC

The precision on the expected signal strength for the combined VBF+ggF signal, based on the shapes of the m_T distributions shown in Figures 75, 76 and 77, is presented in Table 41 for the ggF production mode[1] and for the VBF+ggF combination. The precision on the ggF+VBF signal strength reaches $\approx 10\%$ and improves only for a few percent by increasing the dataset from 300 fb^{-1} to 3000 fb^{-1}. Contrary to the $\Delta\hat{\mu}_{\text{VBF}}$ projections, the precision on the combined ggF+VBF measurement is not limited by the statistics at 300 fb^{-1} but it rather limited by the systematic uncertainties.

9.6 CONCLUSIONS

The precision on the Higgs signal strength measurement depends on many factors; data statistics, understanding of theoretical and experimental uncertainties and of course on the design of the future ATLAS detector. Even if we do not have a complete picture of the future detector and its performance, some projections of physics measurements can still be made.

1 For more details on the event selection and systematic uncertainties used in $n_j \leq 1$ channels see [127].

	$\hat{\mu}_{\text{ggF}}$	$\hat{\mu}_{\text{ggF+VBF}}$
no reduction		
300 fb^{-1}	$1^{+0.18}_{-0.15}$	$1^{+0.14}_{-0.13}$
3000 fb^{-1}	$1^{+0.16}_{-0.14}$	$1^{+0.10}_{-0.09}$
50% reduction		
300 fb^{-1}	$1^{+0.12}_{-0.11}$	$1^{+0.11}_{-0.10}$
3000 fb^{-1}	$1^{+0.10}_{-0.09}$	$1^{+0.07}_{-0.07}$

Table 41.: Projections for the precision on the expected ggF and ggF+VBF signal strength measurement at 300 fb^{-1} and 3000 fb^{-1}, once with no reduction in the signal theoretical uncertainties and once with 50% reduction (the systematic uncertainties assumed in the ggF analysis can be found in [127]). The different background uncertainties are uncorrelated between n_j bins.

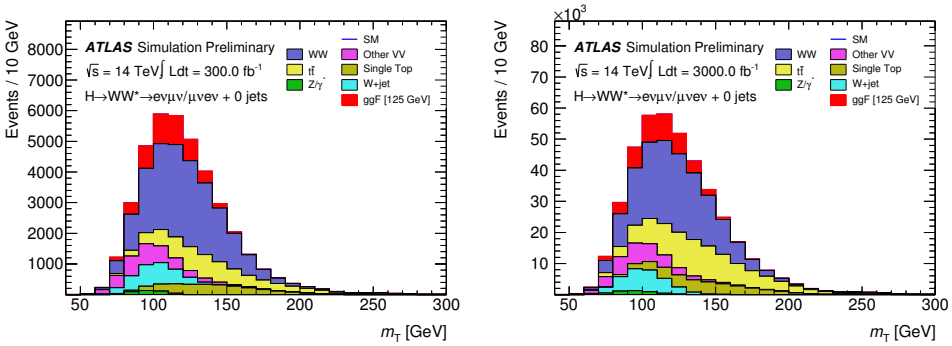

Figure 76.: The m_T distribution before the final m_T requirement, in the ggF $n_j = 0$ analysis for $\langle\mu\rangle = 50$ and 300 fb^{-1} (left) and for $\langle\mu\rangle = 140$ and 3000 fb^{-1} (right).

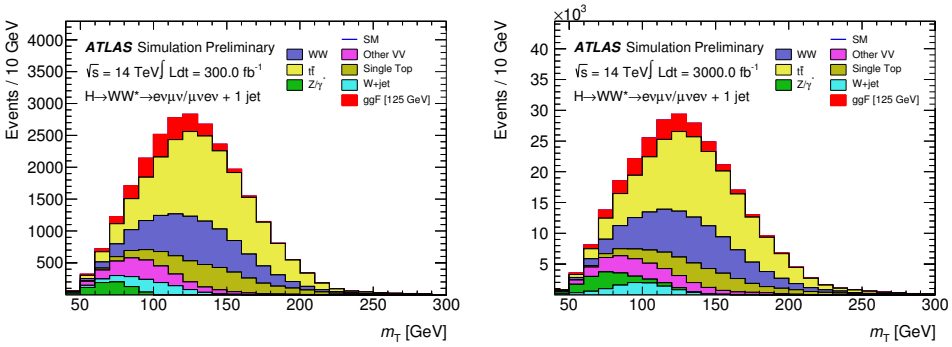

Figure 77.: The m_T distribution before the final m_T requirement, in the ggF $n_j = 1$ analysis for $\langle\mu\rangle = 50$ and 300 fb^{-1} (left) and for $\langle\mu\rangle = 140$ with 3000 fb^{-1} (right).

The Run-1 baseline analysis observed the VBF $H \to WW^{(*)}$ signal strength with a precision of 48%. The (BDT) VBF analysis presented in this thesis (see Chapters 5 - 7) measured the VBF signal strength with a $\sim$ 42% precision. Both of the Run-1 μ_{VBF} measurements are mostly

dominated by the statistical uncertainties. Using the assumptions outlined in this chapter, the precision on μ_{VBF} at 300 fb^{-1} improves. It reaches $\sim$ 25% but the largest contribution to the uncertainty still originates from the statistical uncertainties. The increased dataset at HL-LHC increases the precision on μ_{VBF} for additional $\sim$ 40%, reaching $\Delta\mu_{\text{VBF}} \sim 15\%$.

The precision on the combined ggF+VBF $H \to WW^{(*)}$ signal strength reaches $< 10\%$ at 3000 fb^{-1} and is only marginally improved with respect to 300 fb^{-1}.

10 VECTOR BOSON SCATTERING AT THE HL-LHC

The measurement of the vector boson scattering (VBS) provides a unique probe into the nature of the electroweak symmetry breaking (EWSB) and into possible contributions from New Physics. Starting with a brief theoretical overview of the interplay between the VBS, the Higgs mechanism and the New Physics in Section 10.1, this chapter presents the results of a feasibility study analysing the impact of the extended ITk coverage (see Section 8.4) on the sensitivity of the *same-sign* (same electric charge) *WW scattering* (ssWW), $W^{\pm}W^{\pm} \rightarrow W^{\pm}W^{\pm}$. This study was done under the scope of the Large Eta Task Force and its final report can be found in [145].

10.1 Theoretical overview of the Vector Boson Scattering

The spontaneous breaking of the EW symmetry produces three Goldstone bosons which are absorbed into the *longitudinal* polarisation states of the gauge bosons $V = W^{\pm}, Z$. As a consequence, the gauge bosons become massive.

The scattering of the massive vector bosons $V(q_1)V(q_2) \rightarrow V(q_3)V(q_4)$ can proceed either through the Higgs boson exchange diagrams or through the vector bosons self-interaction terms, resulting in triple or quartic gauge couplings - TGC or QGC, respectively. The diagrams are shown in Figure 78.

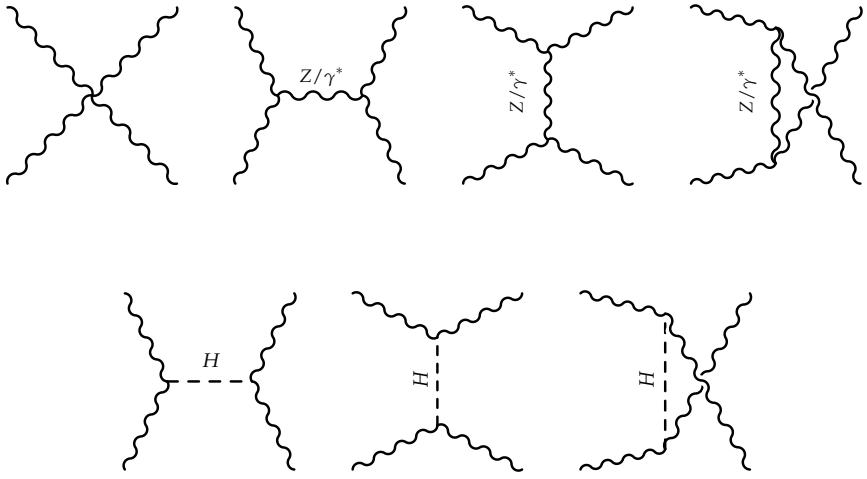

Figure 78.: The tree-level Feynman diagrams for the $VV \rightarrow VV$ scattering. First row: *Gauge terms:* self-interactions of electroweak gauge boson with a quartic and triple gauge boson vertices. Second row: *Higgs terms:* interactions featuring a Higgs boson exchange.

The transverse and longitudinal polarisation vectors, $\epsilon_{\pm}^{\mu}$ and ϵ_{L}^{μ} respectively, are estimated as [11, 19, 148]

$$\epsilon_{\pm}^{\mu} = \frac{1}{\sqrt{2}}(0, 1, \pm i, 0) \quad \text{and} \quad \epsilon_{L}^{\mu} = \frac{1}{m_V}(p_z, 0, 0, E) \xrightarrow{E \gg m_V} \frac{p^{\mu}}{m_V}, \tag{107}$$

for a vector boson travelling in the z-direction. In the high energy limit, $E \gg m_V, m_H$, the longitudinal polarization increases with energy and *dominates* over transversal components. This makes it possible to approximate the VBS as the scattering of only its longitudinal components. Thus, the leading term in the W^+W^- scattering amplitude without the Higgs contributions (gauge terms from the upper row in Figure 78) can be written as [149, 150]

$$i\mathcal{M}_{\text{gauge}} \approx -i\frac{g_W^2}{4m_W^2}u, \tag{108}$$

where $u = (q_1 - q_4)^2$ represents one of the Mandelstam variables. With the increasing energy, the $\mathcal{M}_{\text{gauge}}$ grows as well, which leads towards the violation of perturbative unitarity. Fortunately, the Higgs boson restores it. The scattering amplitude of the Higgs exchange terms (the bottom row of Figure 78) for $E \gg m_V, m_H$ equals to

$$i\mathcal{M}_{\text{Higgs}} \approx +i\frac{g_W^2}{4m_W^2}u \tag{109}$$

and precisely *cancels out* the divergent gauge term from Equation 108. This is of course true only if the properties of the Higgs boson and the values of TGCs and QGCs are *exactly* as predicted by the SM. Without the SM Higgs boson, the VBS cross-section would continue to grow at higher energies as is indicated on Figure 79.

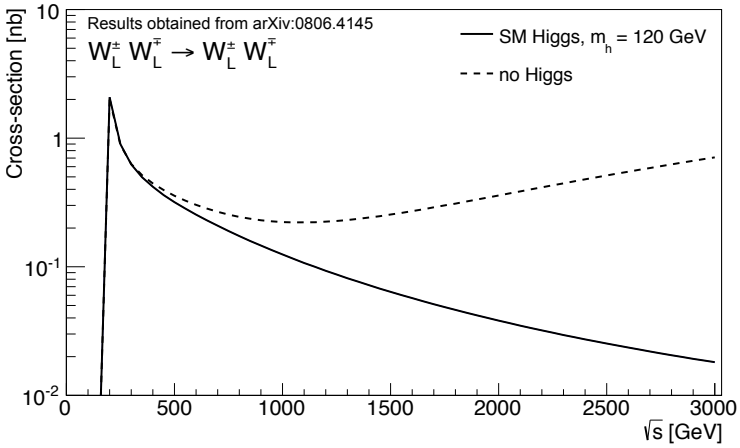

Figure 79.: The cross-section for the scattering of the longitudinal $W^{\pm}$ bosons with and without the SM Higgs boson diagrams, for $m_H = 120\,\text{GeV}$. Results are taken from [151].

A Higgs boson has been found. Whether it is indeed the SM one can be also probed through the properties of the VBS. If the Higgs mechanism is not completely responsible for the EWSB, some New Physics processes (e.g. higher dimensions or Technicolor models) should appear at the TeV scale to cancel the divergent high energy behaviour of the VBS and

restore unitarity. In addition, in case the discovered scalar boson is completely responsible for the EWSB, this does not exclude the presence of other scalar bosons (e.g. Higgs doublet models, etc.) which could influence the Higgs boson couplings and consequently the $\mathcal{M}_{\text{Higgs}}$. Therefore, *precisely* measuring the Higgs boson couplings and the triple/quartic gauge couplings is very important to gather more insights into the nature of the EWSB and to probe for NP contributions in the EW sector. Any deviation from the SM predictions would indirectly prove the presence of NP.

This thesis focuses only on the NP contributions affecting the quartic gauge vertex in the ssWW scattering via *anomalous* quartic-gauge couplings (aQGC). In order to independently scan for various possible NP models which result in aQGCs, the *Effective Field Theory* framework is adopted and is described next.

10.1.1 The Effective Field Theory

The *Effective Field Theory* (EFT) provides a model independent approach to look for effects of New Physics through novel interactions of the existing SM particles [152]. The EFT is built by adding higher-dimension operators (products of fields) to the SM Lagrangian [153], and is general enough to capture effects of any NP model as long as all known SM particles are included[1]. The EFT Lagrangian is defined as

$$\mathcal{L}_{\text{EFT}} = \mathcal{L}_{SM} + \sum_{d>4} \sum_{i} \frac{c_i^{(d)}}{\Lambda^{d-4}} \mathcal{O}_i^{(d)}, \tag{110}$$

where $\mathcal{O}_i^{(d)}$ are the high-dimension ($d > 4$) operators, $c_i^{(d)}$ represent dimensionless coupling strengths of the NP with the SM particles, and Λ^{d-4} represents the scale of the New Physics, somewhere between 1 TeV and the Planck scale.

The Lagrangian and all the SM operators have a dimension of at most the fourth power of energy, $[\text{TeV}]^4$. Higher-dimension operators are accordingly suppressed by the scale of the NP, and the dominant contributions therefore always come from the operators with lower dimensionality. The EFT is valid only if the scale of the NP is larger than the experimentally accessible energies $s \ll \Lambda$, and recovers the SM results in the limit $\Lambda \to \infty$. All in all, the EFT provides a *guidance* to where the NP effects are hiding.

10.1.2 Quartic Gauge Couplings in the Vector Boson Scattering

The vector boson self-interaction terms, resulting in the quartic vertex (see Figure 80), are in the SM described by a term proportional to $\propto g_W^2 Tr[W_\mu, W_\nu]^2$ (see Equation 20), where W_μ are the three massless vector boson fields of the $SU(2)_L$ symmetry. The SM predicts five QGCs[2]; $g_{W^\pm W^\mp \to W^\pm W^\mp}$, $g_{W^\pm W^\pm \to W^\pm W^\pm}$ and $g_{W^+W^- \to Z/\gamma^* Z/\gamma^*}$.

Many EFT operators result in the aQGCs in the ssWW scattering. The lowest dimension operators in $\mathcal{L}_{\text{EFT}}$ are of dimension-6 [3], but such operators also modify double and triple

1 The EFT should respect the Lorentz invariance, unitarity and the gauge symmetry of the SM and should recover the SM results in an appropriate limit. Additionally, the EFT is also adaptable - in case a new particle is discovered, the EFT should to be rewritten to include all the *low-energy* particle content, including contributions from the newly discovered particle.

2 Neutral QGCs are not present in the SM and may proceed only through Higgs exchange or box diagrams featuring a quark or W exchange.

3 The $\mathcal{L}_{\text{EFT}}$ includes only even-dimension operators since the odd-dimension operators violate lepton and baryon numbers [152].

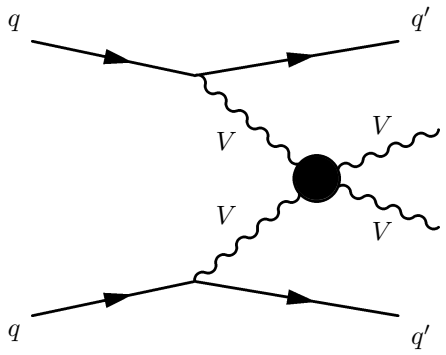

Figure 80.: A Feynman diagram for the electroweak vector boson scattering $VV \to VV$ at the LHC. The black circle represent any connected diagram with the matching external lines at the leading order - like the diagrams in Figure 78. It also stands for any NP process with different coupling strength with respect to the SM prediction.

gauge couplings and can be better constrained in other processes. Thus, the lowest dimension operators which modify *only* quartic gauge couplings are of dimension-8.

The dimension-8 operators which lead to aQGC are parametrised by the $SU(2)_L \times U(1)_Y$ gauge-invariant operators, including the covariant derivative of the Higgs field $D^\mu\phi$ (see Equations 34 and 51) and $SU(2)$ field strength tensors $W^i_{\mu\nu}$ and $B_{\mu\nu}$ (see Equations 36, 19 and 11) [154]. All in all, there are 20 dimension-8 operators affecting the QGCs in the VBS processes (listed in [154]), out of which only 3 of them affect the quartic gauge boson vertex in the $WW \to WW$ scattering:

$$\begin{aligned}
\mathcal{O}_{T,0} &= Tr\left[W_{\mu\nu}W^{\mu\nu}\right] \times Tr\left[W_{\alpha\beta}W^{\alpha\beta}\right], \\
\mathcal{O}_{T,1} &= Tr\left[W_{\alpha\nu}W^{\mu\beta}\right] \times Tr\left[W_{\mu\beta}W^{\alpha\nu}\right], \\
\mathcal{O}_{T,2} &= Tr\left[W_{\alpha\mu}W^{\mu\beta}\right] \times Tr\left[W_{\beta\nu}W^{\nu\alpha}\right].
\end{aligned} \tag{111}$$

Focusing only on the same-sign WW scattering, the operator which is the most sensitive to the contributions from the NP is $\mathcal{O}_{T,1}$. It causes the strongest enhancement in the ssWW cross-section, up to 150 times compared to the SM value [155]. The dimension-8 Lagrangian describing the contribution from the $\mathcal{O}_{T,1}$ operator is defined as

$$\mathcal{L}_{T,1} = \frac{f_{T,1}}{\Lambda^4}\mathcal{O}_{T,1}, \tag{112}$$

where $f_{T,1}$ represents the coupling strength of the NP to the SM particles. By measuring the $f_{T,1}$, various BSM processes contributing to aQGCs in ssWW scattering can be distinguished among each other.

10.2 Same-Sign $W^\pm W^\pm$ Scattering

In the p-p collisions, the VBS occurs when the two initial quarks radiate vector bosons which later scatter, resulting in the final state with two vector bosons and two jets - $VVjj$. The VBS is an EW process, however the $VVjj$ final state occurs also in processes involving the strong

interaction. Processes with only EW vertices that lead to the $VVjj$ final state include VBS diagrams and other non-VBS contributions, which cannot be gauge invariantly separated from the VBS diagrams [156]. At the Born level, they are described by α_{EW}^4, where α_{EW} is the strength of the EW interaction. Interactions with EW and strong vertices that result in the $VVjj$ final states are described by $\alpha_S^2\alpha_{EW}^2$ at the Born level, where α_S is the strength of the strong interaction. The Feynman diagrams for the ssWW process are shown in Figure 81, including both EW and EW+strong contributions. The same-sign $W^\pm W^\pm$ production does

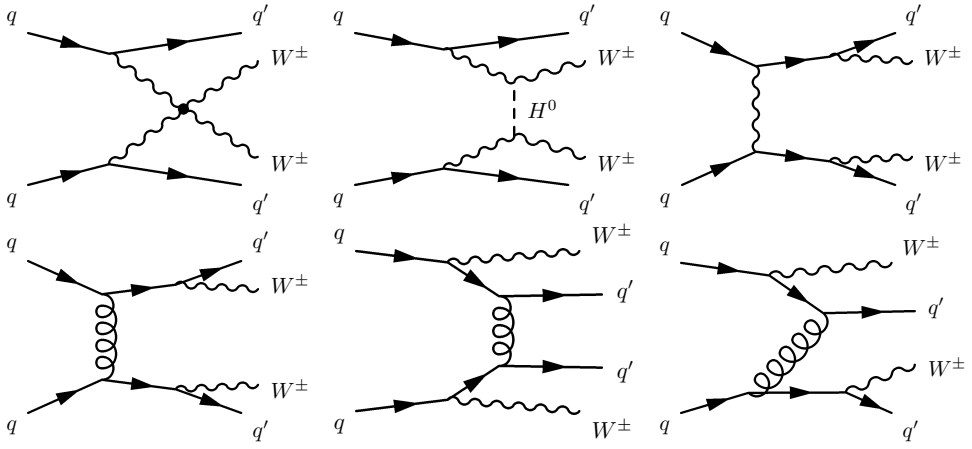

Figure 81.: Feynman diagrams for the $W^\pm W^\pm jj$ final states. The top row shows the electroweak contributions; quartic gauge boson vertex, Higgs exchange and non-VBS diagrams, respectively. The bottom row shows the strong contributions.

not contain s-channel $Z/\gamma^*/H$ exchange diagrams, but only the quartic gauge vertex and the t- , u-channel $Z/\gamma^*/H$ exchange diagrams. Compared to other VBS processes, like $W^+W^- \to W^+W^-$ or $W^\pm Z \to W^\pm Z$, the EW production in the ssWW scattering dominates over the strong production cross section, making the ssWW channel a prime candidate to study QGCs.

The $W^\pm W^\pm jj$ production was already studied by ATLAS [157] using the 20.3 fb^{-1} of the Run-1 data at $\sqrt{s} = 8$ TeV, where the evidence for the EW $W^\pm W^\pm jj$ production was observed with $3.6\,\sigma$, while $2.8\,\sigma$ was expected from the SM, and the combined EW and strong production was observed with $4.5\,\sigma$ with $3.4\,\sigma$ expected. The same channel was also studied with the CMS detector [158].

10.3 Performance assumptions at the HL-LHC

To summarise; the HL-LHC will operate at $\sqrt{s} = 14$ TeV where the luminosity will reach up to $7 \cdot 10^{34}$ cm^{-2} s^{-1}, allowing experiments to collect 3000 fb^{-1} of integrated luminosity during its operation time. Such a high luminosity leads up to in average $\langle\mu\rangle = 140$ interactions per bunch-crossing.

Several studies have already investigated the prospects for the VBS at the HL-LHC [159, 160]. This analysis focuses only on the possible benefits of an extended tracker for the ssWW process. Two possible extension scenarios in the ITk η coverage are considered: the medium tracker (MT) with $|\eta| \leq 3.2$ and the extended tracker (ET) with $|\eta| \leq 4.0$, and the benefits of both are compared to the nominal η coverage (NT) with $|\eta| \leq 2.5$.

This analysis models the ATLAS detector effects by using the DELPHES [161] fast detector simulation. DELPHES allows to study the impact of pileup effects on the signal significance and was the only tool at the beginning of this study offering this feature. The Run-1 DELPHES ATLAS detector model is properly validated in [162] showing a slightly more conservative performance with respect to the performance of the ATLAS detector.

The upgraded DELPHES ATLAS detector model is constructed by modifying the existing Run-1 DELPHES ATLAS detector model, using the performance assumptions from the Phase-II ATLAS upgrade. The performance assumptions at the HL-LHC are either taken from the Phase-II LoI [130] or from the studies done under the scope of the European Strategy [147] or European Committee for Future Accelerators [146]. The performance at $|\eta| = 2.5$ is extrapolated up to $|\eta| = 3.2$ or 4.0, assuming a continuous performance in the extended tracker region. In the case where performance assumptions for the upgraded ATLAS detector are not available, the performance at Run-1 is assumed. The following assumptions are made for the extended tracker region:

- Tracking efficiencies are 80% (94%) and 99% (99%) for electrons and muons with $p_T < 100\,\text{GeV}$ ($p_T > 100\,\text{GeV}$), respectively [130].
- The muon and charged track p_T resolution is 5% for $p_T < 100\,\text{GeV}$ and 7% for $p_T > 100\,\text{GeV}$ [130].
- The reconstruction efficiency for muons is approximately 97%, 85% for electrons and 76% for photons. For electrons and photons it depends on their p_T [146, 147].
- Trigger efficiencies are 88% for electrons and 86% for muons [146].
- Electron energy resolution, and muon and charged hadron momentum resolution are shown in Tables 55 and 56 in the Appendix.

More information about the performance assumptions for the extended tracker region can be found in the Appendix, Section B.1.

10.4 Backgrounds and Sample Generation

The signal topology of the ssWW scattering is very similar to the VBF Higgs production described in Chapter 5. The two initial quarks which radiate two W bosons hadronise into two well separated, highly energetic forward jets. The final state $W^\pm W^\pm jj$ consists of two Ws with the same electric charge and this analysis considers only their leptonic decays into a lepton-neutrino pair. The two final state leptons are energetic and isolated, they have the same electric charge and tend to be in the central rapidity region with respect to the two tag jets. A large missing transverse momentum is expected as well.

The background composition in this study is based on the 8 TeV analysis [157], where the observed signal to background ratio is ≈ 1. The dominant background contribution comes from the "prompt lepton backgrounds", like $W^\pm Z/\gamma^*$ decays to $\ell^\pm\ell^\mp\ell^\pm\nu$, whenever additional leptons are not reconstructed or are outside of the experimental acceptance. The $WZ/\gamma^* jj$ is the largest background and represents $\approx 50\%$ of the total background yields. The second largest contribution ($\approx 25\%$) comes from the "conversion backgrounds" including the $W\gamma$ production and processes giving oppositely charged prompt leptons, mainly Drell-Yan and $t\bar{t}$ decays where misidentification of lepton charge occurs predominantly due to hard electron bremsstrahlung followed by photon conversion. The remaining backgrounds include leptons from hadron decays ($\approx 15\%$) and the strong $W^\pm W^\pm jj$ production ($\approx 9\%$).

Particularly for this study, only two background processes from the 8 TeV analysis are explicitly generated; the strong $W^{\pm}W^{\pm}jj$ production labelled as $W^{\pm}W^{\pm}jj - QCD$, and the $WZ/\gamma^{*}jj$ background. The signal $W^{\pm}W^{\pm}jj - EW$ and both background samples are generated at $\sqrt{s} = 14$ TeV in their inclusive final states with two hard-scattered jets, using the LO MADGRAPH5 MC generator and PYTHIA8 for modelling of the additional jets from parton showers, hadronization and the underlying event. Table 42 shows their LO cross-sections. All processes consider only final states with electrons or muons, excluding tau leptons. The renormalisation and factorisation scales are set to the default MADGRAPH dynamic scale, based on the central m_T^2 scale after k_T-clustering of the event [163]. The G_F scheme is used for the electroweak processes and `cteq6l1` is used as a parton distribution function. The generator level phase space selection and the dependence of cross-section on the increase in lepton acceptance are shown in the Appendix, Section B.2.

Process	Final state	Cross Section [fb]
$W^{\pm}W^{\pm}jj - EW$	$\ell^{\pm}\nu\ell^{\pm}\nu jj$	16
$WZ/\gamma^{*}jj$	$\ell^{\pm}\nu\ell\ell jj$	255
$W^{\pm}W^{\pm}jj - QCD$	$\ell^{\pm}\nu\ell^{\pm}\nu jj$	12

Table 42.: The LO cross-sections for the SM $W^{\pm}W^{\pm}jj - EW$ signal and $WZ/\gamma^{*}jj$ and $W^{\pm}W^{\pm}jj - QCD$ background processes produced by MADGRAPH5+PYTHIA8. The error on the cross-section calculation is less than 0.05%.

Other backgrounds (jets misidentified as leptons, mismeasurement of lepton's electric charge, etc.) at the 8 TeV analysis are either estimated by the data or arise due to detector effects. Since the material distribution of the upgraded ATLAS detector is still unknown and the MC modelling of all the remaining backgrounds (labelled as "other SM bkgs.") is out of the scope of this study, they are not explicitly generated. Instead, their contributions is estimated as being equal to 70% of the event yields from both generated background processes, $WZ/\gamma^{*}jj$ and $W^{\pm}W^{\pm}jj - QCD$, in order to reproduce the same background composition as it was observed in the 8 TeV analysis[4]. The total background yields therefore equal to $1.7 \cdot (WZ/\gamma^{*}jj + W^{\pm}W^{\pm}jj - QCD)$.

10.5 Pileup, Object Reconstruction and Event Selection

10.5.1 Pileup

Additional p-p interactions (in-time pileup) can be added to the DELPHES detector model on an event-by-event basis. Pileup events are drawn from an external minimum bias sample generated with HERWIG++ [164] and are randomly placed along the beam axis with a maximum longitudinal spread of 10 cm. The number of pileup events follows a Poisson distribution around the mean number of interactions per bunch crossing, $\langle\mu\rangle$. For this study, the average number of pileup events is taken to be either 0, 80 or 140 [5].

4 A similar relative background composition between the 8 TeV and the future analysis at the HL-LHC is assumed. In reality, the relative background composition may change at the HL-LHC, for example due the increased material in the forward region which would increase the $W + \gamma$ background contribution, but studying such effects is out of the scope of this study.

5 Even though the foreseen average number of pileup interactions at the HL-LHC is $\langle\mu\rangle = 140$, the nominal pileup scenario at the beginning of this study, agreed within the SM LETF, was set to $\langle\mu\rangle = 80$ since most of extrapolation assumptions for the upgraded detector response were made for $\langle\mu\rangle = 80$ scenario.

10.5.2 Object reconstruction

All analysis objects are reconstructed in DELPHES. Electrons, muons and photons are identified from the generator level particles and reconstructed with a certain reconstruction efficiency when they are within the tracking volume. The electrons and photons are clustered using the generator level particle information. The electron energy is smeared with a resolution specified according to the calorimeter region it points to, and a Gaussian smearing is applied to the muon transverse momentum.

Jets are reconstructed from all objects which deposit energy in the calorimeter, including electrons and photons, using the anti-k$_T$ algorithm with $R = 0.4$. Jets associated to a parent b-quark are identified assuming an identification efficiency as a function of jet p_{T} and η [146, 147], simulating $\approx 70\%$ b-tagging efficiency.

The reconstruction of the missing transverse momentum is based on the calorimeter energy deposits and charged track information using the particle-flow algorithm [162]. The E_T^{miss} is defined as a negative vector sum of transverse momenta associated with tracks or calorimeter objects as selected by the particle-flow algorithm.

DELPHES subtracts pileup interactions using reconstructed vertices from jets and isolated electrons, muons and photons. The contribution from charged particles in pileup interactions is removed by discarding tracks which are displaced from the primary vertex by more than $\Delta z = 0.1$ mm. The pileup contribution to the calorimeter energy is estimated by the FastJet area method [165], using the anti-k$_T$ algorithm with $R = 0.4$.

10.5.3 Event selection

The final state objects in the $W^{\pm}W^{\pm}jj - EW$ signal include two forward, energetic jets, two same-charge energetic and isolated leptons and a large E_T^{miss}. The $W^{\pm}W^{\pm}jj - EW$ signal region for the 14 TeV analysis is therefore defined through various kinematic selections based on these objects and closely follows the SR definition from the 8 TeV analysis.

Events are preselected by accepting only events with more than two leptons with $p_{\mathrm{T}} > 15$ GeV. Later, these criteria are tightened by selecting only events with *exactly two* leptons having the same electric charge ($e^{\pm}e^{\pm}$, $\mu^{\pm}\mu^{\pm}$ or $e^{\pm}\mu^{\pm}$) and $p_{\mathrm{T}} > 25$ GeV. In addition, the selected leptons should be well separated ($\Delta R_{\ell\ell} > 0.3$), be within the tracking acceptance ($|\eta| < 2.5$, $|\eta| < 3.2$ or $|\eta| < 4.0$), and their invariant mass should be larger than 20 GeV. Events with additional leptons (more than three leptons with $p_{\mathrm{T}} > 7$ GeV or $p_{\mathrm{T}} > 6$ GeV for electrons and muon, respectively) are rejected, reducing the contribution from the $WZ/\gamma^{*}jj$ background. In order to reduce the contamination from the $Z \to ee$ decays, a Z-veto $|m_{ee} - m_Z| > 10$ GeV is imposed in the ee final states[6]. Events are additionally required to have at least two jets with $p_{\mathrm{T}} > 30$ GeV and $|\eta| < 4.5$. Jets and leptons should be well separated, $\Delta R_{\ell j} > 0.3$. Events with b-jets are vetoed with $\approx 70\%$ identification efficiency. The leading and subleading jet in p_{T} - the tag jets, are required to have a large invariant mass, $m_{jj} > 500$ GeV, and a large pseudorapidity gap, $\Delta\eta_{jj} > 2.4$. These selection criteria, including the cut on the missing transverse momentum $E_T^{\mathrm{miss}} > 40$ GeV, define the 8 TeV SR and are collectively named the "VBS-8TeV" criteria.

Along the course of this study, several selection criteria have been optimised for the HL-LHC conditions and some new selection criteria have been added. The Final Selection criteria are described in Section 10.7.4.

6 Charge misidentification for $\mu\mu$ final states is negligible.

10.6 The Significance Method

The 3000 fb^{-1} of integrated luminosity at the HL-LHC will deliver enough data to reduce statistical uncertainties in the physics measurements, making their systematic uncertainties the dominant contribution to their precision. This study assumes an analytical form of the likelihood function $\mathcal{L}$ defined in [166], where the observed number of events n follows a Poissonian distribution with a mean of $s+b$ and is convoluted with a Gaussian distribution to account for the uncertainty on the background estimation

$$\mathcal{L}(b) = \frac{(s+b)^n}{n!} e^{-(s+b)} \cdot \frac{1}{\sqrt{2\pi}\sigma_B} e^{-(m-b)^2/2\sigma_B^2}. \tag{113}$$

s represents the expected number of signal events, b is the unknown parameter and represents the expected number of background events, and m is the measured number of background events following the Gaussian distribution with a known standard deviation σ_B. For this analysis, the relative background uncertainty σ_B is set to 15%, which roughly corresponds to the 8 TeV results from [157]. The discovery significance can be expressed as [120, 166–168]

$$Z_{\sigma_B} = \sqrt{2\left[(s+b)\log\left(\frac{s+b}{b_0}\right) + b_0 - s - b\right] + \frac{(b-b_0)^2}{\sigma_B^2}}, \tag{114}$$
$$b_0 = \frac{1}{2}\left(b - \sigma_B^2 + \sqrt{\left(b-\sigma_B^2\right)^2 + 4(s+b)\sigma_B^2}\right),$$

where b_0 maximises $\mathcal{L}$ for the tested background-only hypothesis.

10.7 Performance Studies

Increased center of mass energy, luminosity and pileup at the HL-LHC, and the extension of the tracking region require additional optimisation and performance studies to maximise the signal significance. These studies are described in this section. Starting with *loosening* the isolation criteria in DELPHES, performance studies focus on how to benefit from the extended tracker by rejecting additional leptons and pileup jets in the forward region and finish with the definition of the Final Selection criteria.

10.7.1 Lepton isolation

The lepton isolation criteria are applied at the reconstruction stage in DELPHES and help to improve the quality of the charged lepton collection. For each reconstructed electron, muon or photon the isolation variable $I(P)$ is defined as

$$I(P) = \frac{\sum_{i\neq P}^{\Delta R_{max}<R,\ p_T(i)>p_T^{min}} p_T(i)}{p_T(P)}, \tag{115}$$

where the denominator is the transverse momentum of the particle of interest $P = e, \mu, \gamma$, and the numerator represents the sum of the transverse momenta above p_T^{min} of all particles[7] within a cone of ΔR_{max} around the particle P, excluding P. Typically, values of $I \approx 0$ indicate isolated particles.

7 The particle-flow objects (tracks and calorimeter towers) enter the isolation variable [162].

The default DELPHES isolation criteria are defined as

$$\Delta R_{max} = 0.5,\ p_{\mathrm{T}}^{min} = 0.5\ \mathrm{GeV},\ I < 0.1, \tag{116}$$

and create a dependency of the final event yields on the pileup scenario - a 50% (40%) difference in the $W^{\pm}W^{\pm}jj - EW$ event yields, at the end of the VBS-8TeV selection, is observed between $\langle\mu\rangle = 0$ and $\langle\mu\rangle = 140$ (80). These large discrepancies are due to the fact that the default isolation criteria allow more pileup interactions in the vicinity ($\Delta R_{max} < 0.5$) of the object of interest, failing the isolation criteria. As the mean pileup $\langle\mu\rangle$ increases, the probability that a pileup interaction is near the primary vertex increases as well and with it the probability that an object lies within $\Delta R_{max} < 0.5$. By tightening the ΔR_{max} cone, or by raising the p_T^{min} threshold, a fewer number of objects appear in the vicinity of the object of interest, making it isolated and passing the isolation criteria.

Various isolation criteria are tested by modifying ΔR_{max}, p_T^{min} threshold or I. Figure 82 shows the VBS-8TeV selection efficiencies and the signal-to-background ratio for all considered isolation criteria.

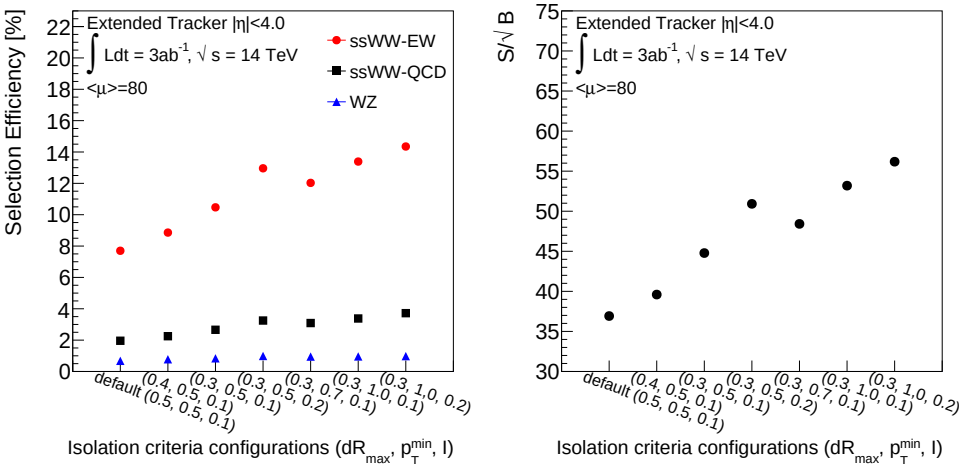

Figure 82.: The efficiency of the VBS-8TeV selection criteria - percentage of events left at the end of the VBS-8TeV event selection (left), and the signal-to-background ratio, $S/\sqrt{B}$ (right), both as a function of the considered isolation criteria. The results are shown for the extended tracker $|\eta| \leq 4$ with $\mathcal{L} = 3\ \mathrm{ab}^{-1}$ and $\langle\mu\rangle = 80$.

The looser selection

$$\Delta R_{max} = 0.3,\ p_{\mathrm{T}}^{min} = 1.0\ \mathrm{GeV},\ I < 0.1, \tag{117}$$

is chosen as the *optimal* isolation criteria: the choice of $\Delta R_{max} = 0.3$ is motivated by the 8 TeV analysis where ΔR_{max} was also set to 0.3 and the value of $p_T^{min} > 1$ GeV has been agreed upon between all LETF SM analyses. The isolation criterion with $\Delta R_{max} = 0.3, p_{\mathrm{T}}^{min} = 1.0$ GeV, $I < 0.2$ gives a slightly better $S/\sqrt{B}$ ratio, but since the increase is only $\sim 5\%$ [8] and because the cut on p_T^{min} is already tight enough compared to the default isolation requirement, and in addition, $I \approx 0.1$ was also the default choice in the 8 TeV analysis, a more conservative choice of $I = 0.1$ has been chosen for the optimal isolation criterion. Figure 83 shows the $m_{\ell\ell}$

8 A 5% increase in the $S/\sqrt{B}$ ratio is negligible with respect to the sensitivity of this analysis which is estimated to be between 10% and 20%.

distribution after the lepton preselection, using the default and optimal isolation criteria for various pileup scenarios. At the preselection stage, the differences in the event yields among the different pileup scenarios are $\approx 10\%$ when using the optimal isolation criteria and reduce to the percent level at the end of the event selection.

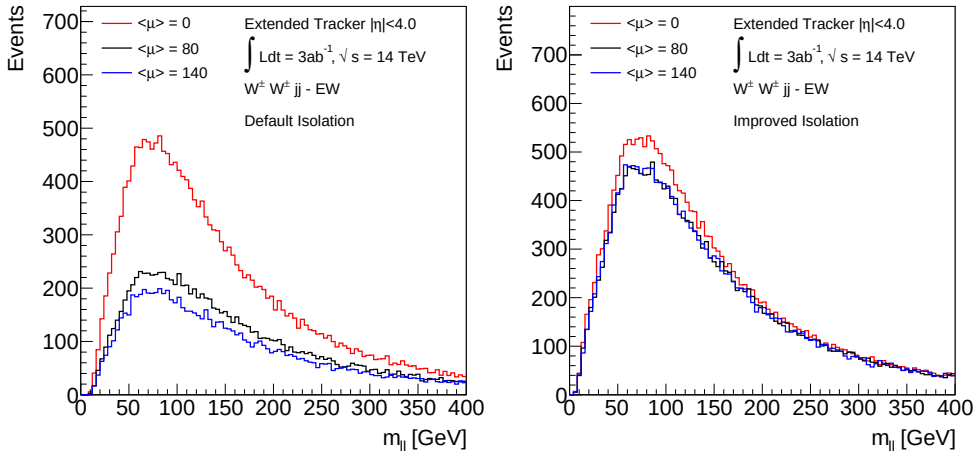

Figure 83.: The $m_{\ell\ell}$ distribution of the $W^{\pm}W^{\pm}jj - EW$ signal sample for various pileup scenarios, using the default lepton isolation criteria (left) and the optimal lepton isolation criteria (right), shown at the preselection stage.

10.7.2 Additional lepton veto

Rejecting any additional lepton accompanying the two signal leptons reduces background contribution in the ssWW analysis, e.g. the $WZ/\gamma^{*}jj$ background which contains three leptons in the final states.

The *additional,* 3^{rd} *lepton veto* criterion, rejects events with ≥ 3 leptons in the final state. An extended tracker would increase the lepton acceptance, making the 3^{rd} lepton veto more effective. Figure 84 shows the η distribution of the additional leptons for $\langle\mu\rangle = 140$ and Table 43 shows the number of additional leptons in the $WZ/\gamma^{*}jj$ sample in different η ranges. Extending the tracker up to $|\eta| \leq 3.2$ increases the number of additional leptons that could be rejected by 14% and extending the tracker even further, up to $|\eta| \leq 4.0$, accounts for 6% more of the additional leptons in the acceptance of the tracker. Therefore, an extended tracker provides a further background rejection, and increases the sensitivity of the ssWW analysis by $\approx 20\%$ compared to the nominal tracker, as shown in Table 43.

10.7.3 Rejection of pileup jets

Extended tracker coverage can improve pileup rejection whenever pileup identification uses track information, like the jet vertex fraction method (see Section 4.3). Unfortunately, the DELPHES fast simulation does not provide track information in the final output, thus a simplified method, the *Unmatched Jet Removal* (UJR) criterion, is designed to simulate the effects of pileup jet removal.

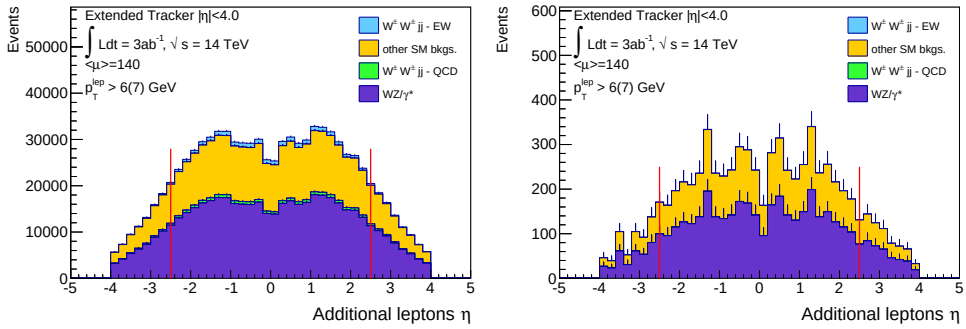

Figure 84.: The η distribution of additional leptons with $p_T > 6(7)$ GeV for $e(\mu)$, after lepton preselection (left) and after all VBS-8TeV criteria excluding the 3rd lepton veto (right). Line at $|\eta| = 2.5$ indicates the border between NT and MT or ET.

	Lepton preselection		VBS-8TeV selection	
	N	Δ	N	Δ
$\|\eta\| < 2.5$	102434	80%	910	82%
$2.5 < \|\eta\| < 3.2$	18584	14%	137	12%
$3.2 < \|\eta\| < 4.0$	8242	6%	67	6%
$2.5 < \|\eta\| < 4.0$	26826	21%	204	18%

Table 43.: The number of additional leptons in the $WZ/\gamma^* jj$ sample N, for various pseudorapidity regions and their percentage Δ with respect to the total number of additional leptons at the lepton preselection stage and after the VBS-8TeV selection for $\langle\mu\rangle = 140$. The 3rd lepton veto was not included in the VBS-8TeV selection.

The potential pileup jets are identified using the *truth information*: reconstructed tag jets are matched to the generator level truth jets that originated solely from the hard interaction. If a reconstructed tag jet is within the cone of $\Delta R < 0.35$ around a hadronic truth jet with $p_T > 20$ GeV, a tag jet is labelled as "matched tag jet". Otherwise, the tag jet is called an "unmatched tag jet" and is rejected with a certain efficiency depending on its η; an unmatched tag jet is removed with 95% efficiency if it is found in the central rapidity region (CR) $|\eta| \leq 2.5$ and with 90% efficiency whenever it belongs to an extended region (ER), $2.5 < |\eta| \leq 4.0$. The UJR efficiencies follow the recommendations from [130].

Figure 85 shows the η distribution of matched and unmatched tag jets. The η distribution of matched tag jets has the expected two peaks in the forward region, specific for the VBS topology. The structure of unmatched tag jets arises mostly due to the calorimeter structure and segmentation. For $\langle\mu\rangle = 0$, the unmatched tag jets represent mostly jets from parton showering and the underlying event, peaking in the central rapidity region. With the increasing $\langle\mu\rangle$, two peaks arise at $|\eta| \approx 2.5$ and $|\eta| \approx 3.2$. The first peak at $|\eta| \approx 2.5$ is due to the increased scattering of hard scatter jets or jets from the underlying event with the detector material (that area has many "cracks" in the detectors coverage). Since the UJR criterion is very rough and since around $|\eta| \approx 2.5$ there are more jets to choose from, the UJR might be mis-identifying more real jets as pileup jets than in other areas. The second peak at $|\eta| \approx 3.2$ is due to the transition to the FCal and its segmentation. A study using $Z \to \nu\bar{\nu}$ events showed that an increase in the segmentation of the FCal reduces the peak at $|\eta| \approx 3.2$

in the unmatched tag (pileup) jets distribution. The increased granularity of the FCal allows a better distinction between jets (clearer boundaries between jet cones) and consequently a better identification of the pileup jets, and is a good motivation for the installation of the sFCal in the ATLAS detector at the HL-LHC. However, studying these effects in more detail is outside of the scope of this analysis.

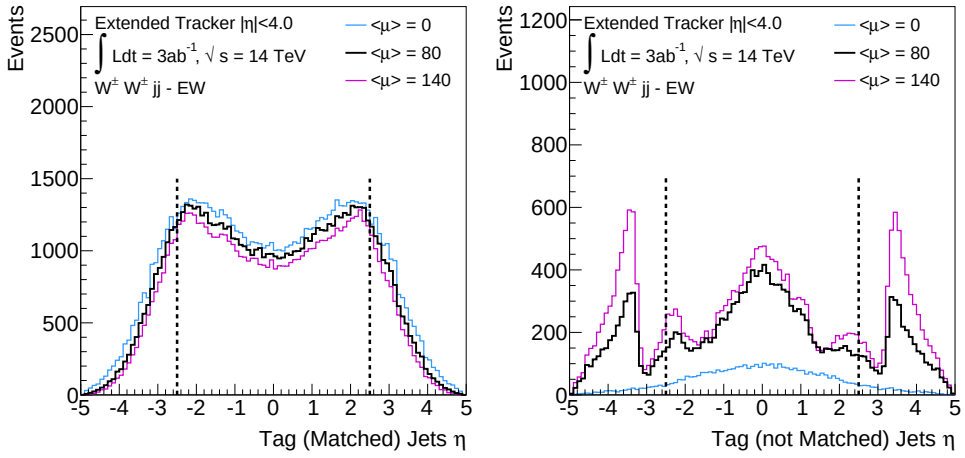

Figure 85.: The η distribution of the matched tag jets (left) and unmatched tag jets (right) in the $W^{\pm}W^{\pm}jj - EW$ signal sample. A reconstructed tag jet is matched to a generator level truth hadronic jet originating from the primary vertex if $\Delta R(\text{truth, reco}) < 0.35$. Distributions are shown at the preselection stage. The dashed line indicates $|\eta| = 2.5$.

An additional rejection of the pileup jets is possible by raising the jet p_{T} threshold. A higher p_{T} threshold does not explicitly benefit from the extended tracker coverage, but a good measurement of jet p_{T} is still needed in the forward region which is mostly dominated by the unmatched tag jets.

Various combinations of the VBS-8TeV selection, the UJR criterion and various jet p_{T} thresholds are tested for the final selection. Table 44 presents their effects on the event yield of matched and unmatched tag jets, compared to the baseline VBS-8TeV selection. The combination of VBS-8TeV + UJR removes 77% more events with an unmatched tag jet with respect to to the VBS-8TeV selection, while at same time removing only 9% more signal (matched tag) jets. Similarly, the combination of VBS-8TeV and $p_{\text{T}}^{\text{jet}} > 60\,\text{GeV}$ removes 58% (17%) more of the unmatched (matched) tag jets compared to the VBS-8TeV selection. The most optimal selection criterion is the combination of VBS-8TeV, UJR and $p_{\text{T}}^{\text{jet}} > 60\,\text{GeV}$ criteria, removing in total 89% (21%) more pileup (signal) jets as in the VBS-8TeV selection and it is added to the Final Selection. Figure 86 shows the η distribution of the matched and unmatched tag jets for all considered scenarios.

10.7.4 Final selection criteria

In order to adapt the ssWW event selection to the environment at the HL-LHC, the UJR and the $p_{\text{T}}^{\text{jet}} > 60\,\text{GeV}$ criteria are added to the VBS-8TeV selection. Additionally, various other kinematic selections are optimised to increase the signal-to-background ratio. The optimisation is done by maximising the significance Z_{σ_B} (Equation 114), separately for the

Selection	Percent difference in event yields wrt. VBS-8TeV	
	Matched Tag Jets	Unmatched Tag Jets
VBS-8TeV + $p_T^{jet} > 60\,GeV$	17%	58%
VBS-8TeV + $p_T^{jet} > 100\,GeV$	49%	92%
VBS-8TeV + UJR	9%	77%
VBS-8TeV + UJR - CR (95%) only	2%	20%
VBS-8TeV + UJR - ER (90%) only	7%	61%
VBS-8TeV + UJR + $p_T^{jet} > 60$ GeV	**21**%	**89**%
VBS-8TeV + UJR + $p_T^{jet} > 100\,GeV$	49%	98%

Table 44.: Percent difference in final event yields of various scenarios with respect to the VBS-8TeV only selection. The results are shown for the $W^{\pm}W^{\pm}jj - EW$ signal sample at $\langle\mu\rangle = 140$. The selection in bold is chosen for the Final Selection.

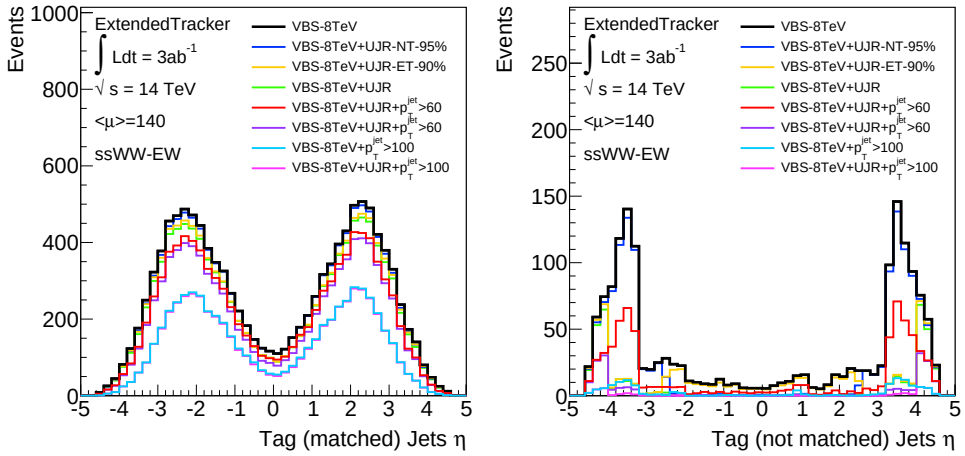

Figure 86.: The η distributions for matched (left) and unmatched (right) tag jets for different combinations of VBS-8TeV, UJR and p_T^{jet} selection criteria. The UJR and p_T^{jet} criteria are applied at the end of VBS-8TeV selection.

nominal (NT) and the extended (ET) tracker. At the time of the optimisation studies, the nominal pileup scenario was set to $\langle\mu\rangle = 80$. During the course of this analysis, it changed to $\langle\mu\rangle = 140$ but the same results as obtained from the optimisation studies at $\langle\mu\rangle = 80$ are assumed also for the $\langle\mu\rangle = 140$ scenario. Therefore, further improvements can be expected from optimising the kinematic selections at $\langle\mu\rangle = 140$.

The signal significance is maximised for m_{jj} and lepton centrality ζ, which is defined as

$$\zeta = \min[\max(\eta_{l1}, \eta_{l2}) - \min(\eta_{j1}, \eta_{j2}), \max(\eta_{j1}, \eta_{j2}) - \max(\eta_{l1}, \eta_{l2})]. \quad (118)$$

Lepton centrality ζ measures how central are the final state leptons with respect to the tag jets and in the VBS topology the two final state leptons are expected to be more central than the two tag jets. In the optimisation procedure all VBS-8TeV selection criteria are applied, including the UJR and $p_T^{jet} > 60\,GeV$ criteria, except for the criterion under the optimisation.

The highest significance is reached for $m_{jj} > 2\,\text{TeV}$ and $\zeta > 2.0$. Since the optimisation revealed similar results, within the statistical uncertainties, for the NT and ET, the same optimal values are chosen for both trackers. Table 45 summarises the final $W^{\pm}W^{\pm}jj - EW$ SR selection criteria.

Cut	Description
Lepton preselection	$N_\ell \geq 2$ with $p_{\text{T}} > 15\,\text{GeV}$
VBS-8TeV selection:	
lepton selection	$N_\ell \equiv 2$, lepton trigger, $p_{\text{T}}^{\ell} > 25\,\text{GeV}$, $\lvert\eta_\ell\rvert < 2.5$ (or 3.2 or 4.0)
3$^{\text{rd}}$ lepton veto	removes events with ≥ 3 leptons with $p_{\text{T}} > 6\,(7)\,\text{GeV}$
$m_{\ell\ell}$ cut	$m_{\ell\ell} > 20\,\text{GeV}$
same-sign leptons	accept only leptons with the same electric charge
jet selection	$N_{\text{jets}} \geq 2$, $p_{\text{T}}^{\text{jet}} > 30\,\text{GeV}$ within $\lvert\eta_{\text{jet}}\rvert < 4.5$
$\Delta R_{\ell\ell,jj}$	$\Delta R_{\ell\ell} > 0.3$, $\Delta R_{\ell j} > 0.3$
Z-veto in ee channel	$\lvert m_{ee} - m_Z\rvert > 10\,\text{GeV}$
MET	$E_T^{\text{miss}} > 40\,\text{GeV}$
m_{jj}	$m_{jj} > 500\,\text{GeV}$
b-jet veto	$\sim 70\%$ b-jet identification efficiency
$\Delta\eta_{jj}$	$\Delta\eta_{jj} > 2.4$
Final selection: VBS-8TeV selection +	
UJR criterion	removes unmatched tag jets: $\Delta R(\text{truth,reco}) > 0.35$ 95% in the central region $\lvert\eta\rvert < 2.5$ 90% in the extended region $2.5 < \lvert\eta\rvert < 4.0(3.2)$
jet p_{T} criterion	$p_{\text{T}}^{\text{jet}} > 60\,\text{GeV}$
m_{jj}	$m_{jj} > 2\,\text{TeV}$
lepton centrality	$\zeta > 2.0$

Table 45.: The VBS-8TeV and the Final Selection criteria defining the $W^{\pm}W^{\pm}jj - EW$ signal region. The Final Selection contains all VBS-8TeV criteria with a few modified/added cuts.

10.8 The SM Results

The benefits of an extended tracker for the ssWW scattering rely mostly on the ability to reject additional leptons and pileup jets in the forward region.

This analysis considers three tracker scenarios; NT, MT and ET. The event yields for all three pseudorapidity ranges are summarised in Table 46 and the signal significances Z_{σ_B}, assuming a 15% uncertainty on the background estimation, are presented in Table 47.

The improvement in signal significance due to the ET is mostly pronounced for higher pileup scenarios; at $\langle\mu\rangle = 140$ the extended tracker improves the significance by $\approx 100\%$ compared to the nominal tracker and improves the precision of the cross-section measurement by a factor of 2. The benefit of the medium tracker is not so pronounced; at $\langle\mu\rangle = 140$ only a 3% improvement in signal significance is observed while at $\langle\mu\rangle = 0$ (which is of course an unrealistic scenario at the HL-LHC) the MT improves the Z_{σ_B} measurement by 24%. The reason for such a low improvement of the MT with respect to the NT at higher pileup scenarios is due to the UJR criterion. Figure 87 shows the η distribution of the leading

	Nominal Tracker		Medium Tracker		Extended Tracker	
Cut	Signal	Background	Signal	Background	Signal	Background
lepton selection	12600 ± 50	367000 ± 700	14600 ± 60	422000 ± 700	15300 ± 60	443000 ± 700
3rd lepton veto	12600 ± 50	344000 ± 700	14600 ± 60	391000 ± 700	15300 ± 60	407000 ± 700
$m_{ll} > 20$ GeV	12500 ± 50	342000 ± 700	14500 ± 60	388000 ± 700	15200 ± 60	404000 ± 700
jet selection	7800 ± 40	59000 ± 300	8800 ± 50	68000 ± 300	9100 ± 50	71000 ± 300
UJR cut	7500 ± 40	51000 ± 200	8300 ± 40	58000 ± 200	7900 ± 40	53000 ± 200
$\Delta R_{ll,lj} > 0.3$	7500 ± 40	51000 ± 200	8300 ± 40	58000 ± 200	7800 ± 40	53000 ± 200
ee Z veto	7300 ± 40	49000 ± 200	8100 ± 40	56000 ± 200	7700 ± 40	52000 ± 200
MET > 40 GeV	6900 ± 40	46000 ± 200	7700 ± 40	52000 ± 200	7200 ± 40	48100 ± 200
$m_{jj} > 2000$ GeV	1200 ± 20	1100 ± 40	1300 ± 20	1300 ± 40	1200 ± 20	780 ± 30
b-jet veto	1200 ± 20	1100 ± 30	1300 ± 20	1300 ± 40	1200 ± 20	760 ± 30
$\Delta\eta_{jj} > 2.4$	1200 ± 20	990 ± 30	1300 ± 20	1200 ± 40	1200 ± 20	670 ± 30
$\zeta > 2.0$	190 ± 10	150 ± 10	180 ± 10	150 ± 10	160 ± 10	40 ± 10

Table 46.: The $W^{\pm}W^{\pm}jj - EW$ signal and background ($1.7 \cdot (WZ/\gamma^{*}jj + W^{\pm}W^{\pm}jj - QCD)$) event yields at $\langle\mu\rangle = 140$ and $\mathcal{L} = 3$ ab^{-1}. Only statistical uncertainties are shown.

$\langle\mu\rangle$	Nominal Tracker		Medium Tracker			Extended Tracker		
	Z_{σ_B}	σ_σ	Z_{σ_B}	$\Delta_{MT/NT}$	σ_σ	Z_{σ_B}	$\Delta_{ET/NT}$	σ_σ
0	22 ± 3	$4\% \pm 1\%$	28 ± 4	24%	$4\% \pm 1\%$	26 ± 4	13%	$4\% \pm 1\%$
80	15 ± 1	$7\% \pm 1\%$	15 ± 1	3%	$7\% \pm 1\%$	29 ± 4	98%	$4\% \pm 0\%$
140	6.5 ± 0.5	$15\% \pm 1\%$	6.7 ± 0.5	3%	$15\% \pm 1\%$	13 ± 1	98%	$8\% \pm 1\%$

Table 47.: The Z_{σ_B} signal significance for the SM $W^{\pm}W^{\pm}jj - EW$ measurement shown for the nominal, medium, and extended tracker for different pileup scenarios using the final event selection. The results are shown for $\langle\mu\rangle = 140$ and $\mathcal{L} = 3$ ab^{-1}. Only statistical uncertainties are shown. A 15% systematic uncertainty is assumed on the background prediction in the Z_{σ_B} calculation. The $\Delta_{ET/NT}$ ($\Delta_{MT/NT}$) indicates the percent difference of the extended (medium) tracker with respect to the nominal tracker and σ_σ indicates the expected precision of the cross-section measurement, estimated as $1/Z_{\sigma_B}$.

and subleading tag jets. The forward region ($|\eta| > 2.5$) shows a clear increase in background contributions due to the pileup jets and other poorly reconstructed jets. The increase in the background yields is especially pronounced for the subleading jet distributions around $|\eta| \approx 3.5$, where the ATLAS detector has the transition region between the central and forward calorimeters. The UJR criterion removes the unmatched tag jets, but since the majority of the pileup jets dwell in the region with $|\eta| > 3.5$, they are just out of reach of the MT, while covered by the ET - the UJR criterion in the NT and MT removes only approximately 15% of the background events, while removing approximately 25% of the background yields in the ET. This effect negates an overall benefit of the MT with respect to the NT. However, the event selection was never optimised specifically for the MT due to the time shortage. In addition, the simulation of the forward calorimeters in DELPHES may also impact the results, thus further improvements are expected with additional optimisation of the event selection and studies of the forward calorimeters.

In addition to the forward pileup jets rejection, the extended tracker provides a better background rejection (3rd lepton veto). Figure 88 shows the η distribution of the leading lepton for the NT and ET. Naturally, an increase in the tracker acceptance also increases the background contribution in the forward region, thus a cut of $|\eta| < 2.5$ for the signal leptons might be beneficial and is considered as a possible improvement to the future event selection.

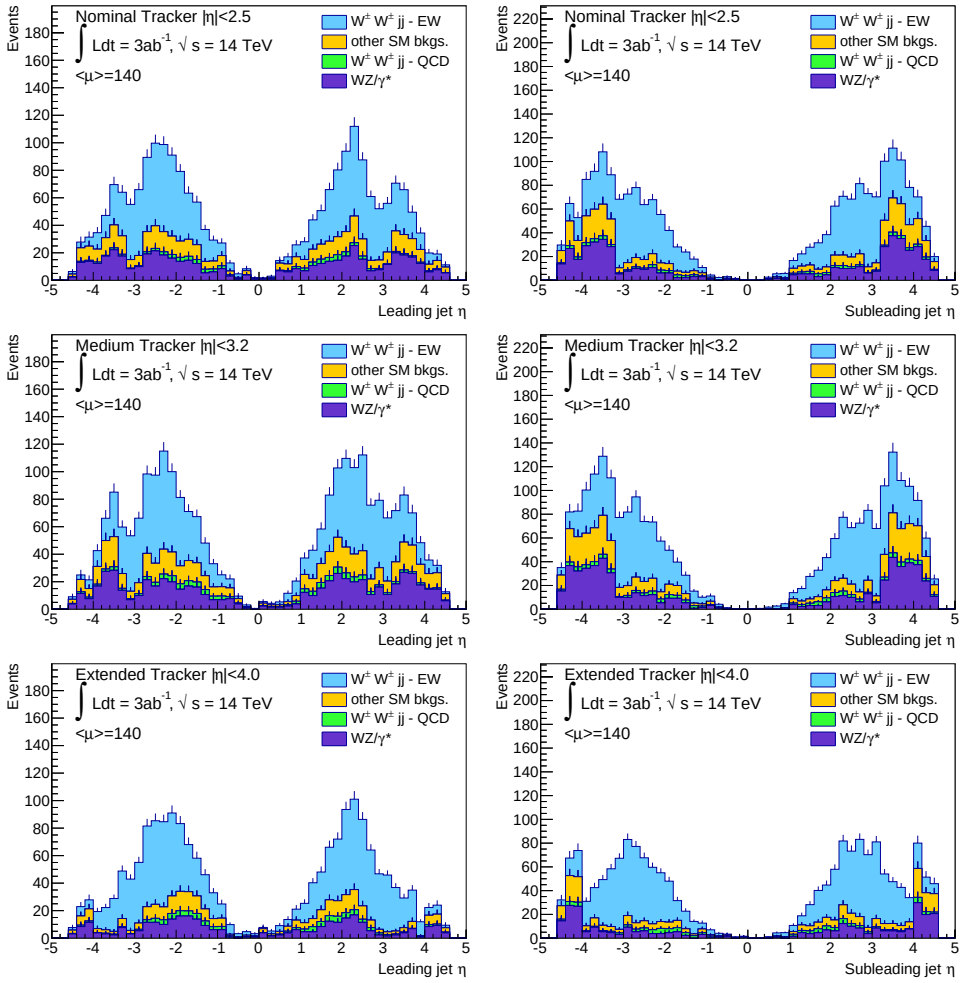

Figure 87.: The leading (left) and sub-leading (right) jet η distributions shown for the nominal tracker (top), medium tracker (middle), and the extended tracker (bottom) after the final event selection (excluding the ζ criterion) for $\langle\mu\rangle = 140$ at $\mathcal{L} = 3\ \text{ab}^{-1}$.

Figure 89 shows the m_{jj}, $\Delta\eta_{jj}$, ζ and $m_{jj\ell\ell}$ (the invariant mass of the final state leptons and jets) distributions after the Final Selection, excluding the cut on lepton centrality[9], for the NT and ET. The extended tracker coverage reduces the background contributions in all distributions.

10.8.1 Comparison of DELPHES results with other studies

The results from the 8 TeV ssWW data analysis [157] are compared to the analysis using the Run-1 DELPHES ATLAS detector model and VBS-8TeV event selection criteria with the signal and backgrounds samples generated at $\sqrt{s} = 8\,\text{TeV}$. The expected significance from

9 The criterion on the lepton centrality highly reduces statistics and is left out just for presentation purposes.

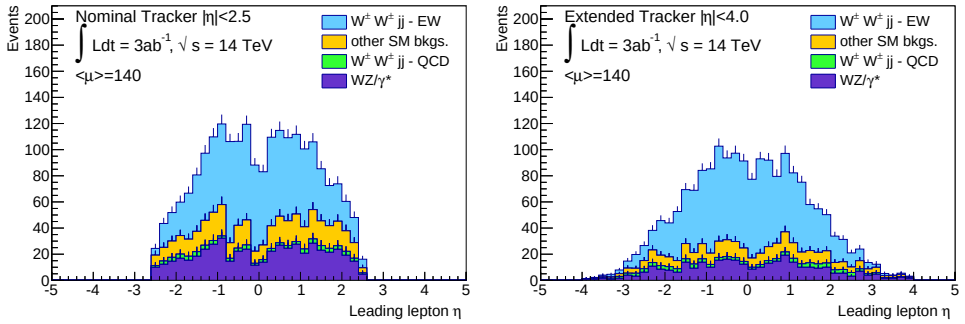

Figure 88.: The leading lepton η distribution shown for the nominal tracker (left) and the extended tracker (right) after the final event selection (excluding the ζ criterion) for $\langle\mu\rangle = 140$ at $\mathcal{L} = 3\ \text{ab}^{-1}$.

the 8 TeV data analysis is $2.8\,\sigma$, while $Z_{\sigma_B} = 2.0\,\sigma$ is obtained using the DELPHES detector model. The $\approx$ 30% agreement between the two analyses is expected considering the fact that DELPHES gives more *conservative* predictions of the ATLAS detector performance (see validation studies in [162]), only two background processes have been explicitly included in the analysis, and the signal and background samples have been generated only at the LO.

The results of the analysis described in this thesis are additionally cross-checked by an independent study using `TruthToReco` smearing functions [169], where the signal objects are smeared according to the mean number of pileup events, but no additional pileup is added. In this study, the WHIZARD [170] MC generator is used to generate the $W^{\pm}W^{\pm}jj - EW$ signal sample while the two background samples are generated by MADGRAPH5. The expected significances for the NT and ET at $\langle\mu\rangle = 80$ are compared between the two analyses, using the same event selection criteria and a reasonable agreement between them is obtained - the DELPHES method shows a 19% improvement while the `TruthToReco` method shows a 29% improvement in Z_{σ_B} for the extended tracker with respect to the nominal tracker.

An approximately 30% discrepancy between the two analyses is expected, since the two methods use different MC generators for the signal sample and consequently use different renormalisation and factorisation scales, which accounts for $\sim$ 10% discrepancy in the final signal event yields. Additionally, they use different generator level selection criteria, resulting in a 5% difference and a 15% discrepancy is estimated to come from different detector simulations methods, all in all totalling 30%.

10.9 THE NEW PHYSICS RESULTS

Several NP $W^{\pm}W^{\pm}jj - EW$ signal samples have been generated for different values of $f_{T,1}$ using the LO MADGRAPH5+PYTHIA8, and their cross-sections are shown in Table 48. In this case, the SM $W^{\pm}W^{\pm}jj - EW$ signal is considered as a background.

Figure 90 shows the $m_{jj\ell\ell}$ distribution for the nominal and the extended tracker for two New Physics scenarios; $f_{T,1}/\Lambda^4 = 0.2\,\text{TeV}^{-4}$ and $f_{T,1}/\Lambda^4 = 0.4\,\text{TeV}^{-4}$. The $m_{jj\ell\ell}$ is the most robust and sensitive variable to detect NP contributions [159, 160], which are mostly visible at high $m_{jj\ell\ell}$ values.

Table 49 shows the Z_{σ_B} for the NT and ET at $\langle\mu\rangle = 140$. An extended tracker can improve the NP significance potential by $\approx$ 40% for $f_{T,1}/\Lambda^4 = 0.2\,\text{TeV}^{-4}$ and by $\approx$ 50% for

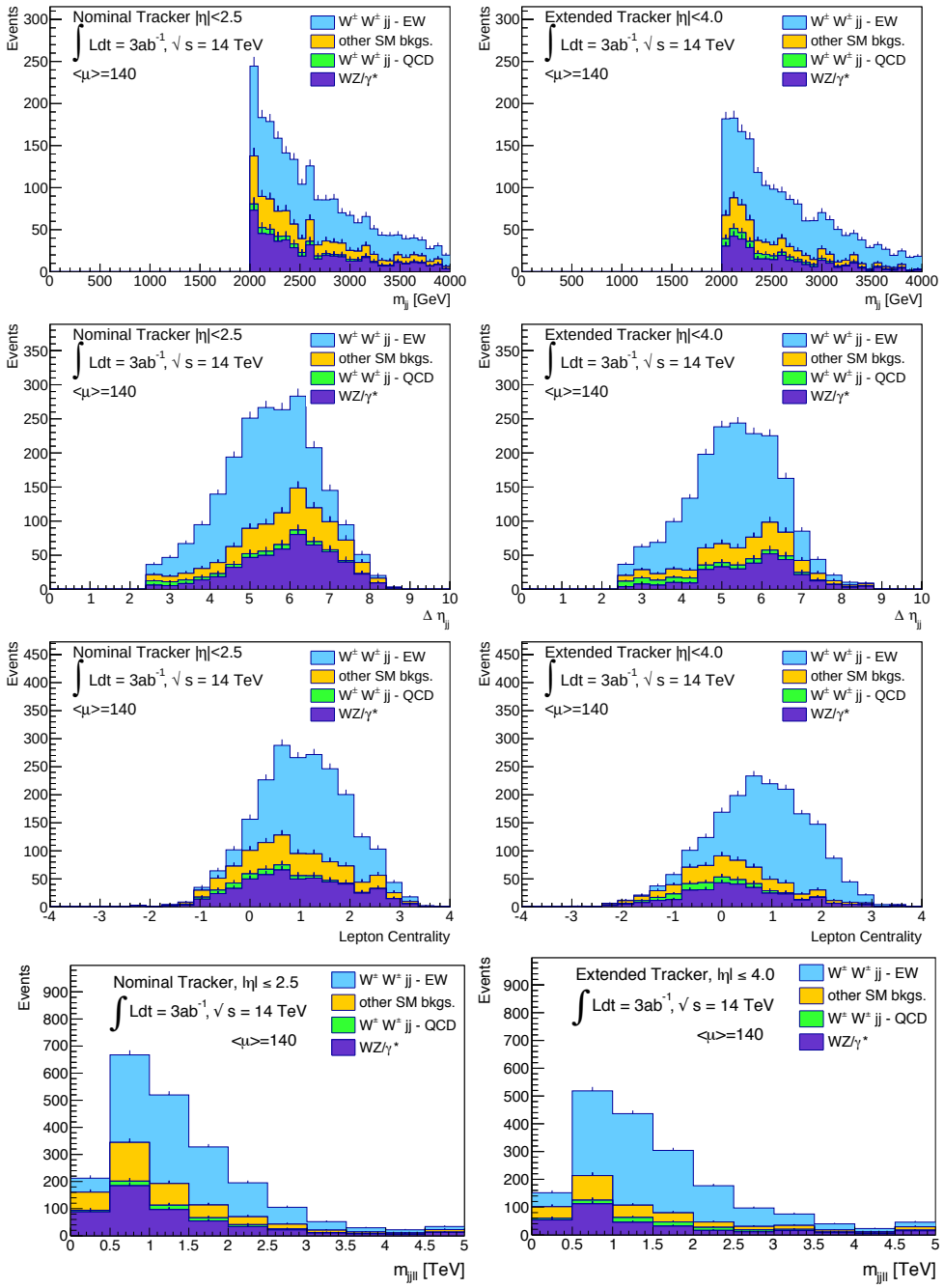

Figure 89.: The m_{jj} (first/top row), $\Delta\eta_{jj}$ (second row), ζ (third row) and $m_{jj\ell\ell}$ (fourth/bottom row) distributions shown for the nominal tracker (left) and the extended tracker (right) after the Final Selection, excluding the criterion on ζ. The distributions are shown for $\langle\mu\rangle = 140$ and $\mathcal{L} = 3$ ab^{-1}.

$f_{T,1}/\Lambda^4$ [TeV^{-4}]	Cross Section [fb]
0.05	16.1
0.08	16.2
0.1	16.2
0.2	16.7
0.4	18.9

Table 48.: The NP $W^{\pm}W^{\pm}jj - EW$ cross-sections for various $f_{T,1}/\Lambda^4$ coupling strengths. The samples are produced by MADGRAPH5+PYTHIA8. No corrections to account for unitarity violation are considered in the sample generation.

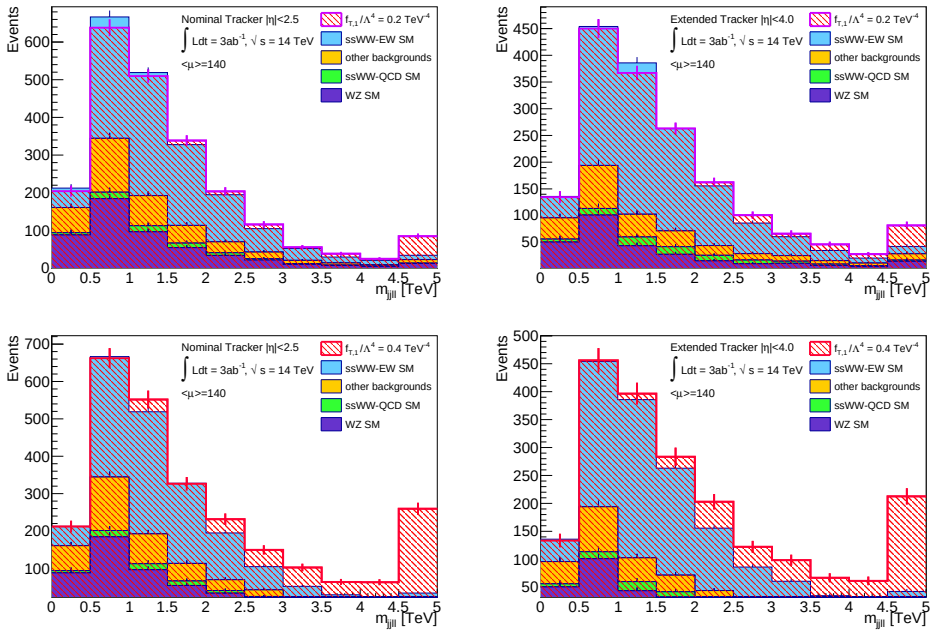

Figure 90.: The invariant mass of the two leading jets and leptons, $m_{jj\ell\ell}$, for the new physics scenario with $f_{T,1}/\Lambda^4 = 0.2\,\text{TeV}^{-4}$ (top) and $f_{T,1}/\Lambda^4 = 0.4\,\text{TeV}^{-4}$ (bottom) for the nominal tracker (left) and the extended tracker (right). The distributions are shown after the final selection, excluding lepton centrality, with $\langle\mu\rangle = 140$ at $\mathcal{L} = 3\,\text{ab}^{-1}$. The last bin contains the overflow. Only statistical error bars are plotted. A 15% systematic uncertainty is used in the Z_{σ_B} calculation.

$f_{T,1}/\Lambda^4 = 0.4\,\text{TeV}^{-4}$. The NP significance potential is estimated without further optimisations targeting specifically the NP contributions, and additional improvements are expected with the optimised event selection.

$f_{T,1}/\Lambda^4$	Nominal Tracker	Extended Tracker	
$[\text{TeV}^{-4}]$	Z_{σ_B}	Z_{σ_B}	$\Delta_{(ET-NT)/NT}$
0.05	3.58 ± 0.08	4.87 ± 0.10	36%
0.08	3.45 ± 0.05	4.46 ± 0.06	29%
0.1	3.45 ± 0.06	4.39 ± 0.06	27%
0.2	3.36 ± 0.06	4.74 ± 0.07	41%
0.4	4.25 ± 0.03	6.49 ± 0.04	53%

Table 49.: The Z_{σ_B} significance for various NP scenarios with different coupling strengths $f_{T,1}/\Lambda^4$ of the dimension-8 operator, $\mathcal{O}_{T,1}$, shown for the nominal and extended tracker at $\langle\mu\rangle = 140$ and $\mathcal{L} = 3$ ab^{-1}. $\Delta_{(ET-NT)/NT}$ represents the percent difference in Z_{σ_B} between NT and ET.

10.10 CONCLUSIONS

This analysis investigates the benefits of extending the ITk coverage (up to $|\eta| \leq 3.2$ - medium tracker or 4.0 - extended tracker) on the signal significance of the same-sign WW scattering, using the DELPHES fast simulation. The extended tracker improves the background rejection (a $\approx 20\%$ increase in the sensitivity due to the 3$^{\text{rd}}$ lepton veto) and pileup jets rejection in the forward region. All in all, almost a $\approx 100\%$ improvement in the significance measurement is observed due to the extended tracker. The improvement in Z_{σ_B} for the medium tracker is only at the percent level due to the effects of the Unmatched Jet Removal criterion, but additional analysis optimisation may improve this result. The extended tracker improves the sensitivity for the New Physics contributions as well, up to $\approx 50\%$ with no additional optimisations of the event selection.

The Large Eta Task Force (LETF) considered various other physics processes to study the benefits of the extended tracking. One of them was the VBF Higgs production with the Higgs boson decaying into WW. Specifically for the VBF $H \to WW^{(*)}$ analysis, extending the η coverage of the ITk could be beneficial due to improved tagging of forward (signal) jets, possible b-tagging in the forward region which could reduce the contamination from the top background, and using the track information from the forward region to improve the estimation of the $p_T^{\text{miss, jet-corr}}$ and $p_{\text{T}}^{\text{sum}}$. The LETF VBF $H \to WW^{(*)}$ analysis is a continuation of the VBF $H \to WW^{(*)}$ analysis described in Chapter 9 with a few optimisations[10] and observes a $\sim 27\%$ increase in the signal significance when extending the η coverage up to 4.0 and an improvement of $\sim 8\%$ when extending it to 3.2. Assuming a $\sim$ 10-fold better pileup rejection these values increase to $\sim 54\%$ and $\sim 13\%$, respectively.

The two analyses cannot be directly compared since they both use different analysis methods and apply different assumptions. However, both of them show an improvement when extending the tracking range up to $|\eta| \leq 4.0$. Even if absolute values of significance measurements change in the future analyses, one of the main messages of these studies is that the pileup jets in the forward region will represent a big challenge at the HL-LHC and new, efficient methods ought to be developed to suppress them.

10 The LETF VBF $H \to WW^{(*)}$ analysis uses the same MC samples as the analysis presented in Chapter 9 and the same performance assumptions. Nevertheless, some optimisations are done to the event selection in order to cope with pileup jets in the forward region and are described in [145].

CONCLUSIONS

The search for the Higgs boson has been the focus of particle physics for more than 40 years and its discovery in 2012 completes the Standard Model, provided the observed particle is indeed the SM Higgs boson. To test the true nature of the discovered boson, all its properties need to be precisely measured.

The Run-1 of the LHC provided the first measurements of its mass $m_H = 125.09 \pm 0.21(\text{stat.}) \pm 0.11(\text{syst.})\,\text{GeV}$ [23] and its spin and CP, which favour the SM prediction of $J^{CP} = 0^{++}$ [26, 27]. Some of the Higgs boson couplings to the SM particles and its production and decay rates have also been observed. But not all.

This thesis is dedicated to the search of one particular combination of Higgs production and decay mode that has not been observed so far - the Higgs boson produced via vector boson fusion (VBF) decaying into two W bosons and subsequently into a lepton-neutrino pair; VBF $H \to WW^{(*)} \to \ell^+\nu_\ell\ell^-\bar{\nu}_\ell$. The VBF production mode is important as it probes for the direct couplings of the Higgs boson with the vector bosons.

The data analysis presented in this thesis includes the full 2011 and 2012 datasets and observes *the first evidence* for the VBF production mechanism in the $H \to WW^{(*)}$ channel with 3.2 standard deviations. The signal strength of the VBF $H \to WW^{(*)}$, μ_{VBF} equals to $1.27\,^{+0.44}_{-0.41}\,(\text{stat.})\,^{+0.30}_{-0.21}\,(\text{syst.}) = 1.27\,^{+0.53}_{-0.45}$.

The measurements of the signal strengths and Higgs couplings (Yukawa couplings through the gluon-fusion and vector boson couplings through VBF) in the $H \to WW^{(*)}$ channel agree with the SM predictions and show no signs of New Physics contributions, *within their uncertainties*. The measured signal strengths are greatly dominated by their statistical uncertainties, especially μ_{VBF}. Future runs of the LHC will deliver more statistics and therefore reduce their impacts on the precision of measurements. A feasibility study described in this thesis, analysing the VBF $H \to WW^{(*)}$ signal strength measurement at 300 fb^{-1} (Run-3) revealed that the precision on μ_{VBF} improves from current $\sim$ 42% to $\sim$ 25%. If the amount of accumulated data increases by an additional factor of 10, reaching 3000 fb^{-1} (Run-4), the precision on μ_{VBF} improves even further to $\sim$ 15%. Higher amounts of accumulated data reduce the impact of statistical uncertainties and consequently increase the importance of systematic uncertainties. The understanding of different contributions of systematic uncertainties on the signal and backgrounds processes, which has been also extensively studied in this thesis, is therefore becoming increasingly more important.

Figure 91 compares the final Run-1 results across all considered Higgs decay channels with their prospects at the upgraded LHC. The signal strength precision in the most sensitive Higgs boson channels, $H \to ZZ$, $H \to \gamma\gamma$ and $H \to WW^{(*)}$ (combining all production modes) improves, reaching $\sim$ 5% during Run-4 of the LHC. In addition, $3000\,\text{fb}^{-1}$ also provide $\mathcal{O}(10\%)$ precision for other decay channels, like $H \to \mu\mu$, which currently suffer from large statistical uncertainties.

In the SM, the Higgs mechanism is fully responsible for the electroweak symmetry breaking (EWSB), a mechanism which provides masses for the SM particles. Whether this is really the case, or whether there are additional mechanisms at the TeV scale, can be most elegantly studied through vector boson scattering (VBS). The cross-section for scattering of longitudinally polarised vector bosons increases with energy and the SM Higgs boson precisely cancels

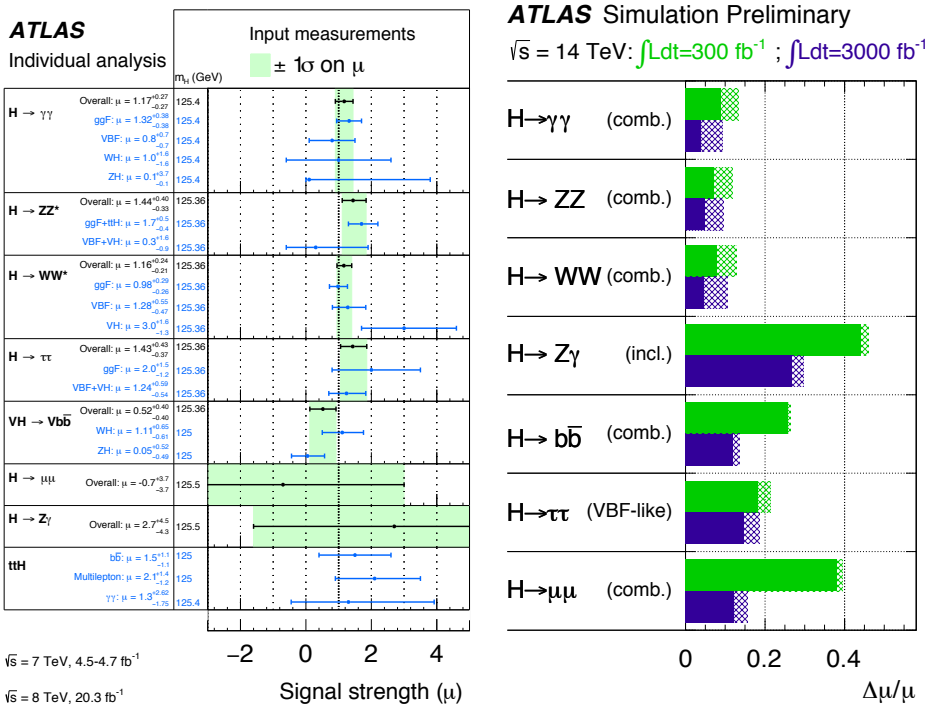

Figure 91.: Measurement of the observed signal strengths from the combination of all considered Higgs decay channels with the Run-1 data [171] (left) and their prospects at the HL-LHC [160] (right). The green bands indicate a $\pm 1\,\sigma$ band around the μ measurement.

these unitarity-violating effects. If some New Physics contributes to the EWSB can be tested by precisely measuring the vector boson self-couplings and their couplings to the Higgs boson. This thesis studied the VBS in terms of the benefits of an extended tracking coverage of the future Inner TracKer (ITk), an ATLAS sub-detector which is to replace the Inner Detector at the HL-LHC, to the sensitivity of VBS and New Physics. Increasing the tracker up to $|\eta| \leq 4.0$ increases the SM signal significance by almost 100% with respect to the nominal tracker coverage of $|\eta| < 2.5$ and improves the sensitivity for New Physics searches by $\approx 50\%$. The biggest benefit of an extended tracker comes from an improved background and pileup jets rejection in the forward region. Extending the tracking coverage improves the sensitivity of physics measurements, especially those with forward topologies, like VBS or VBF Higgs production[1] and is considered as a possible improvement to the current designs of the ITk.

The SM is not the complete and ultimate theory of everything, it is merely its low-energy approximation. There are phenomena that the SM does not have an explanation for, like the origin of dark matter. One would think that the discovery of the Higgs boson would bring some peace of mind to the particle physicists, yet it does not. The existence of the observed Higgs boson actually triggers further questions, like: *Is the observed Higgs boson the only one?*, *Is it fully responsible for the EWSB?*, *Why is the Higgs mass so small, compared to the huge quantum-corrections?*, and many others. Future runs of the LHC will hopefully provide answers to

1 The improvement in significance of VBF $H \to WW^{(*)}$ measurement due to the extended tracker is $\sim 27\%$ with respect to the nominal tracker and $\sim 54\%$ with the tenfold increase in pileup rejection.

these questions. The second run on the LHC has just started and interesting new results are on their way. No one knows what the p-p collisions are hiding this time but we all long for a surprise. The next big discovery may come in the form of a supersymmetric particle or as a discrepancy of precisely measured Higgs couplings to vector bosons with respect to the SM predictions, hinting on the presence of New Physics.

APPENDICES

A THE $H \to WW^{(*)} \to \ell^+\nu_\ell\ell^-\bar{\nu}_\ell$ EVENT SELECTION FOR GGF AND VBF BDT ANALYSES

A.1 The VBF BDT event selection

Before the BDT training, the events have to pass the preselection criteria (see Section 5.3.1 in Chapter 5), $\geq$ 2-jets selection and the b-jet veto.

In order to discriminate the VBF signal from the backgrounds, the boosted decision tree is trained upon the following eight input variables:

- top-quark background rejection: $\mathbf{p}_{\mathrm{T}}^{\mathrm{sum}}$;
- enhancing VBF topology: lepton centrality $\sum C_\ell$, Δy_{jj}, m_{jj}, $\sum m_{\ell j}$;
- $H \to WW^{(*)}$ decay topology: $m_{\ell\ell}$, $\Delta\phi_{\ell\ell}$, m_T.

The lepton centrality C_ℓ is defined as: $C_\ell = \left|\eta_\ell - \frac{\sum\eta_{jj}}{2}\right| / \frac{\Delta\eta_{jj}}{2}$, with $\sum\eta_{jj} = \eta_j^{\mathrm{lead}} + \eta_j^{\mathrm{sublead}}$. The value of C_ℓ is greater than zero if η_ℓ is between the two tag jets. It is equal to one if η_ℓ is aligned with either of the tag jets, and is greater than one in case $|\eta_\ell| > |\eta_j|$. The sum of both final state lepton centralities is defined as $\sum C_\ell = C_\ell^{\mathrm{lead}} + C_\ell^{\mathrm{sublead}}$.

The $\sum m_{\ell j}$ discriminant is defined as the sum of all four (leading, subleading) jet-lepton combinations and it is used in the BDT analysis due to the different $\sum m_{\ell j}$ shapes of the Higgs signal with respect to the backgrounds.

Table 50 shows the event yields in the VBF BDT analysis after BDT classification for events with $\mathcal{O}_{\mathrm{BDT}} > -0.48$.

Selection	Summary						Composition of N_{bkg}									
	$N_{\mathrm{obs}}/N_{\mathrm{bkg}}$	N_{obs}	N_{bkg}	N_{signal}			N_{WW}		N_{top}		N_{misid}		N_{VV}	N_{dy}		
				N_{ggF}	N_{VBF}	N_{VH}	$N_{\mathrm{WW}}^{\mathrm{QCD}}$	$N_{\mathrm{WW}}^{\mathrm{EW}}$	$N_{t\bar{t}}$	N_t	N_{Wj}	N_{jj}		$N_{\ell\ell}$	$N_{\tau\tau}^{\mathrm{QCD}}$	$N_{\tau\tau}^{\mathrm{EW}}$
$e\mu/\mu e$	8.66 ± 2.41	57	44.3	4.6	11.5	0.1	6.8	1.7	19.1	3.5	3.7	2.1	3.5	-	4.4	0.6
$ee/\mu\mu$	9.11 ± 2.91	73	53.8	2.3	6.4	0.1	3.9	1.0	11.7	2.0	1.0	0.2	1.2	31.1	2.0	0.2

Table 50.: Event selection for the 8 TeV VBF BDT analysis for $e\mu/\mu e$ and $ee/\mu\mu$ final states with $\mathcal{O}_{\mathrm{BDT}} > -0.48$. The expected signal yield is split into N_{ggF}, N_{VBF}, and N_{VH} contributions. The N_{ggF} is treated as a background in the VBF analysis and is included in N_{bkg}. The expected yields of the dominant backgrounds are normalised. Entries 0.0 (-) indicate less than 0.1 (0.01) events. Energy-related quantities are in GeV.

A.2 The ggF event selection

Besides the VBF production mode, the $H \to WW^{(*)}$ analysis probes for the ggF production mode as well. The ggF analysis is split into three categories, differing in the number of jets that are accompanying the final state leptons: $n_j = 0$ and $n_j = 1$. The ggF signal is quite

considerable ($\sim$ 20%) in the $n_j \geq 2$ category as well and in order to further increase the sensitivity of the ggF measurements, the ggF signal in $n_j \geq 2$ category is analysed as well. All jet categories follow the common set of preselection criteria (see Section 5.3.1 in Chapter 5) before their selections start to differ.

ggF - the $n_j = 0$ category

The 0-jet category is heavily dominated by the Drell-Yan and the WW-irreducible backgrounds, even after the requirements on the missing transverse momentum at the preselection stage. Events with mismeasured $\mathbf{p_T}^{\text{miss, jet-corr}}$ are rejected by requiring that the $\mathbf{p_T}^{\text{miss, jet-corr}}$ points away from the dilepton transverse momentum $p_{\text{T}}^{\ell\ell}$, $\Delta\phi_{\ell\ell,p_{T,\text{rel}}^{\text{miss, jet-corr}}} > \pi/2$. With no reconstructed jets to balance the final state leptons, the $p_{\text{T}}^{\ell\ell}$ is expected to be large, while small for DY events. Requiring $p_{\text{T}}^{\ell\ell} > 30\,\text{GeV}$ highly reduces the $Z/\gamma^* \to \ell\ell$ background, which can be even further suppressed by selecting $p_{T,\text{rel}}^{\text{miss, jet-corr}} > 40\,\text{GeV}$.

Even after all these selection criteria, a significant fraction of $Z/\gamma^* \to \ell\ell$ events still contaminates the signal. The missing transverse momentum in such events is fake (no neutrinos in the final state) and the dilepton system can only be balanced by the soft hadronic recoil system. The variable f_{recoil}, measures the strength of the recoil system relative to the dilepton system and is defined as

$$f_{\text{recoil}} = \frac{\left|\sum_{\text{soft-jets}} |\text{JVF}| \cdot \mathbf{p_T^j}\right|}{p_{\text{T}}^{\ell\ell}}, \tag{119}$$

where the pileup jets are suppressed by weighting the jet's p_{T} by their JVF value. A cut on $f_{\text{recoil}} < 0.1$ reduces the DY events in the $ee/\mu\mu$ channel by a factor of seven.

The WW background is reduced by the Higgs boson topological selection; $\Delta\phi_{\ell\ell} < 1.8$ and $m_{\ell\ell} < 55\,\text{GeV}$. The $m_T < 130\,\text{GeV}$ requirement is added at the end of the event selection.

ggF - the $n_j = 1$ category

The $n_j = 1$ SR requires exactly one additional jet after the preselection criteria. The presence of one additional jet makes the top quark decays the dominant background at first, but after rejecting all events with a b-jet (the b-jet veto), WW and DY events dominate over the signal.

In order to reduce the contributions from multijets and $Z/\gamma^* \to \tau\tau$ backgrounds, the transverse mass of both leading and subleading leptons, defined as

$$m_{T\,\ell_i} = \sqrt{2 p_{T\,\ell_i} p_T^{\text{miss, jet-corr}} \left[1 - \cos\Delta\phi(p_{T\,\ell_i}, p_T^{\text{miss, jet-corr}})\right]}, \tag{120}$$

is required to be larger than 50 GeV in the $e\mu/\mu e$ channel.

In the $ee/\mu\mu$ channel, a tighter criterion on $p_{T,\text{rel}}^{\text{miss, jet-corr}}$ is imposed ($> 35\,\text{GeV}$) to reject the multijets background and therefore the cut on $m_{T\,\ell_i}$ is not required any more.

At this stage, the events in the $e\mu/\mu e$ channel are mostly dominated by $Z/\gamma^* \to \tau\tau$ and are rejected by the $Z \to \tau\tau$-veto.

The remaining selection criteria are the same as in the 0-jet channel: $f_{\text{recoil}} < 0.1$, where $p_{\text{T}}^{\ell\ell}$ is replaced by $p_{\text{T}}^{\ell\ell j} = p_{\text{T}}^{\ell\ell} + p_T^j$, and Higgs topological cuts.

ggF - the $n_j \geq 2$ category

After the preselection criteria, the ggF+2jets signal region is defined by requiring ≥ 2 jets, followed by the b-jet veto and the $Z \to \tau\tau$-veto in order to reject the top-quark and $Z/\gamma^* \to \tau\tau$

backgrounds respectively. The ggF+2jets events are further selected so that they are mutually exclusive to the VBF events - they must fail at least one of the VBF topological criteria, depending on which VBF analysis is used: $\Delta y_{jj} > 3.6$, $m_{jj} > 600\,\text{GeV}$, CJV or OLV for the cut-based VBF analysis, and either the CJV, OLV or $O_{\text{BDT}} > -0.48$ requirement for the BDT VBF analysis.

In addition to ensuring the VBF orthogonality, the VH events must also be rejected from the ggF+2jets category. The two leading jets from a VH event usually come from the vector bosons V (W, Z) decaying hadronically, which makes their rapidity gap smaller ($\Delta y_{jj} < 1.2$), and their invariant mass corresponding to the invariant mass of the vector boson, $|m_{jj} - 85| < 15\,\text{GeV}$. Inverting one of these two requirements is called a "VH-veto" and is a necessary cut for ensuring ggF+2jets orthogonality to VH events. The remaining criteria enhancing the Higgs signal are the same as in other analyses; $\Delta\phi_{\ell\ell} < 1.8$, $m_{\ell\ell} < 55\,\text{GeV}$ and $m_T < 130\,\text{GeV}$. The final event yields after the m_T requirement, for all three ggF categories, are summarised in Table 51. The summary of all requirements defining the ggF and VBF signal regions of the $H \to WW^{(*)}$ analysis is presented in Table 52.

Selection	Summary					Composition of N_{bkg}							
	$N_{\text{obs}}/N_{\text{bkg}}$	N_{obs}	N_{bkg}	N_{sig}		N_{WW}	N_{top}		N_{misid}		N_{VV}	N_{DY}	
				N_{ggF}	$N_{\text{VBF}}N_{\text{VH}}$		$N_{t\bar{t}}$	N_t	N_{Wj}	N_{jj}		$N_{\ell\ell}$	$N_{\tau\tau}$
0-jet category													
$e\mu/\mu e$	1.20 ± 0.04	1129	940	131	2.2	660	40	21	133	0.8	78	4.3	2.3
$ee/\mu\mu$	0.99 ± 0.05	510	517	57	1.3	349	11	8	53	-	31	64	0.1
1-jet category													
$e\mu/\mu e$	1.21 ± 0.06	407	335	42	6.6	143	76	30	40	0.5	42	1.1	2
$ee/\mu\mu$	1.11 ± 0.10	143	129	14	2.0	59	23	11	11	-	11	14	-
$\geq$ 2-jet category													
$e\mu/\mu e$	1.05 ± 0.07	210	200	13.3	4.5	35	131		16		15	3	

Table 51.: Final event yields for all three ggF 8 TeV analyses, presented separately for $e\mu/\mu e$ and $ee/\mu\mu$ final states at the $m_T < 130\,\text{GeV}$ stage. The expected signal yields are shown separately for N_{ggF} and $N_{\text{VBF}} + N_{\text{VH}}$ contributions. The expected yields of the dominant backgrounds are normalised. Entries are shown as 0.0 (-) if they represent less than 0.1 (0.01) events. Energy-related quantities are in GeV.

B GENERATOR LEVEL STUDIES FOR THE VBS AT HL-LHC

B.1 Performance assumptions for the extended tracker

The ATLAS detector effects are simulated using the DELPHES 3.2.1 fast-simulation. The detector performance is modified via DELPHES_card_ATLAS_PileUp.tlc card. The current DELPHES implementation does not consider the fake rates for electrons, muons or photons, but this effect is expected to be small in the VBS analysis[1].

Tables 53 and 54 show the assumed tracking and reconstruction efficiencies at the HL-LHC as implemented in the DELPHES simulation. Energy resolution for electrons and momentum resolution for muons and pions are shown in Tables 55 and 56. The same momentum resolution is assumed for muons and pions since no prediction for the pion momentum resolution at the HL-LHC was available at the beginning of this study. Trigger efficiencies, shown in Table 57, are applied at the analysis level assuming that the electron and muon single trigger efficiencies in the extended tracker region are comparable with the central region.

1 The misidentified leptons are the second smallest background in the VBF $H \to WW^{(*)}$ analysis (see Section 6.5), contributing only $\approx 9\%$ to the total background yield in the VBF SR. Since the VBS event topology is very similar to the VBF one, the effect of misidentified leptons on the VBS signal is assumed to be small as well.

Objective		ggF-enriched			VBF-enriched	
		$n_j = 0$	$n_j = 1$	$n_j \geq 2$ ggF	$n_j \geq 2$ VBF cut-based	$n_j \geq 2$ VBF BDT
Preselection	All n_j	$p_{\mathrm{T}}^{\mathrm{lead}} > 22$ for the leading lepton $p_{\mathrm{T}}^{\mathrm{sublead}} > 10$ for the subleading lepton Opposite-charge leptons $m_{\ell\ell} > 10$ for $e\mu/\mu e$ $m_{\ell\ell} > 12$ for $ee/\mu\mu$ $\lvert m_{\ell\ell} - m_Z \rvert > 15$ for $ee/\mu\mu$				
		$p_T^{\text{miss, jet-corr}} > 20$ for $e\mu/\mu e$ $E_{T,\text{rel}}^{\text{miss}} > 40$ for $ee/\mu\mu$	$p_T^{\text{miss, jet-corr}} > 20$ for $e\mu/\mu e$ $E_{T,\text{rel}}^{\text{miss}} > 40$ for $ee/\mu\mu$	$p_T^{\text{miss, jet-corr}} > 20$ for $e\mu/\mu e$ -	No MET requirement for $e\mu/\mu e$ -	
Background rejection	DY	$p_{T,\text{rel}}^{\text{miss (trk)}} > 40$ for $ee/\mu\mu$ $f_{\text{frecoil}} < 0.1$ for $ee/\mu\mu$ $p_{\mathrm{T}}^{\ell\ell} > 30$ $\Delta\phi_{\ell\ell,\text{MET}} > \pi/2$	$p_{T,\text{rel}}^{\text{miss (trk)}} > 35$ for $ee/\mu\mu$ $f_{\text{frecoil}} < 0.1$ for $ee/\mu\mu$ $m_{\tau\tau} < m_Z - 25$ -	- - $m_{\tau\tau} < m_Z - 25$ -	$p_T^{\text{miss, jet-corr}} > 50$ (40 for BDT) for $ee/\mu\mu$ $E_T^{\text{miss}} > 55$ (45 for BDT) for $ee/\mu\mu$ $m_{\tau\tau} < m_Z - 25$ -	
	Misid.	-	$m_T^{\ell} > 50$ for $e\mu/\mu e$	-	-	
	Top	$n_j = 0$ - -	$n_b = 0$ - -	$n_b = 0$ - -	$n_b = 0$ $p_{\mathrm{T}}^{\text{sum}} < 15$	$p_{\mathrm{T}}^{\text{sum}}$ input to BDT $\sum m_{\ell j}$ input to BDT
VBF topology		-	-	rejection of one of VBF & VH topological cuts	$m_{jj} > 600$ $\Delta y_{jj} > 3.6$ OLV central jet veto	m_{jj} input to BDT Δy_{jj} input to BDT $\sum C_\ell$ input to BDT $C_\ell^{lead} < 1$ and $C_\ell^{lead} < 1$ $O_{\text{BDT}} > -0.48$
$H \to WW^{(*)}$ $\to \ell^{\pm}\nu_\ell\ell^{\mp}\nu_\ell$ decay topology		$m_{\ell\ell} < 55$ $\Delta\phi_{\ell\ell} < 1.8$ No m_T requirement	$m_{\ell\ell} < 55$ $\Delta\phi_{\ell\ell} < 1.8$ No m_T requirement	$m_{\ell\ell} < 55$ $\Delta\phi_{\ell\ell} < 1.8$ No m_T requirement	$m_{\ell\ell} < 50$ $\Delta\phi_{\ell\ell} < 1.8$ No m_T requirement	$m_{\ell\ell}$ input to BDT $\Delta\phi_{\ell\ell}$ input to BDT m_T input to BDT

Table 52.: Summary of the event selection in the $H \to WW^{(*)} \to \ell^+\nu_\ell\ell^-\bar{\nu}_\ell$ analysis. Requirements apply for both $e\mu/\mu e$ and $ee/\mu\mu$ channels, unless it is specified otherwise. A dash (-) indicates no selection. All energy-related units are given in GeV.

	$\lvert\eta\rvert \leq 1.5$			$1.5 < \lvert\eta\rvert \leq 4.0$ (2.5)		
p_T [GeV]	electron	muon	pions	electron	muon	pions
$0.1 \leq p_T \leq 1.0$	0.73	0.75	0.70	0.50	0.70	0.60
$1.0 \leq p_T \leq 100$	0.90	0.99	0.92	0.80	0.99	0.85
$p_T > 100$	0.96	0.99	0.94	0.94	0.99	0.89

Table 53.: DELPHES tracking efficiencies for the upgraded ATLAS detector with an extended tracker coverage. Tracking efficiencies represent the probability that a charged particle is reconstructed as a track in the inner tracker volume with a perfect angular resolution. These efficiencies were combined from the Run-1 ATLAS detector efficiencies as implemented in DELPHES 3.2.1 and the tracking efficiencies of the upgraded ATLAS detector at HL-LHC [130]. Tracking efficiencies for tracks with $p_T < 0.1$ GeV or $\lvert\eta\rvert > 4.0$ (2.5) are assumed to be zero.

η	muons	electrons	photons
$\lvert\eta\rvert \leq 0.1$	0.54	$0.85 - 0.91 \cdot \exp(1 - p_T/20\text{GeV})$	$0.76 - 1.98 \cdot \exp(-p_T/16.1\text{GeV})$
$\lvert\eta\rvert > 0.1$	0.97		

Table 54.: DELPHES reconstruction efficiencies for the upgraded ATLAS detector with an extended tracker coverage. Reconstruction efficiencies for muons and photons are taken from [146], while the reconstruction efficiency for electrons is taken from [147]. No fake rate is assumed for electrons, muons or photons. Reconstruction efficiencies for leptons and photons with $\lvert\eta\rvert >$ 4.0 (2.5) are zero.

η	σ_E^2 [GeV]	parameters
$\eta \leq 1.4$	$0.3^2 + S^2E + C^2E^2$	$S = 0.10$, $C = 0.010$
$1.4 < \eta \leq 4.0$ (2.5)		$S = 0.15$, $C = 0.015$

Table 55.: Electron energy resolution in the upgraded ATLAS detector with an extended tracker coverage, taken from [147].

	Muon and pion momentum resolution; σ_{p_T}	
p_T [GeV]	$\lvert\eta\rvert \leq 1.5$	$1.5 < \lvert\eta\rvert \leq 4.0$ (2.5)
$p_T \leq 100$	0.015	0.05
$p_T > 100$	0.02	0.07

Table 56.: Muon and pion momentum resolution in the upgraded ATLAS detector with an extended tracker coverage, taken from [130].

	Trigger efficiencies	
η	electron	muon
$\lvert\eta\rvert \leq 1.05$	0.88	0.70
$1.05 < \lvert\eta\rvert \leq 4.0$ (2.5)	0.88	0.86

Table 57.: Trigger efficiencies in the upgraded ATLAS detector with an extended tracker coverage, taken from [146]. Trigger efficiencies are implemented at the analysis level.

B.2 Generator level selection

All SM and NP samples are generated by the MADGRAPH 5.2.1.1 MC generator and showered by PYTHIA8. Table 58 shows the selection criteria applied in MADGRAPH5 at the generator level.

Center of mass energy	$\sqrt{s} = 14$ TeV
Missing transverse momentum	$E_T^{\text{miss}} = 30$ GeV
Pseudorapidity	$\lvert\eta\rvert \leq 5$
Minimum transverse momentum	$p_{T,\text{jets}}^{\text{min}} = 20$ GeV
	$p_{T,\text{leptons}}^{\text{min}} = 1$ GeV
	$p_{T,\gamma}^{\text{min}} = 10$ GeV
Distance between objects	$\Delta R_{jj} = 0.35$
	$\Delta R_{\ell x} = 0.25$
	$\Delta R_{\gamma x} = 0.25$
Invariant mass	$m_{jj} = 50$ GeV
	$m_{\ell\ell} = 4$ GeV

Table 58.: Generator level selection criteria used in the MADGRAPH5 MC generator. The symbol x stands for jets, leptons or photons.

Figure 92 shows the LO cross-sections obtained at the parton level by MADGRAPH5, as a function of the increasing lepton rapidity acceptance, from $|\eta| \leq 2.5$ to $|\eta| \leq 4.9$. A 12% increase in the SM ssWW signal cross-section is expected due to the increase in the lepton pseudorapidity range from $|\eta| \leq 2.5$ to $|\eta| \leq 3.2$, and an additional 3% when extending fully to $|\eta| \leq 4$. The cross-section increases also for the $WZ/\gamma^* jj$ background sample, indicating an even greater impact when applying the 3$^{\text{rd}}$ lepton veto to reduce this background.

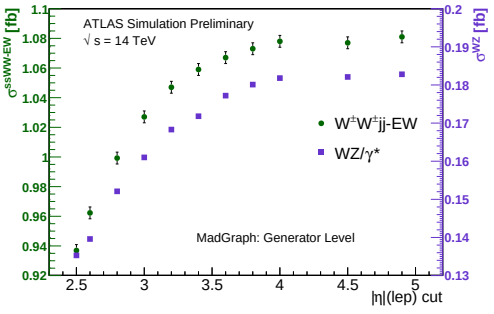

Figure 92.: The MADGRAPH5 MC LO cross-sections at the parton level in a fiducial region described by the VBS-8TeV selection with $m_{jj} > 2$ TeV, for the $W^{\pm}W^{\pm}jj - EW$ and $WZ/\gamma^* jj$ processes. Note the different axis labels for the $W^{\pm}W^{\pm}jj - EW$ and $WZ/\gamma^* jj$ production cross-sections.

BIBLIOGRAPHY

[1] P. W. Higgs, *Broken Symmetries and the Masses of Gauge Bosons*, *Phys. Rev. Lett.* 13 (1964) 508–509, DOI: 10.1103/PhysRevLett.13.508.

[2] P. W. Higgs, *Broken Symmetries, Massless Particles and Gauge Fields*, *Phys. Lett.* 12 (1964) 132–133, DOI: 10.1016/0031-9163(64)91136-9.

[3] P. W. Higgs, *Spontaneous Symmetry Breakdown without Massless Bosons*, *Phys. Rev.* 145 (1966) 1156–1163, DOI: 10.1103/PhysRev.145.1156.

[4] F. Englert and R. Brout, *Broken Symmetry and the Mass of Gauge Vector Mesons*, *Phys. Rev. Lett.* 13 (1964) 321–322, DOI: 10.1103/PhysRevLett.13.321.

[5] G. S. Guralnik, C. R. Hagen and T. W. B. Kibble, *Global Conservation Laws and Massless Particles*, *Phys. Rev. Lett.* 13 (1964) 585–587, DOI: 10.1103/PhysRevLett.13.585.

[6] T. W. B. Kibble, *Symmetry breaking in non-Abelian gauge theories*, *Phys. Rev.* 155 (1967) 1554–1561, DOI: 10.1103/PhysRev.155.1554.

[7] The LEP Collaborations, *Search for the Standard Model Higgs Boson at LEP*, *Phys.Lett. B* 565 (2003) 61–75, DOI: 10.1016/S0370-2693(03)00614-2, arXiv: 0306033v1 [hep-ph].

[8] The Tevatron Collaborations, *Combined CDF and D0 Search for Standard Model Higgs Boson Production with up to* 10.0 fb^{-1} *of Data* (2012), arXiv: 1203.3774 [hep-ph].

[9] The ATLAS Collaboration, *Observation of a new particle in the search for the Standard Model Higgs boson with the ATLAS detector at the LHC*, *Phys. Lett.* B716 (2012) 1–29, DOI: 10.1016/j.physletb.2012.08.020, arXiv: 1207.7214 [hep-ex].

[10] The CMS Collaboration, *Observation of a new boson at a mass of 125 GeV with the CMS experiment at the LHC*, *Phys. Lett.* B716 (2012) 30–61, DOI: 10.1016/j.physletb.2012.08.021, arXiv: 1207.7235 [hep-ex].

[11] M. Thomson, *Modern particle physics*, Cambridge University Press, 2013.

[12] K. A. Olive et al., *Review of Particle Physics*, *Chin. Phys.* C38 (2014) 090001, DOI: 10.1088/1674-1137/38/9/090001.

[13] D. Griffiths, *Introduction to Elementary particles*, 2nd ed., Wiley-VCH, 2010.

[14] S. Weinberg, *A Model of Leptons*, *Phys. Rev. Lett.* 19 (1967) 1264–1266, DOI: 10.1103/PhysRevLett.19.1264.

[15] S. L. Glashow, *Partial Symmetries of Weak Interactions*, *Nucl. Phys.* 22 (1961) 579–588, DOI: 10.1016/0029-5582(61)90469-2.

[16] A. Salam, *Weak and Electromagnetic Interactions* (), Originally printed in *Svartholm: Elementary Particle Theory, Proceedings Of The Nobel Symposium Held 1968 At Lerum, Sweden*, Stockholm 1968, 367-377.

[17] G. Altarelli and M. W. Grünewald, *Precision electroweak tests of the standard model*, *Phys. Rept.* 403-404 (2004) 189–201, DOI: 10.1016/j.physrep.2004.08.013, arXiv: hep-ph/0404165 [hep-ph].

[18] M. Baak, J. Cuth, J. Haller et al., *The global electroweak fit at NNLO and prospects for the LHC and ILC*, *Eur. Phys. J.* C74 (2014) 3046, DOI: 10.1140/epjc/s10052-014-3046-5, arXiv: 1407.3792 [hep-ph].

[19] A. Djouadi, *The Anatomy of electro-weak symmetry breaking. I: The Higgs boson in the standard model*, *Phys.Rept.* 457 (2008) 1–216, DOI: 10.1016/j.physrep.2007.10.004, arXiv: hep-ph/0503172 [hep-ph].

[20] J. Ellis, J. R. Espinosa, G. F. Giudice et al., *The Probable Fate of the Standard Model*, *Phys. Lett.* B679 (2009) 369–375, DOI: 10.1016/j.physletb.2009.07.054, arXiv: 0906.0954 [hep-ph].

[21] R. Assmann, M. Lamont and S. Myers, *A brief history of the LEP collider*, *Nucl. Phys. Proc. Suppl.* 109B (2002), [,17(2002)] 17–31, DOI: 10.1016/S0920-5632(02)90005-8.

[22] S. Holmes, R. S. Moore and V. Shiltsev, *Overview of the Tevatron Collider Complex: Goals, Operations and Performance*, *JINST* 6 (2011) T08001, DOI: 10.1088/1748-0221/6/08/T08001, arXiv: 1106.0909 [physics.acc-ph].

[23] The ATLAS and CMS Collaborations, *Combined Measurement of the Higgs Boson Mass in pp Collisions at $\sqrt{s} = 7$ and 8 TeV with the ATLAS and CMS Experiments*, *Phys. Rev. Lett.* 114 (19 May 2015) 191803, DOI: 10.1103/PhysRevLett.114.191803.

[24] J. Elias-Miro, J. R. Espinosa, G. F. Giudice et al., *Higgs mass implications on the stability of the electroweak vacuum*, *Phys. Lett. B* 709 (2012) 222–228, DOI: 10.1016/j.physletb.2012.02.013.

[25] D. Buttazzo, G. Degrassi, P. P. Giardino et al., *Investigating the near-criticality of the Higgs boson* (2014), DOI: 10.1007/JHEP12(2013)089, arXiv: 1307.3536v4 [hep-ph].

[26] The CMS Collaboration, *Constraints on the spin-parity and anomalous HVV couplings of the Higgs boson in proton collisions at 7 and 8 TeV*, *Phys. Rev.* D92.1 (2015) 012004, DOI: 10.1103/PhysRevD.92.012004, arXiv: 1411.3441 [hep-ex].

[27] The ATLAS Collaboration, *Study of the spin and parity of the Higgs boson in HVV decays with the ATLAS detector*, tech. rep. ATLAS-CONF-2015-008, CERN, Mar. 2015.

[28] T. Gleisberg, S. Hoeche, F. Krauss et al., *Event generation with SHERPA 1.1*, *JHEP* 0902 (2009) 007, DOI: 10.1088/1126-6708/2009/02/007, arXiv: 0811.4622 [hep-ph].

[29] LHC Higgs Cross Section Working Group, *LHC Higgs Cross Sections*, 2014, URL: https://twiki.cern.ch/twiki/bin/view/LHCPhysics/LHCHXSWG.

[30] The ATLAS Collaboration, *Observation of an Excess of Events in the Search for the Standard Model Higgs Boson in the $H \to WW^{(*)} \to \ell\nu\ell\nu$ Channel with the ATLAS Detector*, tech. rep. ATLAS-CONF-2012-098, CERN, July 2012.

[31] L. Evans and P. Bryant, *LHC Machine*, *JINST* 3 (2008) S08001, DOI: 10.1088/1748-0221/3/08/S08001.

[32] The ATLAS Collaboration, *The ATLAS Experiment at the CERN Large Hadron Collider*, *JINST* 3 (2008) S08003, DOI: 10.1088/1748-0221/3/08/S08003.

[33] *CERN web page*, 2015, URL: http://www.cern.ch/.

[34] *The ATLAS experiment web page*, 2015, URL: http://www.atlas.ch.

[35] The ATLAS Collaboration, *ATLAS Inner Detector: Technical design report. Vol. 1*, CERN-LHCC-97-16, ATLAS-TDR-4 (1997).

[36] T. Sjöstrand, S. Mrenna and P. Z. Skands, *PYTHIA 6.4 Physics and Manual*, *JHEP* 0605 (2006) 026, DOI: 10.1088/1126-6708/2006/05/026, arXiv: hep-ph/0603175 [hep-ph].

[37] T. Sjöstrand, S. Mrenna and P. Z. Skands, *A Brief Introduction to PYTHIA 8.1*, *Comput.Phys.Commun.* 178 (2008) 852–867, DOI: 10.1016/j.cpc.2008.01.036, arXiv: 0710.3820 [hep-ph].

[38] G. Corcella, I. G. Knowles, G. Marchesini et al., *HERWIG 6: An Event generator for hadron emission reactions with interfering gluons (including supersymmetric processes)*, *JHEP* 0101 (2001) 010, DOI: 10.1088/1126-6708/2001/01/010, arXiv: hep-ph/0011363 [hep-ph].

[39] J. M. Butterworth, J. R. Forshaw and M. H. Seymour, *Multiparton interactions in photoproduction at HERA*, *Z.Phys.* C72 (1996) 637–646, DOI: 10.1007/s002880050286, arXiv: hep-ph/9601371 [hep-ph].

[40] J. Alwall, M. Herquet, F. Maltoni et al., *MadGraph 5 : Going Beyond*, *JHEP* 1106 (2011) 128, DOI: 10.1007/JHEP06(2011)128, arXiv: 1106.0522 [hep-ph].

[41] M. L. Mangano, M. Moretti, F. Piccinini et al., *ALPGEN, a generator for hard multiparton processes in hadronic collisions*, *JHEP* 0307 (2003) 001, DOI: 10.1088/1126-6708/2003/07/001, arXiv: hep-ph/0206293 [hep-ph].

[42] B. P. Kersevan and E. Richter-Was, *The Monte Carlo event generator AcerMC versions 2.0 to 3.8 with interfaces to PYTHIA 6.4, HERWIG 6.5 and ARIADNE 4.1*, *Comput.Phys.Commun.* 184 (2013) 919–985, DOI: 10.1016/j.cpc.2012.10.032, arXiv: hep-ph/0405247 [hep-ph].

[43] P. Nason, *A New method for combining NLO QCD with shower Monte Carlo algorithms*, *JHEP* 0411 (2004) 040, DOI: 10.1088/1126-6708/2004/11/040, arXiv: hep-ph/0409146 [hep-ph].

[44] S. Frixione, P. Nason and C. Oleari, *Matching NLO QCD computations with Parton Shower simulations: the POWHEG method*, *JHEP* 0711 (2007) 070, DOI: 10.1088/1126-6708/2007/11/070, arXiv: 0709.2092 [hep-ph].

[45] S. Alioli, P. Nason, C. Oleari and E. Re, *A general framework for implementing NLO calculations in shower Monte Carlo programs: the POWHEG BOX*, *JHEP* 1006 (2010) 043, DOI: 10.1007/JHEP06(2010)043, arXiv: 1002.2581 [hep-ph].

[46] S. Frixione and B. R. Webber, *Matching NLO QCD computations and parton shower simulations*, *JHEP* 0206 (2002) 029, DOI: 10.1088/1126-6708/2002/06/029, arXiv: hep-ph/0204244 [hep-ph].

[47] M. A. Dobbs et al., "Les Houches guidebook to Monte Carlo generators for hadron collider physics", *Physics at TeV colliders. Proceedings, Workshop, Les Houches, France, May 26-June 3, 2003*, 2004 411–459, arXiv: hep-ph/0403045 [hep-ph].

[48] The ATLAS Collaboration, *ATLAS Computing: technical design report*, tech. rep. CERN-LHCC-2005-022. ATLAS-TDR-017, 2005.

[49] The ATLAS Collaboration, *The ATLAS Simulation Infrastructure*, *Eur.Phys.J.* C70 (2010) 823–874, DOI: 10.1140/epjc/s10052-010-1429-9, arXiv: 1005.4568 [physics.ins-det].

[50] J. Boudreau and V. Tsulaia, *The GeoModel Toolkit for Detector Description*, July 2015, URL: https://cds.cern.ch/record/865601.

[51] S. Agostinelli, J. Allison, K. Amako et al., *Geant4 - a simulation toolkit*, *Nuclear Instruments and Methods in Physics Research Section A: Accelerators, Spectrometers, Detectors and Associated Equipment* 506.3 (2003) 250–303, DOI: http://dx.doi.org/10.1016/S0168-9002(03)01368-8.

[52] O. S. Brüning, P. Collier, P. Lebrun et al., *LHC Design Report Vol.1: The LHC Main Ring*, tech. rep., 2004.

[53] The ATLAS Collaboration, *ATLAS Data Summary*, 2015, URL: https://atlas.web.cern.ch/Atlas/GROUPS/DATAPREPARATION/DataSummary..

[54] ATLAS Luminosity Public Results, 2014, URL: https://twiki.cern.ch/twiki/bin/view/AtlasPublic/LuminosityPublicResults.

[55] The ATLAS Collaboration, *ATLAS Run-1 Detector Status*, 2015, URL: https://twiki.cern.ch/twiki/bin/view/AtlasPublic/ApprovedPlotsATLASDetector.

[56] The ATLAS Collaboration, *Observation and measurement of Higgs boson decays to WW* with the ATLAS detector*, *Phys. Rev.* D92.1 (2015) 012006, DOI: 10.1103/PhysRevD.92.012006, arXiv: 1412.2641 [hep-ex].

[57] The ATLAS Collaboration, *Performance of the ATLAS Silicon Pattern Recognition Algorithm in Data and Simulation at $\sqrt{s} = 7$ TeV*, ATLAS-CONF-2010-072 (2010).

[58] The ATLAS Collaboration, *Performance of primary vertex reconstruction in proton-proton collisions at $\sqrt{s}$ =7 TeV in the ATLAS experiment*, ATLAS-CONF-2010-069 (2010).

[59] The ATLAS Collaboration, *Performance of the ATLAS Inner Detector Track and Vertex Reconstruction in the High Pile-Up LHC Environment*, ATLAS-CONF-2012-042 (2012).

[60] R. Frühwirth, W. Waltenberger and P. Vanlaer, *Adaptive vertex fitting*, *J.Phys.* G34 (2007) N343, DOI: 10.1088/0954-3899/34/12/N01.

[61] The ATLAS Collaboration, *ATLAS Inner Detector Tracking Performance Guidelines*, 2014, URL: https://twiki.cern.ch/twiki/bin/viewauth/AtlasProtected/InDetTrackingPerformanceGuidelines.

[62] The ATLAS Collaboration, *ATLAS Data Preparation*, 2014, URL: https://twiki.cern.ch/twiki/bin/viewauth/Atlas/MC12bWiki.

[63] The ATLAS Collaboration, *Tau Reconstruction and Identification Performance in ATLAS*, ATLAS-CONF-2010-086 (2010).

[64] The ATLAS Collaboration, *Performance of the Reconstruction and Identification of Hadronic Tau Decays in ATLAS with 2011 Data*, ATLAS-CONF-2012-142 (2012).

[65] The ATLAS Collaboration, *Identification of the Hadronic Decays of Tau Leptons in 2012 Data with the ATLAS Detector*, ATLAS-CONF-2013-064 (2013).

[66] The ATLAS Collaboration, *Calorimeter Clustering Algorithms: Description and Performance*, ATLAS-LARG-PUB-2008-002 (2008).

[67] The ATLAS Collaboration, *Electron performance measurements with the ATLAS detector using the 2010 LHC proton-proton collision data*, *Eur. Phys. J.* C72 (2012) 1909, DOI: 10.1140/epjc/s10052-012-1909-1, arXiv: 1110.3174 [hep-ph].

[68] The ATLAS Collaboration, *Improved electron reconstruction in ATLAS using the Gaussian Sum Filter-based model for bremsstrahlung*, ATLAS-CONF-2012-047 (2012).

[69] The ATLAS Collaboration, *Electron reconstruction and identification efficiency measurements with the ATLAS detector using the 2011 LHC proton-proton collision data*, *Eur. Phys. J.* C74 (2014) 2941, DOI: 10.1140/epjc/s10052-014-2941-0, arXiv: 1404.2240 [hep-ex].

[70] The ATLAS Collaboration, *Electron efficiency measurements with the ATLAS detector using the 2012 LHC proton-proton collision data*, ATLAS-CONF-2014-032 (2014).

[71] S. Hassani et al., *A muon identification and combined reconstruction procedure for the ATLAS detector at the LHC using the (MUONBOY, STACO, MuTag) reconstruction packages*, *Nucl. Instrum. Meth.* A572 (2007) 77–79, DOI: 10.1016/j.nima.2006.10.340a.

[72] T. Lagouri, *Muon Identification and Combined Reconstruction Study in Higgs to Four Muons Physics Events with the ATLAS Detector at the LHC at CERN*, *IEEE Trans. Nucl. Sci.* 51.ATL-PHYS-CONF-2006-016 (2004) 3030–3033.

[73] The ATLAS Collaboration, *Measurement of the muon reconstruction performance of the ATLAS detector using 2011 and 2012 LHC proton-proton collision data*, *Eur. Phys. J.* C74 (2014) 3130, DOI: 10.1140/epjc/s10052-014-3130-x, arXiv: 1407.3935 [hep-ex].

[74] The ATLAS Collaboration, *Expected Performance of the ATLAS Experiment; Detector, Trigger and Physics*, CERN-OPEN-2008-020 (2008).

[75] M. Cacciari, G. P. Salam and G. Soyez, *The anti-k_T jet clustering algorithm*, *JHEP* 0804 (2008) 063, DOI: 10.1088/1126-6708/2008/04/063, arXiv: 0802.1189 [hep-ph].

[76] The ATLAS Collaboration, *Jet energy measurement and its systematic uncertainty in proton-proton collisions at $\sqrt{s} = 7$ TeV with the ATLAS detector*, *Eur. Phys. J.* C75 (2015) 17, DOI: 10.1140/epjc/s10052-014-3190-y, arXiv: 1406.0076 [hep-ex].

[77] The ATLAS Collaboration, *Jet energy measurement with the ATLAS detector in proton-proton collisions at $\sqrt{s} = 7$ TeV*, *Eur.Phys.J.* C73.3 (2013) 2304, DOI: 10.1140/epjc/s10052-013-2304-2, arXiv: 1112.6426 [hep-ex].

[78] The ATLAS Collaboration, *Pile-up subtraction and suppression for jets in ATLAS*, ATLAS-CONF-2013-083 (2013).

[79] The ATLAS Collaboration, *Commissioning of the ATLAS high-performance b-tagging algorithms in the 7 TeV collision data*, tech. rep. ATLAS-CONF-2011-102, CERN, July 2011.

[80] The ATLAS Collaboration, *Calibration of the performance of b-tagging for c and light-flavour jets in the 2012 ATLAS data*, ATLAS-CONF-2014-046 (July 2014).

[81] The ATLAS Collaboration, *Calibration of b-tagging using dileptonic top pair events in a combinatorial likelihood approach with the ATLAS experiment*, ATLAS-CONF-2014-004 (Feb. 2014).

[82] The ATLAS Collaboration, *Performance of Missing Transverse Momentum Reconstruction in ATLAS studied in Proton-Proton Collisions recorded in 2012 at 8 TeV*, ATLAS-CONF-2013-082 (2013).

[83] The ATLAS Collaboration, *Pile-up Suppression in Missing Transverse Momentum Reconstruction in the ATLAS Experiment in Proton-Proton Collisions at $\sqrt{s}$ = 8 TeV*, ATLAS-CONF-2014-019 (May 2014).

[84] The ATLAS Collaboration, *Combined search for the Standard Model Higgs boson using up to 4.9 fb^{-1} of pp collision data at $\sqrt{s} = 7$ TeV with the ATLAS detector at the LHC*, *Phys.Lett.* B710 (2012) 49–66, DOI: 10.1016/j.physletb.2012.02.044, arXiv: 1202.1408 [hep-ex].

[85] The ATLAS Collaboration, *Search for the Standard Model Higgs boson in the $H \to WW(*) \to \ell\nu\ell\nu$ decay mode with 4.7 fb^{-1}of ATLAS data at $\sqrt{s} = 7$ TeV*, *Phys.Lett.* B716 (2012) 62–81, DOI: 10.1016/j.physletb.2012.08.010, arXiv: 1206.0756 [hep-ex].

[86] The ATLAS Collaboration, *Measurements of the properties of the Higgs-like boson in the $WW^{(*)} \to \ell\nu\ell\nu$ decay channel with the ATLAS detector using 25 fb^{-1} of proton-proton collision data*, tech. rep. ATLAS-CONF-2013-030, CERN, Mar. 2013.

[87] A. Höcker, J. Stelzer, F. Tegenfeldt et al., *TMVA - Toolkit for Multivariate Data Analysis*, *PoS* ACAT (2007) 040, arXiv: physics/0703039 [PHYSICS].

[88] N. Kauer, *Interference effects for $H \to WW/ZZ \to \ell\bar{\nu}_\ell\bar{\ell}\nu_\ell$ searches in gluon fusion at the LHC*, *JHEP* 1312 (2013) 082, DOI: 10.1007/JHEP12(2013)082, arXiv: 1310.7011 [hep-ph].

[89] H.-L. Lai, M. Guzzi, J. Huston et al., *New parton distributions for collider physics*, *Phys.Rev.* D82 (2010) 074024, DOI: 10.1103/PhysRevD.82.074024, arXiv: 1007.2241 [hep-ph].

[90] J. Pumplin, D. R. Stump, J. Huston et al., *New generation of parton distributions with uncertainties from global QCD analysis*, *JHEP* 0207 (2002) 012, DOI: 10.1088/1126-6708/2002/07/012, arXiv: hep-ph/0201195 [hep-ph].

[91] M. Grazzini and H. Sargsyan, *Heavy-quark mass effects in Higgs boson production at the LHC*, *JHEP* 1309 (2013) 129, DOI: 10.1007/JHEP09(2013)129, arXiv: 1306.4581 [hep-ph].

[92] A. Bredenstein, A. Denner, S. Dittmaier and M. M. Weber, *Precise predictions for the Higgs-boson decay $H \to WW/ZZ \to 4$ leptons*, *Phys.Rev.* D74 (2006) 013004, DOI: 10.1103/PhysRevD.74.013004, arXiv: hep-ph/0604011 [hep-ph].

[93] A. Djouadi, J. Kalinowski and M. Spira, *HDECAY: A Program for Higgs boson decays in the standard model and its supersymmetric extension*, *Comput.Phys.Commun.* 108 (1998) 56–74, DOI: 10.1016/S0010-4655(97)00123-9, arXiv: hep-ph/9704448 [hep-ph].

[94] J. M. Campbell, R. K. Ellis and C. Williams, *Vector boson pair production at the LHC*, *JHEP* 1107 (2011) 018, DOI: 10.1007/JHEP07(2011)018, arXiv: 1105.0020 [hep-ph].

[95] M. Czakon and A. Mitov, *Top++: A Program for the Calculation of the Top-Pair Cross-Section at Hadron Colliders*, *Comput.Phys.Commun.* 185 (2014) 2930, DOI: 10.1016/j.cpc.2014.06.021, arXiv: 1112.5675 [hep-ph].

[96] N. Kidonakis, *Next-to-next-to-leading-order collinear and soft gluon corrections for t-channel single top quark production*, *Phys.Rev.* D83 (2011) 091503, DOI: 10.1103/PhysRevD.83.091503, arXiv: 1103.2792 [hep-ph].

[97] N. Kidonakis, *Two-loop soft anomalous dimensions for single top quark associated production with a W- or H-*, *Phys.Rev.* D82 (2010) 054018, DOI: 10.1103/PhysRevD.82.054018, arXiv: 1005.4451 [hep-ph].

[98] N. Kidonakis, *NNLL resummation for s-channel single top quark production*, *Phys.Rev.* D81 (2010) 054028, DOI: 10.1103/PhysRevD.81.054028, arXiv: 1001.5034 [hep-ph].

[99] S. Catani, L. Cieri, G. Ferrera et al., *Vector boson production at hadron colliders: a fully exclusive QCD calculation at NNLO*, *Phys.Rev.Lett.* 103 (2009) 082001, DOI: 10.1103/PhysRevLett.103.082001, arXiv: 0903.2120 [hep-ph].

[100] S. Catani and M. Grazzini, *An NNLO subtraction formalism in hadron collisions and its application to Higgs boson production at the LHC*, *Phys.Rev.Lett.* 98 (2007) 222002, DOI: 10.1103/PhysRevLett.98.222002, arXiv: hep-ph/0703012 [hep-ph].

[101] A. Sherstnev and R. S. Thorne, *Parton Distributions for LO Generators*, *Eur.Phys.J.* C55 (2008) 553–575, DOI: 10.1140/epjc/s10052-008-0610-x, arXiv: 0711.2473 [hep-ph].

[102] V. D. Barger, R. J. N. Phillips and D. Zeppenfeld, *Mini - jet veto: A Tool for the heavy Higgs search at the LHC*, *Phys.Lett.* B346 (1995) 106–114, DOI: 10.1016/0370-2693(95)00008-9, arXiv: hep-ph/9412276 [hep-ph].

[103] F.-P. Schilling, *Top Quark Physics at the LHC: A Review of the First Two Years*, *Int.J.Mod.Phys.* A27 (2012) 1230016, DOI: 10.1142/S0217751X12300165, arXiv: 1206.4484 [hep-ex].

[104] S. Frixione, P. Nason and G. Ridolfi, *A Positive-weight next-to-leading-order Monte Carlo for heavy flavour hadroproduction*, *JHEP* 0709 (2007) 126, DOI: 10.1088/1126-6708/2007/09/126, arXiv: 0707.3088 [hep-ph].

[105] P. Nason and B. Webber, *Next-to-Leading-Order Event Generators*, *Ann. Rev. Nucl. Part. Sci.* 62 (2012) 187–213, DOI: 10.1146/annurev-nucl-102711-094928, arXiv: 1202.1251 [hep-ph].

[106] M. L. Mangano, M. Moretti, F. Piccinini and M. Treccani, *Matching matrix elements and shower evolution for top-quark production in hadronic collisions*, *JHEP* 0701 (2007) 013, DOI: 10.1088/1126-6708/2007/01/013, arXiv: hep-ph/0611129 [hep-ph].

[107] P. Nason, *Recent Developments in POWHEG*, *PoS* RADCOR2009 (2010) 018, arXiv: 1001.2747 [hep-ph].

[108] S. Dittmaier, C. Mariotti, G. Passarino et al., *Handbook of LHC Higgs Cross Sections: 1. Inclusive Observables*, *CERN-2011-002* (CERN, Geneva, 2011), DOI: 10.5170/CERN-2011-002, arXiv: 1101.0593 [hep-ph].

[109] D. Bourilkov, R. C. Group and M. R. Whalley, *LHAPDF: PDF use from the Tevatron to the LHC* (2006), arXiv: hep-ph/0605240 [hep-ph].

[110] D. R. Ball et al., *NNPDF*, 2015, URL: https://nnpdf.hepforge.org.

[111] V. N. Gribov and L. N. Lipatov, *Deep inelastic e - p scattering in perturbation theory*, *Sov.J.Nucl.Phys.* 15 (1972) 438–450.

[112] G. Altarelli and G. Parisi, *Asymptotic Freedom in Parton Language*, *Nucl.Phys.* B126 (1977) 298, DOI: 10.1016/0550-3213(77)90384-4.

[113] Y. L. Dokshitzer, *Calculation of the Structure Functions for Deep Inelastic Scattering and e^+e^- Annihilation by Perturbation Theory in Quantum Chromodynamics.*, *Sov.Phys.JETP* 46 (1977) 641–653.

[114] V. V. Sudakov, *Vertex parts at very high-energies in quantum electrodynamics*, *Sov.Phys.JETP* 3 (1956) 65–71.

[115] The ATLAS Collaboration, *Measurement of $t\bar{t}$ production with a veto on additional central jet activity in pp collisions at sqrt(s) = 7 TeV using the ATLAS detector*, *Eur.Phys.J.* C72 (2012) 2043, DOI: 10.1140/epjc/s10052-012-2043-9, arXiv: 1203.5015 [hep-ex].

[116] The ATLAS Collaboration, *Comparison of Monte Carlo generator predictions for gap fraction and jet multiplicity observables in top-antitop events*, tech. rep. ATL-PHYS-PUB-2014-005, CERN, May 2014.

[117] P. Z. Skands, *Tuning Monte Carlo Generators: The Perugia Tunes*, *Phys.Rev.* D82 (2010) 074018, DOI: 10.1103/PhysRevD.82.074018, arXiv: 1005.3457 [hep-ph].

[118] S. Dittmaier, C. Mariotti, G. Passarino et al., *Handbook of LHC Higgs Cross Sections: 2. Differential Distributions*, *CERN-2012-002* (CERN, Geneva, 2012), DOI: 10.5170/CERN-2012-002, arXiv: 1201.3084 [hep-ph].

[119] J. Alwall, R. Frederix, S. Frixione et al., *The automated computation of tree-level and next-to-leading order differential cross sections, and their matching to parton shower simulations*, *JHEP* 07 (2014) 079, DOI: 10.1007/JHEP07(2014)079, arXiv: 1405.0301 [hep-ph].

[120] Glen Cowan, Kyle Cranmer, Eilam Gross and Ofer Vitells, *Asymptotic formulae for likelihood-based tests of new physics*, *Eur.Phys.J.* C71 (2011) 1554, DOI: 10.1140/epjc/s10052-011-1554-0, arXiv: 1007.1727 [physics.data-an], *Erratum to: Asymptotic formulae for likelihood-based tests of new physics*, *Eur.Phys.J.* C73 (2013) 2501, DOI: 10.1140/epjc/s10052-013-2501-z.

[121] A. L. Read, *Presentation of search results: the CLs technique*, *Journal of Physics G: Nuclear and Particle Physics* 28.10 (2002) 2693.

[122] The ATLAS Collaboration, *Measurement of the Higgs boson mass from the $H \to \gamma\gamma$ and $H \to ZZ^* \to 4\ell$ channels with the ATLAS detector using 25 fb^{-1} of pp collision data*, *Phys.Rev.* D90.5 (2014) 052004, DOI: 10.1103/PhysRevD.90.052004, arXiv: 1406.3827 [hep-ex].

[123] The ATLAS Collaboration, *Measurements of Higgs boson production and couplings in diboson final states with the ATLAS detector at the LHC*, *Phys.Lett.* B726 (2013) 88–119, DOI: 10.1016/j.physletb.2014.05.011, 10.1016/j.physletb.2013.08.010, arXiv: 1307.1427 [hep-ex].

[124] S. Dittmaier, C. Mariotti, G. Passarino et al., *Handbook of LHC Higgs Cross Sections: 3. Higgs Properties*, *CERN-2013-004* (CERN, Geneva, 2013), DOI: 10.5170/CERN-2013-004, arXiv: 1307.1347 [hep-ph].

[125] *Longer term LHC schedule*, July 2015, URL: http://lhc-commissioning.web.cern.ch/lhc-commissioning/schedule/LHC-long-term.htm.

[126] *LHC/ HL-LHC Plan*, July 2015, URL: http://hilumilhc.web.cern.ch/about/hl-lhc-project.

[127] The ATLAS Collaboration, *Projections for measurements of Higgs boson cross sections, branching ratios and coupling parameters with the ATLAS detector at a HL-LHC*, tech. rep. ATL-PHYS-PUB-2013-014, CERN, Oct. 2013.

[128] The ATLAS Collaboration, *Prospects for benchmark Supersymmetry searches at the high luminosity LHC with the ATLAS Detector*, tech. rep. ATL-PHYS-PUB-2013-011, CERN, Sept. 2013.

[129] The ATLAS Collaboration, *Letter of Intent for the Phase-I Upgrade of the ATLAS Experiment*, tech. rep. CERN-LHCC-2011-012. LHCC-I-020, CERN, Nov. 2011.

[130] The ATLAS Collaboration, *ATLAS Letter of Intent Phase-II Upgrade*, tech. rep. LHCC-I-023, CERN, Dec. 2012.

[131] R. Bartoldus, C. Bee, D. Francis et al., *Technical Design Report for the Phase-I Upgrade of the ATLAS TDAQ System*, tech. rep. CERN-LHCC-2013-018. ATLAS-TDR-023, Final version presented to December 2013 LHCC.: CERN, Sept. 2013.

[132] M. Shochet, L. Tompkins, V. Cavaliere et al., *Fast TracKer (FTK) Technical Design Report*, tech. rep. CERN-LHCC-2013-007. ATLAS-TDR-021, ATLAS Fast Tracker Technical Design Report: CERN, June 2013.

[133] S. McMahon, P. Allport, H. Hayward and B. Di Girolamo, *Initial Design Report of the ITk: Initial Design Report of the ITk*, tech. rep. ATL-COM-UPGRADE-2014-029, CERN, Oct. 2014.

[134] S. Fartoukh, *Pile up management at the high-luminosity LHC and introduction to the crab-kissing concept*, *Phys. Rev. ST Accel. Beams* 17 (11 Nov. 2014) 111001, DOI: 10.1103/PhysRevSTAB.17.111001.

[135] S. Burdin, T. Cornelissen, C. Debenedetti et al., *Tracking Performance of the Proposed Inner Tracker Layout for the ATLAS Phase-II Upgrade*, tech. rep. ATL-UPGRADE-PUB-2013-001, CERN, Feb. 2013.

[136] N. Hessey, *Building a Stereo-angle into strip-sensors for the ATLAS-Upgrade Inner-Tracker Endcaps*, July 2015, URL: http://www.nikhef.nl/~r29/upgrade/petalwafer.pdf.

[137] N. Hessey, *Sensors for petals with stereo built-in*, July 2015, URL: http://www.nikhef.nl/~r29/upgrade/.

[138] N. Hessey, *ITk end-cap sensor parameters*, July 2015, URL: http://www.nikhef.nl/~r29/upgrade/SensorsApr2015/.

[139] *Geant4 User Documentation*, July 2015, URL: https://geant4.web.cern.ch/geant4/support/userdocuments.shtml.

[140] N. Hessey, *Layout parameter book for Utopia simulations.* July 2015, URL: https://edms.cern.ch/file/1064078/1/layoutparamVerI.pdf.

[141] ATLAS VP1 team, *ATLAS VP1*, July 2015, URL: https://atlas-vp1.web.cern.ch/atlas-vp1/home/.

[142] N. Hessey, *User Manual and Guide to developing geometries with the GeoModelXml Package*, July 2015, URL: http://www.nikhef.nl/~r29/upgrade/gmx2geo.pdf.

[143] N. Hessey, *Implementing LoI layout With GeoModelXml*, July 2015, URL: http://www.nikhef.nl/~r29/upgrade/stripGeomInXml2014-01-15-2.pdf.

[144] N. Hessey, *First Digitization of LoI Layout*, July 2015, URL: http://www.nikhef.nl/~r29/upgrade/firstLoIdigitization.pdf.

[145] A. M. Henriques Correia, K. Einsweiler et al., *ATLAS Large eta task force report*, tech. rep. ATL-UPGRADE-INT-2015-001, CERN, May 2015.

[146] The ATLAS Collaboration, *Performance assumptions based on full simulation of an upgraded ATLAS detector at a High-Luminosity LHC*, tech. rep. ATLAS-PHYS-PUB-2013-009, CERN, Sept. 2013.

[147] The ATLAS Collaboration, *Performance assumptions for an upgraded ATLAS detector at a High-Luminosity LHC*, tech. rep. ATLAS-PHYS-PUB-2013-004, CERN, Apr. 2013.

[148] V. Barger, K. Cheung, T. Han and R. J. N. Phillips, *Strong W^+W^+ scattering signals at p p supercolliders*, *Phys. Rev. D* 42 (9 Nov. 1990) 3052–3077, DOI: 10.1103/PhysRevD.42.3052.

[149] J. Chang, K. Cheung, C.-T. Lu and T.-C. Yuan, *WW scattering in the era of post-Higgs-boson discovery*, *Phys.Rev.* D87 (2013) 093005, DOI: 10.1103/PhysRevD.87.093005, arXiv: 1303.6335 [hep-ph].

[150] S. D. Rindani, *Strong gauge boson scattering at the LHC* (2009) 145–155, DOI: 10.1007/978-81-8489-295-6_10, arXiv: 0910.5068 [hep-ph].

[151] A. Alboteanu, W. Kilian and J. Reuter, *Resonances and Unitarity in Weak Boson Scattering at the LHC*, *JHEP* 0811 (2008) 010, DOI: 10.1088/1126-6708/2008/11/010, arXiv: 0806.4145 [hep-ph].

[152] C. Degrande, N. Greiner, W. Kilian et al., *Effective Field Theory: A Modern Approach to Anomalous Couplings*, *Annals Phys.* 335 (2013) 21–32, DOI: 10.1016/j.aop.2013.04.016, arXiv: 1205.4231 [hep-ph].

[153] C. Degrande, O. J. P. Eboli, B. Feigl et al., *Monte Carlo tools for studies of non-standard electroweak gauge boson interactions in multi-boson processes: A Snowmass White Paper* (2013), arXiv: 1309.7890 [hep-ph].

[154] O. J. P. Eboli, M. C. Gonzalez-Garcia and J. K. Mizukoshi, *$pp \to jje^{\pm}\mu^{\pm}\nu\nu$ and $jje^{\pm}\mu^{\mp}\nu\nu$ at $\mathcal{O}(\alpha_{em}^6)$ and $\mathcal{O}(\alpha_{em}^4\alpha_s^2)$ for the study of the quartic electroweak gauge boson vertex at CERN LHC*, *Phys.Rev.* D74 (2006) 073005, DOI: 10.1103/PhysRevD.74.073005, arXiv: hep-ph/0606118 [hep-ph].

[155] C. Degrande, J. L. Holzbauer, S.-C. Hsu et al., *Studies of Vector Boson Scattering And Triboson Production with DELPHES Parametrized Fast Simulation for Snowmass 2013* (2013), arXiv: 1309.7452 [hep-ph].

[156] E. Accomando, A. Ballestrero, A. Belhouari and E. Maina, *Isolating vector boson scattering at the CERN LHC: Gauge cancellations and the equivalent vector boson approximation versus complete calculations*, *Phys. Rev. D* 74 (7 Oct. 2006) 073010, DOI: 10.1103/PhysRevD.74.073010.

[157] The ATLAS Collaboration, *Evidence for Electroweak Production of $W^{\pm}W^{\pm}jj$ in pp Collisions at $\sqrt{s} = 8$ TeV with the ATLAS Detector*, *Phys.Rev.Lett.* 113.14 (2014) 141803, DOI: 10.1103/PhysRevLett.113.141803, arXiv: 1405.6241 [hep-ex].

[158] The CMS Collaboration, *Study of Vector Boson Scattering and Search for New Physics in Events with Two Same-Sign Leptons and Two Jets*, *Phys. Rev. Lett.* 114 (5 Feb. 2015) 051801, DOI: 10.1103/PhysRevLett.114.051801.

[159] P. Anger, P. Bernat, M. Campanelli et al., *Studies of Vector Boson Scattering with an Upgraded ATLAS Detector at a High-Luminosity LHC*, tech. rep. ATL-UPGRADE-PUB-2012-006, CERN, Dec. 2012.

[160] The ATLAS Collaboration, *Studies of Vector Boson Scattering And Triboson Production with an Upgraded ATLAS Detector at a High-Luminosity LHC*, tech. rep. ATL-PHYS-PUB-2013-006, CERN, June 2013.

[161] S. Ovyn, X. Rouby and V. Lemaitre, *DELPHES, a framework for fast simulation of a generic collider experiment* (2009), arXiv: 0903.2225 [hep-ph].

[162] J. de Favereau et al., *DELPHES 3, A modular framework for fast simulation of a generic collider experiment*, *JHEP* 1402 (2014) 057, DOI: 10.1007/JHEP02(2014)057, arXiv: 1307.6346 [hep-ex].

[163] *MadGraph Wiki*, June 2015, URL: https://cp3.irmp.ucl.ac.be/projects/madgraph/wiki/FAQ-General-13.

[164] M. Bähr, S. Gieseke, M.A. Gigg et al., *Herwig++ Physics and Manual*, *Eur.Phys.J.* C58 (2008) 639–707, DOI: 10.1140/epjc/s10052-008-0798-9, arXiv: 0803.0883 [hep-ph].

[165] M. Cacciari and G. P. Salam, *Pileup subtraction using jet areas*, *Phys.Lett.* B659 (2008) 119–126, DOI: 10.1016/j.physletb.2007.09.077, arXiv: 0707.1378 [hep-ph].

[166] G. Cowan, *Discovery sensitivity for a counting experiment with background uncertainty*, 2012, URL: http://www.pp.rhul.ac.uk/~cowan/stat/notes/medsigNote.pdf.

[167] G. Cowan, *Comparison of significance from profile and integrated likelihoods*, 2008, URL: https://twiki.cern.ch/twiki/pub/AtlasProtected/ATLASStatisticsFAQ/PLvsInt.pdf.

[168] G. Cowan and E. Gross, *Discussion and guidelines on significance*, 2009, URL: https://twiki.cern.ch/twiki/pub/AtlasProtected/ATLASStatisticsFAQ/PLvsInt.pdf.

[169] *RootCore Package Truth-To-Reco Functions*, June 2015, URL: http://svnweb.cern.ch/trac/atlasgroups/browser/PhysicsAnalysis/EuropeanStrategy/TruthToRecoFunctions.

[170] W. Kilian, T. Ohl and J. Reuter, *WHIZARD: Simulating Multi-Particle Processes at LHC and ILC*, *Eur.Phys.J.* C71 (2011) 1742, DOI: 10.1140/epjc/s10052-011-1742-y, arXiv: 0708.4233 [hep-ph].

[171] The ATLAS Collaboration, *Measurements of the Higgs boson production and decay rates and coupling strengths using pp collision data at $\sqrt{s} = 7$ and 8 TeV in the ATLAS experiment* (2015), arXiv: 1507.04548 [hep-ex].

[172] A. Purcell, *Go on a particle quest at the first CERN webfest*, August 2015, URL: https://cds.cern.ch/record/1473657?ln=en.

SUMMARY

With the risk of sounding poetic, I have been always fascinated by the Universe and all its *mysteries*. Already as a child I was impressed by the countless stars in our Milky Way, by the concept of black holes, and when immersed in the world of science fiction I was always day-dreaming of one day exploring space myself. Unfortunately, humankind did not manage to invent the *warp drive* yet, so there was no chance of me cruising the Milky Way on board of an *Enterprise*. Although it would have been much more thrilling to encounter wormholes, one can explore the Universe from the cosiness of our home planet as well. As a PhD researcher I was lucky to be a part of one of the greatest "microscopes" on Earth that allows us to look into the structure of space and time - the Large Hadron Collider (LHC), stationed at CERN in Geneva. The LHC is a circular accelerator that accelerates and collides protons at very high energies and so reproduces the conditions that existed one billionth of a second after the Big Bang, which allows us to explore what the Universe is made of and how it started. In the next paragraphs I will summarise my PhD research presented in this manuscript with the title of *Fusing the vector bosons: Higgs production through VBF and WW scattering at the current and future LHC*.

The theory that describes the world of particles is called the Standard Model (abbreviated as SM) and divides the particles into those that constitute matter and those that are in charge of interactions between them. The building blocks of matter are particles like electrons (e), electron neutrinos (ν_e) and quarks (u, d, s, c, t, b), the latter forming hadrons, like protons and neutrons. The interactions between them are governed by the three fundamental forces: the well known electromagnetic force that is mediated by photons (γ), the weak force which plays an important role in nuclear decays and is mediated by the vector bosons W and Z, and the strong force which holds the atomic nuclei together and is mediated by gluons (g). All the SM particle content is presented in Figure 93.

In the past decades various experiments confirmed the existence of all the particles predicted by the SM. Their properties agree with the SM theoretical predictions with a high precision. However, the SM by itself has one fundamental flaw. It assumes that all the particles from Figure 93 are *massless* which is not at all what we observe. This issue was resolved already in 1964 with the *Higgs mechanism*, which is now considered as an integral part of the SM. The Higgs mechanism predicts the existence of an omnipresent Higgs field (excitation of which is the Higgs boson particle) and when the SM particles interact with it, they obtain their masses. The Higgs field can be viewed as an invisible *syrupy* substance that fills up the Universe. The more the *Higgs syrup* sticks to the particles, the more resistance the particles feel when traversing through it and the heavier they are, while those particles which do not interact with the Higgs filed are massless.

For many years, particle physicists have been searching for the Higgs boson in order to confirm the Higgs mechanism and therefore fully verify the SM. In the summer of 2012, the two general purpose experiments at the LHC, ATLAS and CMS, finally (after a 40 year long search) confirmed an existence of a Higgs boson with $m_H \approx 125\,\text{GeV}$ [1] with more than 5 standard deviations[2]. After the discovery, large efforts have been put into studying all

1 The electronvolt, eV, is the unit of energy equivalent to $1.6 \cdot 10^{-19}$ J. In particle physics, assuming natural units where $c^2 = 1$, the eV is also used as a unit of mass and is equivalent to $1.8 \cdot 10^{-36}$ kg.

2 The probability of this observations being a random fluctuation and not really a new particle is one in 3.5 million.

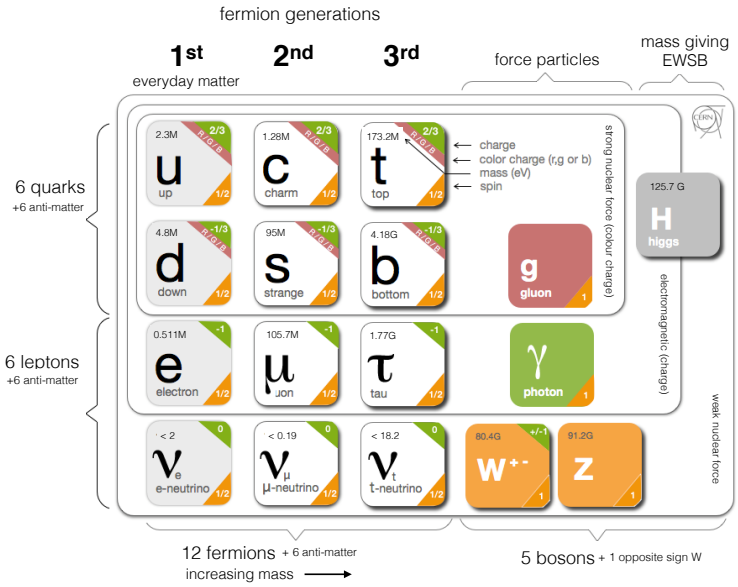

Figure 93.: The SM particles and their properties. Figure modified from [172]. Mass values taken from [12].

the properties of the newly discovered particle to confirm if it is indeed the Higgs boson predicted by the SM or a new riddle to solve.

Even though the SM correctly describes many physical concepts, we know it is not the complete and ultimate theory of the Universe. There are far too many open questions to claim otherwise. For example, we still do not know how to incorporate gravity among the three fundamental forces between particles and we do not know what the dark matter really is. All these open questions point to the existence of some New Physics, the laws of which are still unknown to us. These expected yet elusive New Physics contributions can be detected by directly searching for novel interactions and/or novel particles or by very precisely measuring the properties of the Higgs and other SM particles, their production and decay rates, and look for any deviations from their theoretical SM predictions.

The SM predicts various production and decay mechanisms for the Higgs boson and each production and decay mode needs to be thoroughly explored to confidently confirm that the discovered new particle is indeed the SM Higgs boson. The two most frequently occurring production modes at the LHC (the ones with the highest cross-sections), are the gluon-gluon fusion (ggF) and the vector boson fusion (VBF), with their Feynman diagrams presented in Figure 94. The more dominant ggF mechanism explores the couplings between the Higgs boson and heavy quarks (t, b) and the VBF probes for the couplings of the Higgs boson with the vector bosons, W and Z. The Higgs boson with $m_H \sim 125\,\text{GeV}$ most frequently decays into a pair of b-quarks ($b\bar{b}$) or a pair of vector bosons. So far, not all of the production and decay modes of the Higgs boson have been observed and this manuscript is dedicated to the search for one of these production-decay combinations, more precisely, to the search for the VBF production mode in the Higgs boson decaying into two W bosons which subsequently decay into a lepton-neutrino pair, $H \to WW^{(*)} \to \ell^+\nu_\ell\ell^-\bar{\nu}_\ell$.

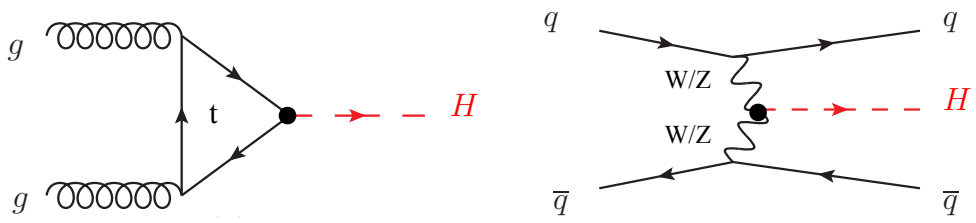

Figure 94.: The Feynman diagrams indicting gluon-gluon fusion (left) and vector boson fusion (right) Higgs production. The black circles indicate the couplings between the heavy quarks (ggF) or vector bosons (VBF) with the Higgs boson.

The VBF $H \to WW^{(*)}$ analysis described in this thesis, studies the accumulated proton-proton collisions recorded by the ATLAS detector during the 2012 data-taking, when the two proton beams collided at the center of mass energy of 8 TeV. The analysis observes an excess of signal events with respect to the backgrounds equal to 3.2 standard deviations, which, for the first time, confirms the *evidence* for the VBF production in the $H \to WW^{(*)}$ decay channel. Figure 95 (left) shows the observed excess of data events in the transverse mass m_T distribution that represents the invariant mass of the final state particles in the transverse plane and is used as the discriminant in the final fit[3].

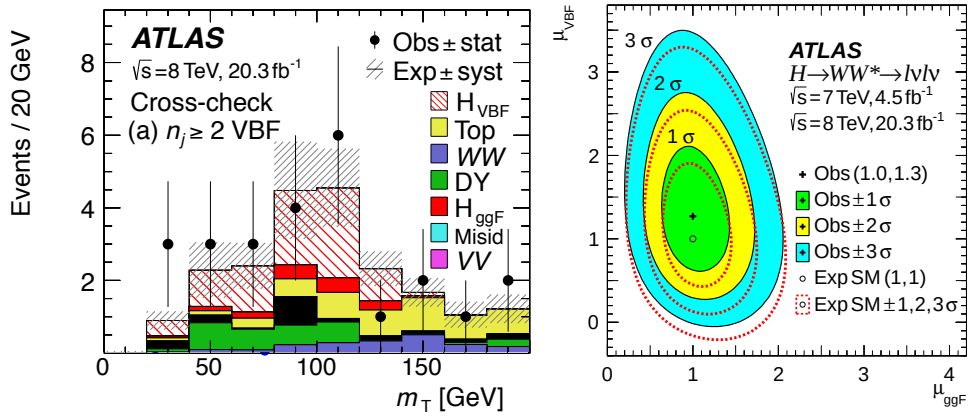

Figure 95.: Left: The transverse mass distribution at the end of the event selection for the Higgs boson produced through vector boson fusion and decaying into $H \to WW^{(*)} \to \ell^+\nu_\ell\ell^-\bar{\nu}_\ell$ final states. Right: A 2D likelihood contour of μ_{VBF} versus μ_{ggF} comparing their observed and expected values for the 2012 dataset recorded at the center of mass energy of 8 TeV and the 2011 dataset recorded at the center of mass energy of 7 TeV. The best-fit observed value is presented by a cross symbol while the open circle represents the SM expected value.

3 The VBF $H \to WW^{(*)}$ analysis has been performed by two independent methods; the cut-based analysis which selects the signal events based on the consecutive selection criteria and the multivariate analysis (MVA). The latter resulted in a higher expected significance of the VBF signal and has been therefore chosen as the nominal VBF $H \to WW^{(*)}$ analysis. The cut-based analysis, which has been the one presented in this thesis, observed a significance of 3.0 standard deviations and its m_T distribution is shown in Figure 98 (left). The MVA analysis observed a significance of 3.2 standard deviations and has been combined with the ggF production in the final fit (see Figure 95 right)

In order to test how well the observed VBF production rate compares to the SM prediction, the *signal strength* μ_{VBF} is evaluated and represents the ratio between the two;

$$\mu_{\text{VBF}} = \sigma^{\text{SM}}_{\text{VBF}} / \sigma^{\text{obs}}_{\text{VBF}}. \tag{121}$$

If $\mu_{\text{VBF}} = 1$, the observed data agree with the SM predictions.

The observed signal strength for the VBF production mode in the $H \to WW^{(*)}$ channel equals to

$$\hat{\mu}^{\text{obs}}_{\text{VBF}} = 1.27\,^{+0.44}_{-0.41}\,(\text{stat.})\,^{+0.30}_{-0.21}\,(\text{syst.}) = 1.27^{+0.53}_{-0.45}. \tag{122}$$

The final signal strength of the $H \to WW^{(*)}$ channel includes both dominant production modes, ggF+VBF, (see Figure 95, right) and results in

$$\mu^{\text{obs}}_{\text{ggF+VBF}} = 1.09\,^{+0.16}_{-0.15}\,(\text{stat.})\,^{-0.14}_{+0.17}\,(\text{syst.}). \tag{123}$$

To conclude, the (VBF) $H \to WW^{(*)}$ analysis observes no signs of New Physics in the measured signal strengths, at least *within their uncertainties*, and so confirms the validity of the SM. At this point, the signal strengths, especially μ_{VBF}, are still greatly dominated by the uncertainties. Mainly by the statistical uncertainties that arise due to a small size of the recorded dataset. However, in the next decades, the LHC and all its experiments will undergo various upgrades to further increase the amount of recorded proton-proton collisions at higher center of mass energies. With these upgrades, the ATLAS detector will be able to reduce the currently limiting statistical uncertainties. To investigate what impact these upgrades will have on the precision of the $H \to WW^{(*)}$ signal strengths, a feasibility study has been concluded and is described in this thesis. This study revealed that with a tenfold increase in the recorded dataset, the precision on μ_{VBF} improves from the current $\sim$ 42% to $\sim$ 25%. If the amount of accumulated data increases by an additional factor of 10 (a factor of 100 higher compared to the current recorded dataset), the precision on μ_{VBF} improves even further, to $\sim$ 15%.

The systematic uncertainties have a smaller effect on the precision of μ_{VBF}. However, higher amounts of accumulated data from the future LHC runs will reduce the impact of statistical uncertainties, making the systematic uncertainties increasingly more important. For a correct interpretation of the data, it is therefore crucial to understand and reduce all the various contributions of systematic uncertainties. A special focus in this thesis is put on one of these contributions, namely on the systematic uncertainty on the modelling of one of the largest backgrounds in the VBF $H \to WW^{(*)}$ analysis - the top-quark pair production (hereafter referred as the top background). The overall systematic uncertainty on the top background modelling is composed of various sources of systematic uncertainties. After studying these sources and after optimisation studies of the top background event selection, several of the initially considered sources have been neglected, reducing the impact of the top background systematic uncertainty on the signal significance by at most 50%.

Concluding the studies related to the VBF Higgs production, this summary now turns to the topic of WW-scattering. The scattering cross-section of the two longitudinally polarised W bosons increases with the increasing scattering energy and would at some point violate the unitarity if the Higgs boson would not precisely cancel out the unitarity-violating effects. Precisely examining the WW-scattering presents a prime opportunity to study whether the Higgs boson is indeed solely responsible for keeping the WW-scattering cross-section under control, or whether there are other, yet unknown, contributing New Physics mechanisms.

This thesis studied the WW-scattering in terms of the benefits an extended tracking coverage of the future ATLAS detector (that will be operational around 2026) could bring to the

sensitivity of the SM and New Physics measurements. Increasing the tracking coverage[4] up to $|\eta| \leq 4.0$, increases the SM signal significance by almost 100% with respect to the current tracker coverage of $|\eta| < 2.5$ and improves the sensitivity for New Physics searches by $\approx 50\%$.

The first run of the LHC data-taking is behind us and it provided one of the greatest discoveries of our time - the Higgs boson. All the measurements of the properties of the Higgs boson point to the fact that it is indeed the one predicted by the SM. However, the existence of a SM-like Higgs boson with $m_H \sim 125\,\text{GeV}$ triggers additional questions, like; *Is this the only Higgs boson (and why?)* or *are there more of them?* In my opinion, the beauty of physics lies in precisely the fact that for every question we answer, a few new ones emerge. There is always something else to describe, to discover and to understand. The Universe is a never ending supply of thrilling puzzles and the re-start of the LHC earlier this spring at the higher collision energy of 14 TeV will hopefully bring surprising new insights about what the Universe is made of and how it started.

4 The tracking coverage is expressed in pseudorapidity η, that represents an angle of particle's trajectory relative to the beam axis and is defined as $\eta = -\ln\tan(\theta/2)$. $\eta = 0$ represents the trajectory perpendicular to the beam axis and $\eta = \infty$ represent the trajectory parallel to the beam axis.

SAMENVATTING

Ondanks dat het misschien wat poëtisch klinkt, ben ik al mijn hele leven gefascineerd door het universum en al haar *mysteries*. Als kind al was ik onder de indruk van de ontelbare sterren in onze Melkweg en door zwarte gaten. En ondergedompeld in de wereld van science fiction dagdroomde ik ervan om ooit zelf het heelal te kunnen onderzoeken. Maar jammer genoeg heeft de mensheid de *warp drive* nog steeds niet uitgevonden, dus acht ik de kans klein dat ik ooit de ruimte door zal zoeven aan boord van een *Enterprise*...

En hoewel het natuurlijk veel spannender zou zijn om wormgaten van dichtbij te bekijken, kan je het universum ook hier onderzoeken, op onze eigen vertrouwde thuisplaneet. Als PhD-onderzoeker had ik het geluk om te mogen werken aan de grootste "microscoop" op aarde, die ons in staat stelt om de structuur van tijd en ruimte zelf te bestuderen - de Large Hadron Collider (LHC) op CERN in Genève. De LHC is een cirkelvormige versneller die protonen versnelt tot hoge energie en ze vervolgens laat botsen. Op die manier worden de condities nagebootst die een miljardste van een seconde na de oerknal heersten, en zo kunnen we bestuderen waaruit ons heelal is opgebouwd en hoe het ooit is ontstaan.

De titel van mijn PhD-onderzoek is *Fusing the vector bosons; Higgs production through VBF and WW scattering at the current and future LHC*, en in de volgende paragrafen zal ik dat onderzoek samenvatten.

Het standaardmodel is de theorie die de deeltjeswereld beschrijft. Dit model maakt onderscheid tussen materiedeeltjes en deeltjes die betrokken zijn bij hun onderlinge interacties. De bouwstenen van materie zijn deeltjes als het elektron (e), elektronneutrino's (ν_e) en quarks (u, d, s, c, t, b), waarbij de laatste zogenoemde hadronen vormen, zoals protonen en neutronen. De onderlinge interacties kunnen worden opgedeeld in drie fundamentele krachten: de welbekende elektromagnetische kracht met als bijbehorend deeltje het foton (γ), de zwakke kernkracht, die een belangrijke rol speelt bij het vervallen van atoomkernen en gepaard gaat met zogeheten "vectorbosonen" zoals het W deeltje en het Z deeltje, en als laatste de sterke kernkracht die atoomkernen bij elkaar houdt via gluonen (g). Al de deeltjes in het standaardmodel staan weergegeven in figuur 96.

In de afgelopen tientallen jaren hebben verschillende experimenten het bestaan bevestigd van de deeltjes zoals ze worden voorspeld door het standaardmodel. Tevens bleken hun eigenschappen zeer nauwkeurig te kloppen met de theorie. Toch had de eerste formulering van het standaardmodel één fundamentaal zwak punt. Het ging er namelijk van uit dat alle deeltjes zoals weergegeven in figuur 96 *massaloos* zijn, volkomen in tegenstelling met onze waarnemingen. Dit probleem werd al in 1964 opgelost door de introductie van het *higgsmechanisme*, dat sinds die tijd als onderdeel van het standaardmodel wordt gezien. Het higgsmechanisme voorspelt het bestaan van een alomtegenwoordig higgsveld. De zogenoemde excitaties van dit veld vormen de higgsdeeltjes, ook wel higgsbosonen genoemd. Als de deeltjes uit het standaardmodel interacties aangaan met dit higgsveld, verkrijgen ze hun massa. Je zou het higgsveld kunnen zien als een siroopachtige substantie dat ons heelal vult. Hoe meer deze "higgssiroop" aan de deeltjes "kleeft", hoe meer weerstand de deeltjes voelen terwijl ze door het veld bewegen. Op die manier worden de deeltjes "zwaarder", terwijl deeltjes die geen interactie hebben met het higgsveld massaloos blijven.

Om de werking van dit higgsmechanisme aan te tonen, en daarmee ook de juistheid van het standaardmodel, hebben deeltjesfysici jarenlang naar het higgsdeeltje gezocht. In de

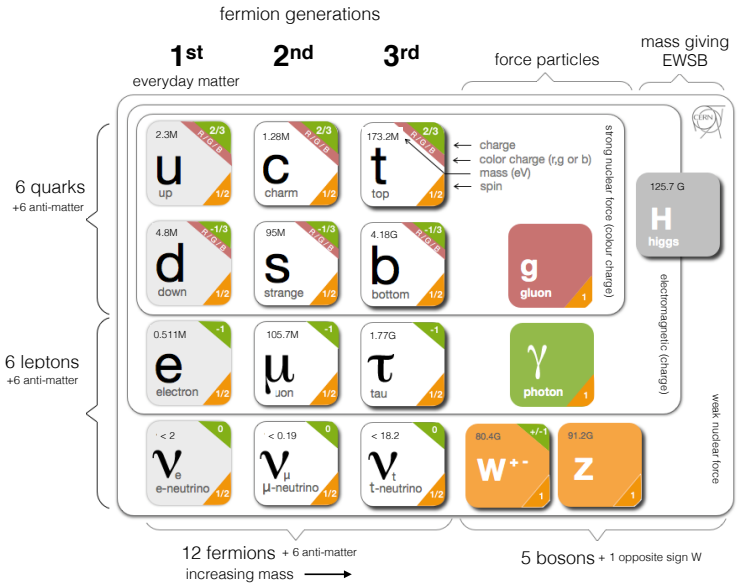

Figure 96.: De deeltjes in het standaardmodel en hun eigenschappen. Figuur komt oorspronkelijk uit [172]. De waarden voor de massa's komen uit [12].

zomer van 2012 was het zover: de twee grote experimenten van de LHC, ATLAS en CMS geheten, bevestigden het bestaan van een higssboson met een massa van $m_H \approx 125\,\text{GeV}$ [1] met een nauwkeurigheid van meer dan 5 standaarddeviaties[2]. Na deze ontdekking heeft men de eigenschappen van dit nieuwontdekte deeltje bestudeerd om te bevestigen dat het hier inderdaad om het higgsboson gaat zoals voorspeld door het standaardmodel, of dat het hier misschien een nieuw raadsel betreft dat opgelost moet worden.

We weten dus dat het standaardmodel veel fysische concepten nauwkeurig beschrijft, en toch weten we tegelijkertijd ook dat het niet de meest complete en ultieme theorie van ons universum is. Zo weten we niet hoe we de zwaartekracht in het model van de deeltjesinteracties kunnen inpassen en we hebben ook geen idee wat donkere materie precies is. Dit soort open vragen wijzen erop dat er "Nieuwe Fysica" zou moeten zijn.

Er zijn twee manieren om deze tot nu toe onzichtbare bijdragen van Nieuwe Fysica tóch te detecteren. Allereerst kunnen we op zoek gaan naar nieuwe interacties en/of nieuwe deeltjes. Een andere manier zou zijn om heel precies de eigenschappen van het higgsdeeltje en andere deeltjes uit het standaardmodel te meten, zoals hun productie- en vervalsnelheden, en zo op zoek te gaan naar afwijkingen van hun theoretische voorspellingen.

Het standaardmodel voorspelt verschillende productie- en vervalmechanismen voor het higgsboson. Zoals gezegd moet elk van deze mechanismen nauwkeurig onderzocht worden om met zekerheid vast te stellen dat het nieuwontdekte deeltje inderdaad het higgsboson is. De twee meest voorkomende productiemechanismen in de LHC (oftewel, degene met de

1 De electronvolt, of eV, is een eenheid van energie overeenkomend met $1.6 \cdot 10^{-19}$ J. In de deeltjesfysica rekenen we vaak in "natuurlijke eenheden", en dan geldt dat $c^2 = 1$. In dat geval kan de eV ook als massaeenheid worden gezien, overeenkomend met $1.8 \cdot 10^{-36}$ kg.

2 Dit betekent dat de waarschijnlijkheid dat deze observatie een toevallig fluctuatie is en dus niet een nieuw deeltje, één op de 3,5 miljoen is.

grootste werkzame doorsnede of *cross section*), zijn gluon-gluonfusie (ggF) en vectorbosonfusie (VBF). De Feynman-diagrammen van deze processen staan weergegeven in figuur 97.

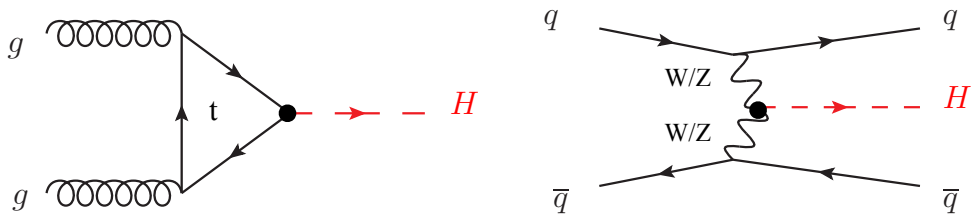

Figure 97.: De Feynman-diagrammen voor higgsproductie via gluon-gluonfusie (links) en vectorbosonfusie (rechts). De zwarte punten stellen de koppelingen voor tussen de zware quarks en het higgsboson (in het geval van ggF) of tussen de vectorbosonen en het higgsboson (in het geval van VBF).

Het ggF mechanisme zegt iets over de koppelingen van het higgsboson met de zware quarks (t,b), terwijl het minder vaak voorkomende VBF mechanisme iets zegt over de koppelingen van het higgsboson met de vectorbosonen, namelijk de W en de Z. Het higssboson met $m_H \sim 125\,\text{GeV}$ vervalt het vaakst in een $b\bar{b}$ quarkpaar of een paar van vectorbosonen.

Tot nog toe zijn niet alle combinaties van productie- en vervalmechanismen van het higgsboson waargenomen. Dit proefschrift bevat het onderzoek naar één zo'n combinatie van productie en verval: higgsproductie via VBF en het verval naar twee W bosonen, die vervolgens uit elkaar vallen naar een lepton-neutrinopaar: $H \to WW^{(*)} \to \ell^+\nu_\ell\ell^-\bar{\nu}_\ell$.

De VBF analyse bestudeert alle data van proton-protonbotsingen die in 2012 met de ATLAS detector is verzameld. Gedurende die periode was de botsingsenergie (*center of mass*) van de protonbundels 8 TeV. De analyse laat een piek van signaal-*events* zien van 3,2 standaarddeviaties ten opzichte van de achtergrond. Daarmee is deze meting het eerste bewijs van het bestaan van VBF productie in het $H \to WW^{(*)}$ vervalskanaal. Figuur 98 (links) laat de geobserveerde "overmaat" aan data zien in de distributie van de transverse massa m_T. Deze grootheid stelt de invariante massa van de deeltjes in de eindtoestand in het loodrechte vlak voor en wordt als discriminant gebruikt in de uiteindelijke fit[3].

Om te bepalen hoe goed de geobserveerde VBF productiesnelheid overeenkomt met de voorspelling van het standaardmodel, wordt de *signaalsterkte* μ_{VBF} gedefinieerd, die de verhouding weergeeft tussen deze twee grootheden:

$$\mu_{\text{VBF}} = \sigma^{\text{SM}}_{\text{VBF}} / \sigma^{\text{obs}}_{\text{VBF}}. \tag{124}$$

Als $\mu_{\text{VBF}} = 1$, dan geldt dat de data overeenkomt met het standaardmodel. De geobserveerde signaalsterkte voor de VBF productiemodus in het $H \to WW^{(*)}$ kanaal is gelijk aan

$$\hat{\mu}^{\text{obs}}_{\text{VBF}} = 1.27\,^{+0.44}_{-0.41}\,(\text{stat.})\,^{+0.30}_{-0.21}\,(\text{syst.}) = 1.27^{+0.53}_{-0.45}\,. \tag{125}$$

3 De VBF $H \to WW^{(*)}$ analyse is op twee onafhankelijke manieren uitgevoerd; de *cut-based* analyse die signaal-*events* selecteert op basis van achtereenvolgende selectiecriteria en de *multivariate* analyse (MVA). De laatste resulteerde in een hogere verwachte significantie van het VBF signaal en is daarom gekozen als de nominale VBF $H \to WW^{(*)}$ analyse. De *cut-based* analyse, die in dit proefschrift beschreven staat, resulteert in een significantie van 3,0 standaarddeviaties. De bijbehorende distributie van m_T staat weergegeven in figuur 98 (links). De MVA analyse vindt een significantie van 3,2 standaarddeviaties en is gecombineerd met de ggF productie in de uiteindelijke fit (zie figuur 98, rechts)

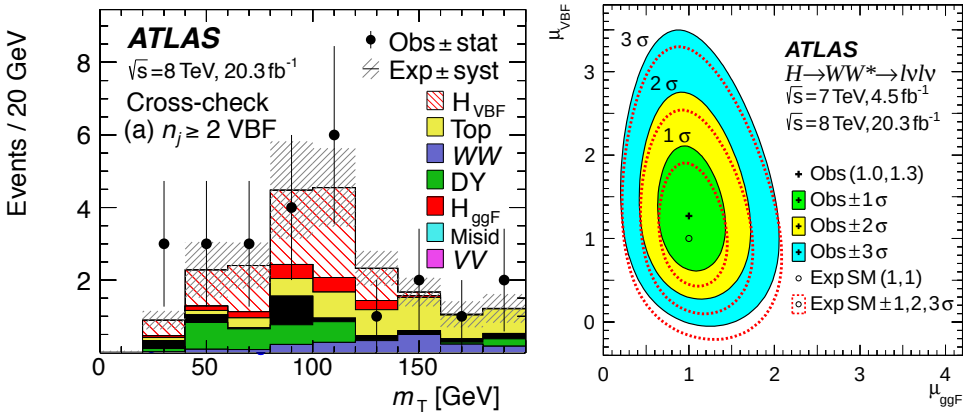

Figure 98.: Links: distributie van de *transverse massa* na dataselectie voor het higgsboson geproduceerd door vectorbosonfusie en vervallen naar $H \to WW^{(*)} \to \ell^+\nu_\ell\ell^-\bar{\nu}_\ell$ eindtoestanden. Rechts: contourplot van de 2D *likelihood* van μ_{VBF} versus μ_{ggF}. Vergeleken worden de geobserveerde en voorspelde waarden voor de dataset uit 2012 (met een botsingsenergie van 8 TeV) en de dataset uit 2011 (met een botsingsenergie van 7 TeV). De waarde voor de beste fit is aangegeven met een kruisje. Het open rondje is de waarde zoals verwacht door het standaardmodel.

Deze meting is vervolgens gecombineerd met de ggF meting voor de signaalsterkte in het $H \to WW^{(*)}$ kanaal, zie ook figuur 98 (rechts). Uit die combinatie komt

$$\mu^{\text{obs}}_{\text{ggF+VBF}} = 1.09\,^{+0.16}_{-0.15}\,(\text{stat.})\,^{-0.14}_{+0.17}\,(\text{syst.}). \tag{126}$$

De conclusie is dat de gemeten signaalsterkte geen aanwijzing geeft voor het bestaan van Nieuwe Fysica: binnen de onzekerheden bevestigt deze meting het standaardmodel.

Momenteel worden de signaalsterktes, vooral μ_{VBF}, nog gedomineerd door de statistische onzekerheden, vanwege de kleine dataset. In de komende tientallen jaren zal echter veel meer data verzameld worden, zal de botsingsenergie toenemen en zullen zowel de LHC als de LHC-experimenten verschillende upgrades krijgen.

Vanwege die upgrades is in dit proefschrift een haalbaarheidsonderzoek gedaan naar de VBF $H \to WW^{(*)}$ signaalsterkte in een toekomstige LHC. Met tien keer zoveel data zal de precisie van μ_{VBF} verbeteren van de huidige $\sim$ 42% naar $\sim$ 25%. Met 100 keer meer data wordt $\sim$ 15% verwacht.

De systematische onzekerheden hebben een kleiner effect op μ_{VBF}. Maar naarmate de datasets groter worden, neemt het belang van de statistische onzekerheden af, waardoor de systematische onzekerheden belangrijker worden. Voor een juiste interpretatie van de data is het daarom noodzakelijk om de verschillende bijdragen van deze onzekerheden te begrijpen en zo mogelijk te verkleinen.

In dit proefschrift wordt één bepaalde systematische onzekerheid nauwkeurig bestudeerd: het modelleren van *top*-quark paarproductie. Dit vormt een grote achtergrond in de VBF $H \to WW^{(*)}$ analyse, die ook wel de top-achtergrond wordt genoemd. Deze systematische onzekerheid kent verschillende bronnen. Deze bronnen zijn bestudeerd en verder is er een optimalisatie gedaan van de *event*-selectie van de top-achtergrond. Naar aanleiding hiervan bleek dat verschillende bronnen van systematische onzekerheden verwaarloosd kunnen

worden, waardoor de invloed van deze onzekerheden voor de top-achtergrond verminderd wordt tot maximaal 50%.

Het higgsmechanisme genereert niet alleen massa's voor de deeltjes in het standaardmodel, maar het lost ook andere "problemen" op. Een voorbeeld is de verstrooiingsdoorsnede (*scattering cross section*) van de twee longitudinaal gepolariseerde W bosonen. Deze neemt toe met toenemende verstrooiingsenergie en dat zou op een gegeven moment de unitariteit schenden, als het higssboson deze effecten niet precies ongedaan zou maken. Het nauwkeurig bestuderen van de WW verstrooiing zou uitsluitsel kunnen geven over de vraag of het inderdaad alleen het higgsboson is dat verantwoordelijk is voor het onder controle houden van de WW verstrooiingsdoorsnede, of dat er ook andere, tot nu toe onbekende effecten van Nieuwe Fysica bijdragen.

Dit proefschrift bestudeert ook de voordelen van een uitgebreidere dekking van de *tracking*-systemen in een toekomstige ATLAS-detector die operationeel moet zijn in 2026. In het bijzonder wordt dan de WW verstrooiing bekeken en de verbetering in de gevoeligheid voor de standaardmodel- en de Nieuwe Fysicametingen. Het vergroten van deze dekking[4] tot $|\eta| \leq 4.0$ verhoogt de significantie van het standaardmodelsignaal met bijna 100% ten opzichte van de huidige dekking van $|\eta| < 2.5$, en verbetert de gevoeligheid voor Nieuwe Fysica met $\approx 50\%$.

De eerste periode met botsingen in de LHC ligt achter ons en heeft één van de grootste ontdekkingen van onze tijd opgeleverd: het higssboson. Alle eigenschappen die we tot nu toe van dit higgsdeeltje hebben gemeten wijzen erop dat het inderdaad het higgsdeeltje is zoals voorspeld door het standaardmodel. Desondanks leidt de ontdekking van dit deeltje met $m_H \sim 125\,\text{GeV}$ onmiddellijk tot nieuwe vragen, zoals: is dit het enige higgsdeeltje of zijn er meer, en waarom dan? Voor mij ligt daar de schoonheid van de natuurkunde: dat voor elke vraag die we beantwoorden, er meteen weer nieuwe bijkomen. Er is altijd iets nieuws om te beschrijven, om te ontdekken en om te begrijpen. Het universum is een onophoudelijke bron van spannende puzzels. Daarom hoop ik dat de herstart van de LHC in het afgelopen voorjaar met een hogere botsingsenergie van 14 TeV ons nieuwe, verrassende inzichten zal verschaffen over waaruit het universum is opgebouwd en hoe het ooit is ontstaan.

4 Deze wordt uitgedrukt in de zogeheten *pseudorapidity* η, de hoek tussen de baan van een deeltje ten opzichte van de bundelpijp, gedefinieerd als $\eta = -\ln\tan(\theta/2)$. $\eta = 0$ betekent dat de baan loodrecht op de bundelpijp staat en $\eta = \infty$ betekent een deeltje dat parallel aan de bundelpijp beweegt.

POVZETEK

Mogoče bo ta stavek zvenel preveč poetično, vendar sem bila že od nekdaj očarana nad Vesoljem in vsemi njegovimi *skrivnostmi*. Že kot otrok sem bila navdušena nad črnimi luknjami in številnimi zvezdami v naši Mlečni cesti. Vsakič, ko sem vstopila v svet znanstvene fantastike, sem sanjarila kako bom nekega dne tudi sama raziskovala Vesolje. Na žalost, človeštvu še ni uspelo izumiti *Warp* pogona, zato nisem še imela priložnosti križariti po Mlečni cesti na krovu *Enterprise*-a. Čeprav bi bilo mogoče res bolj razburljivo včasih naleteti na črvine, pa lahko v današnjem času raziskujemo Vesolje tudi v udobju našega domačega planeta. Kot doktorska študentka sem imela možnost prisostvovati pri najmočnejšem "mikroskopu" na Zemlji, ki nam dovoljuje vpogled v strukturo protora in časa. To je veliki hadronski pospeševalnik (LHC), ki je stacioniran v CERNu, v Ženevi. LHC je krožni pospeševalnik, ki pospešuje in trka protone pri zelo velikih energijah. Tako ustvarja pogoje enake tistim nastalim eno bilijoninko sekunde po Velikem Poku, kar nam dovoljuje vpogled v to iz česa je Vesolje sestavljeno in kako se je vse skupaj sploh začelo. V naslednjih odstavkih bom povzela svoje doktorsko delo z naslovom *Fusing the vector bosons: Higgs production through VBF and WW scattering at the current and future LHC* (*Fuzija vektor bozonov: produkcija Higgsovega bozona preko VBF in sipanje WW bozonov pri trenutnem in prihodnjem LHC-ju*).

Teorija, ki opisuje svet osnovnih delcev, se imenuje Standardni model (krajše SM) in deli delce na tiste, ki sestavljajo snov okoli nas in na tiste, ki posredujejo interakcije med njimi. Osnovni gradniki snovi so delci, kot so: elektron (e), elektronski nevtrino (ν_e) in kvarki (u, d, s, c, t, b), kateri sestavljajo hadrone, kot sta proton in nevtron. Tri fundamentalne sile opisujejo interakcije med osnovnimi delci. Prva je vsem dobro poznana elektromagnetna sila, ki jo prenaša foton (γ), druga je šibka sila, ki igra ključno vlogo pri jedrskih razpadih in jo prenašata W in Z vektor bozona, tretja pa je močna sila, ki poskrbi, da so protoni in nevtroni vezani v atomsko jedro in jo prenašajo gluoni (g). Osnovni delci SM so prikazani na sliki 99.

Številni poskusi so v preteklih desetletjih potrdili obstoj vseh osnovnih delcev, ki jih napoveduje SM in njihove izmerjene lastnosti se z veliko natančnostjo skladajo s teoretičnimi napovedmi. SM pa ima vseeno bistveno pomankljivost, saj predpostavlja, da so vsi osnovni delci *brez* mase, kar pa se ne sklada z našimi opažanji. Higgsov mehanizem, ki je bil zasnovan že leta 1964, odpravi to pomankljivost in danes predstavlja osnovni del SM. Higgsov mehanizem napove obstoj vseprisotnega Higgsovega polja (vzbuditev katerega je delec - Higgsov bozon), ki prek interakcije z osnovnimi delci le-tem ustvari maso. Higgsovo polje si lahko predstavljamo kot nekakšno nevidno, *medu* podobno snov, ki zapolnjuje Vesolje. Bolj kot se *Higgsov med* lepi na osnovne delce, več upora čutijo medtem ko potujejo po njem, kar se izraža v njihovi večji masi. Tisti delci, ki pa ne interagirajo s *Higgsovim medom* ostanejo brez mase, kot na primer foton.

Fiziki že vrsto let iščejo Higgsov bozon, da bi lahko potrdili Higgsov mehanizem in s tem dokončno potrdili veljavnost SM. Po 40-ih letih iskanja sta dva splošna LHC-jeva eksperimenta, ATLAS in CMS, julija 2012 končno potrdila obstoj Higgsovega bozona (z maso $m_H \approx 125\,\mathrm{GeV}$ [1]) s signifikanco več kot 5 standardnih deviacij[2]. Od takrat pa znanstveniki z

1 Enota elektronvolt, eV, je enota za energijo, ki je enaka $1.6 \cdot 10^{-19}$ J. V fiziki osnovnih delcev (s predpostavko t.i. naravnih enot, kjer je $c^2 = 1$) se enota eV uporablja tudi za enoto mase in je enaka $1.8 \cdot 10^{-36}$ kg.

2 Verjetnost, da bi bila ta meritev le naključna fluktuacija in ne nov delec, je 1 : 3.5 milijonov.

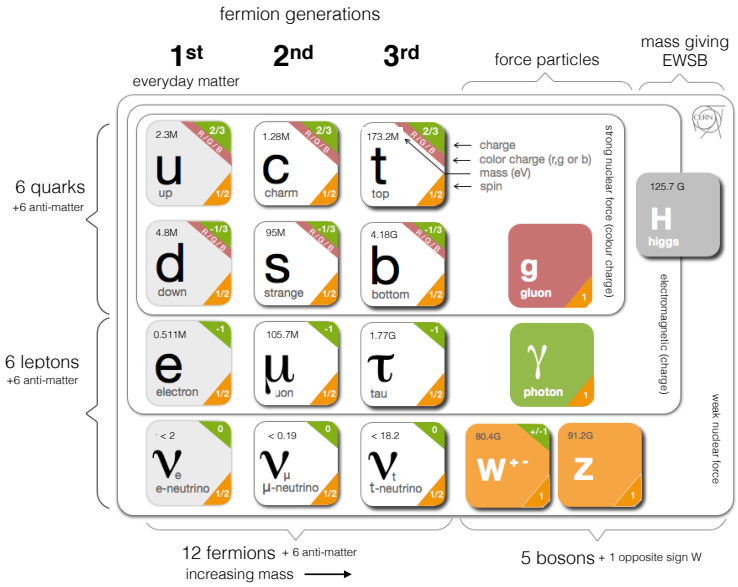

Figure 99.: Osnovni delci v SM in njihove lastnosti. Slika je bila spremenjena po [172]. Mase osnovnih delcev so vzete iz [12].

velikim zanimanjem natančno merijo vse lastnosti novega delca, saj je potrebno preveriti ali je novo odkriti Higgsov bozon resnično tak kot ga napoveduje SM ali pa je le še ena uganka več, ki jo moramo rešiti.

Čeprav SM pravilno opiše številne fizikalne pojave vemo, da to ni končna teorija Vesolja. Preveč je odprtih vprašanj, da bi lahko trdili drugače. Na primer, še vedno ne vemo kako vpeljati gravitacijo med ostale tri fundamentalne sile in še vedno ni povsem jasno kaj je to črna snov. Vsa odprta vprašanja potrjujejo obstoj Nove Fizike, katere zakoni so nam še neznani. Novo Fiziko lahko zaznamo tako, da iščemo nove interakcije med delci ali pa kar nove osnovne delce. Lahko pa tudi z izjemno natančnostjo izmerimo lastnosti Higgsovega bozona in vseh ostalih osnovnih delcev Standardnega modela, njihove produkcijske in razpadne načine in te meritve primerjamo s teoretičnimi napovedmi SM. Vsako najmanjše odstopanje meritev od teoretičnih napovedi nam lahko pove nekaj o strukturi Nove Fizike.

Higgsov bozon lahko nastane in razpade na več različnih načinov. Vse te načine je potrebno temeljito preučiti, da lahko potrdimo ali je novo odkriti delec res Higgsov bozon, kot ga napoveduje SM. Dva najpogostejša načina nastanka Higgsovega bozona pri trkih protonov na LHC-ju sta fuzija gluonov (ggF) in fuzija vektor bozonov (VBF). Njuna Feynmanova diagrama sta prikazana na Sliki 100. Prek ggF lahko izmerimo sklopitev Higgsovega bozona s težkimi kvarki (t, b), prek VBF pa sklopitev Higgsovega bozona z vektor bozoni W in Z. Higgsov bozon, z maso $m_H \sim 125\,\mathrm{GeV}$, najpogosteje razpade na par b-kvarkov ($b\bar{b}$) in na par vektor bozonov. V letih po odkritju Higgsovega bozona nam še ni uspelo izmeriti vsake možne kombinacije njegovega nastanka in razpada. Ta doktorska disertacija je posvečena eni izmed teh kombinacij, in sicer iskanju Higgsovega bozona, ki nastane prek fuzije vektor bozonov in razpade na par W bozonov, kateri posledično razpadejo na par elektron-nevtrino, $H \to WW^{(*)} \to \ell^+\nu_\ell\ell^-\bar{\nu}_\ell$.

Analiza meritev VBF $H \to WW^{(*)}$, ki jo to doktorsko delo opisuje, vključuje trke protonov zbrane z detektorjem ATLAS v letu 2012, pri težiščni energiji trkov 8 TeV. Presežek

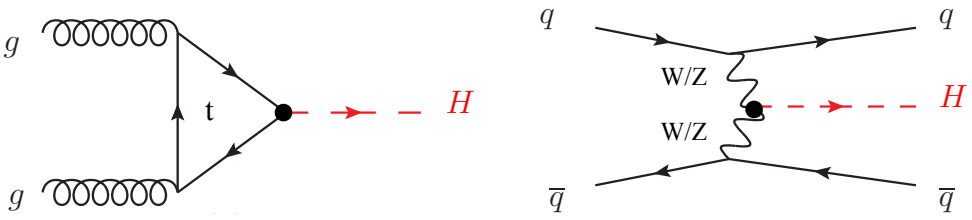

Figure 100.: Feynmanova diagrama nastanka Higgsovega bozona prek fuzije gluonov - ggF (levo) in fuzije vektor bozonov - VBF (desno). Črni krogci nakazujejo sklopitev med Higgsovim bozonom in težkimi kvarki (ggf) ter vektor bozoni (VBF).

izmerjenih dogodkov VBF $H \to WW^{(*)}$ nad ozadjem[3] je ekvivalentno signifikanci signala 3.2 standardnih deviacij in prvič potrdi *dokaz* za produkcijo VBF Higgsovega bozona v razpadu $H \to WW^{(*)}$. Slika 101 (levo) prikazuje presežek izmerjenih dogodkov VBF $H \to WW^{(*)}$ kot funkcijo transverzalne mase m_T (invariantna masa vseh končnih delcev v transverzalni ravnini), ki predstavlja diskriminanto v statistični analizi.

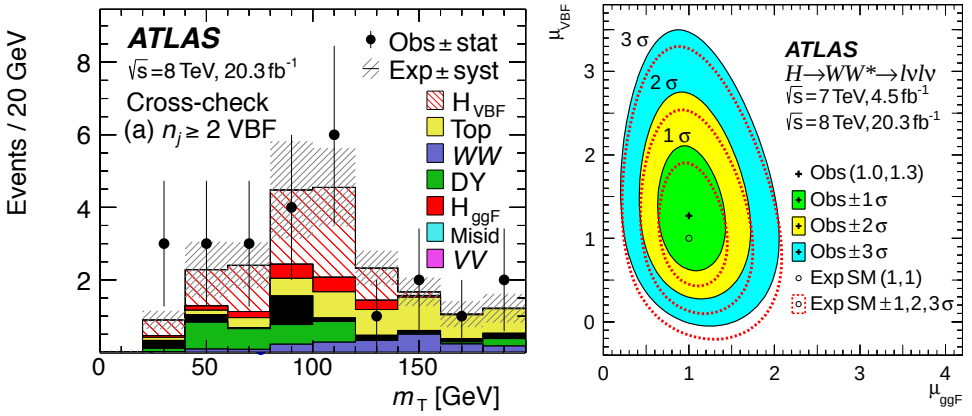

Figure 101.: Levo: Distribucija transverzalne mase na koncu izbire dogodkov VBF $H \to WW^{(*)} \to \ell^+\nu_\ell\ell^-\bar{\nu}_\ell$. Desno: 2D verjetnostna porazdelitev μ_{VBF} proti μ_{ggF}, ki primerja njune pričakovane in izmerjene vrednosti za podatke iz leta 2012 pri težiščni energiji 8 TeV in leta 2011 pri težiščni energiji 7 TeV. Najboljše ujemanje izmerjenih vrednosti je prikazano s križcem. Krožec pa prikazuje pričakovano vrednost po SM.

Da bi lahko primerjali izmerjeno vrednost VBF produkcijskega reda Higgsovega bozona z napovedmi SM, zapišemo *moč signala* kot razmerje med teoretično napovedjo in meritvijo;

$$\mu_{\text{VBF}} = \sigma^{\text{SM}}_{\text{VBF}} / \sigma^{\text{obs}}_{\text{VBF}}. \tag{127}$$

Če je μ_{VBF} enaka ena, se meritev sklada s teoretičnimi napovedmi SM.

Izmerjena moč signala je za produkcijski red VBF pri $H \to WW^{(*)}$ razpadu enaka

$$\hat{\mu}^{\text{obs}}_{\text{VBF}} = 1.27\,^{+0.44}_{-0.41}\,(\text{stat.})\,^{+0.30}_{-0.21}\,(\text{syst.}) = 1.27^{+0.53}_{-0.45}. \tag{128}$$

3 To so različni razpadi delcev, ki zakrivajo Higgsov signal, kot so na primer razpadi top kvarkov (označeni "Top" na sliki 101 levo) ali pa process $Z \to ee, \mu\mu$ (označeni "DY" na sliki 101 levo).

V končni meritvi za $H \to WW^{(*)}$ razpad je meritev produkcije VBF združena s produkcijo ggF (glej sliko 101 desno) in moč signala za ggF+VBF znaša

$$\mu^{\text{obs}}_{\text{ggF+VBF}} = 1.09\,^{+0.16}_{-0.15}\,(\text{stat.})\,^{-0.14}_{+0.17}\,(\text{syst.}). \tag{129}$$

Izmerjena vrednost moči signala potrjuje veljavnost SM v skladu z napakami. Natančnost trenutnih meritev je (še posebej za μ_{VBF}) zaznamovana s statističnimi napakami (napake zaradi premajhnega števila izmerjenih dogodkov) in ne toliko s sistematičnimi napa- kami. Za LHC in njegove eksperimente so v naslednjih desetletjih predvidene nadgradnje, ki bodo omogočale, da detektorji zberejo večjo količino trkov (pri večjih težiščnih energijah) in s tem zmanjšajo statistične napake. Rezultati študije, opisane v tem doktorskem delu, kažejo na to, da se pri desetkratnemu povečanju količine zabeleženih trkov, natančnost meritve μ_{VBF} izboljša iz trenutnih $\sim 42\,\%$ na $\sim 25\,\%$. S še dodatnim desetkratnim povečanjem količine izmerjenih trkov (stokrat več od trenutnih vrednosti), se natančnost meritve μ_{VBF} izboljša na $\sim 15\,\%$.

Večje število zabeleženih trkov pri prihodnjem LHC-ju bo zmanjšalo vpliv statističnih napak na natančnost meritve μ_{VBF} in s tem povečalo vpliv sistematičnih napak. Za pravilno interpretacijo meritev je ključno, da vse prispevke k sistematičnim napakam dobro razumemo in jih zmanjšamo. Sistematične napake imajo posebno mesto tudi v tem doktorskem delu, kjer jih obravnavamo v sklopu enega največjih ozadij v analizi VBF $H \to WW^{(*)}$ - produkcija para top kvarkov (od tu naprej poimenovanega top ozadje). S pomočjo študije opisane v tem doktorskem delu, smo lahko zanemarili več različnih prispevkov k sistematični napaki top ozadja in s tem zmanjšali njen vpliv na končno meritev signifikance signala za največ 50 %.

Poleg tega, da priskrbi maso določenim osnovnim delcem, Higgsov mehanizem razreši tudi druge, ne-fizikalne pojave, kot je sipanje dveh W bozonov. Sipalni presek za sipanje dveh longitudinalno polariziranih W bozonov narašča z naraščujočo energijo sipanja in bi na neki točki lahko kršil unitarnost. Higgsov bozon, kot ga napove SM, pa ravno pokrajša člene, ki povzročajo kršitev unitarnosti. Prav zato je podrobno preučevanje sipanja dveh WW bozonov odlična priložnost za raziskovanje ali je Higgsov bozon res edini odgovoren za ohranjanje unitarnosti ali pa je mogoče prisoten še kakšen mehanizem Nove Fizike. V tem doktorskem delu smo analizirali prednosti večje pokritosti sledilnega sistema prihodnjega detektorja ATLAS (v uporabi nekje okoli 2026) na mertive signifikance sipanja WW bozonov. Z razširitvijo detektorja[4] od $|\eta| < 2.5$ do $|\eta| \leq 4.0$, se za skoraj 100 % poveča signifikanca signala in za skoraj 50 % občutljivost na prispevke Nove Fizike.

Prvi del LHC-jevega zajemanja podatkov, ki je poskrbel za enega največjih odkritij našega časa - Higgsov bozon, je za nami. Vse izmerjene lastnosti Higgsovega bozona kažejo na to, da je to res Higgsov bozon, ki ga napoveduje SM. Čeprav je odkritje Higgsovega bozona razrešilo 40-let staro uganko, nam je obenem postavilo nova vprašanja, kot recimo: Ali je to edini Higgsov bozon (in zakaj?) ali pa jih je več? Zame je lepota fizike ravno v tem, da se nam za vsako vprašanje na katerega najdemo odgovor, poraja še nekaj novih vprašanj. Vedno je še nekaj kar lahko odkrijemo, opišemo in razumemo. Vesolje je neskončna zaloga zanimivih ugank in ponovni zagon LHC-ja v začetku letošnje pomladi, z višjo težiščno energijo trkov (14 TeV), nam lahko že v bližnji prihodnosti prinese presenetljiva nova dognanja o tem iz česa je Vesolje sestavljeno in kako se je vse skupaj sploh začelo.

4 Pokritost detektorja za sledenje se izraža s pseudorapidnostjo η, ki predstavlja kot trajektorije delca relativno na smer protonskega žarka in je definirana kot $\eta = -\ln\tan(\theta/2)$. $\eta = 0$ predstavlja trajektorijo, ki je vzporedna smeri vpadnih protonov in $\eta = \infty$ predstavlja trajektorijo, ki je pravokotna na smer vpadnih protonov.

ACKNOWLEDGEMENTS

Looking back, these past four years were some of my most intense years so far. I have gained so many new experiences and insights, but most importantly, I have met so many amazing people who made these four years even more special and colourful. For that, I am very grateful. Because *feeling gratitude and not expressing is like wrapping a present and not giving it* and because I strongly believe in *sharing is caring*, I would like to say thank you to all the remarkable people who walked with me on this road to obtain my PhD, whether just passing by or steadily by my side.

I will start by thanking my two co-promotors; Dr. Pamela Ferrari and Dr. Nigel Hessey and to my promotor Prof. Dr. Stan Bentvelsen.

Pamela, you took me under your wing when I went to CERN and remained my supervisor until the very end for which I am very grateful. Thank you for all the fruitful discussions, guidance and advice you have given me, but most importantly, thank you for your honesty and for your personal touch. I am glad we had the chance to work together and I hope we will manage to have a real caipiroska soon!

Nigel, thank you for your support, especially at the beginning of my PhD. Even if work-wise things did not turn out the way we initially planned, I really enjoyed working with you. Thank you for introducing me to the ATLAS upgrade, for cycling across Stanford campus, for giving me the opportunity to have my photo taken with Morgan Freeman and thank you for all the laughs and stories.

Stan, I am very grateful for the opportunity you have given me to be a part of the ATLAS group at Nikhef. I still vividly remember my first skype interview and how you made my crazy plan work of finishing my diploma thesis, arranging everything for my 3 months of travelling and starting my PhD the moment I landed back home. Thank you for your enthusiasm about particle physics!

I would also like to thank Dr. Tatjana Lentz, Prof. Dr. Olya Igonkina, Prof. Dr. Els Koffeman, Dr. Wim Beenakker, Prof. Dr. Paul de Jong, Dr. Jos Engelen and Prof. Dr. Raimond Snellings for being in my doctorate committee and for all their constructive comments that further improved this thesis.

During my PhD I have met many great physicists with whom I worked. Sharing and discussing ideas, and together solving problems is for me one of the perks of a being a physicist. Among others I would like to thank Dr. Jennifer Pai-hsien Hsu, Dr. Johanna Bronner, Dr. Heberth Torres, Dr. Richard Polifka, Dr. Doug Schaefer, Dr. Doug Schouten, Dr. Jessica Metcalfe, Dr. Stefano Frixione and Dr. Bryan Webber for their help, advice, and support.

The summer of 2009 was one of the best summers of my life. It was my first summer at CERN and at that point I completely fell in love with the world of particle physics. Just being there was thrilling enough but on top of that, I was surrounded by many extraordinary people who enriched my life and some of them continue to do so until this day.

Alis, *Parece que el ciclón ya se fue y ya se pueden ver las estrellas* - don't even try to deny it, we both know this is your favourite song too. Thank you for all the talks we had lurking in

the Nikhef hallways, thank you for your Cuban warmth (maybe fire is a better word for it), friendship, honesty and for re-defining the concept of 'consistency' in my dictionary.

Jeroen, looking back you were somehow connected with all the big steps I took in the past six years. Thank you for your inspiring empathy, late night walks and philosophising, thank you for your friendship, enthusiasm, creativity and your delicious cooking. Thank you for showing me how free a person can be.

Thanks to all the happy people at Nikhef and CERN who made my working days shorter: (in no particular order) Panos, Ingrid and Vince (thanks for the tapas and cervecitas muy frescitas in Barcelona), Nikos, Joerg, Antonino, Fernando (thank you for your Argentinian spirit and all the alfajores), Joern, Rolf, Afroditi, Koen, Rogier, Daniël, John, Ivan, Tim, Gabrielle, Roel, Siim, Elmar the Australian and Habibi (thank you for Hungary), Magdalena, Andrej and Matevž (for keeping the Slovenian spirit high, all the pizzas and all the Irish folk music) and all the other Nikhef/CERN colleagues and personnel who helped making my PhD days lighter.

Rosemarie, thank you for your laughter and for all the talks we had. Thank you for your enthusiasm over life, for being happy and bouncy. Having you as an officemate and as a friend made the last year of my PhD so much more special.

To Pier and Pierfrancesco, I say thank you for the music! Pierito - thank you for the amazing time we had at CERN. Thank you for all the guitar lessons, for being my unofficial postdoc and for all the advice and help you have given me. "Thank you" for making me addicted to crepes and pizzas from R1. I wanted to write you a poem from all the songs we both adore, but *I ain't no lady writer*; so thank you for *the fez*, for *the attitude*, for *the lust for life* and most importantly for *the fireplug*. Peolino - thank you for your sincerity and your relaxed perspective on life, for making me laugh so many times and for all that Thai. You made each Veldhoven a bit friskier. Thank you both for being my paranymphs, for the Rolling Stones and for all the numerous puns and jokes we make when we manage to end up in the same time and space. And remember, *looove is eeeeverywheeeere...*

Just living in Amsterdam is an experience in itself, yet a few people managed to make it even more incredible.

Daan and Serena, you were the best roommates I could ever wish for. Thank you! The Tweede Looiersdwarsstraat housed several of my most memorable times in Amsterdam. Somehow, a common point to most of them was the amazing roof terrace...do you remember our pool party?

Robin, Mirna and Isolde, thank you for keeping the summer spirit alive and kicking under the -30° and 100 km/h winds at Vlieland.

Kat and Saskia, you two made Dutch sound easy, thank you for all the good times we had together and let's never let the distance come between us.

M'n halfje Jorik, there aren't enough words to describe how grateful I am to/for you, thank you for making everything look so simple and easy, for making me smile, for all the shenanigans, for sitting tight with me during this roller-coaster ride called thesis writing. Your endless amount of patience, kindness and love, curiosity and wittiness never cease to amaze me. Thank you for the past three years! Sharing them with you made everything a bit brighter and more colourful. And let's not forget the *joy* your silly jokes bring me. I'm looking forward to all of our future adventures, and I promise: it will never be boring!

Knowing Jorik significantly enlarged my circle of friends. Thanks to 'the gang' (Flori, Rianne, Arul, Paul, Victoria, Nai Jai) for all the movie nights, games and fun! The Kool -

Kwakkel families, thank you for the gezelligheid and for being my second family away from home. Jaap and Carla, thank you for your hospitality, warmth and all the walks. Marijn, thank you for your serenity and all the inspiring conversations.

Leaving home is never easy and I am very grateful to my family for all their love and support. Mama, hvala, ker vedno vidiš lepoto in dobroto v ljudeh. Hvala, ker me znaš vedno potolažiti. Hvala za tvojo skrb in hvala za vse konzerve Rio Mare, za vse potice in marmelade in paketke Barcaffeta, ki mi jih vztrajno pošiljaš v Amsterdam. Tata, hvala za nasvet, ki mi je zelo olajšal te zadnje, stresne mesece; ko stvari letijo iz rok je potrebno samo nekajkrat vdihniti in izdihniti (magari it še na kako passeggiato), se vprašati kaj sploh počneš v tistem trenutku in vse bo šlo na svoje mesto. Žuža, ti si eden najbolj ljubečih in skrbnih ljudi kar jih poznam in gledati kako se spreminjaš in rasteš mi je v veliko inspiracijo. Hvaležna sem za najin skupni smeh in zato, ker nama po petih minutah, ko se ponovno vidiva vedno uspe priti nazaj na stopnjo pet-letnega otroka. Hvala ti za vse neumnosti, ki sva jih (in jih še bova) ušpičili in za vsa potovanja, ki so vedno polna dogodivščin. Hvala šeštra, ne! Hvala še mojim fantastišim tetam - Bredi, Danjeli, Marini ter nonama, nonotu in teti Mariji za njihovo navdušenje vsakič, ko pridem domov.

In nenazadnje, hvala še vsem mojim ne-krvnim sestram in njihovim otročkom: Tamara in Svarun, hvala vama, da sem bila lahko del vajine zgodbe od začetka. Hvala za vse navdihujoče pogove in misli. Hvala, ker sta vedno z mano - čarovnija, ki se je zgodila 19.10.2013 me vedno spremlja. Mateja in Izabela, hvala za vse kapučinčke v Nane baru in za to, da ko pridem domov se vedno počutim kot, da nikoli sploh ne bi odšla. Petra, hvala, ker nama vedno uspe ustaviti čas, ko se vidiva. Eva in Ivana, hvala za vse žurkice in za vajine navdihujoče štorje.

Nika Valenčič, Amsterdam, August 2015.